KU LEUVEN

ARENBERG DOCTORAL SCHOOL

FACULTY OF SCIENCE

Universiteit Antwerpen

Chemistry and Plasma Physics Challenges for 2D Materials Technology

September 2019

Markus H. Heyne

Supervisors:
Prof. Stefan De Gendt
Prof. Erik C. Neyts

Dissertation presented in partial
fulfilment of the requirements for the
degree of Doctor of Science (PhD): Chemistry

CHEMISTRY AND PLASMA PHYSICS CHALLENGES FOR 2D MATERIALS TECHNOLOGY

Markus Hartmut Heyne

Supervisors:
Prof. Stefan De Gendt (KUL)
Prof. Erik C. Neyts (UA)

Members of the
Examination Committee:
Prof. Marc Heyns (KUL)
Prof. Steven De Feyter (KUL)
Prof. Annelies Delabie (KUL)
Prof. Annemie Bogaerts (UA)
Prof. Fred Roozeboom (TU/e)
Dr. Jean-François de Marneffe (imec)

Dissertation presented in partial fulfilment of the requirements for the degree of Doctor of Science (PhD): Chemistry

September 2019

Uitgegeven in eigen beheer, Markus Heyne, Leuven

Acknowledgment

The research on 2D materials has grown tremendously over the last years and I am glad to have gotten the opportunity to enter this field in such an exciting time. This offered the chance for discovering pioneering inventions in a very competitive field. I grew a lot with all the solved and unsolved challenges of this project and learned what it means to have a clear vision, plan, and analysis of observations and how important it is to look very closely into the details of a phenomenon. Besides the impact of all those technical challenges, the surrounding people over the years of research had probably even the larger influence on me. This work would not have been possible without them. I would like to thank Prof. Stefan De Gendt for giving me the opportunity to conduct this research project and for supervising this work. His analytic view on the experimental preparation, the discussions on the outcome, and interpretation of results were essential to sharpen the objective view on every aspect and to put it in the right perspective. Furthermore, I would like to acknowledge Prof. Erik C. Neyts from the University of Antwerp for his valuable comments on this study and for providing insight into the challenging world of computer modelling on plasma surface interactions.

I gratefully thank my daily supervisor Dr. Jean-François de Marneffe for his advice. His creative attitude encouraged me to study novel aspects and to maintain the curiosity for the fascinating topic of 2D materials and plasma technology. I thank Prof. Annelies Delabie for the enriching discussions on the mechanisms of the deposition aspects, which took eventually a larger share in this work as originally planned. Furthermore, I would like to thank Prof. Marc Heyns, Prof. Steven De Feyter, Prof. Annemie Bogaerts, and Prof. Fred Roozeboom for their comments to improve this manuscript.

I would like to thank Dr. Mike Cooke and Dr. Andy Goodyear from Oxford Instruments Plasma Technology for their valuable discussions and access to the ALEt equipment. Furthermore, I thank Prof. Nick Braithwaite for providing the retarding field energy analyzer for the ion energy measurements. Many collaborators contributed in the sample preparation and characterization for this work and should be acknowledged here: Dr. Thomas Nuytten for the Raman characterizations, Dr. Johan Meersschaut and Johan Desmet for the quantitative RBS analysis, Dr. Thierry Conard for the XPS data, Dr. Hugo Bender and Ankit Nalin Mehta for the excellent TEM images in atomic resolution, Danielle Vanhaeren for the AFM characterizations, Kim Baumans, Johan De Cooman, Marcel Lux, Erwin Vandenplas, Rudy Verheyen, and Nicolo Pinna for their assisting processing; Dr. Daniele Chiappe and Dr. Benjamin Groven for advancing the basic investigations on sulfurization and PEALD. Gratitude goes also to Dr. Tom Schram, who fulfilled the incredible vision of integrating the few-layer thin films into devices on 300 mm wafer. I thank also my former management for their trust and their resources into this interdisciplinary topic, Dr. Iuliana Radu, Dr. Inge Asselberghs, Dr. Cedric Huyghebaert, Dr. Daniele Piumi, and Dr. Kathy Barla. The financial support by the strategic basic research grant from the agency for innovation by science and technology (IWT, later VLAIO) was a great honor and ensured the scientific independence of this study.

Many people enriched this work with their pure presence – from the etch team, I would like to thank Liping helping me with the first steps in imec, Daniil for the deep plasma discussions and continuation of the work on atomic layer etching, Mikhail, Murad, Alexey, Romain, BT, Efrain, Eddy, Stefan, Laurent, Hubert, and Dunja for all the challenges encountered with the etch tools. From the 2D team, I would like to thank Maria, Cesar, Steven, Ken, Augustin, and Chiara, who made every research day a constructive and good day. Thanks also to Karel for cross-checking the abstract. I would also like to thank the students Eoin Barrett and Jianran Zhang for exploring the topics beyond this project on plasma-modification for top contacts and H_2 plasma cleaning on 2D materials, respectively.

Infinite gratitude goes to the following people, who ensured the correct work-life-balance and became great friends: Sébastien for the mutual motivation to win the scholarship, founding and leading the first ECS student chapter in Belgium, and the quality time over those years; Felix, Robby, Andreas, and Christian to remind me the roots and keep Little Germany in Leuven alive, Nadiia for unforgettable moves on the dancefloor, Gabriele, Davide, Alicia, Abhitosh, Finub, Pavlo, Carolina, Alessandra, and Flavia on the volleyball court, on the excursions, home-brewed beer and bread tastings, or in the *cursus Nederlands*. Despite the scattering across Europe, also the DSMI06, my former fellow students, deserve recognition for cross-motivating each other from the Bachelor till PhD with the sufficient portion of humor: Elle, Tony, Felix, Micha, and Nobby. I would like to thank also the clique in Germany supporting each other regardless of any distance already since secondary school: Jenny, Krissi, Flori, and Caro – thanks for the long-lasting friendship.

Special appreciation goes to my partner Cecilia – thank you for your understanding, your support, and your warm words during the last years. The ups and downs of life, not only in the framework of such a project, are much more pleasant à deux.

Last, but not least, I thank my parents Heidrun and Hartmut and my sisters Sylvie and Nicole for accompanying and supporting me to this point and giving me always the necessary input to take the right decisions in life.

Markus Heyne
Leuven, September 2019

"A scientist in his laboratory is not a mere technician: he is also a child confronting natural phenomena that impress him as though they were fairy tales."

Marie Curie

Abstract

Transition-metal dichalcogenides such as MoS_2 or WS_2 are semiconducting materials with a layered structure. One single layer consists of a plane of metal atoms terminated on the top and bottom by the chalcogen atoms sulfur, selenium, or tellurium. These layers show strong in-plane covalent bonding, whereas the Van-der-Waals bonds in between adjacent layers are weak. Those weak bonds allow the microcleavage and extraction of a monolayer. Transistors built on such monolayer nanosheets are promising due to high electrostatic controllability in comparison to a bulk semiconductor. This is important for fast switching speed and low-power consumption in the OFF-state. Nonetheless, prototypes of such nanosheet transistors show non-idealities due to the fabrication process. Closed films on a large area cannot be obtained by mechanical exfoliation from mm-sized crystals. For wafer-level processing, synthetic growth methods are needed. It is a challenge to obtain a few layer thick crystals with large lateral grains or even without grain boundaries with synthetic growth techniques. This requires pre-conditioned monocrystalline substrates, high-temperature deposition, and polymer-assisted transfer to other target substrates after the growth. Such transfer is a source of cracks in the film and degrades the layers' promising properties by residual polymer from the bond material. Apart from transfer, patterning of the stacked 2D layers is necessary to build devices. The patterning of a 2D material itself or another material on top of it is challenging. The integration of the nanosheets into miniaturized devices cannot be done by conventional continuous-wave dry etching techniques due to the absence of etch stop layers and the vulnerability of these thin layers. To eliminate these issues in growth and integration, we explored the deposition methods on wafer-level and low-damage integration schemes.

To this end, we studied the growth of MoS_2 by a hybrid physical-chemical vapor deposition for which metal layers were deposited and subsequently sulfurized in H_2S to obtain large area 2D layers. The impact of sulfurization temperature, time, and partial H_2S pressure on the stoichiometry, crystallinity, and roughness were explored. Furthermore, a selective low-temperature deposition and conversion process at 450 °C for WS_2 by the precursors WF_6, H_2S, and Si was considered. Si was used as a

reducing agent for WF_6 to deposit thin W films and H_2S sulfurized this film *in situ*. The impact of the reducing agent amount, its surface condition, the temperature window, and the necessary time for the conversion of Si into W and W into WS_2 were studied. Further quality improvement strategies on the WS_2 were implemented by using extra capping layers in combination with annealing. Capping layers such as Ni and Co for metal-induced crystallization were compared to dielectric capping layers. The impact of the metal capping layer and its thickness on the recrystallization was evaluated. The dielectric capping layer's property to suppress sulfur loss under high temperature was explored. The annealings, which were done by rapid thermal annealing and nanosecond laser annealing, were discussed.

Eventually, the fabrication of a heterostack with a MoS_2 base layer and selectively grown WS_2 was studied. Atomic layer etching was identified as attractive technique to remove the solid precursor Si from MoS_2 in a layer-by-layer fashion. The *in-situ* removal of native SiO_2 and the impact towards MoS_2 was determined. The created patterned Si on MoS_2 was then converted into patterned WS_2 on MoS_2 by the selective WF_6/H_2S process developed earlier. This procedure offers an attractive, scalable way to enable the fabrication of 2D devices with CMOS-compatible processes and contributes essential progress in the field 2D materials technology.

Beknopte Samenvatting

Transitie-metaal dichalcogeniden zoals MoS_2 of WS_2 zijn halfgeleidende materialen met een gelaagde structuur. Eén enkele laag bestaat uit een vlak van metaalatomen dat aan de boven- en onderkant wordt afgesloten door de zwavel, seleen of tellurium chalcogeenatomen. Deze lagen vertonen een sterke covalente binding in het vlak, terwijl de Van-der-Waals-bindingen tussen aangrenzende lagen zwak zijn. Die zwakke bindingen maken microsplitsing en extractie van een monolaag mogelijk. Transistors gebouwd op dergelijke monolagennanosheets zijn veelbelovend vanwege de hoge elektrostatische controle in vergelijking met een bulk halfgeleider. Dit is belangrijk voor een hoge schakelsnelheid en een laag stroomverbruik in de OFF-toestand. Toch vertonen prototypen van dergelijke nanoschijftransistoren defecten vanwege het fabricageproces. Gesloten films over een groot oppervlak kunnen niet verkregen worden door mechanische splitsing van millimetersgrote kristallen. Voor verwerking op wafer-niveau zijn synthetische groeimethoden nodig. Het is een uitdaging om met synthetische groeitechnieken enkele lagen te verkrijgen met grote laterale kristallen of zelfs zonder korrelgrenzen. Dit vereist vooraf geconditioneerde monokristallijne substraten, afzetting op hoge temperatuur en polymeerondersteunde overdracht naar andere beoogde substraten. Dergelijke overdracht leidt tot scheuren in de film en het resterend polymeer uit het bindmateriaal degradeert de veelbelovende eigenschappen van de lagen. Afgezien van de overdracht is het vormen van gestapelde 2D-laagpatronen noodzakelijk om elektrische geïntegreerde schakelingen te maken. De vormgeving van een 2D-materiaal, of een ander materiaal erboven, is een uitdaging. De integratie van de nanosheets in geminiaturiseerde schakelingen kan niet worden verwezenlijkt met conventionele droge etstechnieken, met radiofrequent, vanwege de afwezigheid van etsstoplagen en de kwetsbaarheid van de dunne lagen. Om deze problemen in groei en integratie te elimineren, hebben we de depositiemethoden onderzocht op wafer-niveau en lage-schade integratieschema's.

Daarom hebben we de groei van MoS_2 bestudeerd met een hybride fysisch-chemische dampdepositie waarvoor metaallagen werden afgezet en vervolgens in H_2S werden verzwaveld om 2D-lagen met een groot oppervlak te verkrijgen. De invloed van de verzwavelingstemperatuur, tijd, gedeeltelijke H_2S-druk en H_2-toevoeging op de stoichiometrie, kristalliniteit en ruwheid werden onderzocht. Verder werd een selectieve lage temperatuurafzetting-en-conversieproces geanalyseerd bij 450 °C voor WS_2 groei met WF_6, H_2S en Si als precursors. Si werd gebruikt als een reductant voor WF_6 om dunne W-films af te zetten en H_2S converteerde deze film in situ. De impact van de hoeveelheid reductant, de oppervlaktetoestand ervan, het temperatuurvenster en de benodigde tijd voor de omzetting van Si in W en W in WS_2 werden bestudeerd. Verdere kwaliteitsverbeteringsstrategieën op WS_2 werden geïmplementeerd door extra afdeklagen te gebruiken in combinatie met gloeien. Afdeklagen zoals Ni en Co voor metaal-geïnduceerde kristallisatie werden vergeleken met diëlektrische afdeklagen. De impact van de metalen afdeklaag, en de dikte ervan, op de herkristallisatie werd geëvalueerd. De eigenschap van de diëlektrische afdeklaag om zwavelverlies onder hoge temperatuur te onderdrukken, werd onderzocht. De uitstookstappen, die werden uitgevoerd door snelle thermische gloeiing en nanoseconde lasergloeiing, werden besproken.

Uiteindelijk werd de fabricage van een heterostack met een MoS_2-basislaag en selectief gegroeide WS_2 bestudeerd. Atoomlaagetsen werd geïdentificeerd als een aantrekkelijke techniek om de vaste precursor, Si, van het MoS_2 laag-voor-laag te verwijderen. Het in situ verwijderen van natuurlijk groeiend SiO_2 en de impact op MoS_2 werd bepaald. Het gecreëerde Si op MoS_2-patroon werd vervolgens omgezet in een WS_2 op MoS_2-patroon door het eerder ontwikkelde selectieve WF_6/H_2S-proces. Door zijn zelflimiterende karakter biedt deze procedure een aantrekkelijke, schaalbare manier om het vervaardigen van 2D-apparaten met CMOS-compatibele processen mogelijk te maken en draagt deze bij tot essentiële vooruitgang op het gebied van 2D-materiaaltechnologie.

Abbreviations

AES	Auger electron spectroscopy
AFM	Atomic force microscopy
AHM	Ammonium heptamolybdate, $(NH_4)_6Mo_7O_{24}$
ALD	Atomic layer deposition
ALEt	Atomic layer etching
ARXPS	Angle-resolved X-ray photoelectron spectroscopy
BTBT	Band-to-band tunneling
CVD	Chemical vapor deposition
CVT	Chemical vapor transport
CW	Continuous wave
DES	Diethyl sulfide, $C_4H_{10}S$
DEZ	Diethyl zinc, $C_4H_{10}Zn$
DMDS	Dimethyl disulfide, $C_2H_6S_2$
ELA	Excimer laser annealing
FDSOI	fully depleted silicon-on-insulator

FFT	Fast-Fourier-transform
FIB	Focused ion beam
IC	Integrated circuit
ICP	Inductively coupled plasma
IEDF	Ion energy distribution function
IVDF	Ion velocity distribution function
MIC	Metal-induced crystallization
MOCVD	Metal-organic chemical vapor deposition
OPL	Optical path length
PEALD	Plasma-enhanced atomic layer deposition
PECVD	Plasma-enhanced chemical vapor deposition
PL	Photoluminescence
PPE	Personal protective equipment
PTCA	Perylene-3 4 9 10-Tetracarboxylic Acid, $C_{24}H_{12}O_8$
PTCDA	Perylene-3,4,9,10-Tetracarboxylic Dianhydride, $C_{24}H_8O_6$

PVD	Physical vapor deposition
RBS	Rutherford backscattering spectrometry
RF	Radio-frequent
RFEA	Retarding field energy analyzer
RTA	Rapid thermal annealing
SAED	Selected-area electron diffraction
SCE	Short-channel effects
SEM	Scanning electron microscopy
SLS	Self-limiting layer synthesis
TEM	Transmission electron microscopy
TMAH	Tetramethylammonium hydroxide, $C_4H_{13}NO$
TMD	Transition-metal dichalcogenide
XPS	X-ray photoelectron spectroscopy

Symbols

$_1$	-	symmetric with respect to the C_n principle axis, if no perpendicular axis, then it is with respect to σ_v
λ	nm	Characteristic length scale for which bend bending occurs at metal-to-semiconductor interface
C_n	-	$2\pi/n$= number of turns in one circle on the main axis without changing the look of a molecule (rotation of the molecule)
ε_s	-	Relative permittivity of the semiconducting channel
ε_{ox}	-	Relative permittivity of the dielectric gate oxide
E	-	describes the degeneracy of the row in the character table (E=2)
t_s	nm	Thickness of the semiconducting channel
t_{ox}	nm	Thickness of the dielectric gate oxide
μ	$cm^2/(V*s)$	Charge carrier mobility
$_g$	-	symmetric with respect to the inverse
ΔG	kJ/mol	Gibbs free energy
ΔH	kJ/mol	Enthalpy
ΔS	kJ/(mol*K)	Entropy

σ_v - reflection of the molecule horizontally compared to the horizontal highest fold axis.

σ_v - reflection of the molecule vertically compared to the horizontal highest fold axis.

‘ - Symmetric with respect to σ_v

1 Introduction and goals

Transistor scaling has been driven over decades by Moore's law, predicting the doubling of integrated circuit (IC) complexity every two years.[1] The continuous trend of reducing the size of the transistors resulted in higher functional density, higher reliability, lower power consumption, increased speed, and eventually in lower cost per transistor. This enabled the increased use of electronic devices in our everyday life to enhance quality. The shrinking has been a result of tremendous developments in processing technologies in the areas of deposition, lithography, and etching. The so-called lateral scaling aimed to reduce the critical dimension in patterned nanostructures on the lateral scale, which are still built on bulk Si wafers nowadays. However, transistors in bulk semiconductors are limited in their performance due to parasitic effects in sub-100 nm transistor channels.[2,3] New architectures are necessary to confine the charge carriers in a small volume for precise electrostatic control and to switch the transistor fast and properly between the OFF-state with the lowest possible current and the ON-state with the highest possible current.[4] Besides new Si-based architectures such as fully-depleted silicon-on-insulator (FDSOI), FinFETs, or nanowires, ultrathin transition-metal dichalcogenide (TMD) layers with a thickness of a few atoms were identified as promising channel materials.[5] They can be integrated using planar techniques, avoiding the increased processing complexity for extending into the third dimension. Their intrinsic properties and ultrathin body promise a superior short channel behavior for ultra-narrow channel sizes with comparable mobilities as silicon.[6] Transition-metal dichalcogenides such as MoS_2 or WS_2 have a lower dielectric constant than Si, which is expected to positively influence the short-channel behavior and enable high I_{ON}/I_{OFF} current ratios.[6] The sulfur termination of the basal planes determines the absence of dangling bonds and therefore they are predicted to show reduced charge carrier scattering in devices built on TMDs.[7] At least since the exfoliation of graphene, the principle of a stable monolayer film and its use in electronics is demonstrated. But graphene's absent intrinsic bandgap hinders its use as channel material for transistors. The semiconducting TMDs are superior channel materials due to their bandgap. In contrast to graphene, TMDs possess appreciable layer-thickness-dependent bandgaps in the range of 1.3 eV to 2.2 eV and thus, they can be used to build transistors.[8] The ultimate thickness limit of a monolayer as a channel material in a transistor is attractive, since this gives an ideal electrostatic control for switching in contrast to a bulk semiconductor.

Nonetheless, a monolayer material itself is very vulnerable since every atomic defect influences the property of this material. To integrate such a material with the conventional CMOS techniques requires a careful study of their impacts. The domains of growth, quality improvement of the material, patterning as well as the co-integration of different 2D materials on a Si platform are studied in this work.

1.1 Problem statement

Over the last decades, transistors were scaled to smaller dimensions to increase the chips' functional density. The development of advanced processing, mainly in the areas of lithography and etching, resulted in decreasing critical dimensions and enabled smaller transistors. The traditional lateral scaling of transistors was continuously accompanied by the vertical scaling to keep electrical fields ideally constant according to Dennard.[9] However, when device sizes reached the sub-100 nm scale, the device performance degrades due to short channel effects (SCE)[*]. To improve the controllability of the transistors, new device architectures were established. So-called fully depleted ultra-thin body transistors, which are based on thin silicon layers on an insulator, are an extension of conventional Si-technology. An important criterion for scaling of a device is its so-called characteristic length λ:

---

[*] Short channel effect: when depletion zone and transistor channel length are in a comparable size, the threshold voltage is reduced, the charge carrier velocity becomes non-linear, mobility is reduced by surface scattering, and hot electrons can punch through the oxide

$$\lambda = \sqrt{\frac{\varepsilon_s}{\varepsilon_{ox}} t_s t_{ox}}$$

with the permittivity ε of the semiconducting channel and oxide, respectively, as well as the channel thickness t_s and the oxide thickness t_{ox}. If λ is significantly smaller than the physical gate length of a transistor, the undesired SCEs can be considered small.[6] It shows that the reduction of the transistor channel's thickness is a parameter to enable smaller devices. The ultimate thickness limit is the monolayer of a material. Graphene is such a monolayer made of a hexagonal carbon lattice with mobilities higher than 200000 $cm^2 V^{-1}s^{-1}$.[10] However, graphene lacks an intrinsic bandgap and is therefore as a semimetal not appropriate as a replacement for silicon in logic circuits. Layered transition-metal dichalcogenides (TMD) are considered as appropriate candidates, since they are semiconducting with a reasonable bandgap and show smaller dielectric constants in comparison to other semiconductors. Conventional semiconductors as silicon as monolayer in the form of silicene have been considered, but their integration is challenging due to quick oxidation.[11] The TMD layers are in-plane strongly bonded, but out-of-plane they show only weak Van-der-Waals bonds in between individual layers. Those weak Van-der-Waals bonds enable the mechanical exfoliation of individual monolayer flakes from a natural crystal and by this, the demonstration of transistors with an ultrathin body. However, exfoliated flakes are after transfer randomly distributed on the target substrate with undefined size, thickness, and location. In addition, mechanical transfers by a polymer transfer layer leaves organic residues on the exfoliated flakes, which influences the properties of each flake and induces variations. Exfoliation cannot serve as a wafer-scaled deposition growth method for ICs.

Synthetic growth methods are necessary. However, at the start of this research work in 2013, the available methods to grow 2D films were limited. Conventional TMD growth by chemical vapor transport (CVT) yielded only thick crystals, which were not appropriate to investigate low-dimensional films. In addition, these growth techniques required high temperatures of 800 °C and above to form TMDs. These high temperatures can lead to compatibility issues with common substrates for integrated circuit (IC) technology due to the limited temperature budget of the substrates. The high melting point of solid metal-oxide precursors such as WO_3 is an issue as well, since the delivery in very defined amounts above a large area is difficult to control. To date, another disadvantage of the available growth techniques is the use of growth promoters such as diethylzinc or alkali halides, which are known to degrade the reliability in Si devices due to their high diffusion of the alkali elements. Further, some growth techniques of TMDs utilize carbon-containing precursors, which contain the risk to incorporate C in the deposited 2D films and degrade their properties as well. Attempts to grow thinner films resulted in small grain sizes, spiral crystal growth as pyramid, and deposition without control over the location. Attempts to lower the temperature of the growth, resulted in amorphous film formation without the typical 2D film properties.

Besides the challenges in the growth of low-dimensional films, there are also technological challenges. For fabricating devices, the so-called lift-off technique is used nowadays. To this end, a polymer resist layer is patterned by lithography, metal is deposited in the developed trenches and on top of the resist, and then the metal film is removed in the region where it is undesired by lifting off the resist and metal film in solvent. This technique leaves often rough edges, ears, and redeposition of material, which hinders its use for ultra-scaled device fabrication.

Wet chemical etching for patterning or contact formation is often accompanied by the delamination of the TMD films due to their weak adhesion to the substrate, resulting in failure as well. To pattern such small dimensions, anisotropic dry etching is inevitable. However, conventional continuous-wave (CW) radio-frequent (RF) plasmas without any pulsing damage with their high ion energy TMDs easily by breaking the bond between the chalcogen and the metal atom. This simplifies the removal of a 2D material from a dielectric substrate, but it cannot be used to pattern a 2D material on top of another one, because the bottom 2D material would be removed as well due to the lack of selectivity with CW plasmas.

In summary, there are manifold challenges for the growth of the individual TMD films and for the integration to achieve patterned and stacked TMD films. Here we will address the growth by a high temperature and a low temperature process without transfer, the quality improvement of the films by additional treatments, and the patterning of a film on top of a 2D material by atomic layer etching (ALEt) to achieve eventually heterostructures two different TMDs.

1.2 Research goals

The previous section addressed the issues which are related to films exfoliated or transferred by polymers. Therefore, we define the high quality and large area growth of TMDs directly on its target substrate as a main goal for this thesis. In the first approach, large-area MoS_2 films should be obtained by a high-temperature process. The films should have a defined thickness of four to ten layers. The basal planes of the films should be aligned horizontally to the surface of the underlying substrate. The stoichiometric films should have the sulfur/metal ratio 2. The topology should be smooth, ideally with roughness far below the monolayer thickness of 7 Å over areas of a few square centimeters. The material should be deposited directly on the target substrate, which is a dielectric-covered Si-wafer. The growth precursors used for this investigation are carbon-, zinc-, and alkali-free to ensure Si-compatibility. The goal is to maximize the lateral grain size and determine the necessary growth parameters to fulfill the requirements mentioned above. The MoS_2 should be obtained by sulfurization of a pre-deposited metal or metal-oxide film in a closed H_2S environment. This process was chosen since the pre-deposition of the metal precursor on the target substrate can be well controlled with respect to its thickness and the inhomogeneous gas transport of the conventionally used metal precursors with high melting point is circumvented.

A further goal is the deposition of a second TMD, WS_2, at lower temperature than the sulfurization temperature. For this approach, the gas phase precursors WF_6 and H_2S and growth-promoting Si layers are used to cover large wafers with 300 mm diameter. The impact of the Si amount, the presence of native oxide layers, deposition temperature, and selectivity to the underlaying substrate material had to be explored. The understanding of the mechanisms occurring between the gas phase precursors and the silicon layer is crucial. The motivation for choosing this technique is its relatively low deposition temperature and fast conversion through the hefty reaction of WF_6 and Si in absence of undesired growth promoters such as DEZ. This process is free of carbon-containing precursors and it can be used directly on the growth substrate without a transfer process.

Since such low temperature processes yield often small grain sizes for high-melting compounds, additional strategies for improving the quality of the as-deposited films are also required. To this end, the nanosecond laser annealing and the combination of rapid thermal annealing with dielectric or metallic capping layers was studied. The understanding of the anneal parameters on the material quality in terms of their crystalline quality had to be developed. Eventually the surface-sensitive nanosecond laser annealing was compared with conventional rapid thermal annealing (RTA) as a technique to consider substrates' thermal budget to a reasonable range.

The second main goal of this thesis was to proof a concept for realizing patterned heterostructures of MoS_2 and WS_2, combining the previously investigated growth techniques and advanced plasma technologies. Here, the application of atomic layer etching (ALEt) as a technique to remove material in a layer-by-layer fashion was chosen. The removal of a material from another underlying TMD and its impact to the TMD on atomic scale was explored. Eventually, the combination of the processes sulfurization, ALEt, selective conversion, and crystal quality improvement had to be demonstrated as a proof-of-concept study to realize the desired heterostructure.

2 State-of-the-art

The following chapter describes the properties and state-of-the-art in deposition of thin TMDs and summarizes the literature on deposition and dry, low-damage patterning methods for TMDs. Large area deposition as well as selective deposition methods are described. The application of plasma processes for the patterning and controlled thinning of TMDs are explained. A brief introduction to thermodynamics and kinetics is given.

2.1 Properties of transition-metal dichalcogenides

TMDs are described with the general formula MX_2, in which the M is transition metal and the X a chalcogen. Depending on the combination of the transition metal and chalcogen, the MX_2 material can be insulating, metallic, or semiconducting. MoS_2 and WS_2 are such semiconducting TMDs. They all have a hexagonal structure.[12] Depending on the stacking of the X-M-X layers, they appear in different polytypes. The most common polytypes for MoS_2 are trigonal prismatic (2H) or octahedral (1T). The polytype is also related to the electronic properties, namely the 2H phase is semiconducting and the 1T phase metallic. Their typical thickness is 6-7 Å and the M-X bonds are covalent with a M-M bond length between 3.15 Å and 4.03 Å. The layers are terminated by the sulfur and hence, they do not show dangling bonds which makes them resistant against environmental influences.[13] The adjacent MX_2 layers are bound by weak Van-der-Waals forces easing the microcleavage of layers. The bandgap of the TMDs depends on their thickness and increases for MoS_2 towards 1.8 eV for a monolayer.[13] This shift is accompanied by a transition from indirect to a direct bandgap.

2.2 Growth of transition-metal dichalcogenides

2.2.1 Exfoliation

Exfoliation is a technique to obtain few-layered nanosheets of TMDs. To this end, a thick MoS_2 crystal is separated into nanosheets by peeling it several times with Scotch tape.[5,14–17] Due to the weak Van-der-Waals forces between the layers, they are detaching by the microcleavage as it is outlined in Figure 2-1. The figure shows the different possibilities to separate layered materials, either by mechanically separating a layer from the bulk material, separating them by laser irradiation, a peel-off, or by intercalating other elements, which weaken the forces between the layers further so that the single layers can be separated in a solution. With the mechanical exfoliation by repeating microcleavage several times, it is possible to obtain sheets being only one layer thick. This layer can be pressed with the tape onto the target substrate. The transferred layers are contaminated by carbon compounds from the transfer material, which induces variable properties to the 2D material.[18,19] Besides the undesired surface residues, the exact position, lateral size, and thickness of the flakes cannot be controlled and they will be randomly distributed on the substrate. Similar disadvantages hold for films from liquid exfoliation, in which TMD crystals are sonicated in solvent blends and the suspension is then sprayed onto the target substrate.[20] A similar approach with random flake distribution is the liquid exfoliation by intercalation of lithium in between the layers.[21]

Since the nanosheet originates directly from a natural crystal, this procedure yields flakes with a superior intrinsic quality. However, this approach can only yield flakes of a few μm size and only in random locations being not appropriate for reproducible IC fabrication. A growth technique for larger crystals is necessary.

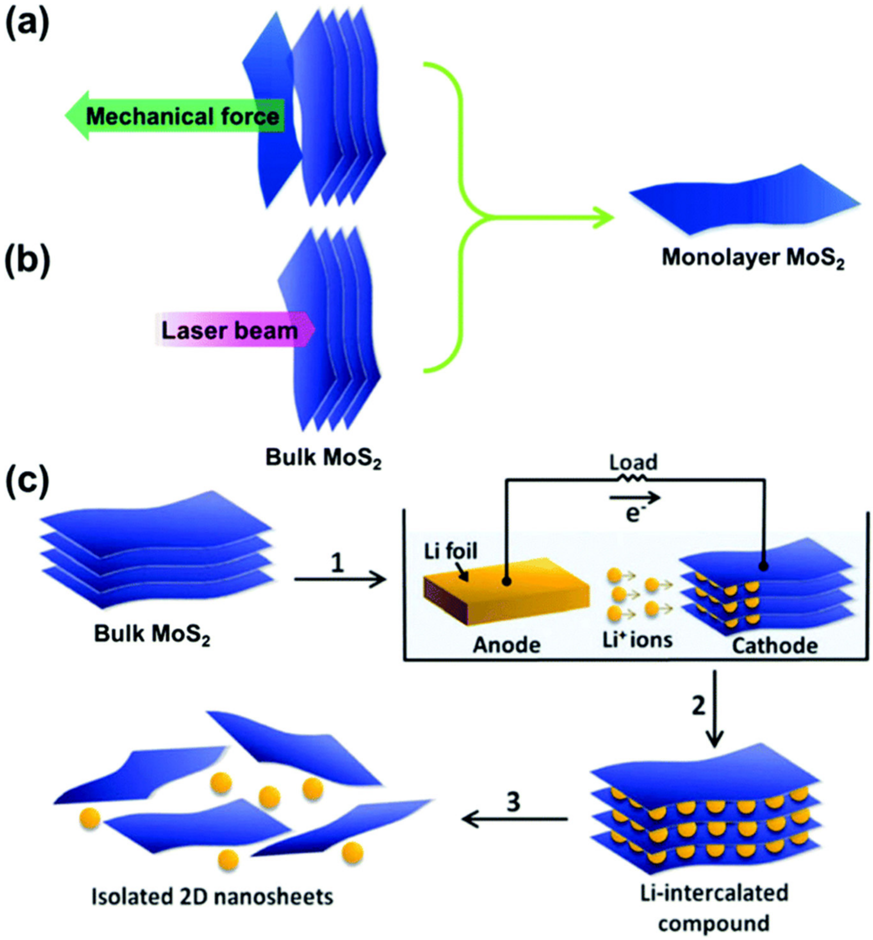

Figure 2-1: Schematics of exfoliation techniques with a) mechanical exfoliation by scotch tape, b) laser beam exfoliation, and c) the exfoliation by Li-intercalation and isolation. Reproduced from doi:10.1039/C5NR06121K.

2.2.2 Chemical vapor growth processes

The vapor phase growth techniques can be distinguished into chemical vapor transport (CVT), chemical vapor deposition (CVD), and atomic layer deposition (ALD).

<u>Chemical Vapor Transport (CVT)</u>

CVT is a growth technique for solids in which the source materials as a powder, such as Mo and S, are sealed together with a reducing transport agent, such as I_2, Br_2, $SeCl_4$, or $TeCl_4$ in high vacuum in a quartz ampoule as shown in Figure 2-2A and B.[22,23] The figure shows a schematic, how the precursors in its powder form are sealed together with the reducing agent and how the crystals are formed in zones of different temperatures. The electron microscopy image shows the layered structure of the obtained crystals. The ampoule is then annealed under a temperature gradient and the transport agent carries the transition metal in the gas phase from the high temperature zone and condensates them as chalcogenide in the low temperature zone according to Schäfer's transfer mechanism.[24,25] The advantage of this technique is the good controllability of the precursor transport rate, the relatively low growth temperature, and the versatility for a large range of TMDs. The individual crystal can reach mm size. However, CVT is limited to small substrates due to its ampoule setup and does not offer any control about the deposition location. In addition, the inclusion of the transport agent into the TMD film was reported to be a source of defects.[26]

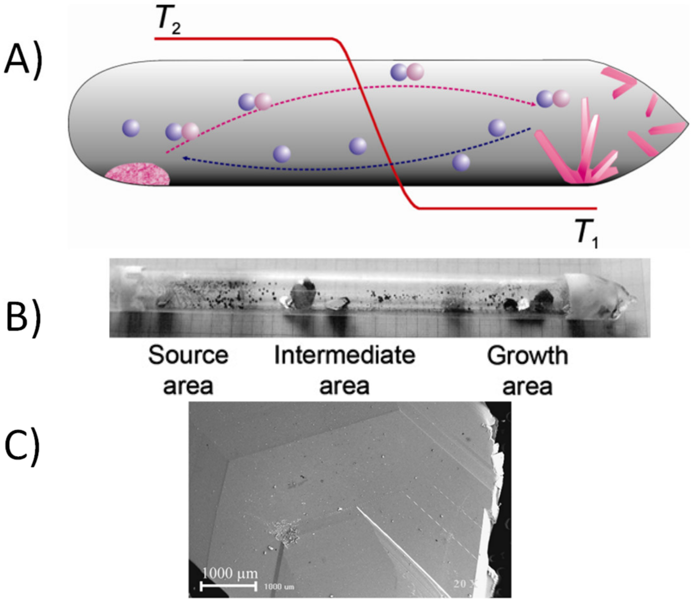

Figure 2-2:A) shows the schematic of chemical vapor transport in a glass tube and B) photo of a glass tube after CVT process. C) Shows a crystal obtained from CVT. Reproduced from doi:10.5772/55547 and doi:10.1016/j.jcrysgro.2012.10.026.

Chemical vapor deposition (CVD)

In CVD the precursors are decomposed in the gas phase and react on the heated sample surface. The first CVD of MoS_2 used the precursors $MoCl_5$ or MoF_6 and H_2S.[27–29] Many efforts went into the synthesis of inorganic nanotubes, filled fullerene-like nanoparticles, and nanoflowers[30]. The horizontal structure, the so-called type-II structures being parallel to the substrate were investigated only later, originally foreseen for solar cells.[31,32] In 2012, right upon the fabrication of the first single MoS_2 monolayer transistor, many efforts were spent on the CVD with MoO_3 and S as precursors. The principle is depicted in Figure 2-3. The image shows a heated tube furnace in which the metal-oxide and the sulfur precursor are brought in proximity to the substrate and in which the mass transport is controlled as well by a carrier gas flow, here N_2.

This approach is conducted in a quartz furnace, in which the sample and the precursors in boats are placed in a carrier gas flow. The growth sample is typically placed at a location with a temperature around 750 °C.[33–36] Perylene-3,4,9,10-tetracarboxylic acid tetra potassium salt (PTAS, PTCTA) were used as seeding layer and promoted the growth of large 2D crystals.[35–37] Similar effect was also shown by the promoter Copper hexadecafluorophthalocyanine ($F_{16}CuPc$).[38] Monolayer triangles of a few tens of micrometer size could be grown by this technique. Further modification of the CVD process based on the solid precursors were

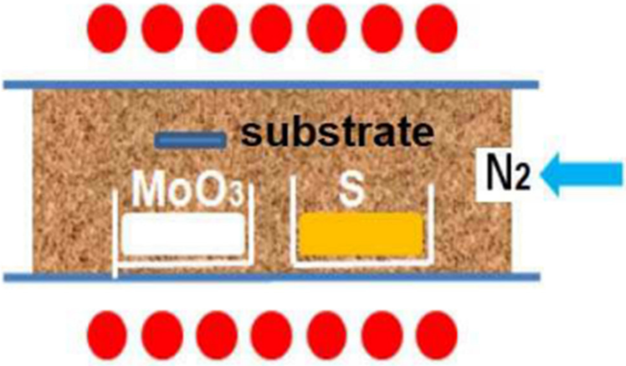

Figure 2-3: Concept of solid precursor evaporation with a carrier gas in a tube furnace. Reproduced from doi: 10.1149/05006.0061ecst.

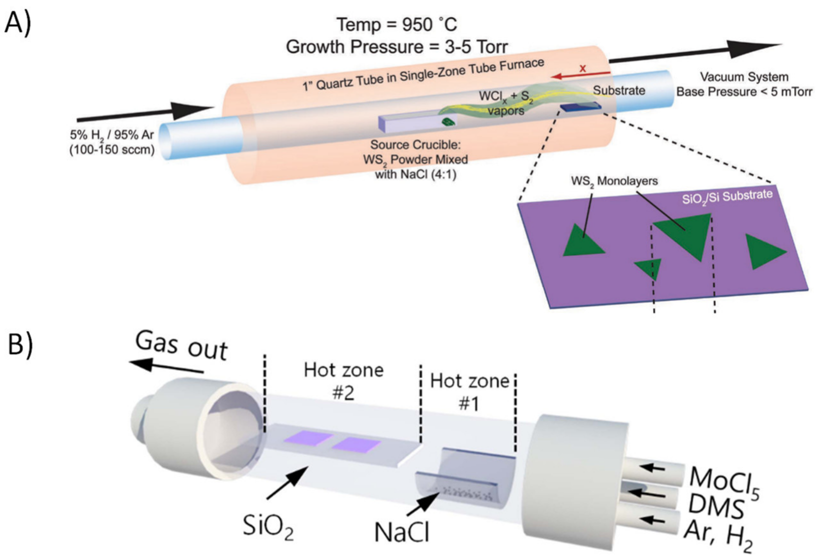

Figure 2-4: A) & B) CVD with the addition of alkali-salts as growth promoter or inhibitor. Reproduced from doi:10.1002/smll.201701232 and doi:10.1088/1361-6528/aa8f15.

achieved by combining the function of halide-containing compounds, namely NaCl or KI. Those compounds can be added directly or indirectly to the precursor as shown in Figure 2-4A and B and form higher volatile chloride compounds during the CVD resulting in large single grains.[39,40] In the first approach, the precursor in form of MX_2 powder is mixed together in a crucible with NaCl. Through the formation of volatile MCl_x compounds and sulfur, the precursors can be delivered to the substrate easily. The second figure in B shows the addition of NaCl into reactor for a process with carbon-containing precursors (dimethyl sulfide). Due to the catalytic effect of the NaCl, the carbon impurities in the deposited MX_2 films are lower than without NaCl. Such higher purity results also in better charge carrier mobility in the films.[40] The NaCl vaporizes, adsorbs on the substrate and reacts with the sulfur to form Na_2S_x. This Na_2S_x reacts then with the $MoCl_5$ precursor to form MoS_2 and vaporizes afterwards as NaCl again. In contrast to the enhanced growth, alkali metal halides have also been shown to decrease the nucleation density when the surface is pre-treated with the alkali metal halides before growth. For smaller nucleation density, there are less centers from which the lateral growth starts, thus this provides more space for the lateral growth before touching another crystal, resulting in larger grains.[41] In case of hindering the lateral growth e.g. by another crystal, undesired spiral 3D growth can occur.[42] Instead of hindering or growing on top of each other, it is desired that the crystals merge into a boundary-free crystal.

There are also plasma-enhanced CVD (PECVD) processes in which H_2S plasma is used to sulfurize thin Mo films. PECVD can be conducted at low temperatures of 150 °C and allowed even the processing on polyimide foils as shown in Figure 2-5.[43] The figure shows a heated polyimide substrate with a metallic Mo layer in an H_2S/Ar plasma. The plasma dissociates the gas and positive charged ions are accelerated through the plasma sheath towards the sample surface. The temperature from heating and the ion bombardment enable the sulfurization of the surface film at the low temperature being appropriate for polymer substrates.

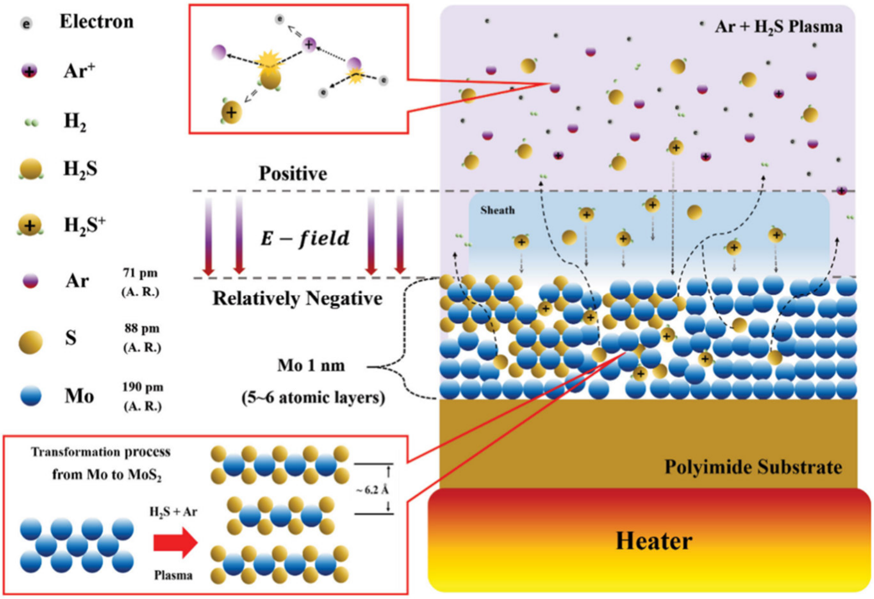

Figure 2-5: PECVD utilizing H_2S plasma for sulfurization; reproduced from doi:10.1002/adma.201501678.

Metal-organic chemical vapor deposition (MOCVD)

The previous described techniques require an elevated temperature above 700 °C to sublimate the MoO_3 precursor. Alternative ways to evaporate the precursors at lower temperatures utilize metal-organic precursors such as $Mo(CO)_6$ or $W(CO)_6$ and dimethyl- or diethyl chalcogenide during the CVD process.[44,45] Large samples have been covered with this technique and good quality films have been achieved, although the growth time of 26 h for a monolayer is slow.[46] MOCVD is also used in pulsed mode to produce polycrystalline films within a short time frame of 90 s for a few layers at a relatively low deposition temperature of 591 °C.[47] Carbon impurities in the films can be incorporated into the film and influence the properties in an undesired way.[47–49] Low temperature approaches yield only amorphous MX_2 films, which would also require further annealing to recrystallize.[50]

Sulfurization / hybrid physical-chemical vapor deposition

Sulfurization is a chemical reaction of the metal-containing film with the sulfur-containing precursor directly on the target substrate. To this end, samples were dipped in $(NH_4)_2MoS_4$ with the subsequent annealing in Ar/H_2 at 500 °C for 1 h and Ar / S at 1000 °C for 1 h as shown in Figure 2-6. The figure shows how a metal-containing precursor is brought on a samples such as sapphire by dip-coating and which was then annealed in two steps. The first step in H_2/Ar mixture decomposes the precursor and the second step at 1000 °C in sulfur-containing environment yielded then the highly crystalline MoS_2. MoS_2 can be also prepared by sulfurization of a Mo film deposited by physical vapor deposition.[51–53] The advantage is the accurately controlled material distribution over the sample by the pre-

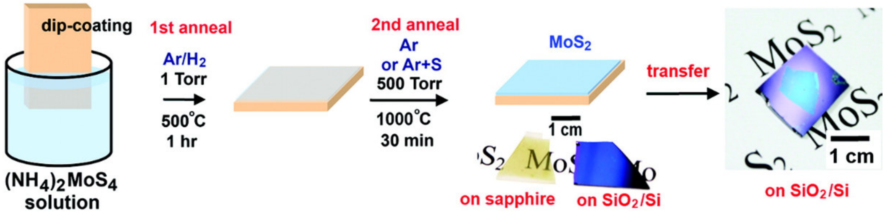

Figure 2-6: Dip-coating of the Mo precursor with the subsequent sulfurization; reproduced from doi: 10.1021/nl2043612.

deposition of the metal or metal-oxide material. Given the fact that this can be achieved with conventional tools, this route was investigated closer within this thesis. The quality of the films is mainly depending on the sulfurization temperature and higher sulfurization temperature increases the quality and thereby the carrier mobility of the MoS_2.[54] The sulfurization approach can also be tuned by oxidation of the pre-deposited metal at high temperature before sulfurization and post-crystallization in N_2 at 1000 °C after sulfurization directly grown on SiO_2.[32]

Atomic layer deposition (ALD)

ALD can be used to deposit 2D materials. Scharf et al. deposited WS_2 on Al_2O_3 by means of WF_6 and H_2S and diethylzinc (DEZ) as reducing agent at a moderate temperature of 300 °C for the use as solid lubricant in MEMS devices.[55–57] The ALD is typically done at temperatures below 500 °C.[58–60] The precursors $MoCl_5$ and H_2S were used by Tan et al.[61] Jin et al. used $Mo(CO)_6$ and DMDS.[62] But due to the low crystallinity reached at such temperatures, additional high temperature annealing to improve the quality is necessary to obtain measurable mobility values. Song et al. used an approach in which a metal oxide layer was deposited by ALD for achieving a defined thickness and sulfurized afterwards at high temperature to MX_2 compound as shown in Figure 2-7A.[58,60,63–66] The figure shows the approach where the desired thickness was determined by the number of ALD cycles and the WS_2 material was obtained by the sulfurization of the oxides. A specific 2D material growth, which does not fit in the typical ALD growth, is the so-called self-limiting synthesis (SLS). Similarly, to ALD, the precursors are pulsed in cycles, but there is no typical ALD regime in which the growth rate is constant. Here the final thickness depends dominantly on the deposition temperature rather than the cycles as depicted in Figure 2-7B.[67] The graph shows the peak distance of the Raman peaks relating directly to the layer thickness in the few-layer regime. At a certain temperature, there is only a maximum thickness which is not exceeded even for exaggerated number of cycles, indicating that the adsorption equilibrium depended only on the temperature in this process. It is believed that this is due to the lack of dangling bonds and the screening effect of the MoS_2 surface. So this is totally different than conventional ALD. Ultra-low

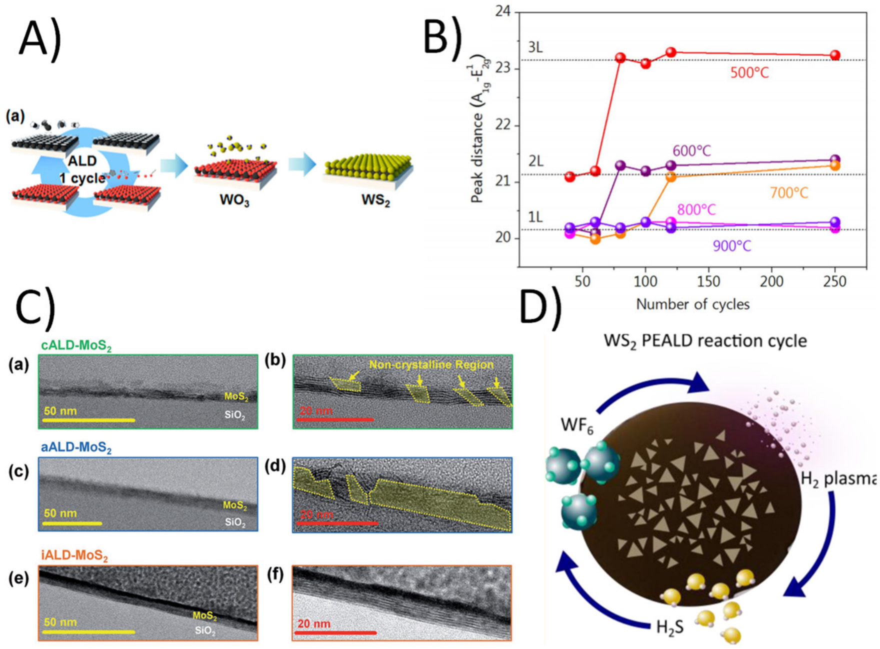

Figure 2-7: A) Sulfurization of ALD-grown WO_3, B) Self-limiting synthesis of ALD-grown films for which the thickness rather depends on the temperature than on the number of cycles; C) iALD shows fully crystalline films in comparison to conventional ALD (cALD) or activator-utilizing ALD (aALD); D) PEALD based on WF_6, H_2 plasma, and H_2S as precursors. Reproduced from A) doi:10.1021/nn405194e, B) doi: 10.1038/srep18754, C) doi: 10.1002/adma.201703031, D) doi: 10.1021/acs.chemmater.6b05214.

temperature ALD at 60 °C was achieved by using $Mo(NMe_2)_4$ and H_2S, although those films are also amorphous.[68] The best performing as-grown ALD MoS_2 films to date were prepared with inhibitor-utilizing ALD (iALD) as it is illustrated in Figure 2-7C. The image shows the comparison of the process results for conventional ALD, an activator-utilizing ALD enhancing the initial growth, and the inhibitor-utilizing ALD slowing down the initial nucleation. Inhibitor-utilizing means that the surface is pre-treated with inhibitor molecules controlling the chemisorption of the metal precursor.[69] Diethyl sulfide (DES) was used as surface pre-treatment and engineered the surface properties to control the Mo adsorption resulting in a grain size > 70 nm.[69]

Our group developed a PEALD process, in which an H_2 plasma pulse is used to reduce the WF_6 precursor and enables the oxidation reaction by sulfur to WS_2 (see Figure 2-7D).[70,71] The figure shows the applied

PEALD cycle in which the target substrate was exposed first to WF_6, then purged with N_2, then activated by a H_2 plasma, purged, and exposed the sulfurizing H_2S. This technique resulted in horizontally aligned layers with a crystal grain size up to 200 nm.[72] PEALD for MoS_2 was demonstrated in a wide temperature range of 150 to 450 °C.[73]

2.2.3 Selective deposition and seeded growth

The large area growth of TMDs has the disadvantages that the nucleation site is random. When grains start to grow from these nucleation sites, they will be randomly distributed, some of the grains will grow together with faster and others slower, resulting in a broad distribution of grain sizes. The grain boundaries in between will induce strong variation in the electronic properties of transistors potentially being integrated on such a grain boundary. Therefore, the control of nucleation and by this the control over the deposition of a grain is attractive, since it can be matched with the advantageous geometry of the devices. A selective deposition method can ensure that the grains nucleate and grow from a defined point and can avoid that the nucleation and overgrowth occur randomly. One possibility to the TMD growth in a specific location is the pre-patterning of the metal precursor. To this end, ammonium heptamolybdate (AHM) or MoO_3 were lithographically pre-patterned, annealed, and sulfurized as depicted in Figure 2-8A.[74] The image shows the flow for creating MoS_2 islands in specific locations. To this end, the metal-containing precursor is deposited by lift-off technique on the substrate, then annealed, which forms beads in the deposited location, and then sulfurized forming the triangles in the specified location. This yields MoS_2 crystals around the pre-patterned area. In contrast to the "activation" of a certain area for nucleation, there are also paths to deactivate areas. Organic layers could be used as well to control the growth. Polymer functional layers (PFL) were derived from photolithography: resist layers were patterned by a O_2 / He plasma and upon wet stripping of the photoresist, a 1 – 2 nm thick polymer residual layer remains. During the CVD on those prepared substrates, the MoS_2 grows only in the regions which were treated with the plasma and growth is inhibited in the areas where the polymer layer is left as shown in Figure 2-8B.[75] This figure shows the flow as described above to form functional polymer layers in which the growth is inhibited and nucleation occurs only in the regions which were cleaned or etched by the plasma.

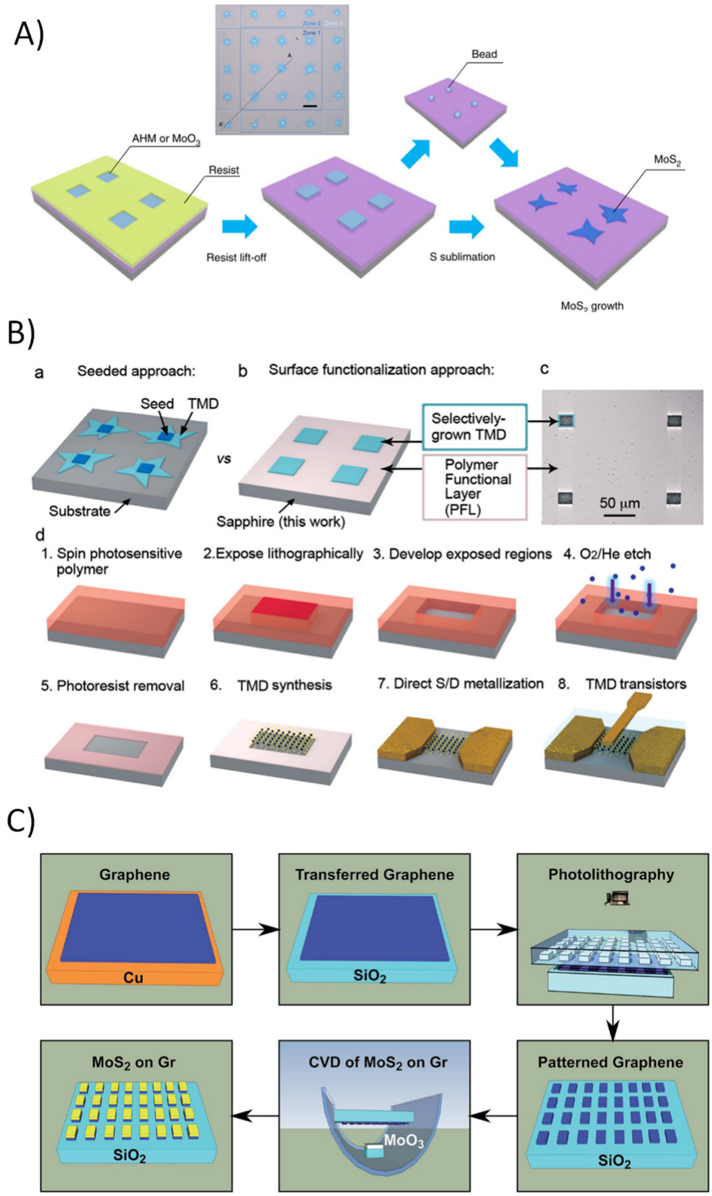

Figure 2-8: A) Seeded growth with pre-deposited and patterned MoO_3 islands, B) Seeded growth with confinement within a region surrounded by a polymer functional layer (PFL), C) Selective growth of MoS_2 on pre-patterned graphene. Reproduced from A) doi:10.1038/ncomms7128, B) doi:10.1088/2053-1583/aa6beb, C) 10.1039/C7RA07772F.

Graphene was shown as preferred nucleation site for TMD as illustrated in Figure 2-8C.[77] This figure shows a flow how MoS_2 can be selectively deposited on graphene. To this end, graphene is transferred and patterned by photolithography and etch. During the CVD, the MoS_2 nucleates predominantly on the graphene. there is also the possibility to modify the surface to improve the adsorption of the growth precursors. Regions for growth can be activated by focused ion beam (FIB). To this end, a first 2D layer was pre-patterned by FIB - the edges of the pre-patterned structure acted as preferred nucleation sites and enabled the in-plane confined growth within the pre-patterned area (Figure 2-9).[76]

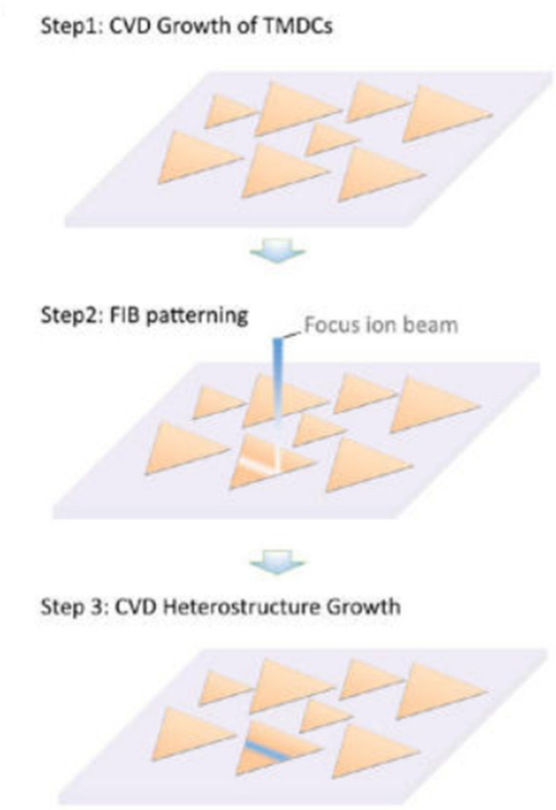

Figure 2-9: Selective growth in focused ion beam (FIB) pre-patterned 2D islands. Reproduced from doi: 10.1021/acsnano.6b06496.

The Figure 2-9 shows the flow for this lateral heterostructure formation: After CVD growth of triangles, patterns were created by FIB in those triangles, which were the preferred nucleation site for the subsequent CVD of a second TMD.

Also the substrate itself could be patterned and the edge of the pre-patterned substrate, e.g. SiO_2, will be the preferred nucleation site (Figure 2-10A&B).[78] The figure shows the process flow creating such a pre-patterned substrate in SiO_2. A Cr layer is used as hardmask to etch holes in the SiO_2. Upon the following CVD, the nucleation of the MoS_2 triangles occurs directly next to the holes as it can be seen also in the light microscopy images.

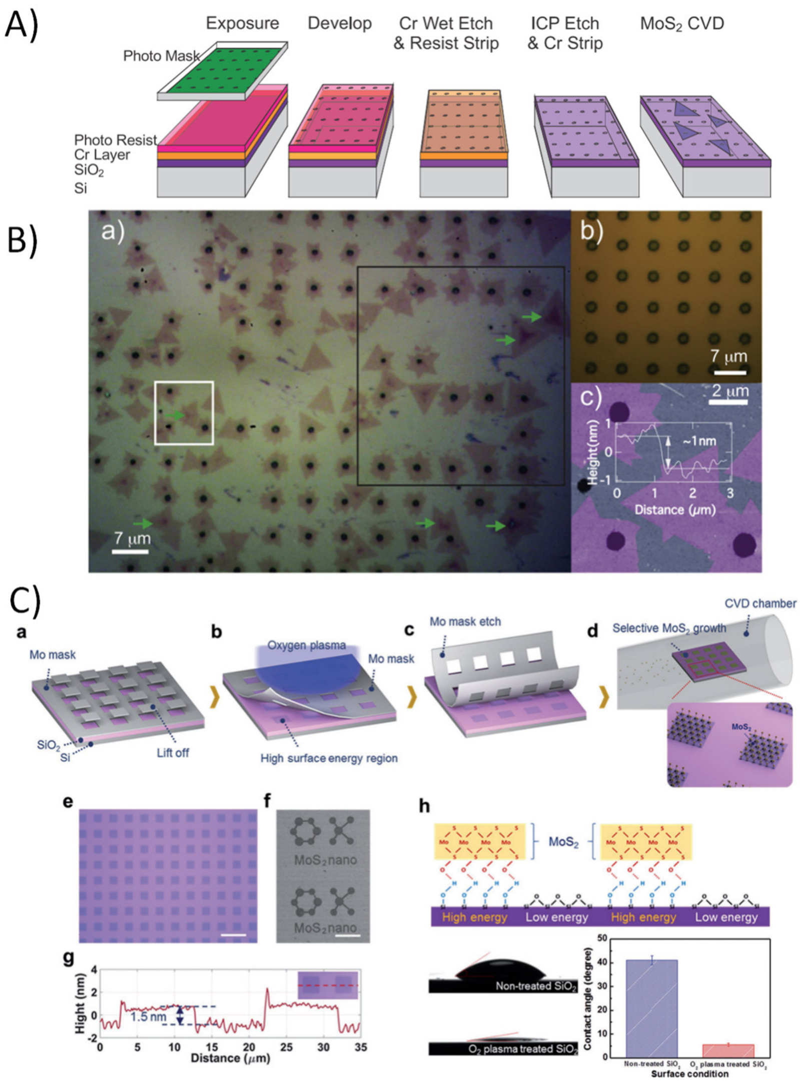

Figure 2-10: A) Schematic of seeded growth on pre-patterned substrates and B)the accompanying microscopy image, C) Selective growth on O_2 plasma-treated SiO_2. Reproduced from A) and B) doi:10.1038/ncomms7128, C) doi:10.1038/srep18754

The nucleation of MoS_2 on SiO_2 could also be controlled by plasma treatment: O_2 plasma applied in regions not being covered by a metal hardmask could make the surface super hydrophilic and make these areas susceptible for preferred nucleation as shown in Figure 2-10C.[79,80] The image shows that a bilayer could be grown and that the contact angle indicates the hydrophilicity of in the MoS_2 regions before the growth.

Chemical conversion of layers and lateral epitaxy to create heterostructures

Laser-assisted conversion processes can be used to convert specific regions under light radiation from sulfides to selenides under gas ambient containing the desired chalcogen.[81] The disadvantage of this technique is the limited spot size of the laser beam.

In-plane heterostructures could also be achieved by tuning the growth to a lateral growth mode and apply then sequential edge epitaxy by changing the gas ratios to form the desired Mo- or WSe_2 layers.[82] Although this could provide laterally alternating in-plane deposition, it is unlikely to realize desired device geometries with this technique, since it will always grow in a triangle shape. In addition, this technique cannot aid in obtaining vertical heterostructures.

2.2.4 Impact of the growth substrate on the epitaxy

To date, the films with the highest charge carrier mobilities are grown on substrates with a hexagonal lattice such as c-face sapphire, mica, or $SrTiO_3$. The TMD can form a continuous film with grains being aligned to the lattice of this substrate.[83–86] The smooth surface reduces the number of nucleation sites and allow the grain to grow laterally. This contrasts with the growth on amorphous substrate on which the MX_2 grains are rarely aligned to each other. The (0001) plane of sapphire coincides with the hexagonal structure of the MX_2 and it was proven that 50x50 μm^2 large WS_2 grains could be grown on it.[87] Despite the large lattice mismatches of 30 % (lattice constants: $MX_2 \sim 0.331$ nm, $Al_2O_3 \sim 0.476$ nm) and the thereby induced strains, the MX_2 grow epitaxially on sapphire.[88] It has been found that the grains grow parallel to step-edges in the sapphire, which enables the alignment of grains towards each other.[84,85] It was shown that the most common orientations of the MX_2 are 0° and 60° on sapphire.[89] The mobilities of MoS_2 achieved on sapphire and mica are typically around 30 cm^2/Vs.[90] Nonetheless, it was also shown that WS_2 in monolayer form can also be grown on SiO_2 substrate as large single triangle, but due to missing alignment this cannot be used for large area films in wafer size.[91] Epitaxial aligned MoS_2 layers were also grown on $SrTiO_3$.[92] Also the epitaxy on hBN is promising.[93]

2.2.5 Assessment of growth parameters

The explained growth techniques yield TMD layers of different quality. The criteria influencing the quality are systemized in Table 2-1. A result of the quality is the charge carrier mobility of the film achieved with the respective deposition technique. It is related to the crystal size, because grain boundaries contribute to charge carrier scattering. The size of a crystal is in many deposition methods determined by the temperature, since a higher temperature increases the crystallization. The precursors must be transported to each location on the substrate in a comparable amount. Control of nucleation and the orientation are other criteria, since grains can only merge if the epitaxy is aligned. At the beginning of this research work the impact of the substrate crystallinity was not set in focus, since there was a low correlation expected due to the low interlayer bonds. Nowadays, it is known that not only the roughness, but also the crystallinity of the substrate itself is crucial especially for merged grains due to their orientation and for multilayer systems. The substrate crystallinity was not specifically reviewed here, since it was not part of this research study. For future research this needs to be taken stronger into account. The scalability of the distinct process is given by the applicability to a certain substrate size.

Table 2-1 shows a summary of experimentally achieved properties of MoS_2 deposited by different techniques. Although exfoliation yields the best mobilities, there is no control about the size and location of the nanosheets. CVT offers the deposition of large crystals, but with limited control about size and thickness and the restriction to small glass ampoules. CVD films show a reasonable mobility, but they are often restricted to tube furnaces and the solid precursor delivery through the gas phase cannot be well controlled. The sulfurization approaches of pre-deposited metal offer the possibility to coat large substrates with multilayer 2D material with a grain size up to 1 µm, which is very attractive to deposit TMD on larger substrates without the difficulty to transport high-melting precursors such as MoO_3 or WO_3 through the gas phase. More controlled gas phase transport is achieved by MOCVD, although the carbon-containing precursor contains the risk of carbon incorporation into the MoS_2 film especially at high temperature larger 950 °C and high pressures > 100 hPa.[94] Carbon-free precursors such as WF_6 and H_2S are here the preferred choice.[95] They are gaseous at room temperature and thus, can be easily delivered to the wafer surface.

The low-temperature approaches for MoS_2 and WS_2 such as ALD or PECVD yield only small grain sizes and are inferior in their quality in comparison to layers deposited at high temperature.

Table 2-1: Summary of 2D deposition techniques and the relation to temperature, substrate, and contacts

Method	*Mobility $/cm^{-1}V^{-1}s^{-1}$*	*Crystal size*	*Temperature*	*Precursors*	*Measurement*	*Substrate / further information*	*Ref.*
Exfoliation	10	Flake size	750 °C – 1250 °C [2]	MoS_2 crystal	Au contacts	Monolayer on SiO_2	[5]
Exfoliation	184	Flake size	750 °C – 1250 °C [2]	MoS_2 crystal	Sc contact	10 nm multilayer on SiO_2	[96]
Chemical vapor transport (CVT)	10	50 µm	300 °C-600 °C	MoO_3, S, I_2	Cr/Au contacts, vacuum	Monolayer on mica, then transfer	[22]
Sulfurization of dip-coated samples	6	>160 nm	650 °C	MoO_3, S, N_2, Ar	Ti/Au	sapphire	[97]
Mo sulfurization on SiO_2	0.04	0.03 µm	750 °C	Mo, S, N_2	Ti/Au	SiO_2, transferred	[53]
Mo sulfurization on sapphire (Reduced & sulfurized)	0.8	Not specified	1000 °C	MoO_3, S, H_2, Ar	Ti/Au	Sapphire, transferred	[51]
CVD with growth promoter	17	20µm	700 °C-1100 °C	MoO_3, S, Ar	Cr/Pd	SiO_2	[33]
Sulfurization of pre-sputtered MoS_2	25	Not specified	700 °C	MoS_2, S, Ar	Ag paste, Hall-measurement	SiO_2	[98]
Sulfurization of pre-annealed MoO_3 with post-crystallization in N_2	80	Not specified	1000 °C	Mo, O_2, S, N_2	Ti/Au	3 -5 layers, SiO_2	[32]
MOCVD	11.5	(1-10) µm	550 °C	$Mo(CO)_6$, $(C_2H_5)_2S$, H_2, Ar	Ti/Au	3 layers, SiO_2	[46]
iALD	13.9	(10 – 70) nm	250 °C	$Mo(CO)_6$, $C_2H_6S_2$	Ti/Au	SiO_2, post deposition annealing 400°C, 30s, Ar in RTP	[69]
PECVD with H_2S plasma	2 – 3.7	(4 – 10 nm)	150 °C – 300 °C	Mo, H_2S, Ar	Hall-mobility	6 layer, PI	[43]

---

[2] Formation temperature of the crystal to be exfoliated was probably typical magma temperature or at least hydrothermal solution

2.3 Plasma patterning of TMDs for 2D device fabrication

If selective deposition is not possible, then the grown TMD films must be patterned to achieve functional devices and especially heterostructures. Plasma technology can be used to achieve the necessary film modifications. The TMD films can be etched away, thinned down, modified for improved capping layer growth, doped, or its structural phase can be changed from the trigonal prismatic (2H) to the octahedral (1T) phase by plasma.

The simple TMD removal is done in O_2- or F_2-containing plasma as well as by purely physical sputtering in Ar plasmas.[99–104] Etching is applied

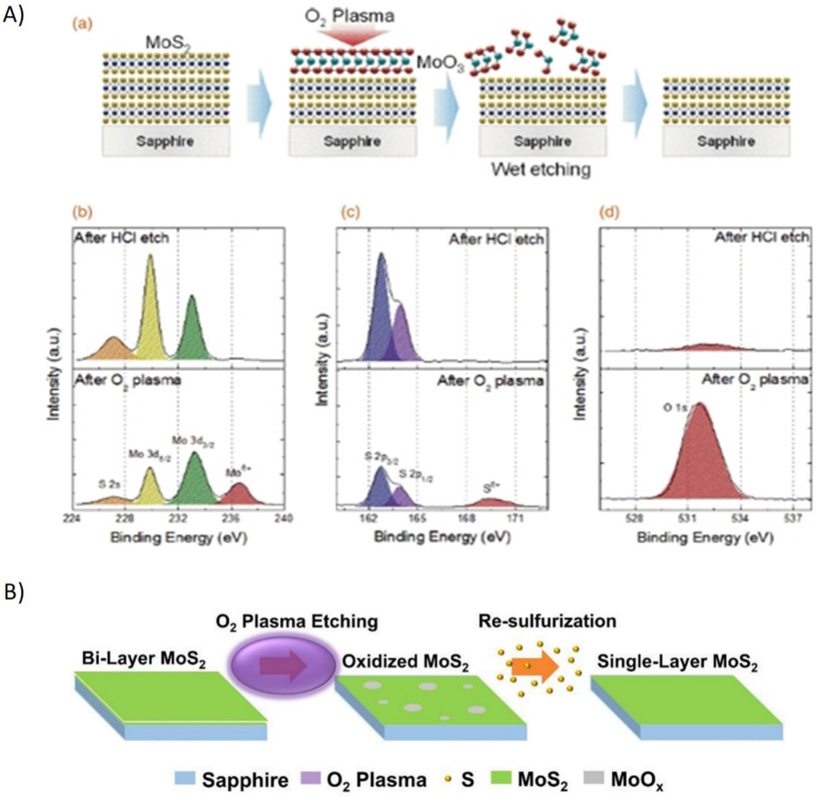

Figure 2-11: A) Oxidation of a monolayer MoS_2 by O_2 plasma and the subsequent removal by wet etching of the oxidized layer by HCl; B) Etching of a monolayer MoS_2 by a soft O_2 plasma and damage of the bottom layer, which is afterwards repaired by re-sulfurization; Reproduced from A) 10.1088/2053-1583/aa75a7 and B) 10.7567/APEX.10.035201.

to shape the 2D material after exfoliation or deposition to define the geometry of the device. The edges can be coated by metal to form a so-called side-contact. Such side-contacts show lower contact resistances than top contacts through the basal plane of the 2D material due to in-plane current injection into the 2D films.[105–107]

Besides the shaping of material, thinning is as well important. Often multilayers are formed during the growth of large area TMDs, although only few or one layer are desired. Thus, a gentle thinning technique is necessary. A layer-by-layer thinning of MoS_2 can be achieved by the combination of a plasma process and a wet process. The plasma process can oxidize the top layer, which can be dissolved in HCl as depicted in Figure 2-11A.[108] However, wet processing is critical for the yield of 2D devices, since large parts of the material tend to delaminate in liquids. Therefore, pure dry etch processes would be preferred.

For a controlled thinning of a multilayer TMD structure, continuous wave (CW) plasmas[3] with a high bias towards the material's surface are inappropriate. CW plasmas contain ions, electrons, radicals, and emit light. The electrons follow the RF electrical field, but the heavy positive ions cannot follow as fast. Due to the electrons' mobility, the cathode is charging negatively and a plasma sheath with a high quasi-DC field is building up. In this sheath, the ions are accelerated toward the sample placed on the cathode. These ions are accelerated with a certain DC bias voltage determining the kinetic energy of the impinging ions on the surface. This bombardment can destroy bonds and induce damage in the material, or it can provide the activation energy for reactive ion etching. The kinetic energy of the impinging ions is typically high so that the Mo-S bond can break. The transition metals can form quickly volatile species in halide-containing plasmas. Hence, there is no control or selectivity in these CW processes.

---

[3] The phrase continuous-wave plasma is used in the plasma community as a description for non-interrupted operation of a radio-frequent plasma in contrast to pulsed plasmas

The TMD layer could only be thinned down in a layer-by-layer fashion to obtain a defined number of MX_2 layers.

Jeon et al. claimed the layer-by-layer etching of MoS_2 layers in a CF_4 plasma.[109] By applying only an inductively coupled power to the plasmas (ICP) and grounding the substrate, they thinned a six layers MoS_2 to a monolayer within 120 s after an incubation time of 20 s (for removing the MoO_x on the surface). Another controllable thinning of MX_2 was achieved by Xiao et al., using a low-energetic SF_6/N_2 plasma.[110] To this end, they used a low-frequency (0.5 MHz) ICP plasma source in E-mode, in which the plasma is capacitively coupled towards the coil and no detrimental ions reached the substrate. With the chosen settings, they achieved etch rates of one layer in 180 s in slow mode or one layer in 12 s in the fast etching mode.[110,111]

A purely physical sputtering approach was followed by Liu et al., who employed a pure Ar plasma with low energy.[112] The controllable removal rate they achieved with this plasma was one layer per 115 s. O_2-based ALEt by soft etching of the first layer and re-sulfurization for healing the defects of the second layer was done by Chen's group by applying only a 20 W plasma as shown in Figure 2-11B.[113] The O_2 plasma was used to oxidize the first layer and sputter it away, but simultaneously the underlying layer was damaged as well and had to be re-sulfurized for healing the film. The removal process induces such damage and they are only time-controlled, which limits the controllability. Variations in the film, but also in the etch equipment impede a precise removal of a defined number of layers.

Cyclic approaches such as ALEt could achieve a true layer-by-layer removal.[114–116] ALEt consist of the reverse mechanism to ALD, namely the adsorption of a reactant for chemical modification without ion exposure. Then a purge removes all non-bound reactants and an activation step in which the modified surface layer is removed under soft ion bombardment.

Such ALEt processes were also investigated on MoS_2. Kim et al. use a Cl-radical adsorption mechanism in a chamber with a metal mesh to filter out all ions and a subsequent low-energetic Ar-ion pulse in another chamber, which can be precisely controlled with a dual grid.[117,118] This setup allows to precisely select the ion energy for the removal step, but requires the *in situ* sample change from the chlorination to the removal chamber after each cycle. Mercado et al. established a chlorine-based ALEt process in an inductively coupled plasma chamber equipped with fast-switching valves. This tool enabled the reproducible layer-by-layer etch of MoS_2.[119] The advantage is that the cycles of dosing, purging, and activation can be controlled in one chamber.[120] This tool was also used for the experiments presented in this thesis and is described in chapter 6.2.

2.4 Example of a transistor flow

To integrate 2D materials in a functional device with a TMD A overlapping with another TMD B, a metal contact to each layer, and a covering dielectric layer, several process steps are necessary. This section explains how such a process flow could look like on the example of a TFET. Two examples will be shown here: at first the conventional fabrication as it is done in a lab based on exfoliation or transfer techniques are explained. At first, a target substrate needs to be prepared. A SiO_2 gate dielectric layer must be deposited on highly doped silicon substrates acting as a so-called back gate. On such substrates, a first lithographic mask is developed, and zero markers are either deposited by the lift-off technique or etched into the substrate. Then, TMD A is either exfoliated from natural crystals or from another growth template to the SiO_2. Then, a second lithographic mask is developed to define the active structure of the TMD A. The second TMD B is then again exfoliated or transferred from another growth substrate on top of the TMD A's active area. TMD B would also require shaping as well, but this is not possible with conventional etching techniques due to the lack of selective etching techniques. The underlying TMD A would be destroyed as well. Hence, the second TMD B needs to stay in an irregular shape. Then, images must be taken to find the locations, where an appropriate overlap of TMD A and B exists and then an individual mask for the contacts must be developed and written by e-beam lithography. Similar action is necessary to define a gate on top of this structure. This procedure shows already, that this can only be a path for a few single devices and cannot be used for a parallel processing with transistors in a repeatable pattern.

Other paths must be considered to enable a parallel fabrication of many transistors in defined locations with an acceptable yield. As an example, a possible integration flow for a tunneling field effect transistor is outlined. Such a flow could start with a substrate and the growth of a TMD A, for instance by sulfurization as it was done for MoS_2 within this thesis and depicted in Figure 2-12. In such a layer, the active area can be defined by lithography and etching. Ideally, the TMD B should be selectively deposited in areas overlapping with TMD A. To this end, a bottom-up growth, seeded growth, or a selective conversion process as developed within this research project, can be used. The advantage of the latter one, is that a sacrificial layer is patterned first with a technique inducing no or low damage on TMD A. The sacrificial layer can then be converted into another TMD B, which is not affecting TMD A. After active areas are defined for TMD A and B, the semiconducting layers can be embedded in a dielectric, the contacts can be defined by another lithography and etching, and eventually, a conventional gate process can be used to form an electrode above the overlapping area of TMD A and TMD B.

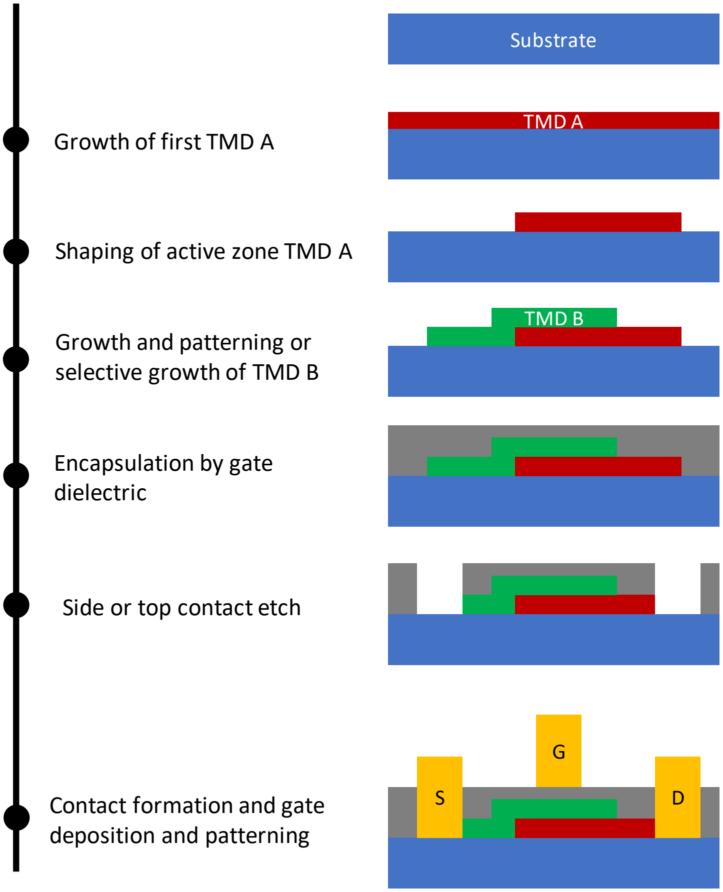

Figure 2-12: Example of a transistor flow containing two TMDs on the example of a TFET.

2.5 Considerations on the thermodynamics and reaction kinetics

An essential part of this thesis investigates the growth of a TMD multilayer film using hybrid physical deposition methods and the combination with a chemical conversion. Further, the quality improvement by thermal annealing processes is studied. All these processes have different thermodynamics and kinetics. Thermodynamic calculations were done, where appropriate, by the software HSC Chemistry to calculate the change in Gibbs free energies based on the enthalpy and entropy change. Negative (exergonic) changes indicate that a reaction is spontaneous in forward direction and positive (endergonic) changes indicate reactions being only spontaneous in reverse direction. However, the observed process, be it conversion or decomposition can only proceed once the activation energy E_A is provided to overcome the energy barrier. The activation energy is related to the kinetics of a process. The reaction rate depends on the rate constant and the concentrations of the base substances. The rate constant depends temperature and its relation is described by the activation energy. For the majority of reactions the activation energy is positive, meaning that the rate constant increase with increasing temperature.

The experiments designed within research project were not designed to quantitatively study the kinetics due to different practical boundaries – it would require observation of short and longer processes, which is not achievable with the used thermal treatment systems. Therefore, only qualitative statements could be made.

Activation energies in literature for W sulfurization is 150 kJ/mol, Mo sulfurization it is 103 kJ/mol to 147 kJ/mol.[121] The activation energy for S removal is estimated at 334 kJ/mol.[122] More values for pure or oxidized base material could not be found.

3 Global research approach and methods

3.1 Approach and thesis structure

The deposition of high-quality, ultrathin layers with only a few layers thickness over large areas was investigated. Due to the restriction in transport capabilities of evaporated metal- or metal oxides with a melting point of a few hundreds of °C, alternative routes had to be explored. A hybrid physical-chemical chemical vapor deposition process was studied, here referred as sulfurization and is described in section 4.1. Metal or metal-oxide films were deposited ex-situ by techniques allowing a low-rate deposition for accurate thickness control, such as physical vapor deposition (PVD) or electron-beam evaporation. The sulfurization with the gas-phase precursor H_2S mixed with H_2 was studied. The influence of the partial H_2S pressure, the processing temperature, and time to achieve layered MoS_2, and basal planes being parallel aligned to the substrate was studied. The sulfurization mechanism of metal-oxide versus metallic base material was compared.

As an alternative to MoS_2 sulfurization, the deposition of the TMD WS_2 from gas phase precursors WF_6 and H_2S was investigated. The role of the starting substrate and the provision of reducing agents in conjunction with an appropriate temperature window in the range of typical CVD temperatures was studied and described in section 4.2. The composition and structure of the resulting films were correlated to the reaction conditions and base materials as metals or the metal-oxides MoO_x and WO_x. The impact of different sulfurization temperatures was studied to determine the necessary temperature window.

Low temperature growth results in low crystallinity. Therefore, rapid thermal annealing (RTA) processes in sulfur-rich and in inert environments was studied to improve the crystallinity. To address the impact of the heating source and the temperature/time profile, RTA was compared to excimer laser annealing (ELA) with ultrashort pulses to heat the material locally. The impact of capping layers on the recrystallization kinetics was evaluated. The principle of metal-induced crystallization (MIC) was applied to the TMD with low crystallinity. In the MIC mechanism, the additional metal catalyzes the atomic diffusion of chalcogen and metal atoms on a stable substrate and is capable to lower the recrystallization temperature far below the melting point of the compound. Dielectric capping layers were used to recrystallize amorphous or low-crystalline WS_2 to a highly ordered phase by confining the crystallization volume and by avoiding chalcogen loss and the formation of sub-stoichiometric films. This quality improvement of 2D films by capped rapid thermal annealing and by nanosecond laser is described in section 5.

The WF_6 reaction with reducing agent Si and the sulfur-containing precursor H_2S were investigated. The hypothesis was that the manipulation of the reducing agent as essential reaction partner could enhance or inhibit the growth of TMD, here specifically WS_2, and enable the selective growth of a material in a specific location. In this thesis, we followed the approach to pattern a few nm thick Si films as the reducing agent on top of an insulator to understand the impact of this reducing agent and to verify a possible selectivity to the substrate as described in section 6.1.

Eventually the formed TMD films had to be integrated as heterostructures using a plasma patterning approach which can stop accurately on a low-dimensional film with minimal damage to the underlayer. Due to the aggressive nature of conventional CW plasmas, ALEt as low-damage plasma was investigated and the damage to underlying layers was evaluated. Furthermore, ion velocity distributions of the ALEt process were determined to explain the plasma-surface interactions on 2D materials. The combined approach to selectively etch Si by ALEt from MoS_2 with minimal damage and conversion of the patterned stack it into a heterostack with WS_2 and MoS_2 is explained in 6.2.

Chapter 7 concludes the obtained results and chapter 8 provides an outline for further research to advance the investigated techniques to obtain functional 2D devices on wafer-level.

3.2 Methods

Spectroscopic and image techniques were used to study the composition and quality of the modified films. The base substrate for material growth as well as etching experiments were silicon wafers coated with one or two dielectric layers. These dielectric layers enabled the visibility of mono or few-layer nanosheets and avoided the reaction of the precursors with the Si substrate. For the sulfurization part in this study, only SiO_2 was used as dielectric interlayer. The base substrate for all the investigations following the chapter about Si-to-W conversion included an additional ALD-deposited Al_2O_3 top layer, which was stabilized against HF by a 1000 °C O_2 annealing. This provided a stable surface against additional wet removal steps for native oxides and mimics the surface of widely used sapphire substrates.

The impact of the treatments was measured by Raman spectroscopy. In Raman spectroscopy, the sample is exposed to monochromatic laser light. The light interacts with the vibrational modes through inelastic scattering by an incoming photon with the electrons in the molecule. The molecule is excited to a virtual energy state and the scattered photon has an energy being

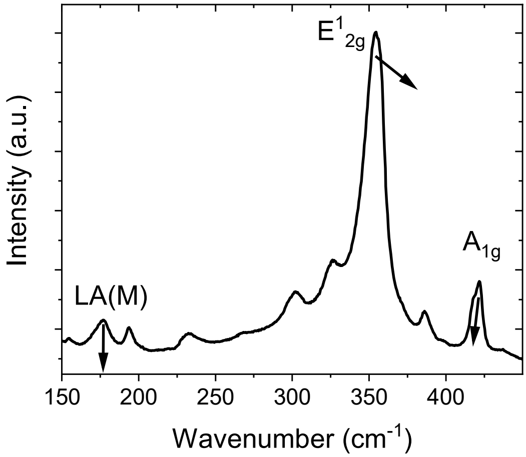

Figure 3-1: Example of a Raman spectrum taken from WS_2. Arrows indicate the frequency shift for decreasing number of layer for the E & A peak and a reduction in case of less defectivity in the LA(M) peak.

different than the excitation energy due to different energy state of the molecule. The allowed transitions are following the selection rules for electronic transitions. A polarizability change is required for Raman scattering. The symbols can be found in the character table: In $E^1{}_{2g}$, E stands for doubly degenerate or two-dimensional, prime/superscript ^{1} means symmetric with respect to σ_h (reflection in horizontal plane); subscript $_2$ means anti-symmetric with respect to the C_n principle axis, if no perpendicular axis, then it is with respect to σ_v; subscript $_g$ symmetric with respect to the inverse. The σ_h is the reflection of the molecule horizontally compared to the horizontal highest fold axis; σ_v is reflection of the molecule vertically compared to the horizontal highest fold axis and C_n is with $2\pi/n=$ number of turns in one circle on the main axis without changing the look of a molecule (rotation of the molecule).[123]

Each material has characteristic modes, which can be identified and are shown for the example of WS_2 in Figure 3-1. The most prominent peaks for WS_2 and equivalent materials are the in-plane $E^1{}_{2g}$ and out-of-plane A_{1g} modes. Their frequency shift can be used to identify the thickness below four layers down to the monolayer.[124] The arrows for these two modes in the figure indicate the shift of decreasing number of layers: the intensity would decrease since less modes are present and a frequency shift corresponds to the thickness change. Another figure of merit is the ratio between the longitudinal acoustic LA(M) mode, which is a defect-related peak, and the $E^1{}_{2g}$ mode. This ratio could be used to compare the quality of a 2D film with a certain thickness.[119] In case of higher quality MX_2, the LA(M) peak would decrease in relation to the $E^1{}_{2g}$ peak. If the quality of a film is repeatable, e.g. at a fixed synthesis temperature, the intensity of these peaks can be used to quantify the amount corresponding to the certain vibrational modes, which correlates then to the thickness. Vice versa, it is possible to determine the quality of the film, which is correlated to the crystallization degree under the assumption that the thickness and topology is similar for films of different quality. A combination of the Raman spectroscopy with an imaging technique such as atomic force microscopy (AFM) or top view scanning electron microscopy (SEM) is inevitable to obtain the correct conclusion from Raman spectroscopy measurements. An additional feature of the Raman spectroscopy is the simultaneous measurement of Raman shift and photoluminescence (PL) of a film in the same tool. Photoluminescence can be interpreted as a quality feature, which is observed already in thin flakes with a weak intensity and which is shifting to higher energies with very high intensity due to a shift from indirect to direct bandgap semiconductor when approaching the thickness of a monolayer. Nevertheless, the photoluminescence needs to be interpreted with care, since particularly edges of 2D crystals show an enhanced PL and should not be interpreted wrongly as an overall quality increase. The characteristic PL peaks are originating from the A and B excitons at 1.85 eV and 1.98 eV for MoS_2, 1.95 eV and 2.05 eV for WS_2, respectively. The Raman spectroscopy and the PL measurements were done with a Horiba LabRAM HR system.

Rutherford backscatter spectrometry (RBS) is another powerful technique to quantify the number of atoms per area in the monolayer range, which corresponds to approximately 1E15 at/cm^2. For this measurement, charged He particles (1.5 MeV) are accelerated with a high energy towards the sample surface and undergo elastic collisions with the sample material.[125] The backscattered ions can be detected, and the energy-resolved spectrum is a function of the amount and depth of the present elements. Through an appropriate fitting procedure, the number of atoms per area can be extracted and delivers for heavy elements such as Mo or W uncertainties of 0.1E15 at/cm^2, hence values in the sub-monolayer range, and for the lighter chalcogens slightly higher uncertainties of 0.3E15 at/cm^2. The stoichiometry can be determined from those absolute values.

The characterization of the grown or plasma-treated film were further complemented by X-ray photoelectron spectroscopy (XPS) for which the sample is irradiated by X-ray beams and emits photoelectrons. The energy distribution of the detected photoelectrons corresponds to the elements and the chemical state on the sample’s surface. The oxidation state of differently bound atoms can be distinguished by high resolution scans. For Mo and W, the sulfide-bonds and the higher oxidation state, i.e. for MoO_3 and WO_3, can be clearly observed by doublets at different peak position. The system used for the analysis of the samples within this thesis was a Theta300 from ThermoInstruments, using a monochromatized Al K_α

X-ray source (1486.6 eV). For more surface-sensitive probing, Auger-electron-spectroscopy (AES) was applied, when necessary.

Roughness analysis was done by a Bruker ICON PT AFM in tapping mode within a scanning area of 1 μm^2.

Although the composition and the surface topology are helpful to assess the modifications, more insight had to be obtained by transmission electron microscopy (TEM). Even though this technique provides only local information, it provides insight on the nanoscale about the alignment of the individual layers, grain size, and defects. For image acquisition either a FEI Tecnai F30 ST or a Titan3 G2 60-300 was used. FIB-cuts were prepared using a Helios 450HP.

The combination of the above described techniques allows to investigate the impact of the growth techniques or the plasma modifications on the films and to derive conclusions to obtain novel insight into the science of 2D materials.

The experimental approaches of sample preparation and procedures are described in each of the following chapters separately.

4 The growth of MoS_2 and WS_2

4.1 Multilayer MoS_2 growth by metal and metal oxide sulfurization

This chapter describes the sulfurization of Mo or MoO_x by the precursor mixture H_2S / H_2. The goal was to form a high quality MoS_2 film with horizontal grain orientation. To this end, PVD deposited Mo and MoO_x films of different nm-thicknesses were sulfurized with H_2S at different sulfurization temperatures, different H_2S partial pressure, and for different duration.

This is a hybrid physical-chemical vapor deposition, since it combines the accurate location distribution of the metal precursor with high melting point on the growth substrate by a physical deposition method and the conversion into a chalcogenide by the volatile sulfur gas phase precursor H_2S at elevated temperature and pressure.

We found that the sulfurization of MoO_3 is thermodynamically favorable in comparison to the direct sulfurization of metal and that the sulfurization of the oxide starts already at a lower temperature than the metal sulfurization. It was found that the low partial H_2S pressure slowed down the sulfurization of metallic Mo. The best sulfurization result was obtained using the highest applicable, tool-limited temperature of 800 °C without any H_2. The obtained film showed a good surface coverage with only a few delamination spots. The films were hydrophobic/mildly hydrophilic and were predominantly sulfur-terminated. Nevertheless, the sulfur-metal ratio was 1.8, thus slightly below 2, which indicates that there are vacancies at the surface or at reactive grain boundaries. The sulfurized films showed photoluminescence representing a decent quality. Nevertheless, the obtained film is polycrystalline and needs further improvement to be used in devices. As a consequence, both alternative WS_2 growth (chapter 4.2) and layer improvement concepts (chapter 5) were pursued.

This chapter was published as:

Heyne, M. H.; Chiappe, D.; Meersschaut, J.; Nuytten, T.; Conard, T.; Bender, H.; Huyghebaert, C.; Radu, I. P.; Caymax, M.; de Marneffe, J.-F.; Neyts, E. C.; De Gendt, S.; Multilayer MoS_2 Growth by Metal and Metal Oxide Sulfurization. J. Mater. Chem. C 2016, 4 (6), 1295–1304.

The author did the design of all experiments, sample preparation, the sulfurization experiments, analysis of the provided data, and the discussions with the co-authors.

Abstract

We investigated the deposition of MoS_2 multilayers on large area substrates. The pre-deposition of metal or metal oxide with subsequent sulfurization is a promising technique to achieve layered films. We distinguish a different reaction behavior in metal oxide and metallic films and investigate the effect of the temperature, the H_2S/H_2 gas mixture composition, and the role of the underlying substrate on the material quality. The results of the experiments suggest a MoS_2 growth mechanism consisting of two subsequent process steps. At first, the reaction of the sulfur precursor with the metal or metal oxide occurs, requiring higher temperatures in the case of metallic film compared to metal oxide. At this stage, the basal planes assemble towards the diffusion direction of the reaction educts and products. After the sulfurization reaction, the material recrystallizes and the basal planes rearrange parallel to the substrate to minimize the surface energy and coalesce. Therefore, substrates with low roughness show basal plane assembly parallel to the substrate. These results indicate that the substrate properties have significant impact on the assembly of low-dimensional MoS_2 films.

4.1.1 Introduction

Transition-metal dichalcogenides (TMD) such as MoS_2 or WS_2 are interesting materials for future transistor applications, but their large-area deposition is challenging. First transistor devices based on TMDs were demonstrated on mechanically exfoliated flakes[5,126]. The mechanical exfoliation allows only the deposition of sheets up to a few µm^2 size, which makes this process inappropriate for high device densities on large areas. In addition exfoliated flakes which are considered as best material quality at this juncture, show spatial variations in their properties[127–129]. TMD films have been deposited by chemical vapor deposition[130–132] on substrates up to a few cm^2. This deposition can be achieved by the vaporization of solid MoO_3 and S in a furnace under inert carrier gas flow. However, this technique is very sensitive to the amount of the precursor, the carrier gas flow in the furnace, and the substrate temperature itself, and therefore it is difficult to scale to larger substrate dimensions. To decrease the vaporization influence of the metal precursor, it is possible to pre-deposit a transition-metal (TM) or transition-metal oxide (TMO) on a substrate with subsequent sulfurization from a S source[53,133–136]. The homogeneous S supply can also be achieved by using a gaseous precursor such as H_2S[137–144]. The present paper elucidates the mechanisms of MoS_2 multilayer synthesis by the sulfurization technique. The influence of the process temperature, annealing time, and ramp rate is studied, as well as the nature of the pre-deposited layers MoO_3, metallic Mo, and the nature of the substrate. The synthesis ambient was compared for mixtures of H_2S/H_2 vs. pure H_2S. The grown films were characterized by various optical, morphological, and structural techniques. The highest quality MX_2 films have been only demonstrated on atomically flat substrates such as graphene or other exfoliated MX_2 substrate layers[145,146], but the deposition on amorphous substrates is desirable due to their availability for large area substrates such as 300 mm wafer. This paper establishes guidelines for the synthesis of horizontally aligned transition-metal dichalcogenide multilayer thin films on SiO_2.

4.1.2 Experimental

4.1.2.1 TM and TMO deposition

The Mo-based TM and TMO films were prepared by physical vapor deposition on top of thermal or native silicon oxide substrates. To deposit TMO, oxygen was added as reactive component in the PVD deposition. We studied a thick 5 nm Mo-film on 270 nm wet thermal silicon oxide (stack A), a thin 2 nm Mo-film on 270 nm wet thermal silicon oxide (stack B), and a 5 nm reactively sputtered MoO_x on thin native silicon oxide (stack C).

4.1.2.2 Sulfurization of the TM and TMO films

The samples were sulfurized ex-situ in a 6-inch rapid thermal processing (RTP) chamber ANNEALSYS-ONE-150 equipped with H_2 and H_2S gas supply. For this purpose, the samples were placed on top of a SiC-coated graphite susceptor in the annealing chamber. The chamber was pumped to vacuum and then the temperature was increased to the target temperature 400 °C, 600 °C, or 800 °C. The gas mixture of 10 % or 100 % H_2S in H_2 was injected until the pressure reached 100 mbar and kept under static conditions for the process duration of 5 min to 30 min. Afterwards, the heating was stopped, the chamber was cooled down and pumped to vacuum again for 20 min.

4.1.2.3 Characterization of the films

The films were analyzed by Rutherford backscattering spectrometry (RBS) to determine the amount of Mo and S after the sulfurization. The accelerator at imec is a 6SDH Pelletron accelerator from the National Electrostatics Corporation (NEC). To this end, a He-beam with an energy of 1.523 MeV and a beam currents of 20 nA to 40 nA were used. The scattering angle was 170° and the tilt angle was 11°. The used goniometer is described in literature[147]. Before the measurement, the incident beam was calibrated

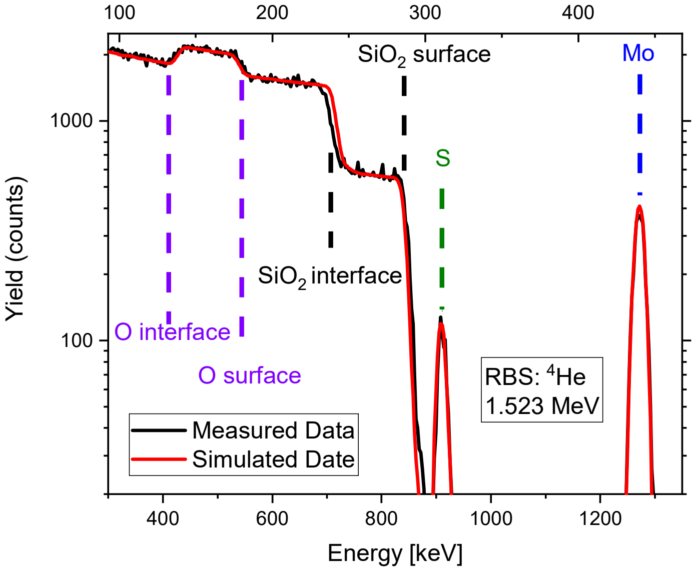

Figure 4-1: RBS spectrum of a MoS_2 film sulfurized from a stack of 2 nm Mo / 270 nm SiO_2 / Si substrate.

to a reference material of an AlW/TiN/Si substrate. A representative spectrum of MoS_2 can be found in Figure 4-1.

Raman spectroscopy with a LabRAM HR tool was used to characterize the films' quality using an excitation wavelength of 532 nm and a grating of 1800 grooves/mm, yielding a theoretical resolution of 0.3 cm^{-1}. A scanning electron microscope (SEM) FEI Nova 200 was used to investigate the surface morphology. Transmission electron microscopy (TEM) cross-section images were obtained with a FEI Tecnai F30 ST at 200 kV and plan-view images with Titan^3 60-300 at 60 kV. The surface roughness was determined by an atomic force microscope (AFM) Dimension-Icon PT. Angle-resolved x-ray photoelectron spectra (ARXPS) were measured with a Theta 300 system from ThermoInstruments. X-ray diffraction characterization was done with Panalytical X'PERT.

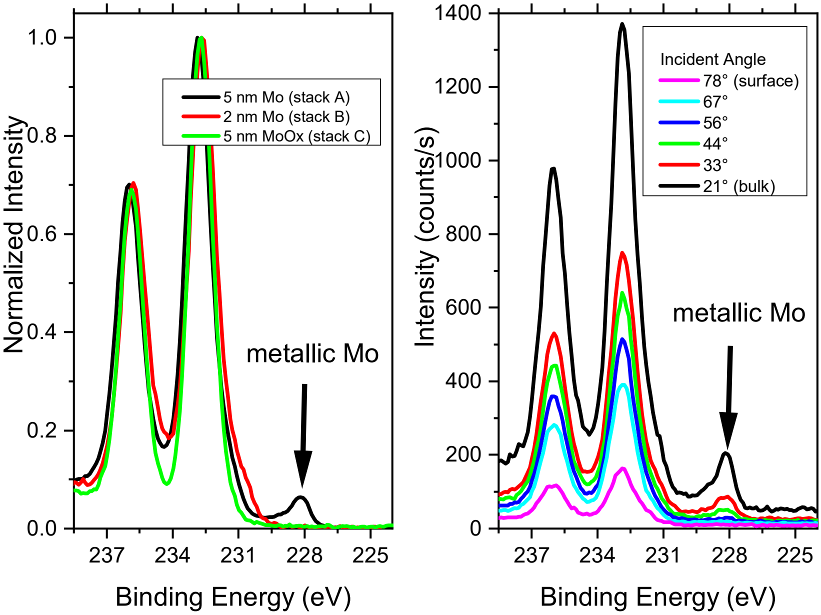

Figure 4-2: ARXPS on stacks A, B, and C before sulfurization showing oxidation of the layers and buried metallic Mo on stack A.

4.1.3 Results

4.1.3.1 Part I: Growth parameter study

4.1.3.1.1 Analysis of the pre-deposited material

TM and TMO films were deposited on 270 nm wet thermal silicon oxide substrates. The 5 nm (stack A) and 2 nm (stack B) metallic films oxidized partially or fully as soon as they were exposed to ambient. SEM images showed continuous films upon deposition. A third test specimen with 5 nm MoO_x (stack C) on thin native silicon oxide was prepared by reactive sputtering. To determine the level of surface oxidation, stacks A, B, and C were analyzed by angle-resolved X-ray photoelectron spectroscopy (ARXPS). Information about the oxidation state was gained from the energy shift of the Mo 3d peak[148,149]. Figure 4-2 shows the all-integrated, normalized Mo 3d peaks in the XPS spectra for the three different stacks and the angle-resolved Mo 3d peak for stack A.

At 78°, the spectra for all three samples overlap, showing no metallic contribution, therefore indicating that all samples, TM and TMO, have an oxidized surface. By probing deeper under the surface, i.e. 21 ° angle, it was found that only stack A shows a peak at the lower binding energy around 228 eV. The spectra for stacks B and C appear similar and they do not show this peak at low binding energy.

4.1.3.1.2 Sulfurization process

Starting from a typical 10 % H_2S/H_2 mixture as it is used in the MoS_2 catalyst preparation[150], the temperature window between 400 °C and 800 °C was investigated. Afterwards, the influence of the H_2S partial pressure on the deposited film was explored. We subsequently tested the impact of the sulfurization time and finally compared the influence of the underlying film on the growth conditions.

4.1.3.1.3 Influence of the processing temperature

The sulfurization of the stacks A,B, and C was carried out at temperatures of 400 °C, 600 °C, and 800 °C. The chamber was heated in vacuum until the target temperature was reached, and subsequently the H_2S gas was introduced and kept in the chamber for 5 min under static conditions. Afterwards, the chamber was evacuated and cooled down passively. The samples were characterized by Rutherford backscattering spectrometry (RBS) and the ratio of the atomic areal density of S and Mo was calculated. The resulting S/Mo ratios are shown in Figure 4-3. The uncertainties shown in this graph originate from the uncertainty of the sulfur, since it is higher than the uncertainty of the molybdenum amount. The surface element analysis of the areal density were delivered with a relative uncertainty.

After sulfurization at 400 °C, the S/Mo ratio did not exceed 0.5 in any of the samples, increasing to the range 0.6 - 1.0 for the 600 °C-treated samples and up to a range 0.6 - 1.9 for the 800 °C-treated samples. At 800 °C, the sulfurization in stack C was higher than in stack B at 800 °C, while in contrast, stack A could not be fully sulfurized in the H_2S/H_2 mixture even at 800 °C within the 5 min processing time in the H_2S/H_2 mixture. In

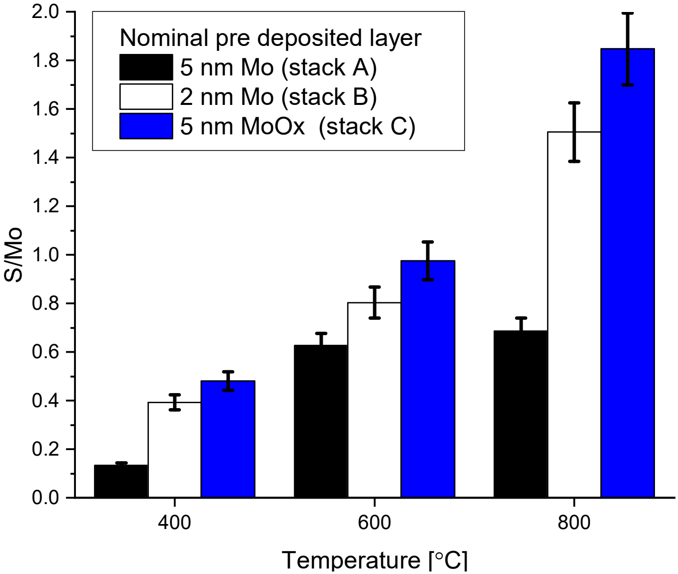

Figure 4-3: S/Mo ratio of different stacks after 5 min sulfurization at different temperatures in a 10 % H_2S/H_2 mixture as determined by RBS.

the next paragraph, the influence of the hydrogen fraction in the gas mixture is described.

4.1.3.1.4 Influence of the H_2S partial pressure in the sulfurization process

Samples of stack A, B, and C were heated to 600 °C and the 10 % H_2S/H_2 mixture or pure 100 % H_2S was injected in the chamber and kept under static conditions for five minutes. Afterwards, the samples were characterized by RBS and the S/Mo ratio was calculated. Stack A had a relatively low S/Mo ratio of below 0.8 for both annealing conditions (Figure 4-4). In contrast, stacks B and C showed significant differences with the 10 % mixture showing a S/Mo ratio of only 0.8 to 1.0 after 5 min, whereas the pure H_2S resulted in a ratio of about 2. The Raman spectra taken after sulfurization in 10 % and 100 % H_2S are depicted in Figure 4-5. The samples annealed in pure H_2S showed higher MoS_2-related peak intensity than in diluted H_2S, further confirming the results from RBS.

We also investigated the time-dependence for TM/TMO film conversion. To this end, the stacks A, B, and C were sulfurized either in 10 % or 100 % H_2S for different times, and the S/Mo ratio was determined by RBS as shown in Figure 4-4.

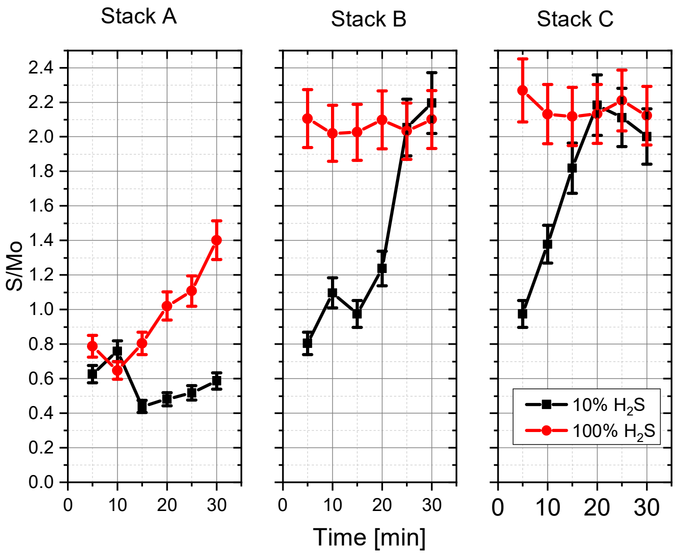

Figure 4-4: S/Mo ratios as calculated from the RBS atomic areal density, for sulfurization of TM and TMO at 600 °C in H_2*-diluted and pure* H_2S*.*

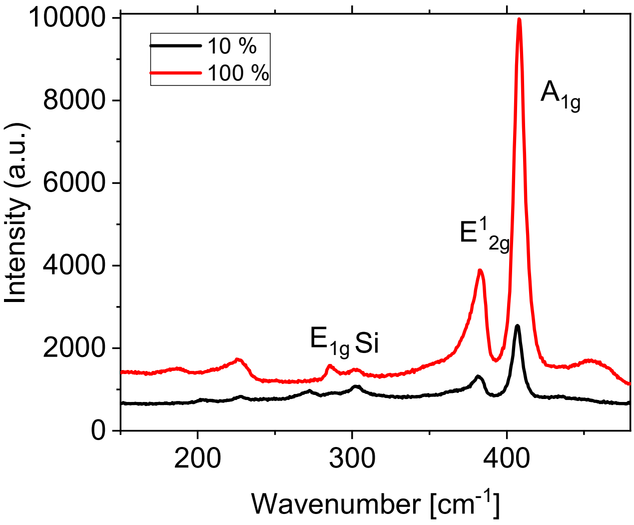

Figure 4-5: Raman spectra of a stack B sample annealed for 5 min at 600 °C in H_2*-diluted and pure* H_2S*.*

Stack A of the 5 nm Mo shows a slow ratio increase and was not reaching the target value of S/Mo = 2 within 30 min, while in the case of H_2 dilution, the sulfurization was even slower on the metallic Mo. So the E_A seems to be high for the sulfurization of pure metallic Mo. In contrast, stacks B and C show significant time-dependent sulfurization under H_2 dilution and even immediate sulfurization with ratios about 2 already after 5 minutes processing time in the case of pure H_2S. Hence, the sulfurization of MoO_x must have a lower activation energy than the metal sulfurization. The sulfurization under H_2 dilution was slower than in pure H_2S in all cases studied due to the difference in partial pressure. Nonetheless, the results show some non-idealities: in principle, such an experiment would require the analysis in a larger time window – for very short times as well as very long time with the simultaneous analysis on the log-scale, then more information could be gathered about kinetics. The use of the rapid thermal annealing system, which is not designed for long-lasting experiments, restricted this analysis. Despite the fact that nowadays RTP systems using light with strong intensity in the infrared range and good excellent temperature control, the lab system especially in conjunction with the toxic gas is not the appropriate setup for studying kinetics.

In addition, some ratios showed values above two, which could indicated that traces of another element binding S was present possibly to insufficient chamber cleaning.

Annealing with best conditions

Promising sulfurization conditions were achieved at 800 °C according to Figure 4-3 and the pure H_2S as concluded from Figure 4-4 on stack A within 30 min. These conditions were applied to different initial thicknesses of deposited Mo on SiO_2 and characterized by RBS after the sulfurization process. Figure 4-6 shows that the S/Mo ratio as calculated from Mo and S amount is between 1.8 and 2. Layers of initially 5 nm metallic Mo resulted in approximately 25 nm MoS_2 films. Nonetheless, the S/Mo ratio was despite the optimized conditions below 2.0. This indicates that a large fraction of the Mo was sulfurized, however, there is a considerable amount of sulfur missing, which must appear as vacancies, grain boundaries, and other defects deteriorating the electronic grade of this material.

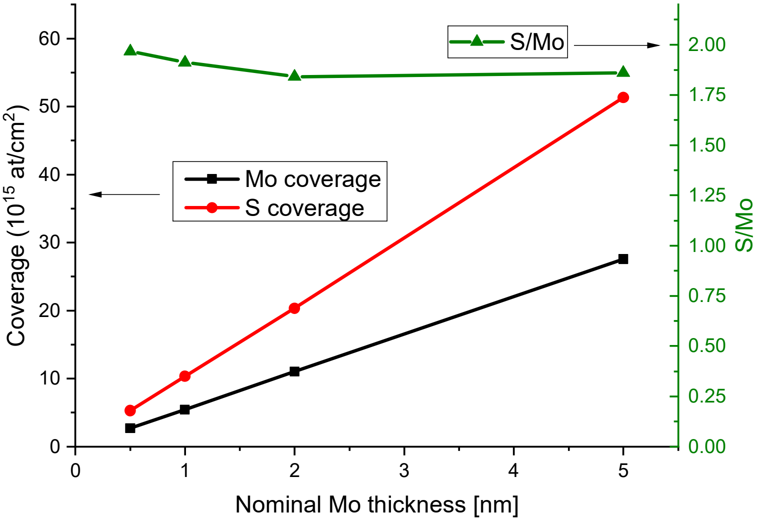

Figure 4-6: Coverage of Mo and S and the S/Mo ratio after 800 °C sulfurization in 100 % H_2S for 30 min as a function of the initial sputtered Mo thickness determined by RBS.

4.1.3.2 Part II: MoS_2 plane orientation

4.1.3.2.1 Effect of ramp rate and interlayer oxide

The surface topology of the stacks B and C was compared by scanning electron microscopy (SEM) and atomic force microscopy (AFM) after annealing without H_2S and after the sulfurization process with 100 % H_2S. The results are illustrated in Table 4-1.

Table 4-1: Comparison of the surface roughness of different stacks after sulfurization at 800 °C in 100 % H_2S for 30 min. The scanned area was 2x2 um^2.

	B	C
pristine	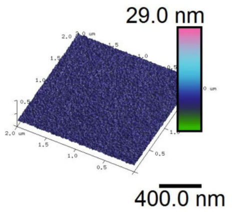	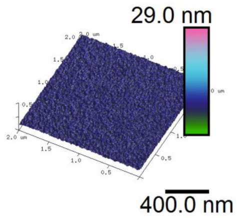
After H_2S annealing	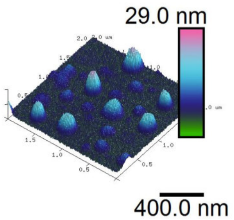	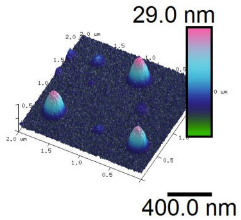

The as-deposited metal and metal-oxide films had an initial RMS roughness of 0.3 nm to 0.4 nm. Neither holes nor agglomeration was observed before the annealing. After annealing in vacuum, the samples of stack B roughened. Annealing in 100 % H_2S increased the surface roughness even more. The arithmetic roughness parameter Ra of the H_2S annealed stack B was Ra = 2 nm.

In contrast, stack C with the TMO on the native oxide showed less roughening than stack B in vacuum as well as in H_2S. The roughness of stack C was only Ra = 1.5 nm. Hence, the samples with the wet-grown silicon oxide underneath roughened to a larger extent than the samples grown on native silicon oxide.

A smooth surface is important for potential integration of planar electronic devices. To investigate this, the samples of stack B and C were measured before and after the sulfurization process.

Significant roughening can be seen after the MoS_2 synthesis process on both sample surfaces and hillocks appeared on the surface. The sulfurized stack B showed a larger density of these hillocks than stack C, and these bumps were higher than 20 nm after sulfurization. The TEM image in Figure 4-7 shows that a delamination occurred at the interface between MoS_2 and SiO_2 substrate. Stack B showed more delamination sites than stack C and hence, MoS_2 on wet thermal oxide formed more hillocks than on native SiO_2. This delamination could have its origin in the surface energies, for which the systems tries to minimize the contact.

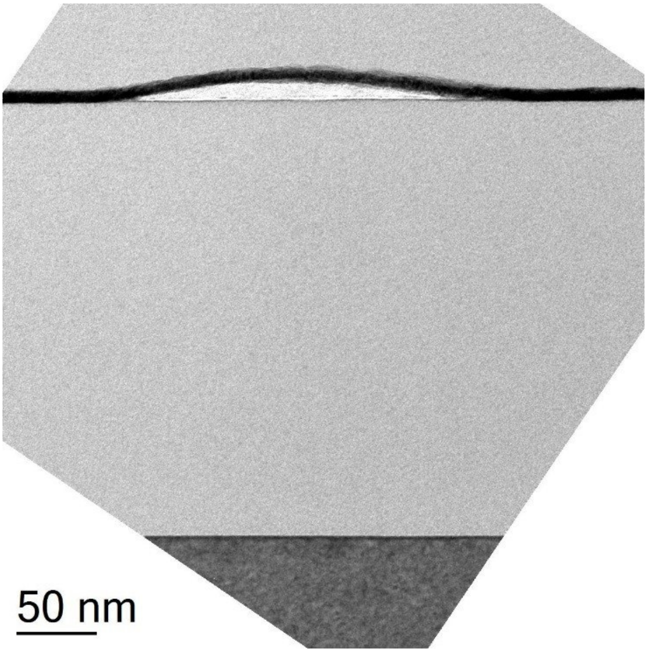

Figure 4-7: TEM image showing delamination of the MoS_2 film (dark) from the SiO_2 substrate (bright).

4.1.3.2.2 Underlying substrate

The role of the underlying substrate on the basal plane arrangement will be studied in this section. To this end, stacks B and C were sulfurized at 600 °C and 800 °C in pure H_2S. The TEM cross section images are shown in Table 4-2.

Table 4-2: TEM images of the stacks sulfurized in 100 % H_2S for 30 min at different temperature.

Sulfurized Stack B at 600 °C in H_2S: MoS_2 on thick SiO_2	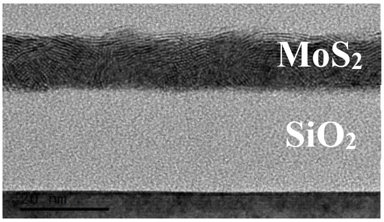
Sulfurized Stack C at 600 °C in H_2S: MoS_2 on thin SiO_2	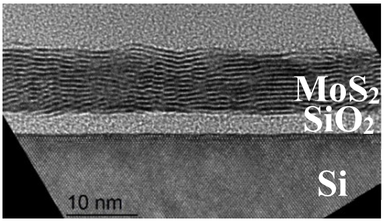
Sulfurized Stack B at 800 °C in H_2S: MoS_2 on thick SiO_2	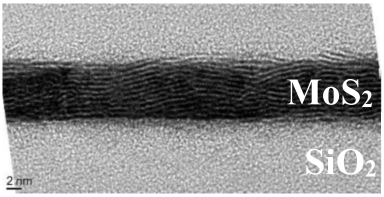

Stack B reveals two preferential layer orientations after the 600 °C sulfurization. While the surface layers appear rather horizontal, the bulk material is oriented more vertical to the substrate. The layered structure can be seen in the whole film and thus, the H_2S precursor is diffusing throughout the whole film, even at 600 °C.

However, stack C revealed a horizontally layered structure over the full thickness after the 600 °C sulfurization. At the same time, the interface oxide of 3 – 4 nm was thicker than the usual native oxide of around 1 nm, meaning that the oxide thickness has increased during the high temperature step despite the reducing atmosphere. Since stack C is MoO_x, there might be an oxygen-sulfur exchange reaction. A similar horizontal assembling like in stack B could only be reached at a higher temperature of 800 °C within the given timeframe, leading us to conclude that the interfacial oxide thickness and substrate type result in an interplay with different sulfurization temperatures to different basal plane assemblies. On thin silicon oxide, the horizontal alignment took place at lower temperature than on thick SiO_2.

The lattice spacing derived from the cross-section TEM images in Table 4-2 are between 0.60 nm and 0.65 nm. The accuracy is low due to the thin layer and irregular oriented planes. The range of the spacing correspond to the expected 0.61 nm for the stoichiometric MoS_2 in 2H phase.

4.1.3.3 Part III: MoS_2 quality

4.1.3.3.1 Hydrophobicity and crystallinity

Ideal horizontally layered MoS_2 is expected to be hydrophobic due to the sulfur surface termination. The hydrophobicity of the surface is determined by its surface energy. Low surface energy results in hydrophobic properties with high water contact angle. The surface energy consist of a dispersive and polar (electrostatic) part. The Mo – S bond itself is a dipolar covalent bond, partially ionic metal-chalcogen bond, but it was found that the surface energy of the MoS_2 basal plane is mainly determined by the dispersive part.[151] This is because of the evenly distributed polar bonds in which the molecule can be still non-polar. In contrast, the edges of the nanolayers and defects in the basal plane contribute to hydrophilicity due to their polar, electrostatic nature. Note that the contact angle of pristine MoS_2 is at 69°, but heavily adsorbs airborne contamination to reduce its surface energy further resulting in contact angles 89° after already one day.[152] Table 4-3 shows a contact angle of 93° for the MoS_2 deposited at 800 °C, which demonstrates the hydrophobic character as compared to SiO_2 or MoO_3 surface. After the sulfurization with the process of the best results within the possible process window (800 °C for 30 min in 100 % H_2S), the sample was characterized by glancing-incidence XRD (GIXRD). The film showed the characteristic MoS_2 (0 0 2) peak around 14.3° as can be seen from Figure 4-8.[153,154]

Table 4-3: Contact angles on a SiO_2 substrate, a molybdenum oxide sample, and an 800 °C sulfurized MoS_2 sample.

SiO_2	MoO_3	MoS_2
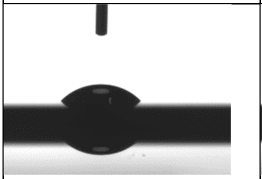	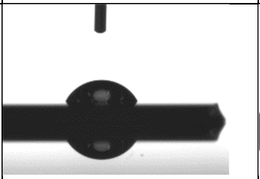	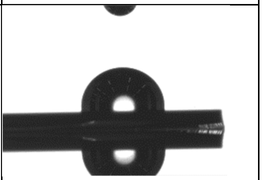
20°	40°	93°

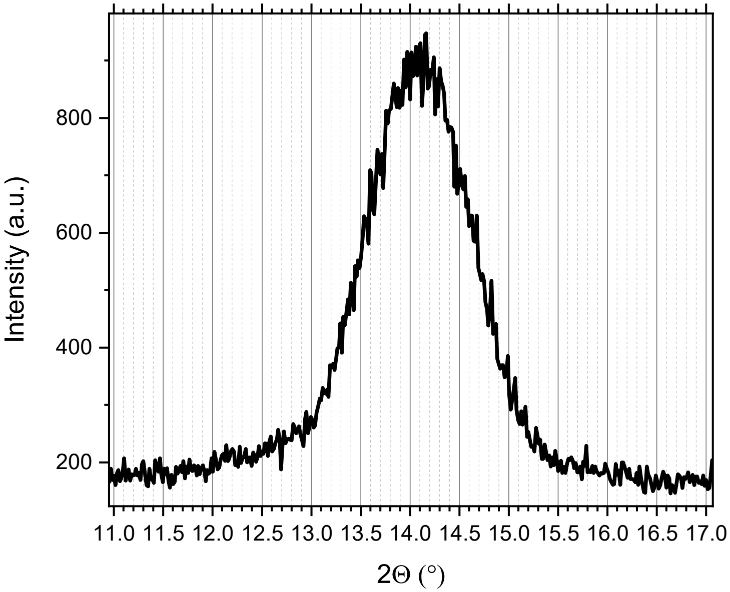

Figure 4-8: GIXRD spectrum of the MoS_2 (0 0 2)-related peak synthesized from stack C at 800 °C in 100 % H_2S during 30 min.

4.1.3.3.2 Plan-view TEM images

Besides the qualitative and quantitative analysis of the MoS_2 crystal structure, the determination of the crystal grain size is essential since grain boundaries act as defects for charge transport, negatively impacting the mobility of these materials. To determine the grain size, the MoS_2 had to be transferred to a thin e-beam-transparent membrane suitable for TEM imaging. To this purpose, the samples were immersed in water and the films peeled off from the substrates[155]. Subsequently the films could be transferred to a thin Si_3N_4 membrane which is nearly transparent for the electron beam. The image in Figure 4-9 shows grain sizes in the 10 to 25 nm range. Due to varying orientation of the crystal planes as can be seen on the cross-sectional TEM images in Table 4-2 and the electron scattering on the underlying Si_3N_4, an atomic pattern was barely observable on the plan-view images. Electron diffraction and Fast-Fourier transformed images in Figure 4-10 show that the MoS_2 is nearly oriented along [0001] with random in-plane orientation of the grains and probably fully in the 2H phase.

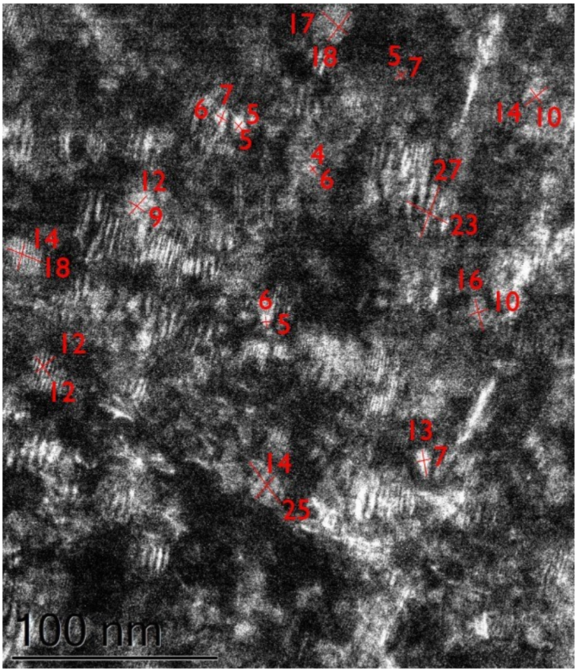

Figure 4-9: TEM image from stack C annealed at 800 °C in dark field mode indicating crystal sizes in the 10-25 nm range.

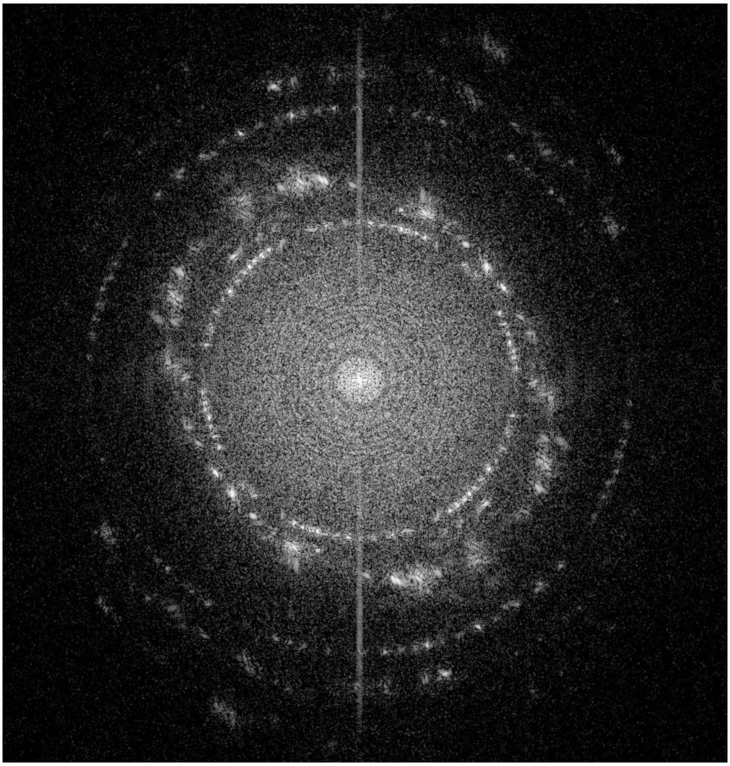

Figure 4-10: Electron diffraction pattern of a MoS_2 film, which was grown on stack C and annealed at 800 °C for 30 min in pure H_2S and then transferred on a TEM specimen holder.

4.1.3.3.3 Surface chemical analysis

The XPS spectra of the Mo 3d peak are depicted in Figure 4-11. After the sulfurization at 800 °C, a peak shift to lower binding energies characteristic for MoS_2, can be seen. The peak appearing around 227 eV is related to the S 2s region.

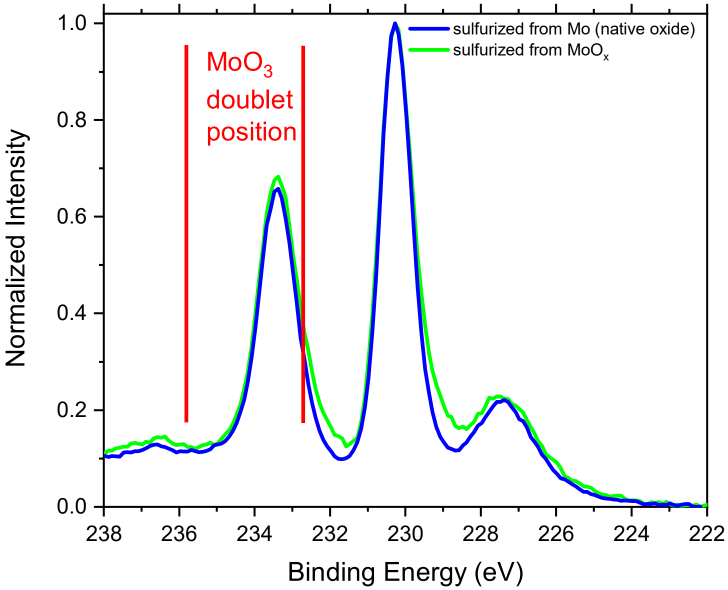

Figure 4-11: Mo 3d peak in XPS spectra for pristine samples and 800 °C in 100 % H_2S sulfurized samples.

4.1.3.3.4 Photoluminescence

A quality feature of thin layers of TMD materials is the photoluminescence (PL) appearing due to the direct bandgap transition as shown in Figure 4-12.[156–159] In the intensity change in the direct excitonic transitions A1 and B1 for different starting Mo thicknesses is plotted, showing a higher PL for thinner sulfurized layers. This evidences the band gap opening towards thinner layers and proves an acceptable material quality.

4.1.4 Discussion

4.1.4.1 Part I: Growth parameter study

4.1.4.1.1 Analysis of deposited material

Only the thick stack A shows a Mo photoelectron peak at lower binding energy indicating a metallic contribution. Together with the angle-resolved measurements, this revealed that the surface was oxidized in air and only the bottom part of the layer at the interface with the substrate was metallic. In contrast, similar spectra for stacks B and C indicated that the chemical state was uniform throughout the entire film, i.e. stack B oxidized completely in air. The formed oxides appear in the XPS as a doublet at relatively high binding energy close to the one of MoO_3 at 233.1 eV. Therefore, the synthetic as well as the native oxides can be assumed to have the trioxide structure. Thus, the TMO of stack B and C was comparable and differed mainly in the underlayer, being a thick thermal oxide in stack B and a thin native oxide in stack C. No major difference could be observed, since

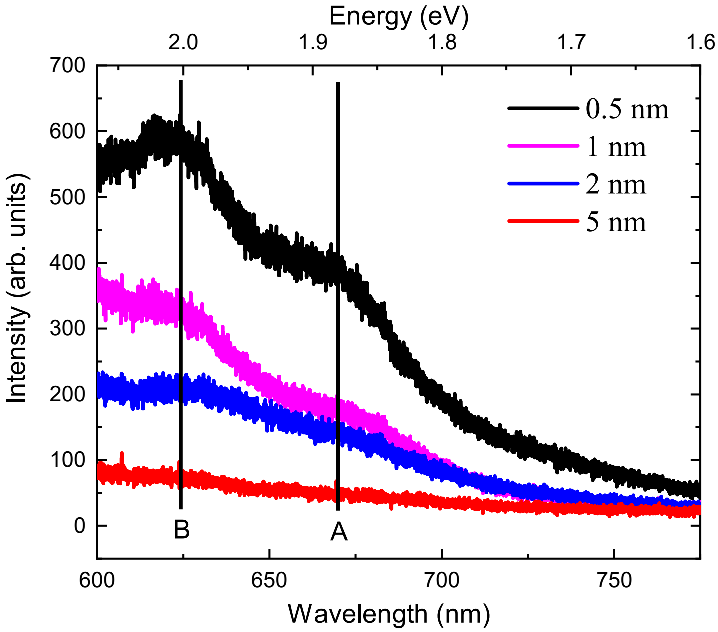

Figure 4-12: Photoluminescence measured on samples synthesized at 800 °C in 100 % H_2S for 30 min from different starting thicknesses.

both oxides were formed at room temperature. Other suboxides could be possibly deposited by heated substrate or further variation in the deposition conditions.

The root-mean-square (RMS) roughness in the range of 0.2 to 0.3 nm was slightly higher than expected on a polished Si surface (0.1 nm), but still reasonable for an oxidized substrate covered with a PVD metallic film. The stack roughness of 0.3 nm was acceptable considering a MoS_2 monolayer thickness of 0.7 nm.

4.1.4.1.2 Sulfurization process optimization

Temperature

Higher temperature resulted in a higher sulfurization degree. Stacks B and C could be sulfurized almost stoichiometrically at 800 °C in the H_2S/H_2 mixture, while lower temperatures only resulted in a partial sulfurization. Stack A containing the metallic Mo could not be sulfurized in the mixture with the timeframe of 30 min. This indicates that the necessary activation energy for the metal sulfurization must be higher than for the oxide sulfurization..

The absolute sulfur content in the sulfurized stack A was compared with the Mo amount in stacks B and C. Stack B represented a metallic film being completely oxidized in air. Thus, the thicker stack A could be assumed to be a double stack of native top Mo-oxide comparable to stack B and C and a metallic part underneath. The ratio of the amount of sulfur to the amount of oxidized Mo was 0.2, 1.4, and 1.6 for 400 °C, 600 °C, and 800 °C, respectively, as shown in Figure 4-3. This is comparable to the S/Mo ratios for stacks B and C, indicating that at 600 °C mainly the oxidized part was sulfurized, but not the metallic part. From these observations, it appears that the sulfurization of MoO_3 proceeds faster at a given temperature than the sulfurization of metallic Mo. Another explanation could be also the formation of a closed MoS_2 layer on top, which screens then the bottom metallic film from being sulfurized due to impermeability. For an investigation of the process kinetics, the experiments would have required another design to specifically analyze the rates. This would have required shorter as well as longer time scales and analysis on the log-scale, but this was difficult to analyze in such used RTP system due to time restriction and the thermal inertia of the system.

The involved reactions are the following:

$$MoO_{3(g)} + 3\ H_2S_{(g)} \rightleftharpoons MoS_{2(s)} + 3\ H_2O_{(g)} + S_{(s)} \tag{4.1}$$

$$Mo_{(s)} + 2\ H_2S_{(g)} \rightleftharpoons MoS_{2(s)} + 2\ H_{2(g)} \tag{4.2}$$

The software module Reaction Equations from the package HSC Chemistry was used to calculate the change in Gibbs free energy for the reactions (4.1) and (4.2) by calculating the differences in enthalpy and entropy taken from a database. The results in the temperature range from 0 °C to 1000 °C are depicted in Figure 4-13, the Gibbs free energy is negative over a large temperature range and thus, both reactions should

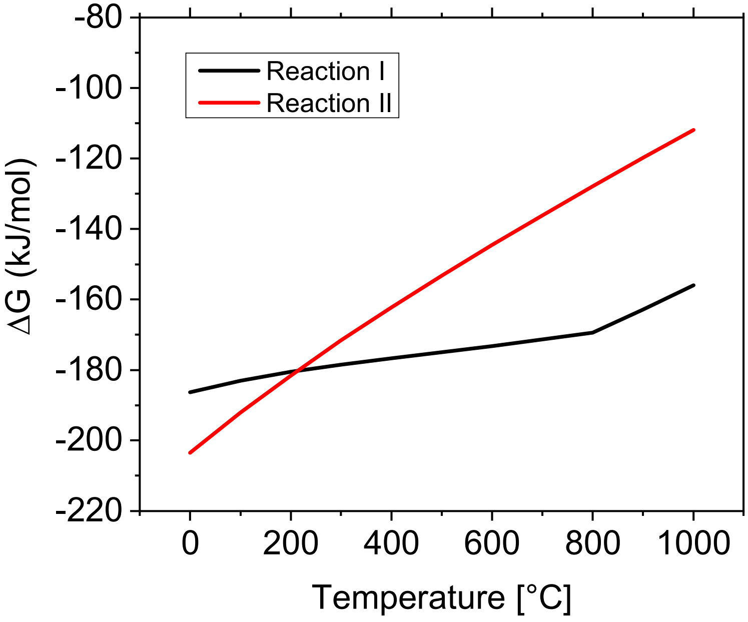

Figure 4-13: Change in Gibbs free energy for reaction I and II as a function of temperature.

proceed spontaneously. However, no conclusion about the kinetics could be drawn from the thermodynamics. We observed that the MoO_3 sulfurization proceeds faster than the Mo sulfurization within the 30 min observation time, which could indicate that the activation energy is lower for the oxide sulfurization. We observed that the metal-containing film's stoichiometry remained below 1.6, even after a long 30 min sulfurization process. This model does not take a possible blocking of the metal from the formed MoS_2 on top into account.

The data also indicated that stack C reached the maximum ratio slightly faster than stack B. This could be because of a different nature in the suboxides of this film but could not be analyzed by XPS data with the given resolution.

Since the provide precursor amount was in the same range and the oxide sulfurization was further progressed in the oxide sulfurization than in the metal sulfurization, it can be predicted that the activation energy for the oxide sulfurization is lower than for the metal sulfurization in case of molybdenum.

Partial pressure and time

H_2 was excluded from the process gasses by switching to pure H_2S. As demonstrated, the sulfurization with pure H_2S was faster compared to the sulfurization with the 10 % mixture. We assume that the sulfurization reaction for either oxidized or metallic Mo occurs alongside reactions (4.1) and (4.2). Reaction (4.1) has a change in Gibbs free energy of -173 kJ/mol, whereas reaction (4.2) has -145 kJ/mol. Thus, both reactions are exergonic and proceed spontaneously. The mixture with H_2 had a smaller partial pressure of H_2S and by this, the reaction rate decreases. While the mixture with hydrogen showed only small S/Mo ratio increase in the sample with metallic core (stack A) between five and 30 min, it can be assumed that the rate is lower than in the oxidized samples. The pure H_2S showed a stronger increase in sulfurization with time, although it reached only 1.6 within this timeframe at 600 °C.

In contrast, stacks B and C showed a time-dependent S/Mo ratio in case of the H_2S/H_2 mixture between five and 30 min, but it reached a ratio about 2 for longer durations than five minutes in case of the pure H_2S. In reaction (4.1), no hydrogen is involved, meaning that the faster process can only be explained by the increase of the H_2S partial pressure from 10 mbar to 100 mbar. The higher H_2S amount results in faster sulfurization, since the concentration is of H_2S is larger. The observations show as well that the activation energy for the metal sulfurization must be higher than for oxide.

From the previous experiments, it can be concluded that a high sulfurization temperature, longer sulfurization time, and higher H_2S partial pressure resulted in enhanced material quality. Although thin films of stacks B and C could be sulfurized at a temperature of 600 °C, the sulfurization of thicker films like in stack A was not possible within 30 min annealing time. Therefore, the sulfurization temperature was further increased to 800 °C in order to facilitate a full sulfurization of the thicker films and to ensure the full conversion of metallic Mo.

To verify the full sulfurization, starting layers of different thicknesses were prepared and annealed under similar conditions (see Figure 4-6). The Mo and S areal densities show a linear trend proportional to the initially deposited Mo thickness. This confirms that the higher temperature is necessary in order to allow the full sulfurization of thicker, metallic layers as well.

4.1.4.2 Part II: MoS_2 plane orientation

After adjusting the annealing conditions for metallic and metal-oxide-based layers, the deposited films were characterized to gain an understanding of the mechanisms which are driving the sulfurization. In the ideal case, two-dimensional films are entirely flat. The surface topology of our samples was characterized by SEM and AFM after annealing, showing different topographical roughness for the different conditions (Table 4-1). Whereas stacks A and B revealed surface delamination after annealing, stack C showed better wetting on the underlayer, and this effect appeared after annealing in vacuum as well as in H_2S environment. However, the latter showed even stronger roughening, which indicates that the delamination is related to both the substrate and the environment as the images in Table 4-1 demonstrate.

The interface material between the MoS_2 film and the substrate was in all cases SiO_2, thus the surface energy of the two substrates can be assumed to be similar. However, the alignment of the MoS_2 basal planes differed between the samples with thick and thin SiO_2. The MoS_2 films on the thick wet-grown SiO_2 show macroscopically rough surface after annealing, whereas the MoS_2 films on the thin SiO_2 had a conformal surface as judged from the SEM images. A possible explanation is the formation and release or consumption of reaction byproducts. The sulfurization reactions release gaseous products which are H_2O in reaction (4.1) and H_2 in reaction (4.2). The deposition process occurs in different steps. Initially, the H_2S approaches the surfaces and the reaction starts there. Subsequently the H_2S needs to diffuse through the layers to react deeper into the sublayers. During this reaction, gaseous products will be formed which have to leave the film again. In case of metallic layers, this formed compound is H_2. However, the sulfurization of oxide results in H_2O formation[160–162]. In case of well-formed film with horizontal alignment, the gas permeability is reduced and could accumulate at the MoS_2/substrate interface and lifted of the film which resulted in rough topology on the MoS_2 on thick silicon oxide or even delamination of the films. Another additional effect resulting in such delamination could be the volume expansion and the film stress due to different thermal expansion coefficients. Possibly, the film delamination could be also explained by the interfacial energies: since the system's energy need to be minimal for the TMD/SiO_2 interface, the delamination could occur since the 2D film tries to minimize the contact with the hydrophilic SiO_2 with high surface energy.

The roughness was induced by the hillocks on the sample surface and by the MoS_2 film itself. However, the surface images showed that the microroughness was superimposed to the hillocks which formed during the delamination of the MoS_2 films from the SiO_2 substrates.

The Ra determined as the arithmetic average from the absolute values reveals another difference between the samples. The sulfurized stack B showed a higher roughness of around 2 nm, whereas the TMO sulfurized stack C showed a roughness of 1.5 nm.

Based on these observations, we conclude that the annealing on a thick SiO_2 layer already introduced roughness in vacuum by dewetting[163].

4.1.4.3 Part III: MoS_2 quality

4.1.4.3.1 Hydrophobicity

The surface wetting by water gives indications on the material quality. The wetting angle as well as the TEM observation of the 800 °C annealed sample are in agreement with results from literature[160], revealing the hydrophobic nature of the surface which is correlated to the growth temperature and thus also with the MoS_2 structure[164]. As shown in the previous sections, material grown at low temperature which might be only partially sulfurized and did not go through the crystallization process yet, tends to form random structures oriented to the reactants' diffusion direction. This results in the exposure of many edge sites at the surface leading to a high surface energy and thus, a more hydrophilic behavior. In contrast, higher temperature favors the crystallization resulting in horizontal planes in which the edge exposure is decreased and hence results in low-energy, hydrophobic surfaces. This observation also confirms the improved quality of the material from the high temperature growth. Nonetheless, the defects on the planes will have an impact on the electronic properties of the film.

4.1.4.3.2 Crystal morphology

Comparing the assembly of the basal planes, the 600 °C sulfurization on thin native silicon oxide resulted in preferential horizontal arrangement of the basal planes. In contrast, layers on thick SiO_2 tend to form relatively rough films with random orientation. During the crystallization, the basal planes orient in a way to reduce their surface energy. Hence, on flat substrates such as native or thermally grown SiO_2, the basal planes will assemble parallel to the substrates and the following MoS_2 planes will orient in alignment with the basal planes[165].

Comparing the sulfurization between a fully oxidized layer and a partially oxidized layer with metallic components, the oxidized films lead to a better film quality at lower temperature. Since the metallic layer needs a higher temperature and is more densely packed, the MoS_2 grown from metallic material suffers from the slow pace of material transport. The H_2S molecules need to diffuse through the metallic layer and induce an additional volume expansion of a factor of 4 which leads to mass transport and distort the structure itself. In contrast, the 5 nm MoO_3 layers are found to expand only by about a factor of 1.6 as is shown in Table 4-2. The observations from stack A confirm this. The TEM images of the thicker sulfurized stacks showed horizontally oriented crystals on the top. This top structure was directly sulfurized from the native oxide, which proceeds fast and efficient even at the relatively low temperature of 600 °C. However, the incompletely sulfurized bulk was vertically layered. This observation suggested that the TMD layered structure orient towards the diffusion direction of the gaseous reaction source material and products. This could proceed e.g. along the grain boundaries of the metal film for thicker films, although this was not evaluated here and would require an analysis for different crystal sizes, which could be analyzed on films of different starting thickness. Only after the reaction has finished and no more reactants force the plane direction, the crystallization process takes place and the planes realign according to the interface with the underlying material. This confirms earlier reports exhibiting relatively random MoS_2 orientation on rough and thick SiO_2[62,166–169]. This recrystallization or coalescence require a much higher E_A than the sulfurization process and therefore it is very slow and questionable, whether the film could have sufficient quality upon 30 min.

4.1.4.3.3 Surface chemical state

The XPS spectra of the as-deposited metal-oxide and metal films can be interpreted mainly as MoO_3 and MoO_3/metallic layer, respectively. The NIST database reports the Mo 3d5/2 doublet for MoO_3 around 232.5 eV[148] and the metallic Mo peak is located at 228 eV[170]. In contrast,

MoO_2 is reported around 229.3 eV and could not be clearly identified in the MoO_x layers. In the sulfurized MoS_2 films, the relatively high binding energy of the Mo 3d doublet of MoS_2 suggests a mainly 2H polytype since the 1T polytype is usually located at lower binding energies[171]. This is also in agreement with the 2H lattice distances measured from the TEM cross-sections[172,173]. The 2H polytype is expected to be semiconducting, whereas the 1T is a more metallic phase making the material promising for integration as a transistor channel. The absence of MoO_3-related peaks in the XPS spectra confirm the full sulfurization of the material in the H_2S atmosphere with the optimized conditions.

4.1.4.3.4 Indirect-to-direct band gap transition

Another characteristic of thin Van-der-Waals bonded layers are the layer-dependent property changes. A special TMD material characteristic is evolution of its PL for monolayers due to the indirect-to-direct bandgap transition. We applied the high temperature (800 °C) recipe with the pure H_2S gas to different thicknesses of TM/TMO. The thinner Mo/MoO_3 layers showed higher PL after the sulfurization process as can be seen in Figure 4-12. This evolving PL indicates the efficiency of the sulfurization process and can be used as an indicator for further process optimization. Since an initial Mo thickness of 0.5 nm corresponds to 3 monolayers, the PL could be further enhanced by using double- or monolayer structures. For an ideal monolayer or bilayer film, even thinner layers would be necessary, which becomes challenging for the deposition to be uniform and controllable.

4.1.5 Conclusions

In this work we investigated the sulfurization of thin transition-metal layers in H_2S and H_2S/H_2 mixtures. The best TMD layers were obtained in pure H_2S ambient. The full sulfurization of metallic TM requires high temperatures of 800 °C resulting in higher film expansion than in the case sulfurization TMOs, which can be sulfurized at a lower temperature of 600 °C.

After full sulfurization, the films recrystallize, and their orientation is found to depend on the surface roughness of the underlying substrate. However the recrystallization require a high E_A and is therefore slow.

The high temperature process resulted in the formation of grains of a few 100 nm^2 and showed evolving PL on the ultra-thin films. This work shows that the sulfurization chemistry and process temperature need to be carefully adjusted for the material to be sulfurized and that the interface roughness plays an important role for the assembly of the basal planes. Further work, in view of a successful very large-scale integration, will have to concentrate on the increase of the lateral grain size to minimize defects and improve electrical properties.

4.1.6 Recent advances in literature and vision on domain

In this section, we investigated the sulfurization of Mo and MoO_3 films by H_2S and published the results in 2016. Since then, progress was made in the areas of substrate preparation, choice and pretreatment of precursors, and the shift to higher temperature regimes than 800 °C. Whereas we used in our research mainly amorphous SiO_2 as underlayer, new insights were obtained from the growth on substrates with hexagonal lattice. Sapphire was shown to be an appropriate substrate on which the crystal orientation of the MoS_2 is aligned with the substrate orientation.[83,174–176] A higher degree of crystallization has been also found after the growth on GaN substrates.[177–180] Also the lattice matching mica or $SrTiO_3$ substrates are demonstrated to lead to higher crystallization degree in contrast to thermal SiO_2.[181,182] The higher crystallinity is linked to the charge carrier mobility in the material due to lower defect density.

Further progress was shown in studies with higher temperatures than the maximal 800 °C used in our studies.[54,183–186] The higher the temperature, the higher is also the crystal size upon growth and therewith the quality of the crystals.

Recent studies show also superior results of high-temperature sulfurization of pre-deposited MoS_x by means of sputtering instead of the metal or metal-oxide.[187–191] This has shown good mobility values even at relatively low annealing temperatures such as 500 °C. Such films have been deposited as well by atomic layer deposition (ALD) and showed reasonable mobilities upon annealing.[192,193]

Our study has shown that sulfurization is a viable tool to convert metal films to the respective stoichiometric sulfides with low roughness. Nevertheless, the high temperature and monocrystalline substrates being necessary to obtain a film with high charge carrier mobility are disadvantages. The whole substrate needs to be heated and because of this, co-integration on one substrate with other building blocks is not possible with temperatures of about 1000 °C being necessary for material with low defects. Starting from a full metal film can also result in defect-rich layers, since the material needs to migrate and forms shapes, which are difficult to convert further into a perfect 2D layer. The mismatch of thermal coefficients between the 2D material and the growth template can also result in wrinkles and non-ideal films. Two ways can be promising to be followed in the sulfurization approach. First, instead of converting a metal or amorphous film, epitaxial or crystallized oxide films could be promising starting materials. Both MoO_3 and MoS_2 have similar space-groups and in thin films of only a few nanometer, the S can replace the O. Crystallinity can be enhanced by the sulfurization of crystalline metal oxide, which could be formed by an PVD-deposited MoO_3 film or epitaxial growth.[194,195] The recrystallization of MoO_3 could be done in O_2 at high temperatures of a few hundred °C.[196]

Second, instead of starting from metal or metal-oxide, the starting precursor could be an amorphous or polycrystalline MoS_2 film formed by other techniques, such as conversion or physical vapor deposition. If the starting film contains already sulfur. Then, the crystallization can start from high stoichiometry and background sulfur can be used to suppress sulfur loss and fill vacancies. In this sense, the sulfurization could be understood rather as a healing or re-crystallization process rather than the recrystallization of metal into a sulfide.

Third, instead of growing large area films, pre-patterned films are an interesting phenomenon to study. Since aggressively scaled transistors are targeted to nanometer-size, the sulfurization area can be also scaled to the envisioned transistor channel size. When the transistor channel size is then in the size of the grain size, defects might play a minor role.

4.2 Converting amorphous Si to WS_2

The TMD growth in the previous section was based on a hybrid CVD approach from a solid metal precursor and a volatile sulfur precursor. In this chapter, we study the TMD deposition from the gaseous precursors WF_6 and H_2S. They can be delivered in a well-controlled manner to sample surfaces in a CVD reactor. The strong interaction of WF_6 with a sacrificial Si and the slow reaction with Al_2O_3 can be used to converting ultra-thin films as they are used for few-layer thickness.

It was found that the reaction between WF_6 and Si substrates is very strong and that a dielectric such as SiO_2 or annealed Al_2O_3 inhibit the reaction and had to be deposited before the deposition reaction. However, WF_6 and H_2S did not spontaneously react on the wafer surface up to a temperature of 450 °C. To enable a reaction between the W-compound and the sulfur precursor, the WF_6 had to be reduced. In this work, PVD amorphous Si was used as reducing agent. The conversion to WS_2 consisted of cycles with a WF_6 step to replace Si by W, a N_2 step to purge remaining WF_6 out of the reactor, an H_2S step, followed by another N_2 purge. It was found that the conversion reaction of a 2 nm Si layer in a W layer, being equivalent to a double layer WS_2, proceeds very fast within the first 15 s of WF_6 exposure. In contrast, the sulfurization of the W in the H_2S step was slower and completed upon several cycles only. This is different to CVD, in the sense that here a step-by-step metallization and sulfurization was done. The films deposited at 450 °C, are stoichiometric and homogeneous over a 300 mm wafer substrate, but they are amorphous and need further quality improvement by subsequent thermal annealing. It was found that for reducing Si films with a thickness larger than 4 nm, the sulfurization temperature of 450 °C is not enough anymore to obtain stoichiometric films due to non-complete sulfurization process. It is worth noting, that the in-situ sulfurization could only take place at 450 °C in case metallic W was present on the surface. WO_x could not be sulfurized at the low temperature of 450 °C anymore, which is an opposite behavior to Mo-constituents as seen in the previous section.

This chapter was published as:

Heyne, M. H.; de Marneffe, J.-F.; Nuytten, T.; Meersschaut, J.; Conard, T.; Caymax, M.; Radu, I.; Delabie, A.; Neyts, E. C.; De Gendt, S. The Conversion Mechanism of Amorphous Silicon to Stoichiometric WS_2. *J. Mater. Chem. C* **2018**, *6* (15), 4122–4130.

The author did the design of all experiments, sample preparation, the sulfurization experiments, analysis of the provided data, and the discussions with the co-authors.

Abstract

The deposition of ultra-thin tungsten films and their related 2D chalcogen compounds on large area dielectric substrates by gas phase reactions is challenging. The lack of nucleation sites complicates the adsorption of W-related precursors and subsequent sulfurization usually requires high temperatures. We propose here a technique in which a thin solid amorphous silicon film is used as reductant for the gas phase precursor WF_6 leading to the conversion to metallic W. The selectivity of the W conversion towards the underlying dielectric surfaces is demonstrated. The role of the Si surface preparation, the conversion temperature, and Si thickness on the formation process is investigated. Further, the in-situ conversion of the metallic tungsten into thin stoichiometric WS_2 is achieved by a cyclic approach based on WF_6 and H_2S pulses at the moderate temperature of 450 °C, which is much lower than usual oxide sulfurization processes.

4.2.1 Introduction

Ultra-thin semiconducting atomic layers such as the transition-metal dichalcogenides (TMDs) WS_2 or MoS_2 show specific properties due to their reduced dimensionality. Monolayers of these TMDs reveal sulfur-terminated basal planes and multilayers are bonded by van der Waals forces, hence, their ideal surface is free of dangling bonds.[197] Due to their lower relative permittivity in comparison to Si, they are also predicted to be more resistant against short-channel effects in field effect transistors and are promising for future scaling in nanoelectronics.[198] Besides this, these materials are promising building blocks in optoelectronics, and spintronics.[199–201] In recent years, much progress on the growth of MX_2 materials has been reported, especially for MoS_2. In comparison to MoS_2, the TMD WS_2 received less attention, despite its higher predicted phonon-limited electron mobility of 700 cm^2/Vs in monolayer due to its lower effective charge carrier mass, in comparison to the value of 440 cm^2/Vs reported for MoS_2.[202–204] Those theoretical performances are smaller in real devices due to structural defects such as grain boundaries and sulfur vacancies, which are occurring as a result of the growth process or post treatment.[205,206]

A common approach for deposition on large areas is the chemical vapor deposition (CVD) by evaporation of MoO_3 and S supported by Ar/H_2 flow in furnaces with different temperature zones.[35,207,208] This allows the deposition of monolayer triangles with lateral dimensions of a few tens of micron. The crystal orientation can be controlled by using crystalline guiding substrates such as sapphire wafers or GaN films.[87,209–211] Besides of MoO_3, metal halides have been used for deposition as well, since their boiling points are smaller than for the oxides and hence, their vapor transport into processing reactors to the substrate surface is facilitated.[28,29,212] The transition-metal chlorides can be evaporated already below 300 °C and the fluorides are even volatile at room temperature. Besides metal halides, also volatile metal-organic precursors are used to deposit thin films.[58,213–215] Those CVD methods can yield large MX_2 grains, if the nucleation starts from one nucleation point and extends laterally to form the characteristic triangles. Next to the CVD methods, also conversion reactions have been widely investigated. In such reactions, pre-deposited metallic or metal-oxide layers are sulfurized in evaporated elemental sulfur or H_2S.[216] However, sulfurization results in much smaller grain size than CVD for a given temperature, since sulfurized films are initially nanocrystalline and need high recrystallization temperatures to enable grain boundary migration.

The majority of studies were done for MoS_2 due to the ease of fabrication by co-evaporation of MoO_3 (melting point at 795 °C) and sulfur in tube furnaces and the MoS_2 deposition directly from the gas phase. [202,204] However, WO_3 needed for WS_2 has a high bond energy and sublimates at temperatures higher than 900 °C, which is less practical than MoO_3. Song et al. deposited thin WO_3 films by ALD at 300 °C and sulfurized these films afterwards at 1000 °C.[63] However, the sulfurization of WO_3 requires those high temperatures to enable the oxygen-sulfur exchange reaction in this oxide with high bond energy.[217,218] We studied in this work an alternative approach, in which the tungsten is sulfurized directly from the metallic state. Normally, a metallic layer is difficult to maintain during the transport of a substrate in air. Therefore, the deposition is done in-situ in one reactor without vacuum break to avoid oxidation. In this paper we elaborate on the process described earlier, in which we convert an amorphous silicon film by WF_6 into metallic W and convert it in situ into WS_2 at a moderate processing temperature of 450 °C in H_2S.[219,220] This study discusses the detailed observations of the formation mechanisms, namely the Si-to-W conversion and the sulfurization directly from metallic W to WS_2. The necessity for the surface preparation and restrictions with regards to thickness control, temperature, and structure are discussed.

The selective deposition of W on Si surfaces by CVD is a well-known process, which is mainly used for W-plug formation in vertical interconnect accesses (VIA) in combination with a Ti buffer layer.[221–223] In contrast, the W deposition on dielectric surfaces is more challenging due to the lack of potential nucleation sites. The formation of a thin W film from the precursor WF_6 on dielectrics such as Al_2O_3, HfO_2, or SiN requires the use of a reductant, since these dielectrics do not provide chemisorption sites for the precursor. Successful nucleation could be achieved by the use of H_2 plasma[219] or gases like Si_2H_6[224], SiH_4[225], B_2H_6[226], GeH_4[227], or solids like

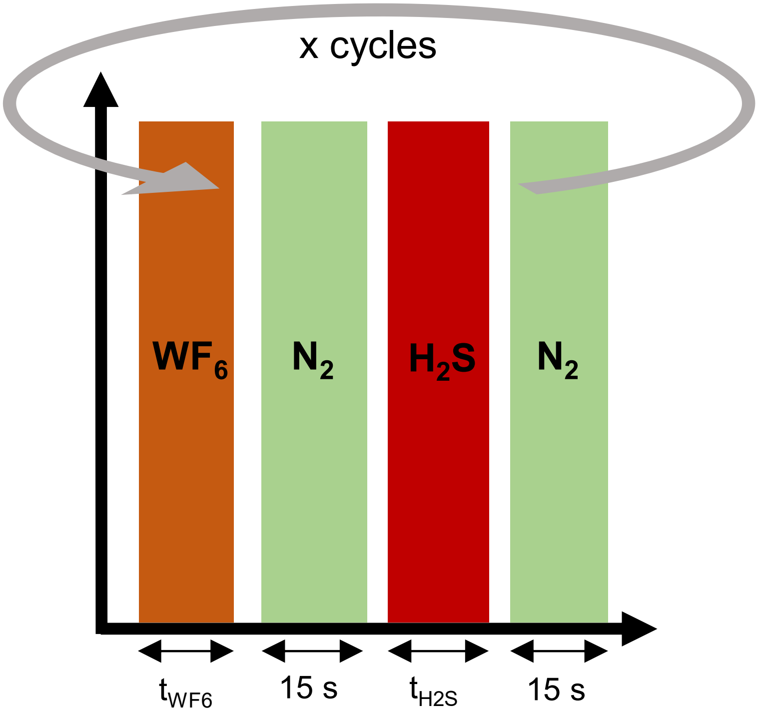

Figure 4-14: Pulse sequence in the CVD reactor with varying pulse times t, separated by 15 s N_2 *purge steps.*

elemental Si[228,229]. The gaseous precursors are used for ALD processes to achieve layer-by-layer deposition of amorphous or polycrystalline films. However, they deposit the target material on the whole substrate and not in specific regions. Nonetheless, a solid precursor like a thin Si film can be pre patterned and controls the areas for the conversion.

In contrast to the above described methods, the technique developed in this paper allows the selective deposition of WS_2 with arbitrary thickness equivalent to multilayer thickness down to a monolayer over wafer sizes of 300 mm diameter and exploits conventional tools for CMOS fabrication such as physical vapor deposition (PVD), wet chemical processing, and CVD. Here we provide insight into the conversion mechanisms with a focus on surface preparation, conversion temperature, and thickness correlation.

This conversion process can be used in combination with advanced techniques such as atomic layer etching (ALEt) to form selectively grown patterns on sensitive underlying films bringing advanced Beyond Si-CMOS concepts, such as tunnel field-effect transistors (TFET) or spintronic devices a step closer.

4.2.2 Methods

Substrates used in this work were 300 mm Si wafers coated with a 20 nm-thick thermally grown SiO_2 layer to provide interference contrast for 2D material visibility. For the analysis with a light microscope, the light is reflected at the interface Si/SiO_2 and interferes on the SiO_2-air surface depending on the refractive index and the thickness of the stack. Although one would expect only a minor impact on light amplitude and phase for such ultrathin materials with multiple thickness of 7 Å, they are well distinguishable in thickness. This is because of the high reflective index of the MX_2 causing multiple reflections in the MX_2 resulting in a large optical path length (OPL).[230] This SiO_2 was covered by an atomic layer-deposited (ALD) Al_2O_3 and crystallized in O_2-rich environment at 1000 °C to chemically mimic a sapphire surface and to protect the Si wafer from reactions with the used gas phase precursor or wet-chemical surface preparations.

Amorphous silicon layers were deposited by PVD with a low deposition rate of 6.8 Å/min. This amorphous silicon is a uniform, sacrificial layer and used as reductant, i.e. it is consumed during the proceeding steps. The native SiO_2 was removed and Si was H-passivated by a 200 s long 0.5 % HF rinse and followed by an extensive H_2O rinse. These layers were immediately exposed to alternating gas pulses of WF_6 and H_2S in a CVD reactor at a temperature of 450 °C according to the scheme shown in Figure 4-14.

This converted the Si film into metallic W and subsequently into WS_2. The 15 s long gas pulses were separated by N_2 purges. The pressure was kept constant at 266 Pa. The conversion mechanism was thoroughly analyzed by Rutherford backscattering spectrometry (RBS) using

1.523 MeV He^+ particles.[125] Raman spectra were measured by a Horiba LabRAM HR with 532 nm excitation wavelength and a grating of 1800 grooves/mm. Angle-resolved X-ray photoelectron spectroscopy (AR-XPS) spectra were acquired with a ThermoInstruments Theta300 system using a monochromatized Al K_α X-ray source (1486.6 eV) and all spectra were integrated over their measurement angles to obtain a high signal-to-noise ratio. Atomic force microscopy (AFM) by a Bruker Dimension ICON PT was used in tapping mode to collect information about the surface roughness. Selected samples were coated with spin-on-carbon (SOC) and cut with a 5 kV Ga^+ focused ion beam (FIB) into transmission-electron microscopy (TEM) specimens and then observed by a FEI Titan3 G2 60-300 with a Super-X EDS detector system. Grazing incidence X-ray diffraction spectra were recorded by a Panalytical X'PERT Pro MPD using an incidence angle of 1°.

4.2.3 Results and discussion

The deposition of WS_2 from gas phase precursors proceeds in two steps, the Si-induced conversion to ultrathin, metallic W layers and the sulfurization of those metallic layers to WS_2. The following section discusses the impact of surface oxidation and the requirements for the Si surface preparation and the quantification of the conversion process from Si to W. Afterwards, the sulfurization and its constraints with respect to penetration depth and temperature are explained. After analyzing both processes separately, the combination was optimized to obtain stoichiometric films on an insulating substrate.

4.2.3.1 Redox reactions based on Si, WF_6, and H_2S

4.2.3.1.1 Si conversion to W: Role of surface passivation

Depending on the temperature, gaseous WF_6 reacts with Si according to the following paths by segregation of Si through thin W and reaction with the gaseous precursor at the surface:[231]

At 400 °C: $3\ Si\ (s) + 2\ WF_6\ (g) \rightleftharpoons 2\ W\ (s) + 3\ SiF_4\ (g)$ (4.3) or

at 700 °C: $3\ Si\ (s) + WF_6\ (g) \rightleftharpoons W\ (s) + 3\ SiF_2\ (g)$ (4.4).

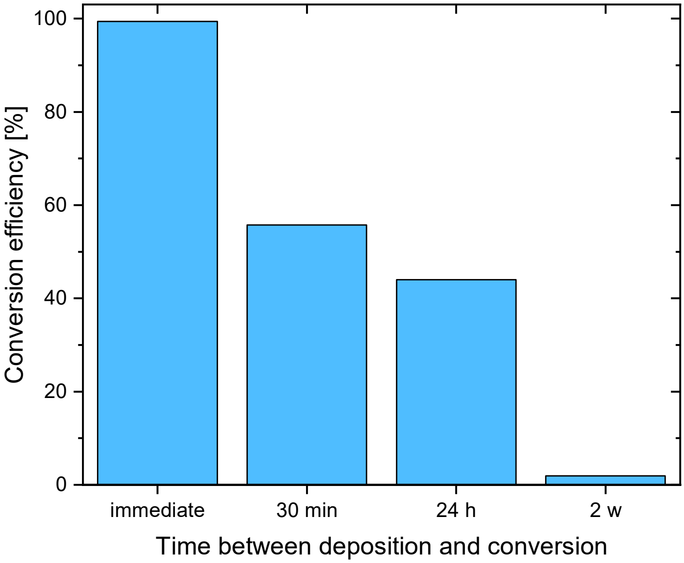

Figure 4-15: Conversion efficiency upon different periods between Si deposition and WF_6 conversion indicate a decreasing W amount. 100 % correspond to 2.47E15 at/cm^2.

Wafers with 7.5 Å-thick Si were exposed to the WF_6 at 450 °C after different periods upon Si deposition and the deposited W amount was quantified by RBS. The expected value for the number of W atoms per area N_W/A in the case of full conversion was calculated by

$$\frac{N_W}{A} = \frac{x}{3} \cdot \frac{N_{Si}}{A} = \frac{x \cdot \rho_{Si} \cdot N_A \cdot t_{Si}}{3 \cdot M_{Si}} \tag{4.5}$$

with the reaction coefficient x for W (either 2 or 1 for equation (4.3) or (4.4), respectively), the pre-deposited Si thickness t_{Si} and the corresponding number of Si atoms per area N_{Si}/A. The amorphous Si density ρ_{Si} can vary between 1.7 and 2.3 g/cm^3 depending on the deposition conditions.[232] With the molar mass M_{Si}, the theoretical density of W after full conversion for reaction (4.3) is in the range of 1.83E15 to 2.47E15 at/cm^2 and for reaction (4.4) it would yield only between 0.91E15 and 1.23E15 at/cm^2. Experimentally the 7.5 Å Si after conversion yielded 2.47E15 at/cm^2 This confirms that reaction (4.3) with the coefficient $x = 2$ occurred and the Si density of the pre deposited Si of silicon is like the crystalline density.

However, this amount was only achieved when the conversion with WF_6 was done immediately after the Si deposition. With increasing delay between the Si deposition and the conversion, less Si was converted to W for a similar Si amount, as shown in Figure 4-15. This is related to the formation of native SiO_2, of which the thickness is time dependent.

The amorphous Si forms a native oxide in air of a few Å. The exact thickness of this native oxide depends on the residence time in air.[233] Upon immediate WF_6 exposure for $t_{WF6} = 15$ s, the nominal Si amount of 7.5 Å resulted in nearly full conversion, whereas after 30 min only 55 % of the expected value was observed, after 24 h only 43 %, and upon two weeks delay, the deposited W amount was only 2 % of the expected value of full conversion.

This reveals the decreasing efficiency of Si-to-W conversion with increasing air exposure time. This observation can be explained by the non-reactivity of WF_6 and SiO_2 at the processing temperature of 450 °C.[234] This process has a high activation energy. It is therefore essential to carefully control the native oxide growth to avoid variability in W deposition. Samples treated with 14 cycles starting with $t_{WF6} = 15$ s WF_6 exposure but 24 h after Si deposition, show residual Si-O in the converted film according to XPS (Figure 4-16a), confirming the strongly limited reactivity of SiO_2 with WF_6. The SiO_2 is represented as the high energetic peak in the Si 2p spectra. In contrast to this, elemental Si being located at lower binding energy could not be quantified and only noise level was detected in this part of the spectrum, hence all elemental Si was consumed in the conversion process. Correspondingly, reaction 4.3 occurred even through a thin native SiO_2 layer, which is not fully closed yet after short delay.

Further analysis of the XPS spectra shown in Figure 4-16b revealed that oxygen was incorporated in the deposited W-compound. The spectrum shows two doublets of the W 4f peak: the lower energetic doublet is related to the W-S bonds, thus it represents the +IV oxidation state of W, which is typically related to WS_2.[235,236] At higher binding energy, there is the W 4f doublet for WO_3 – this corresponds to W in the +VI oxidation state. This doublet is superimposed to the W 5p peak at the binding energy at 39.5 eV in this spectrum. The oxide can be distinguished qualitatively from the pure compound by the evolving shoulder next to the WS_2 doublet, which is part of the oxide characteristic doublet.

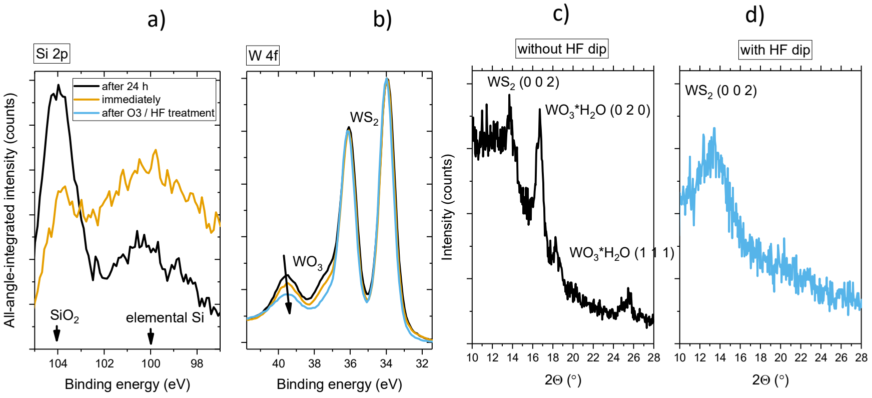

Figure 4-16: XPS spectra of a) Si and b) W after immediate and one day-delayed treatment by the gas sequence WF_6, N_2, H_2S, N_2. The sample treated after one day shows the incorporation of SiO_2 from the native oxide, which was not converted into W-compound. GIXRD graphs showing the W-compounds deposited upon $WF_6/N_2/H_2S/N_2$ pulses on a sample with c) oxidized surface and on d) HF-cleaned surface. The latter one shows pure WS_2 formation and absence of tungstite (hydrous tungsten oxide).

The quantitative oxide fraction of the deposited film was 16 % for the immediate conversion and 19 % for the conversion after 24 h (only partially converted). Both observations show higher oxidation than the typical 10 – 12 % oxidation (full conversion) we observe for the best material, probably originating from minor air oxidation. Typically, S-saturated W atoms oxidize only slowly under dry conditions and are stable for short-term as long as no elevated temperatures or moisture is applied for longer time.[237] The observed WO_3 oxidation implies that another oxygen source is present.

To identify this source, the composition was further analyzed upon deposition. The spectra in Figure 4-16b reveal a higher oxidation level in the film converted after 24 h in comparison to the one which was immediately converted. In addition, GIXRD spectra acquired upon deposition (Figure 4-16c) revealed significant peaks at 16.5 ° and 25.4 ° being characteristic for tungstite, $WO_3{\cdot}H_2O$. This implies that the reaction product results from the interaction of SiO_2, WF_6, and air environment upon processing. SiO_2 cannot be directly etched by WF_6 due to its selectivity.[234,238] However, WF_6 reacts with Si by penetrating through pinholes in the not fully closed native oxide layer, if this is still within the timeframe of a few hours after the HF dip. This forms SiF_4 as byproduct according to reaction 4.3, leading to the formation of a volatile silicon oxyfluoride according to 4.6 [239]:

$$3\ SiF_4\ (g) + SiO_2\ (s) \rightleftharpoons 2\ Si_2OF_6\ (g) \qquad (4.6)$$

The O-containing reaction product from 4.6 is detracted by further reaction with WF_6 in the gas phase forming the metal-oxide compound according to the exergonic reaction ($\Delta G = -300$ kJ/mol):

$$3\ Si_2OF_6\ (g) + WF_6\ (g) \rightleftharpoons WO_3 + 6\ SiF_4\ (g) \qquad (4.7)$$

The oxygen of Si_2OF_6 could react with WF_6 due to the high affinity between both according to reaction 4.7. Upon air exposure, the incorporated oxide can hydrate and form the tungstite as evidenced in Figure 4-16c. To avoid the formation of tungstite and to achieve pure, oxygen-free WS_2, the incorporation of any oxygen on the sample surface must be avoided. The challenges of preparing an O-free surface are twofold: on the one hand, the oxide regrowth on deposited Si is time-dependent and hence, it can vary depending on the time between Si deposition and oxide removal. As a result, the amount of elemental Si left is also time dependent. On the other hand, the oxide regrowth should be avoided to minimize the adsorption of O_2 or H_2O prior to the W-compound deposition step. To tackle the first challenge of time-dependent oxidation, a chemical oxide based on ozonated H_2O was grown on the Si surface to achieve repeatable, constant Si consumption.[240] Ozone was dissolved in water and due to its strong redox potential, it is strongly oxidizing and form a self-limited oxide film on Si. Ozone can be produced on the site of use and does not induce so much waste, hence it is environmentally friendly. Afterwards, 0.5 % HF was applied for 200 s to remove the native/chemical oxide and then followed by an extensive H_2O rinse to passivate the surface with hydrogen, resulting in a hydrophobic surface that remains stable for extended periods of time.[241]

As the GIXRD spectra in Figure 4-16d show, the tungstite peaks are absent for the samples, which received the treatment of chemical oxidation and HF before the conversion process and only tungstenite is visible at 14 °. Additionally, the XPS spectra in Figure 4-16b reveal that the WO_3-related doublet diminishes and only the W 5f peak at high binding energy remains. According to the XPS quantification procedure, the remaining oxidation level of W-bonds is 12 %, which is the lowest value we obtain for any 2D material grown in our laboratory and that we could measure by ex situ analysis. By combination of ozonation and HF treatment the surface oxide can be controlled and removed in a reproducible way leading to a stable H-passivated Si which can be used as a vehicle to study the conversion mechanism.

This conversion reaction was described earlier for W CVD deposition by the upward diffusion of Si through the growing W layer.[231] The segregated Si on top can react with the gaseous precursor, forms volatile SiF_4, and deposits the metallic W layer.

The film was exposed to 3 s WF_6 and a W amount of 2.5E+15 at/cm^2 was achieved. Saturation was observed after 15 s exposure as can be seen from Figure 4-17a. The XPS spectra in Figure 4-17b show remaining elemental Si and SiO_2 after the unsaturated 3 s WF_6 pulse and a Si-free surface for larger doses. This means that the dose for 3 s was too small to convert all the Si, whereas the 15 s are enough for converting all Si into W without any residual Si or SiO_2 incorporated.

Afterwards Si layers with different thicknesses were prepared and converted to W. The linear relationship between the deposited W amount and the pre deposited Si is depicted in Figure 4-18. The intersection with the abscissa (1 nm) represents the amount of silicon which was consumed

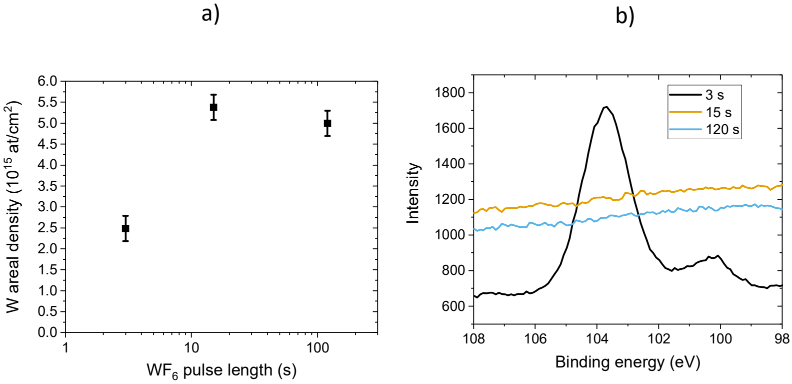

Figure 4-17: a) W after the conversion for different WF_6 exposure times; b) Si 2p XPS peak after different WF_6 exposure times shows that for the 3 s WF_6 not all the Si is consumed, whereas after 15 s and longer conversion, all Si above detection limit is consumed.

during the O_3 / H_2O oxidation and the HF-based SiO_2 removal. The slope derived from the linear fit is 2.51E15 at/cm^2/nm. The linear correlation between W and Si and the absence of any residual Si (Figure 4-17) demonstrate the complete conversion of Si into W at 450 °C and in this way allows a precise controllability of the deposited amount.

WF_6 does not react with the crystallized Al_2O_3 underlayer as long as no other reductant is provided illustrating that this Si-to-W conversion process is selective as demonstrated in an earlier paper.[220]

4.2.3.1.2 Sulfurization reaction for the conversion of W to WS_2

After determining the parameters for a complete conversion of the pre-deposited Si amount, the parameters of the sulfurization pulse were studied to obtain a stoichiometric WS_2. Obviously, this sulfurization pulse was applied in situ to avoid air exposure of the formed metallic compound, since it would oxidize rapidly.[242]

The H_2S pulse converts the deposited material according to:

$$W(s) + 2\ H_2S(g) \rightleftharpoons WS_2\ (s) + 4\ H_2(g) \qquad (4.6)$$

We can assume that all the initially deposited tungsten is in the metallic state, since the H_2S pulse is applied in situ and no O_2 is involved in any of the reactions after cleaning the surface properly. After a t_{H2S} =15 s H_2S pulse at 450 °C, the sulfurization yielded only a S/W ratio of 1.5, hence the film was non-stoichiometric and only 75 % of the maximum sulfur amount was reached since the sulfurization reaction was not complete. A second cycle being equivalent to a dose for 30 s already increased the ratio to 1.7. Adding twelve more cycles with a total H_2S dosing of 210 s resulted in a S/W ratio of 1.8 and saturated around this level for a given initial Si thickness. This was equivalent to 90 % of the total theoretical sulfur amount. This shows also that there also 10% defects, which will be not acceptable for electronic grade. Nonetheless, the activation energy for metallic W sulfurization must be lower than for WO_x sulfurization which is opposite to the behavior in Mo.

4.2.3.1.3 Influence of the processing temperature

According to Figure 4-18, an initial Si thickness of 3 nm is necessary to realize a multilayer structure of four layers of WS_2. For this thickness, the temperature window was investigated. Figure 4-19a shows the S/W ratio after formation at various temperatures between 325 °C and 450 °C. Higher temperatures could not be investigated due to the limits of the chamber. With increasing temperature, the incorporated S amount is increasing as well and is reaching a S/W ratio of 1.8 to 1.9 for 450 °C, but the W amount was constant for all three temperatures. The XPS spectra in Figure 4-19b show decreasing WO_3 doublets for increasing deposition temperatures, before reaching a minimum for 450 °C. We interpret the W-O oxide formation as saturation of metallic bonds upon air exposure, which is a different effect than shown before which was the oxide formation due to an oxide-contaminated surface of the Si precursor. When the sulfurization is conducted at 450 °C, a higher fraction of W is sulfurized and all the accessible W atoms are saturated with sulfur, so that the material is inert against spontaneous oxidation in air. For T < 450 °C, the W films are not completely sulfurized, and remaining W atoms oxidize in air.

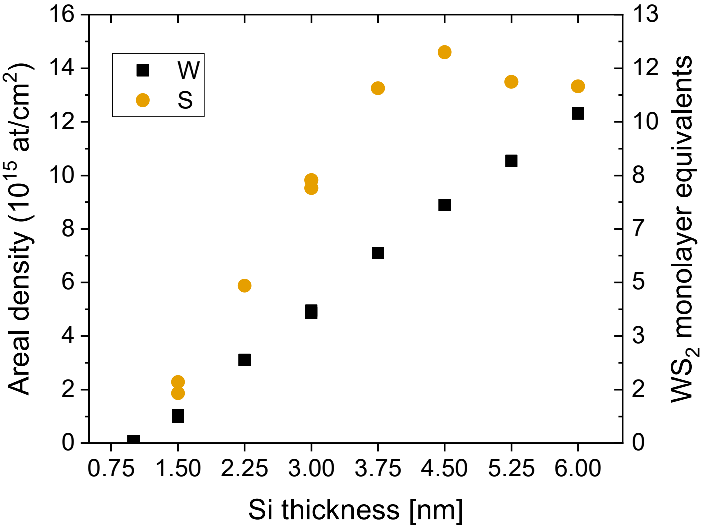

Figure 4-18: Deposited tungsten and sulfur amount as a function of the pre deposited Si thickness. Quantified by RBS.

The Raman spectra in Figure 4-19c show the characteristic peaks for WS_2: The higher the temperature, the higher are the intensities of the 2LA(M)/E^1_{2g} and A_{1g} peaks.[243] The overlapping peaks 2LA(M) and E^1_{2g} describe the second order Raman resonance peak of the longitudinal acoustic mode and the in-plane vibrational modes, respectively. The A_{1g} peaks describe the out-of-plane vibrational modes of the W-S bonds. Note how in contrast, the intensity of the Si 2TA mode at 300 cm^{-1} coming from the substrate remains relatively constant. Together with the rising LA(M) mode, often referred to as a measure for the disorder in MX_2 films, this can be interpreted as an increase in the WS_2 amount.[244]

These observations show that for $T \geq 325$ °C, the limiting step is the sulfurization. For a given temperature, sufficiently long dosing of H_2S had to be provided to convert the thickness of a four layer-equivalent film. This is due to the diffusion of the reactant H_2S through the top layer of WS_x and the out-diffusion of the reaction product H_2 according to reaction 1.6. Diffusion is a temperature-determined process and thus, higher temperatures allow deeper diffusion of sulfur for a given reaction time.

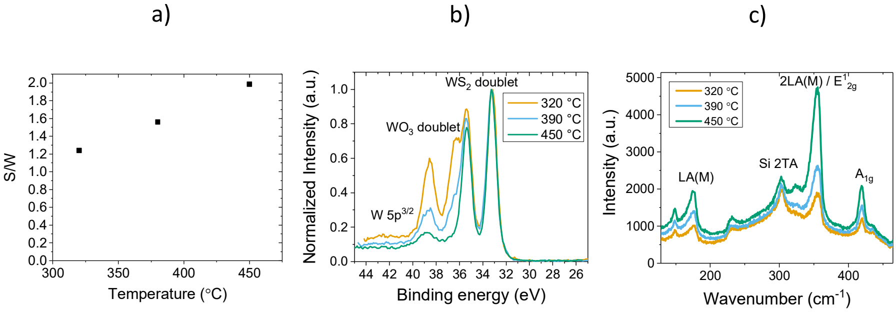

Figure 4-19: a) S and W amount as determined by RBS showing that stoichiometric films can only be obtained at 450 °C; b) XPS spectra of the W region reveal the presence of WS_2 and WO_3. The WO_3 contribution disappeared for the 450 °C process; c) Raman spectra taken upon WS_2 deposition show an increase in the $2LA(M)/E^1{}_{2g}$ and A_{1g} peak for higher deposition temperatures.

At 450 °C the conversion of a 3 nm-thick Si and the stoichiometric sulfurization of the W could be achieved. This temperature was used in all the following experiments to obtain stoichiometric films.

4.2.3.1.4 Influence of the starting Si thickness for controllability of layers

The properties of 2D materials vary significantly with the thickness and the optimal thickness for MX_2 transistors remains under debate.[245,246] In the following we evaluated whether the WS_2 thickness could be modulated by the amount of pre deposited Si.

To achieve the deposition of different thicknesses of stoichiometric WS_2 films, Si films with different thicknesses were pre deposited and converted to WS_2 with $t_{WF6} = t_{H2S} = 15$ s long pulses at 450 °C. The amount of W and S was quantified as shown in Figure 4-18 (p. 84).

While the W amount increases linearly with the amount of pre deposited Si, the S amount increases linearly up to ~3.75 nm Si and then saturates, there is no more sulfur incorporation above this amount. This is related to the limited H_2S diffusion into the deposited film at the temperature used.[216,247] Since the conversion Si →W is done in situ with the H_2S sulfurization, both cycles are conducted at the same temperature. H_2S must penetrate through the surface layer, react with the metal underneath, and H_2 as reaction product evolves. The 450 °C process is capable of sulfurizing

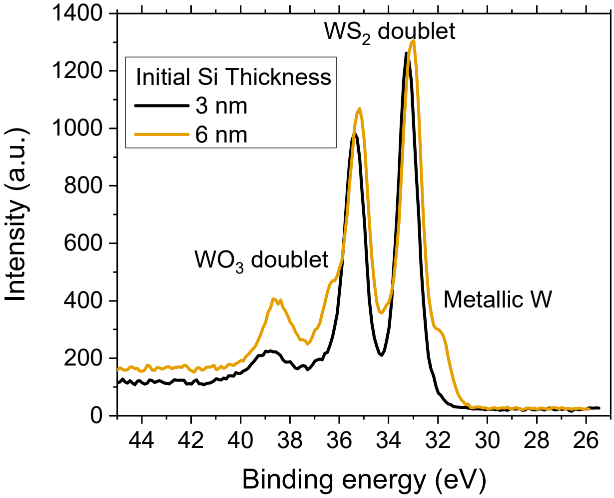

Figure 4-20: XPS spectra with the W-related peaks of a thin and a thick film. The thicker film shows stronger oxidation on the top and a buried metallic contribution, which is not present in the thinner film.

one to six layers at the given H_2S dose and temperature. If the films become too thick, the H_2S is not capable of diffusing deep enough, which can be seen by residual metallic W in the XPS spectra in Figure 4-20. There is also an increased WO_3 amount appearing, being buried at the interface between the sulfur-terminated W-S and the metallic W. This WO_3 is formed due to non-reacted W, which is brought into contact with O_2 from the atmosphere. Hence, O_2 can still diffuse through the top layer oxidizing a part of the metallic W underneath, which can be understood from the smaller Van-der-Waals radius of oxygen of 1.52 Å with respect to the larger one of sulfur with 1.80 Å. Thus, O_2 is assumed to penetrate deeper than H_2S at low temperatures. Diffusion is a temperature-controlled mechanism, therefore only higher temperatures or longer annealing periods could sulfurize thicker layers, but this is out of the range of the available experimental setup and not targeted for the application in few-layered active films. To reduce the conversion rate in the step-by-step process, the precursor could be eventually diluted to reduce the active dose. Reducing the temperature is probably not an option, since the sulfurization will also get slower.

4.2.3.2 Necessity of a cycled process

Introducing the gas pulses sequentially with a saturated WF_6 pulse for conversion and at least partial sulfurization is essential due to the interaction of the solid and gas compounds. We tested the hypothesis whether a partial conversion by a short WF_6 pulse, followed by a long sulfurization step could result in smaller nucleation density and facilitate large crystal growth from fewer nuclei by repeating such cycles. However, we observed that after the first unsaturated WF_6 pulse and the H_2S pulse, no further conversion of Si into W occurred after the second WF_6 cycle, as WF_6 cannot reach the elemental Si underneath anymore and the Si does not diffuse upward through the WS_2. In contrast, the sulfurization reaction continues in the second cycle. Hence the formed WS_2 top layer act as a barrier and prevents the further upward diffusion of Si through the WS_2 film and the Si interaction with WF_6.

The simultaneous injection of WF_6 and H_2S was investigated on the H-terminated Si (CVD regime). We observed the formation of a film with monolayer-equivalent thickness being also stoichiometric. However, the thickness of this film did not scale with deposition time. In this case the surface reaction took place as well, but further surface reaction was strongly reduced and formation of a second layer occurred only very slowly, since the top surface WS_2 film prevented any further exchange between the buried reductant silicon and the gaseous WF_6.

The goal of this work is the deposition of TMD on the insulating substrate without leaving silicon traces behind. We conclude that it is necessary to first fully convert the Si into W, and only afterwards the sulfurization of the W film can be carried out.

Figure 4-21 shows a TEM cross-sectional image of a stoichiometric film deposited with optimized conditions. The image shows in the bottom part the polycrystalline Al_2O_3, in the middle the WS_2 films, and above the spin-on-carbon (SOC) capping layer. In the SOC layer some darker regions are visible, which represents driven-out sulfur by the sample preparation through focused ion beam.

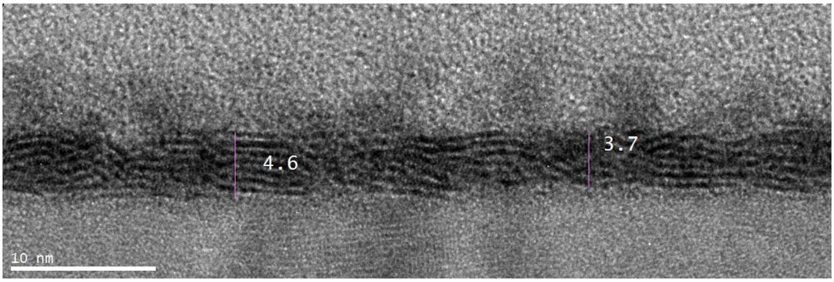

Figure 4-21: TEM cross-sectional image of a stoichiometric WS_2 film prepared with 14 cycles of (WF_6/N_2/H_2S/N_2 of 15 s period for each pulse). The bars with the numbers indicate the thickness of the WS_2 film in nm.

The layered structure of the W and S is visible, but with short-range order. The size of clusters with parallel basal plane structure is less than 3 nm and, in between, areas appear amorphous. The similar random orientation of WS_2 clusters was observed for different thicknesses and similar stoichiometry of the films. In case of thin non-stoichiometric films, the basal planes of the clusters are rather vertically aligned and WO_3 clusters remain in the film. The stoichiometric films can be used for further recrystallization experiments, which is part of further research.[66,248]

4.2.4 Conclusions

A method has been described, allowing to deposit one to six layers WS_2. The method starts from amorphous Si, of which the thickness determines the amount of WS_2 to be formed. To obtain pure WS_2, the Si layer needs to be oxygen-free. Reproducible Si layers can be obtained by the oxidation with a H_2O-O_3 mixture and a subsequent HF treatment, which passivates the surface with H and delays re-oxidation. The silicon layers can be converted to metallic W with WF_6 at $T \geq 325$ °C, then in situ sulfurized by H_2S, which is kinetically faster than the oxygen-sulfur exchange in WO_3 compounds. The formation of WS_2 creates a barrier against a subsequent Si / WF_6 exchange, which imposes that the starting Si film must be fully converted into W in the first cycle. The sulfurization step is a diffusion-driven process and is limited to a thickness equivalent of six layers WS_2 at 450 °C. The obtained WS_2 layers with random basal plane orientation can serve as template for subsequent recrystallization to obtain larger crystals. We believe that this technique can pave the way for a selective deposition on large substrates and could enable heterostructures for TFETs, spintronics, and optical applications.

4.2.5 Recent advances and vision

The production-friendly precursor WF_6 is still a niche-precursor for the deposition of WS_2. Besides the low-temperature methods for the selective conversion of Si to WS_2, the used precursors can be used for plasma-enhanced ALD by means of a H_2 reducing plasma or the self-limited CVD on Al_2O_3. Another group achieved as well the direct growth of WS_2 by WF_6 and H_2S on SiO_2 by using $Ar/H_2S/WF_6$ at 650 °C.[249] Considering the higher evaporation temperature of WO_3 for the solid precursor and higher CVD temperature, the investigation of the combination WF_6/H_2S at higher temperatures than the here used 450 °C could be still interesting. Possibly this is analog to the WF_6/H_2 system, in which W can be deposited on SiO_2 at temperature of 700 °C, hence 650 °C for the WF_6/H_2S system is

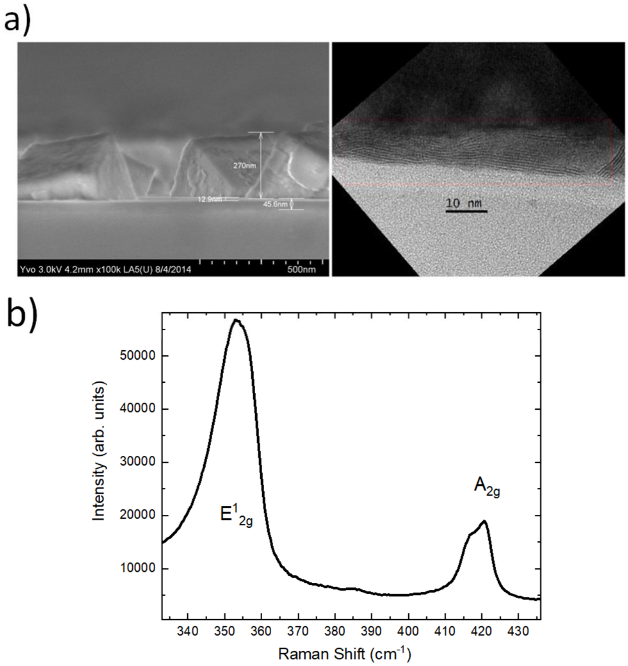

Figure 4-22: a) REM and TEM showing nano cubes consisting of bulk WO_3 and WS_2 at the interface to the substrate; b) Raman spectra of this region shows high intensity WS_2 vibrational modes.

reasonable. Interestingly, locally different growth mechanisms have been observed in the chamber in different locations. On the wafer backside, the region purged with He and located close to the hottest point, the susceptor, the formation of WO_3 nano cubes on the surface of a Si_3N_4 coating has been observed. The interface between the WO_3 and die Si_3N_4 consisted of WS_2, which must have formed purely thermal. This underlines the fact that only a slightly larger temperature than 450 °C is necessary to enable the CVD from WF_6 and H_2S, possible above 50°C to 100 °C higher than on the wafer surface. The source of oxygen could be possibly due to the hot venting in the loadlock.

The use as a H_2 plasma for the reduction of WF_6 on the wafer surface has been also shown promising. Within this work, stoichiometric WS_2 layer in the sub-monolayer range could be deposited on annealed Al_2O_3. This was the base for numerous following investigations on PEALD of WS_2.[70–72]

The approach studied here on the system of Si, WF_6, and H_2S can be also extended to other materials. The approach could be also used to deposit Mo-compounds as well as selenides. Eventually these schemes of a sacrificial promoter participating in the conversion reaction could be also used to synthesize other high-mobility materials such as HfS_2 or $HfSe_2$, which would also have a true mobility advantage over MoS_2 in a device.

5 Quality improvement through crystallization

The previous chapters demonstrated that high quality MoS_2 could be grown by MoO_3 sulfurization, but that the W-based compounds such as WS_2 at the low temperature of 450 °C have only a short-range order of a few nm. However, a high crystallization degree is necessary for good electrical properties. This can be achieved by providing thermal energy to the films. However, the maximum temperature especially in conjunction with S-containing gases is limited by the substrate material, the hardware stability, and the safety concerns for this process.

In the following chapter, paths to improve the crystallinity are investigated. The annealing in inert atmosphere was evaluated and resulted in sulfur loss for annealing temperatures higher than 900 °C. At 900 °C, the crystallinity significantly increased up to 150 s annealing duration but saturated then according to the Raman spectra. Excimer laser annealing (ELA) was investigated as an alternative technique to increase the energy density and minimize the annealing duration. The results were equivalent to the ones obtained from rapid thermal annealing – up to a certain energy density the crystallization degree increased and above this energy, there was a significant loss of sulfur, which was accompanied by the agglomeration of particles on the surface and destruction of the 2D nature of the film.

The process of metal-induced crystallization (MIC) by Ni or Co was investigated for the recrystallization of WS_2. We found that Co added on the WS_2 film could lower the recrystallization temperature significantly and results in a high WS_2 recrystallization degree. The Co film dewets during the recrystallization process and agglomerates as particles at the edge of the grains, which limits the controllability of film preparation and showed 3D regrowth. To confine the recrystallization area to the 2D film area, suppress sulfur loss, and to avoid 3D regrowth, a dielectric capping layer was deposited on top of the amorphous WS_2 film prior to the recrystallization. After recrystallization at 1000 °C, no sulfur loss was observed, photoluminescence appeared, and the defect related LA(M) mode decreased. Therefore, capped annealing could provide a viable way to recrystallize high-quality MX_2 materials.

This chapter was published as:

Heyne, M. H., de Marneffe, J.-F., Radu, I., Neyts, E. C. & De Gendt, S. Thermal recrystallization of short-range ordered WS_2 films. *J. Vac. Sci. Technol. A* **36,** 05G501 (2018).

The author did the design of all experiments, sample preparation, the sulfurization experiments, analysis of the provided data, and the discussions with the co-authors.

Abstract

The integration of Van-der-Waals materials in nanoelectronic devices requires the deposition of few-layered MX_2 films with excellent quality crystals covering a large area. In recent years, astonishing progress in the monolayer growth of WS_2 and MoS_2 was demonstrated, but multilayer growth resulted often in separated triangular or hexagonal islands. These polycrystalline films cannot fully employ the specific MX_2 properties since they are not connected in-plane to the other domains. To coalesce separated islands, ultra-high temperature post-deposition anneals in H_2S are applied, which are not compatible with bare silicon substrates. Starting from the deposition of stoichiometric short-ordered films, the present work studies different options for subsequent high-temperature annealing in inert atmosphere to form crystalline films with large grains from stoichiometric films with small grains. The rapid thermal annealing (RTA), performed over a few seconds, is compared to excimer laser annealing (ELA) in the nanosecond range, which are both able to crystallize the thin WS_2. The WS_2 recrystallization temperature can be lowered using metallic crystallization promoters (Co and Ni). The best result is obtained using a Co cap, due to the circumvention of Co and S binary phase-formation below the eutectic temperature. The recrystallization above a critical temperature is

accompanied by sulfur-loss and 3D regrowth. These undesired effects can be suppressed by the application of a dielectric capping layer prior to annealing. A SiO_2 cap can suppress successfully the sulfur loss during annealing and reveals improved material quality in comparison to non-capped films.

5.1 Introduction

Impressive progress in the growth of high quality 2D or multilayer films was achieved in recent years. Those developments are ranging from rudimentary chemical vapor transport (CVT) in closed quartz tubes[39], over the sulfurization of pre- deposited metal-oxide films[250], evaporation and condensation of solid precursors[251], to the usage of easily-volatilizing metal-organic precursors in different deposition modes like chemical vapor deposition (CVD)[252], atomic layer deposition (ALD)[253], as well as plasma-enhanced (PE) growth techniques.[71,254] The critical point amongst all those techniques is to achieve a sufficient large crystal size in a reasonable time and over a large area. In all mentioned techniques, the process result is a trade-off between deposition time, temperature, and crystal size.

Most studies focused on MoS_2, although the W-related compounds with S or Se are also highly interesting due to their higher predicted mobility and also higher stability against oxidation.[255–257] However, the higher oxidation resistance and intrinsically higher melting point of W and W-based compounds come along with a higher energy barrier for evaporation and recrystallization. The evaporation of WO_3 requires temperatures higher than 800 °C and recrystallization temperatures higher than 1000 °C are needed for sulfide-compounds , as shown for MoS_2.[51] This high activation energy is needed to initiate the grain boundary migration in these films. Such recrystallization is typically done in situ, following the growth process and in a sulfur-rich environment.[258] Laboratory based furnace setups use evaporated elemental sulfur, whereas industrial reactor designs use typically H_2S. The latter one restricts the use of chamber materials and substrates to oxides with high melting point like SiO_2 or Al_2O_3 and which are not reacting with H_2S at this temperature.[259,260] The recrystallization process requires extreme demands to processing equipment and safety measures, since the process gas H_2S is highly flammable, toxic, and corrosive.[261] The corrosion is particularly problematic for processing chambers with stainless steel walls in which sulfide stress cracking can occur.[262,263] By reducing the temperature during the sulfurization, a wider range of substrates and hardware options can be used.

Besides the chalcogen source, the substrate is also of interest. Sapphire is an appropriate substrate due to its hexagonal lattice and atomically flat terraces upon high temperature O_2 annealing for surface preparation.[264] This provides a surface topology favoring epitaxial MoS_2 growth with a majority of grain edge orientations of 0 ° and ± 60 ° and thereby the best growth quality.[89] Due to a lack or large sapphire substrates with diameters of 300 mm on the market and difficulties in the direct integration on sapphire, the direct growth on the final substrate, being compatible with Si integration, would be advantageous.

The goal of this research is to grow the MX_2 (with M = W or Mo; X = S or Se) in two stages: first starting with formation of stoichiometric MX_2 at a low temperature in sulfur-rich atmosphere, followed by a recrystallization step at hot temperature in H_2S-free ambient to achieve larger crystal sizes. In this way, the highly toxic and corrosive H_2S is only applied at low temperatures, avoiding hot temperature hazard. This paper gives insight into rapid thermal annealing (RTA) and excimer laser annealing (ELA) strategies of amorphous or small-grained WS_2 into larger grains in inert atmosphere, which has been poorly described up till now. In addition, the influence of metallic and dielectric capping layers on the recrystallization characteristics is studied.

5.2 Experimental

As described in previous work, stoichiometric WS_2 films can be deposited on substrates with a crystallized Al_2O_3 surface layer by reaction of a pre deposited Si layer with WF_6 vapor and the subsequent sulfurization of the resulting W layer at 450 °C in H_2S.[219,220,265,266] A five layer-equivalent structure was deposited to study the impact of the annealing conditions.

For the first approach, the samples were then cleaved into square pieces of (2.5 x 2.5) cm^2 and annealed on a Si carrier wafer in a RTA system (AG Associates Heatpulse 610), which is a cold-wall furnace design being able to heat the wafer with high intensity light radiation from second to minute range. The temperature was measured and controlled by a pyrometer monitoring the backside of the Si carrier wafer. Before heating, the processing chamber was flushed with 10 sccm Ar flow for 5 minutes. The temperature ramp-up was set at 20 °C/s. At the end of the annealing at the target temperature, the lamps were turned off and the sample cooled down in Ar gas flow for another 15 min before unloading from the tool to prevent oxidation of the annealed films and to avoid the contact of oxygen with a still hot sample surface. For the second approach, excimer laser annealing (ELA) was done in a SCREEN-LASSE Laser Annealer LT-3000/3100, which was flushed with inert gas during the annealing. The XeCl laser with a wavelength of 308 nm and a pulse length in the nanosecond range, covering an area of 15 x 15 mm^2 per laser shot. The high energy of the radiation ensures a surface-confined light absorption and the short pulse lengths result in a fast heating cycle. The typical absorption depth of 308 nm laser light is 6 nm in silicon, which heats up above the melting point of 1414 °C and therefore, the melting depth can be also larger.[267,268]

The annealing effect by means of a capping layer was then studied. For investigating the influence of a metallic capping layer, Co or Ni films of a variable thickness were deposited on the stoichiometric WS_2 using an Alcatel EVA 600 evaporation system. Initially, 50 nm Co or Ni were deposited using a shadow mask to obtain wedge regions with metal (region 1), a transition region with thinner, dispersed metal (region 2), and a metal-free region (region 3).As dielectric capping layer, SiO_2 was deposited on the 2D film using an Oxford Instruments PECVD system PlasmalabSystem 100 with the plasma source ICP380 at 150 °C, 3 sccm SiH_4, 7.5 sccm N_2O at 3.5 mTorr pressure with only inductively-coupled source power of 2000 W, resulting in a deposition of 55 nm SiO_2 within 10 min.

The samples with the metallic or dielectric capping layer were annealed with the similar RTA process as described above.

All samples were inspected using a Horiba Jobin-Yvon HR800 Raman spectrometer with a 532 nm laser, 25 % neutral density filter, and a grating of 1800 grooves/mm (Raman wavenumber) or 600 groves/mm (photoluminescence). The exposure times for the Raman spectra were 100 s for the RTA and ELA-annealed samples and 10 s for the MIC samples due to much higher signal intensity. For comparing the disorder of the films with different crystallization degree, the disorder-related LA(M) mode was divided by the intensity of the convoluted E^1_{2g}/2LA(M) peak. The composition of the samples was analyzed using Rutherford backscattering spectrometry with a 1.523 MeV He^+ beam.[125] The chemical state of the surface layer was examined by an angle-resolved X-ray photoelectron spectrometer Theta300 system from ThermoInstruments with Al K_α X-ray source (1486.6 eV). Spectra shown in this paper are integrated over all angles from 22° to 77° to maximize the signal-to-noise ratio. Transmission electron microscopy images were acquired using a FEI Titan3 G2 60-300 system at 120 kV for cross-section analysis and 60 kV for plan-view imaging.

5.3 Results and Discussion

Three approaches were applied to improve the crystal quality while maintaining the metal-sulfur stoichiometry. The reference RTA process is compared with the short-time laser annealing and the use of metal or dielectric capping layers to promote crystallization at lower temperature and to prevent desulfurization, respectively.

5.3.1 Rapid thermal annealing (RTA)

The application of an inert gas purge maintained at atmospheric pressure and quick ramp-up up to the crystallization temperature could reduce the sulfur loss. Rapid thermal annealing (RTA) can be used to conduct annealings at atmospheric pressures with ramp rates of 20 °C/s and keep them at this temperature for a few seconds or up to a few minutes.

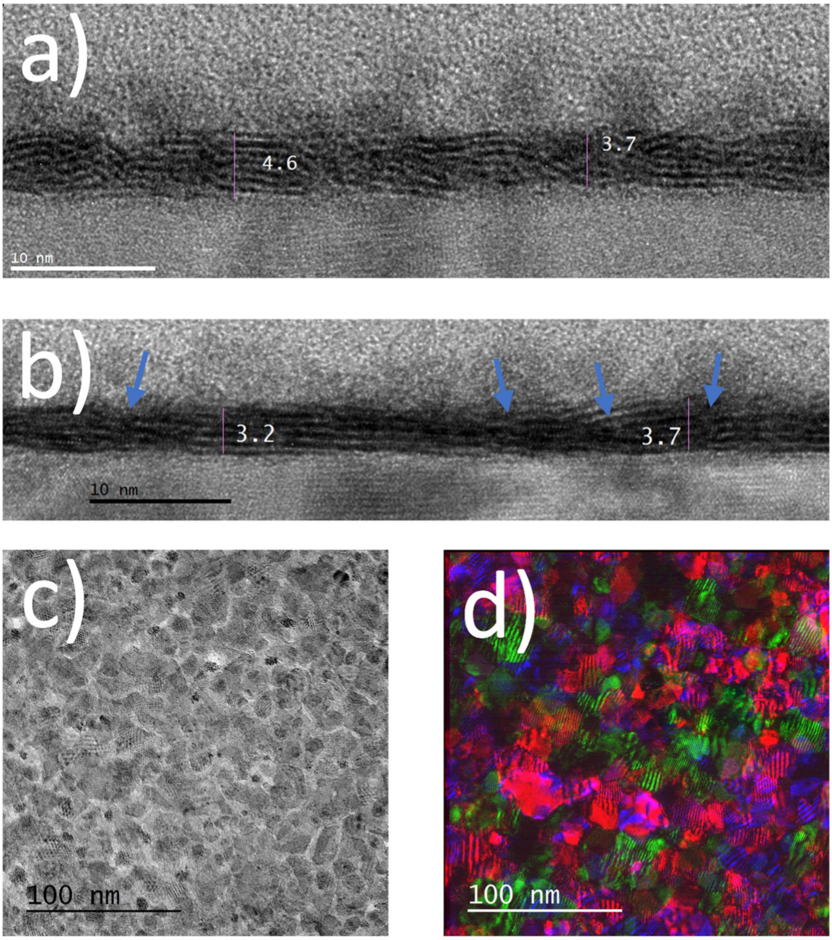

Figure 5-1: TEM cross-section images of a) stoichiometric WS_2 *film as-sulfurized at 450 °C with short-range order and b) recrystallized* WS_2 *films at 900 °C for 150 s in Ar showing preferential horizontal alignment of the basal planes; the numbers indicate the thickness in nm and the arrows the grain boundaries; c) Plan-view TEM image in bright field mode revealing the polycrystalline nature of the grains and Moiré patterns indicate overlapping grains; d) Plan-view TEM image in false-color dark-field mode with colored crystallites showing the random orientation.*

Figure 5-1a and b show TEM cross-section images before and after annealing. Before annealing (Figure 5-1a), the TMD-typical layered structure of metal sandwiched in between sulfur is visible. However, the basal planes are randomly oriented with small grain size of only 2 – 3 nm. The films must undergo a recrystallization to achieve larger grains of the WS_2 with horizontally aligned basal planes.[66]

After annealing (see Figure 5-1b), the basal planes align more horizontally, parallel to the Al_2O_3 surface. The maximum grain size which can be locally seen is 15 nm and grain boundaries separating the domains, are clearly visible. The film remains defective and polycrystalline. Since the TEM cross-section give only local information in two dimensions, the films were transferred onto a TEM grid and analyzed. Figure 5-1c and d show the plan-view bright-field image of the WS_2 and the corresponding false-color dark field TEM image. The three colors represent three differently selected objective aperture positions and therefore different orientations. The appearing Moiré pattern in the bright-field TEM image and the overlapping colors in the dark-field TEM indicate that there is no preferential orientation of the grains and that they are small up to a few tenths of nm. Overlapping colors indicate that even stacked nanosheets are aligned differently with respect to each other. This small grained MX_2 films are not promising with regards to their electrical properties, since every grain boundary and therewith defect is a scattering center for charge carriers and will limit their mobility. In the following, we investigate whether the process parameter of the rapid thermal annealing can influence the material properties to understand the boundaries of this approach.

First, we investigated the effect of ramp rate from room temperature to 900 °C by Raman spectroscopy. The samples with the ramp rate of 20 °C/s yielded the highest $2LA(M)/E^1_{2g}$ peak as depicted in Figure 5-2. Obviously, a high ramp rate is necessary to recrystallize the materials before weakly bonded sulfur can sublimate to the environment in the system. Considering the activation energy for the S-sublimation, it is qualitatively low in comparison to activation energy for the recrystallization, since the sulfur escapes quickly upon heating depending on the environment, but the recrystallization occurs only slowly.

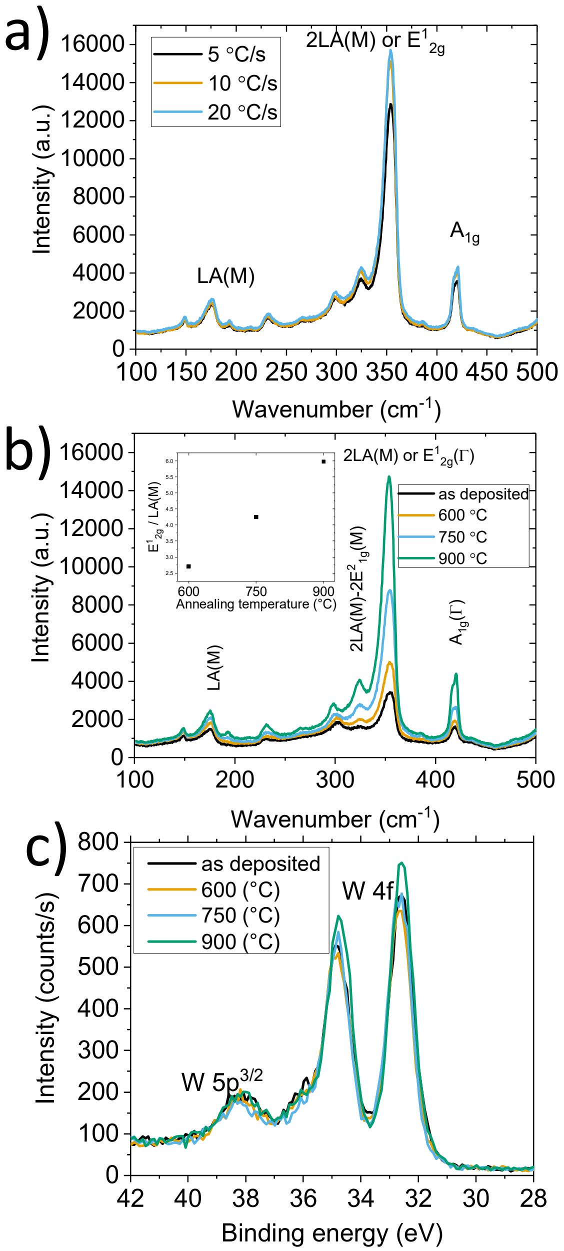

Figure 5-2: a) Raman spectra after annealing with different ramp rate to similar target annealing temperature of 900 °C b) Raman spectra of annealed WS_2 at different temperature c) XPS spectra of the W related compounds show mainly WS_2 doublet and a small oxidation at the 36 eV binding energy shoulder originating from WO_3.

Then the effect of the temperature between 600 °C and 900 °C was assessed. The intensity of the WS_2 related in-plane and out-of-plane vibrational modes increased with a higher temperature up to 900 °C. Note that also the disorder-related LA(M) peak at 174 cm^{-1} is scaling with increasing temperature, suggesting that despite higher crystallinity, a high disorder is still present. At higher temperatures, sulfur bonds would be broken and sublimate resulting in a partially oxidized film. The layers were also analyzed by XPS and the W 4f peak is shown in Figure 5-2c. The spectra range includes the W 4f peak consisting of a doublet for WS_2 compound at low binding energy and WO_3 compound at higher binding energy, which is partially overlapping with the W 5p peak. The spectra are similar for the samples with the annealing temperature up to 750 °C and the WS_2-bond related doublet is even more pronounced after 900 °C annealing. Thus, up to 900 °C, the WS_2 films are stable and do not suffer from significant sulfur loss, which would show up as WO_3 upon air exposure prior to the XPS analysis. The deconvolution of the W peak showed 15 to 20 % oxide fraction in the WS_x films, which was independent of the annealing temperature up to 900 °C. The impact of the annealing time on the Raman intensity of the WS_2 films has been assessed and is shown in Figure 5-3a.

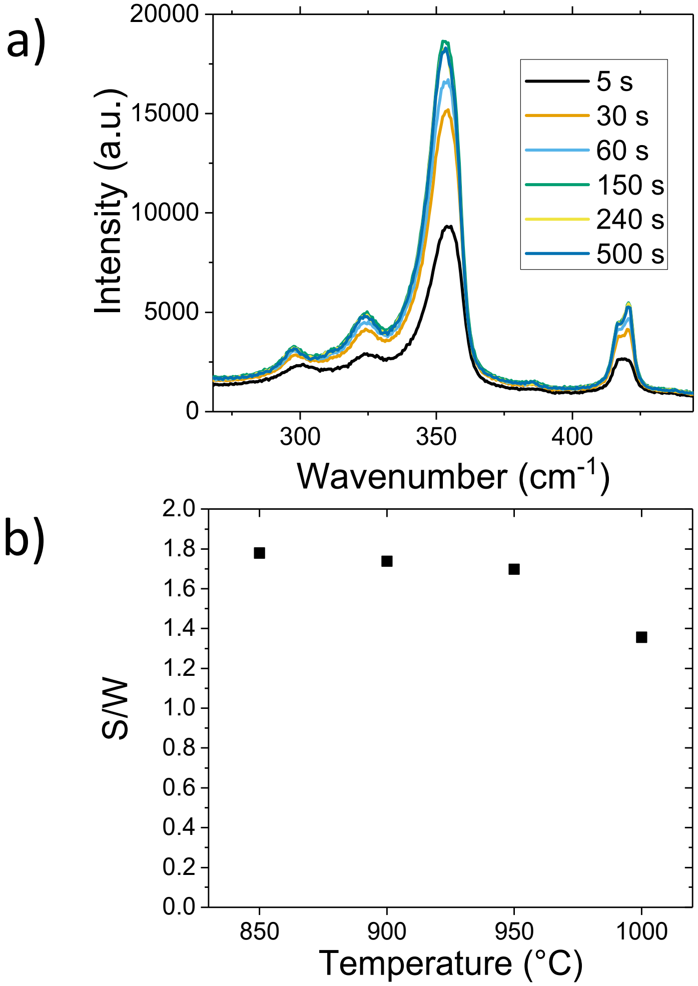

Figure 5-3: a) Raman spectra taken upon annealing at 900 °C for different durations and revealing a saturation after 150 s; b) S/W ratio determined by RBS upon annealing at 900 °C for 30 s. At temperatures higher than 950 °C, sulfur loss could be observed for the longer periods. The initial S/W ratio of as-deposited films was 1.8 before annealing.

At the temperature of 900 °C, the crystallization saturates after 150 s and longer annealing does not significantly increase the crystal size, which can be seen by the saturating phonon modes. This increase of the in-plane 2LA(M)/E^1_{2g} mode especially indicates that the randomly oriented basal plane orientation changed to a mainly horizontal arrangement towards the substrate layer, since the ratio of A_{1g} to E^1_{2g} is a measure for exposed basal plane edges.[269] No significant sulfur loss could be detected with RBS and

XPS analysis upon annealing for those periods at 900 °C (see Figure 5-3b). Longer annealing does not improve the material further within the given timeframe, hence more activation energy is necessary to continue grain boundary migration. However, with the increasing thermal energy, sulfur loss occurs as demonstrated in Figure 5-3b: above 950 °C, the W-S compound significantly loses sulfur. This is occurring with a roughness increase upon annealing of the material over 900 °C (Figure 5-4), which can be correlated to a two-step process: first the cleavage of the metal-sulfur bond by high thermal energy and the evaporation of the cleaved sulfur; afterwards thin, unbound W agglomerates and forms particles which appear as roughness. The addition of higher thermal energy results in continuous loss of sulfur, creating precipitations and preventing any further coalescence of the remaining chalcogenide domains. A congruent effect was observed recently in MoS_2 grain formation by in situ TEM studies in which a liquid TMD precursor was heated and precipitation of hexagonal nanoflakes was observed above a critical temperature.[270] Above 900 °C, an inhomogeneous color distribution on the sample surface was visible, which is a clear indication of surface morphological change and is inappropriate to maintain low-dimensional films. Considering these results, we could claim that the activation energy for the recrystallization process is larger than for the S desorption, which leads to the dilemma that higher crystallinity without sulfur loss in an inert atmosphere can be only reached by a very long process.

We conclude that a conventional RTA in inert atmosphere is not appropriate, since the recrystallization mechanism at a given temperature after a certain time becomes slow and could be not investigated further with the relatively short processing times which were achievable in an RTP system. The film properties cannot be improved further by increasing the temperature either, because the films suffer from sulfur loss above 900 °C, which results in the destruction of the film with loss of its chemical and physical properties. Eventually, the kinetics of the recrystallization process would need more exploration within a broader time window.

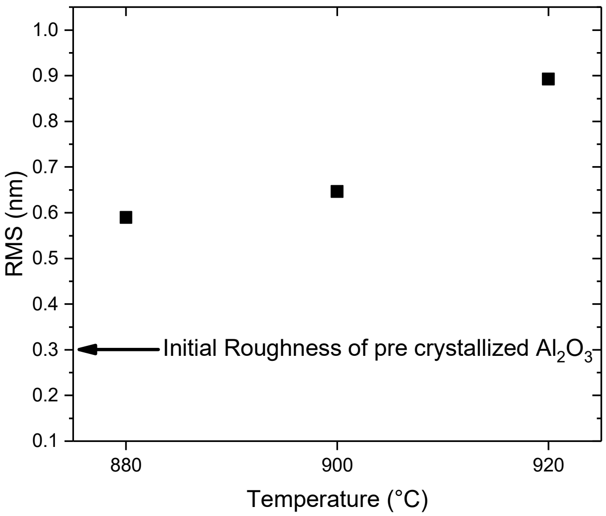

Figure 5-4: Roughness (RMS) after RTA annealing below and above the non-critical recrystallization temperature of 900 °C

5.3.2 Excimer laser annealing (ELA)

In a second approach, we are investigating excimer laser annealing to increase the impact of heating energy input into the film and simultaneously minimize of annealing time to reduce the sulfur loss during crystallization. ELA's low wavelength of 308 nm / 4.02 eV absorbs strongly in conventional bulk semiconductors and very short pulses in the nanosecond range with high energy densities of a few J/cm^2 are achieved.[271],[272–274] Nonetheless, these results will show as well that the activation energies for the sulfur desorption are lower than for the recrystallization. The local temperatures achieved with this approach should be around 1200 °C according to simulations.

Previous experimental efforts of TMD based laser annealing concentrated solely on the contact region, but not on the active semiconductor area for recrystallization.[275–277]

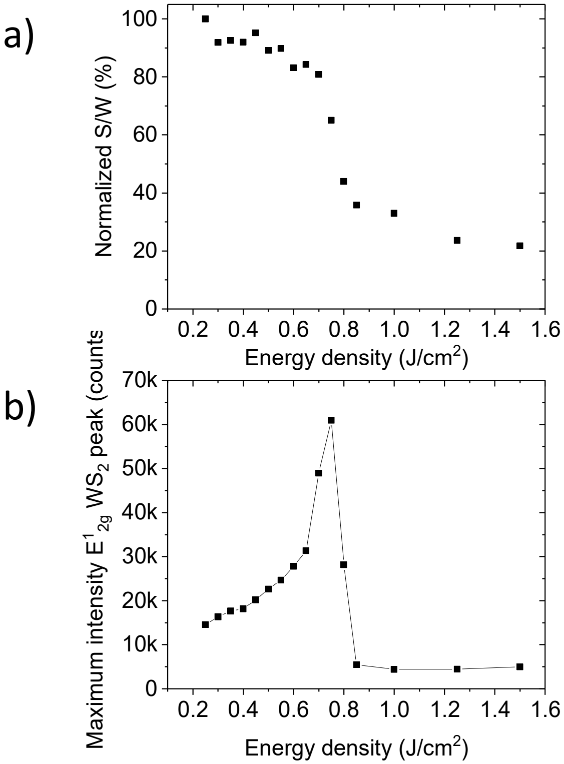

Figure 5-5: a) Sulfur content from RBS upon ELA annealing; b) max. peak intensity extracted from the Raman spectra.

Figure 5-5a shows the sulfur content in a multilayer WS_2 film after annealing as a function of the laser energy density. For low energy densities, the sulfur content remains constant. For energy densities higher than 0.5 J/cm^2, the sulfur amount rapidly drops, and the film roughness increased (see Figure 5-6).

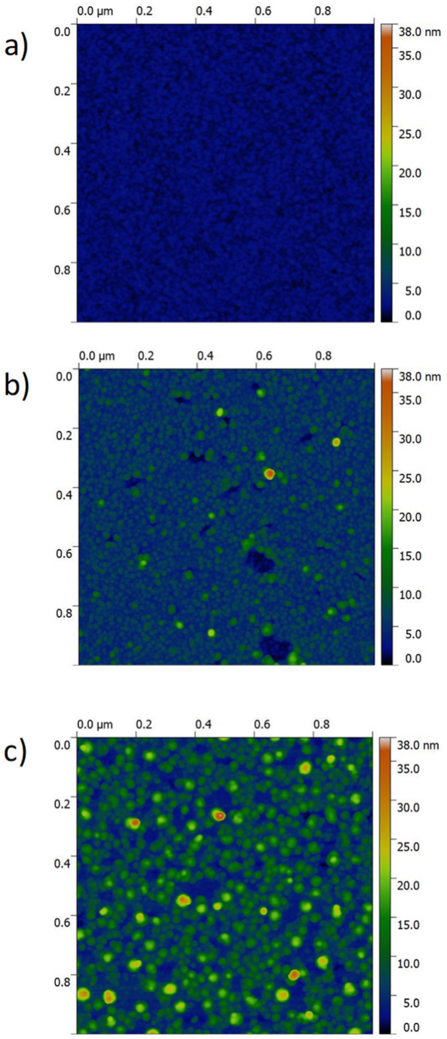

Figure 5-6: AFM topology upon ELA treatment for a) 0.2, b) 0.75, and c) 0.8 J/cm^2 energy density.

The AFM shows the agglomeration of material upon the annealing and the previous shown RBS data, the formation of W or WO_3 particles can be concluded. Raman spectroscopy reveals an increase of the WS_2 related in-plane and out-of-plane vibrational modes of the WS_2, peaking at 0.75 J/cm^2 and then dropping sharply for higher energy densities as it can be seen in Figure 5-5b. There is a loss of sulfur for increasing power, but also an increase in crystallinity of the WS_2 films. This behavior is congruent with the observations from RTA at high temperature, which is characterized by the increase in crystallinity with higher temperature, but simultaneously the decomposition of the film due to sulfur loss. Hence, the difference in the activation energies for the recrystallization and sulfur desorption show that this path has some shortcoming. We must conclude that solely the minimization of treatment time does not result in a better quality. Measures to avoid sulfur loss are necessary and will be described in a later section.

5.3.3 Recrystallization of MX_2 by application of capping layers

5.3.3.1 Lowering the recrystallization temperature by metal-capping - Metal-induced crystallization (MIC)

In previous sections the feasibility of RTA and ELA in sulfur-deficient atmosphere for WS_2 recrystallization was described. In both cases, the major heat source is the silicon wafer under the dielectric substrate layer, because the silicon strongly absorbs the high intensity broad band light used in RTA or the monochromatic light of the laser. For both processes, there was an energy threshold above which S loss and W agglomeration was observed, leading to rough, non-stoichiometric and low-crystalline films. Yet a temperature increase or higher sulfur partial pressure are required to improve crystalline quality. A possibility to decrease the recrystallization temperature is evaluated by using a metal promoter in the so-called metal-induced crystallization.

This approach is known to reduce the recrystallization temperature of semiconductors such as Si, Ge, and even WS_2, but only for thick layers.[278–282] In the case of TMDs, this was only done in sulfur-rich atmosphere.[283] In this work, the use of Ni and Co as recrystallization promotors for low-dimensional films in inert atmosphere is evaluated and insights into the mechanism are given.

Ni and Co show strong interaction with WS_2 and could decrease the recrystallization temperature by a few 100 °C.[284–287] So far, these recrystallizations were only conducted in chalcogen-rich atmosphere. In this work, the role of crystallization promoters in a chalcogen-free, inert atmosphere is investigated to avoid high temperature H_2S exposure for safety reasons. The mechanism behind this, is the reduction in activation energy for recrystallization by a metal donating electrons to weaken the metal-sulfur bond and allow the diffusion of atoms on the surface.

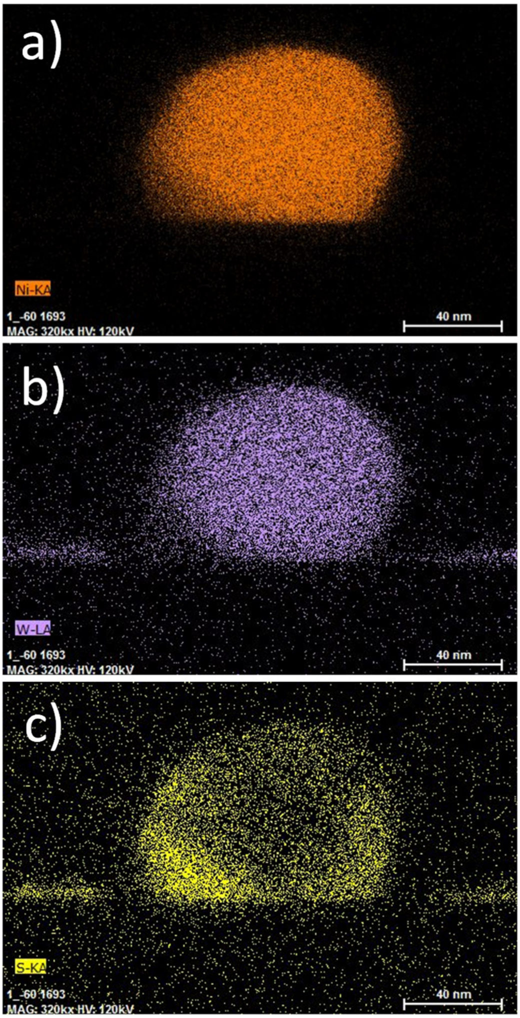

Figure 5-7: EDS images showing the intermixing of Ni with W and S.

Note that the annealing temperature of 700 °C is above the eutectic point in the binary phase diagram for Ni-S, which is 637 °C, but below the eutectic point located at 877 °C in the Co-S phase diagram (see Figure 5-13 and Figure 5-14 in the appendix of this chapter).[288,289]

5.3.3.1.1 Ni as recrystallization promoter in inert atmosphere

In case of Ni, the WS_2 phonon modes in the Raman spectra disappeared after annealing in the deposited Ni pads. Large particles were formed on the surface. However, in this case the resulting particles were an alloy of Ni, S, and W as shown by the EDS analysis in Figure 5-7. The W or WS_x was dissolved in large parts in the Ni and did not crystallize in separate phase. This is different to the effect Brunken et al. observed in chalcogen-rich atmosphere, in which highly oriented WS_2 crystallized from Ni_xS_y melt as in vapor-liquid-solid growth, which is also used for nanowires.[279] During the early stages of crystallization, the Ni_xS_y and WS_2 phase separate in chalcogen-rich atmosphere. In the present experiment in inert atmosphere, Ni and W intermix without phase separation.

From this observation, the Ni-induced dissolution mechanism can be postulated. Upon heating above the eutectic T, the Ni forms with the S liquid Ni_xS_y droplets, which dissolve afterwards the reduced W. In case of the Ni-supported annealing, there was no significant amount of WS_2 detected by Raman anymore. The EDS analysis of the surface particles revealed that a large part of the W was dissolved and form an intermetallic compound with the Ni; S is only located at the shell or edges of the particles overlapping with the Ni regions and appears there in the form of Ni_xS_y. Thus, the recrystallization of WS_2 by means of a Ni Promoter is not possible in inert atmosphere and requires always a chalcogen-rich environment as Ellmer et al. have shown. In this case, the principle is like solid-liquid-solid growth.

5.3.3.1.2 Cobalt as metallic recrystallization promoter in inert atmosphere

After annealing of the Co/WS_2 stack, a strong structural modification was observed as it can be seen in Figure 5-8 .

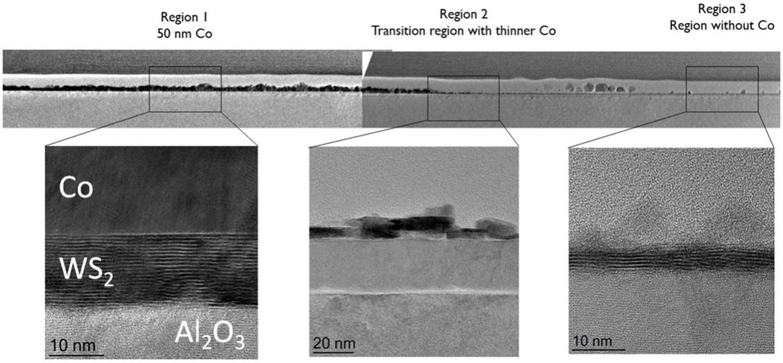

Figure 5-8: TEM cross-section image showing the surface with Co deposited by shadow mask - three regions can be distinguished: 50 nm thick Co through the holes of the shadow mask, the transition region with thinner and dispersed Co and the region far away without Co.

The TEM cross-section image reveals a strong modification of the original five-layer WS_2 film. Whereas the region far away from the Co pads (region 3) shows a highly defective area, the WS_2 film close or under the metal pad consists of horizontally aligned crystals (region 1). Under the 50 nm thick Co metal pad, strong material migration is observed. Areas in which the Co is directly in contact with the Al_2O_3 substrate and areas in which thick WS_2 crystals with a size of a few tens of nanometer are observed. In the transition region from the metal pad to the field without metal (region 2), a smaller cobalt amount is found. In this transition region, the WS_2 migration is less pronounced and stronger crystallization, but less thickness variation than in region 1 can be seen. In addition to this structural observation, the Raman spectra and photoluminescence was measured on those samples and is shown in Figure 5-9. In the Co- metal pads, the same photoluminescence is present at 1.94 eV as observed on exfoliated multilayer WS_2 flakes. This PL indicates an improved crystalline quality of WS_2 in the metal-covered regions in comparison to the WS_2 which is not covered. Although the strong phonon-mode enhancement and the PL appearance are promising, the strong material migration towards regions with thick metal is undesired. The observation, that the film thickness remains uniform in the transition region with dispersed Co suggests that a thinner metal film would allow better control over the WS_2 layers during the recrystallization process. The Figure 5-9c shows the annealing effect on WS_2 covered with 2 nm thick Co films over the whole area. After the recrystallization, the formation of dispersed particles is observed on the surface, as illustrated with the SEM plan-view and representative TEM cross-section images in Figure 5-9d,e.

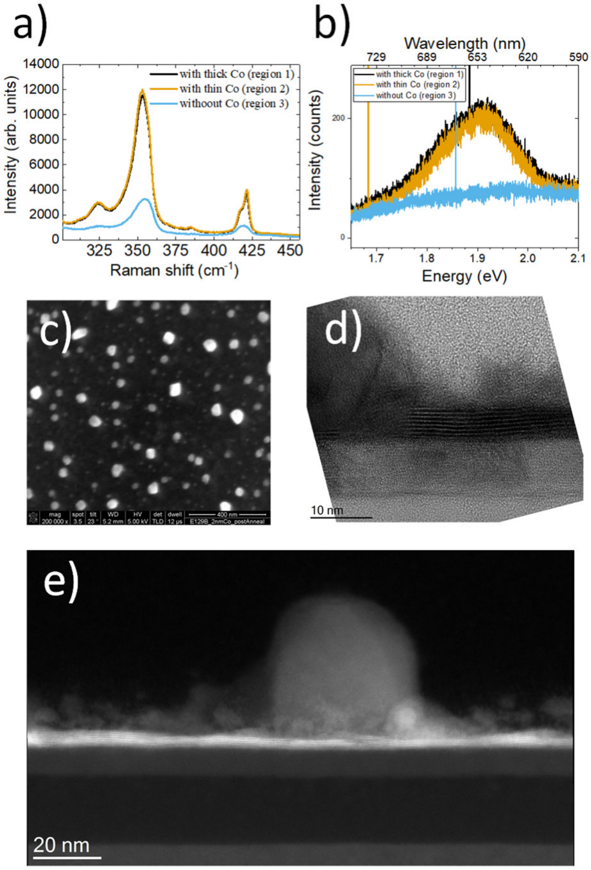

Figure 5-9: a) Raman spectra and b) photoluminescence spectra obtained after annealing in the (original 2 nm) metal covered region and in the non-covered region. The metal-covered regions revealed the highest intensity in WS_2 vibrational modes and photoluminescence at the expected 1.9 eV upon 700 °C annealing; c) SEM plan-view image after annealing reveals the dewetting of the thin Co film into larger particle agglomerations. d),e) TEM and STEM images showing agglomerated Co particles and recrystallized WS_2 film upon annealing. Co particle is in direct contact with the Al_2O_3 underlayer and hence, it displaces WS_2. Therefore, regions with fewer and with more layers are visible.

The evaporated Co-film is not anymore continuous after annealing but agglomerated in larger particles of a few tens of nm, probably to minimize its surface for minimal surface energy. These particles are not on top of the WS_2 layers, but they sit in between, also displacing part of the WS_2 film. Figure 5-10 shows the Raman spectra and photoluminescence of the annealed film which was covered with 2 nm Co. A strong WS_2 Raman signal and a clear symmetric PL are visible, being like the benchmark from exfoliated flakes. The photoluminescence peak at this energy corresponds to A excitonic absorption, but the emission intensity is much smaller than the emission of the bandgap emission.[290]

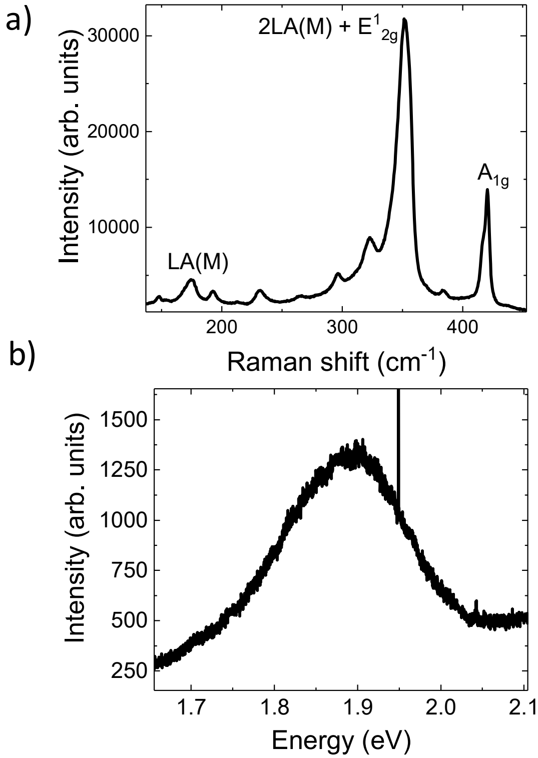

Figure 5-10: a) Raman spectra and b) photoluminescence on WS_2 film which was covered with 2 nm Co and annealed at 700 °C.

Although strong Co migration and agglomeration is observed, the migration and formation of few tens of nm thick WS_2 crystals is suppressed and a continuous WS_2 film remains, with a thickness between 3 and 7 layers. These layers show improved alignment of the basal planes parallel to each other and longer lateral size of the continuous Van-der-Waals layers in comparison to the films which were annealed without cap.

A deeper characterization of the Co particles allows to gain insight into the mechanism of migration and recrystallization of WS_2. As illustrated in the TEM-EDS images (Figure 5-11), the Co particles have a metallic core. The shell of this particle is covered with W and S. Besides this area, also a Co_xS_y region in the bottom left of the particle was observed, as well as WO_x regions (see bottom right of the particle). The existence of a small Co_xS_y particle close to large metallic Co particle was observed repeatedly in several cross-section images. The presence of those compounds allows to propose a crystallization mechanism. Ellmer et al. developed a model describing rapid crystallization, the so-called amorphous solid – liquid – crystalline solid model (aSLcS).[278,283,291–294] This model assumes that the Co-promoter metal forms a supersaturated metal-sulfide solution above the eutectic point in the sulfur-cobalt phase diagram, dissolving W or WS_x, which crystallizes during cool-down from the supersaturated solution and forms the large crystals of WS_2. Ellmer et al. perform their annealing in a chalcogen-rich atmosphere, above the temperature of the eutectic point in the metal-chalcogen phase diagram. In contrast to that work, the Co-WS_2 based system in the present study is annealed at 700 °C in inert atmosphere, i.e. below the eutectic point in the Co-S binary system (877 °C). We observed that the Co core is purely metallic, which means that the largest portion of it does not react with the sulfur from the WS_2 layer, but simply dewets upon heating and forms particles since the system tries to reduce the total energy of all surfaces. However, only a small fraction of the Co was interacting with the WS_x film underneath, forming a Co_xS_y compound. Possibly this is due to the fact that nanoparticles can have a lower melting point than the bulk solid and hence, dissolve some sulfur at a lower temperature.[295,296]

During the dewetting, this Co_xS_y droplet can locally dissolve the WS_x compounds resulting in a supersaturated solution due to the lower melting temperature of nanoparticles. During the metal- and metal-sulfide migration over the surface, the oversaturated solution cools down and forms highly ordered WS_2 crystals. Beside the metal particle, there are also Co_xS_y

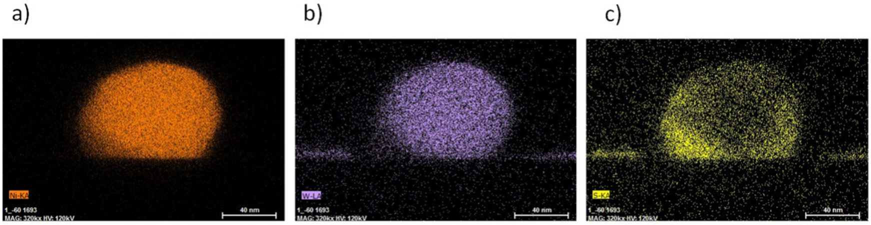

Figure 5-11: EDS images showing Co-particles on WS_2 film after annealing at 700 °C for 60 s. The top row shows a Co particle with a WS_2 shell. No intermixing of WS_2 and metallic Co is present.

particles, which deplete a small fraction of sulfur from the WS_x layer, leaving behind non-bound W metal. This metal forms then upon air exposure WO_3 particles besides the mentioned WS_2 crystals, Co, and Co_xS_y particles. Highly crystalline films can be achieved in an inert atmosphere at 700 °C only (64 % of the WS_2 decomposition temperature of 1250 °C) with a better quality than non-promoted annealing at 900 °C (77 % of the decomposition temperature). We believe that this transformation process takes place due to the interaction mechanism of Co on TMD basal plane edges: Co tends to decorate the edges of TMD basal planes, where it donates electrons to the metal atom and weakens the metal-sulfur bond strength.[297] This effect was also observed in the early studies of hydrodesulfurization catalysis (HDS) in which Co and Ni promoted the HDS activity: These metals make the Mo or W centers more electron-rich and by this, they weaken the Mo-S or W-S bond. This makes the sulfur atom more labile and lowers the crystallization temperature.[298,299] The thermal energy favors then the grains boundary migration due to higher mobility of the sulfur atoms.

Nevertheless, the separation of the promoter metal particles from the WS_2 films cannot be controlled in this way and would require different approaches, e.g. by providing pre-patterning to accumulate the particles outside the active target area after the dewetting according to the principle of templated assembly.[300,301] In synergy with the phase separation and preferential Co positioning at basal plane edges, they could be separated from the active area of interest and can be removed, which will be subject of further research. Our initial tests have shown that concentrated H_2SO_4 can remove Co successfully. Despite the high crystallinity of the obtained grains, the film itself is still very defective as it can be seen from the TEM images. Nevertheless, the dewetting on planar material stacks needs to be prevented with additional techniques as described in the next section.

5.3.3.2 Dielectric capping to reduce TMD decomposition during the annealing

Another possibility is to cap[4] the structure to suppress the desorption of chalcogen from the film. The RTA and ELA showed that in S-deficient atmosphere, there is an energy threshold beyond which the sulfur sublimates out of the films. Consequently, the non-bound metallic atoms dewets from the surface, resulting in the agglomeration of particles that oxidize upon air exposure preventing any crystal growth. Sulfur, which becomes mobile in the recrystallization, will sublimate immediately at annealing temperatures close to 1000 °C and therefore needs to be maintained.

This effect can be minimized by using a S-rich atmosphere, which reveal reduced defect density upon recrystallization.[302] However, it requires 1000 °C annealing for reasonable recrystallization, which is in combination with H_2S detrimental or destructive for co-integrated semiconductors due to thermal vapor etching, especially at high temperatures and high pressures.[258–260,303–309]

To avoid the decomposition of the compound semiconductors, a capping layer can be deposited before the annealing, which was shown to be effective also for GaAs, InP, and others.[303] For the TMDs, this concept has been successfully demonstrated on $MoTe_2$, MoS_2, and WTe_2.[248] The deposition of the capping layer must not damage the TMD film, hence it should not desulfurize the multilayer upon cap deposition. A SiO_2 PECVD process at low temperature of 150 °C was chosen to minimize the sulfur loss or fast thermal oxidation with the precursors SiH_4 and N_2O, which are fragmented in the plasma through electron impact dissociation. The SiO_2 deposition process on the stoichiometric WS_2 films resulted in a loss of a sulfur equivalent to one monolayer WS_2, i.e. the S/W ratio dropped 20 % by the SiO_2 deposition process as shown in Figure 5-12, which corresponds to

---

[4] Note that this was done without Co promoter.

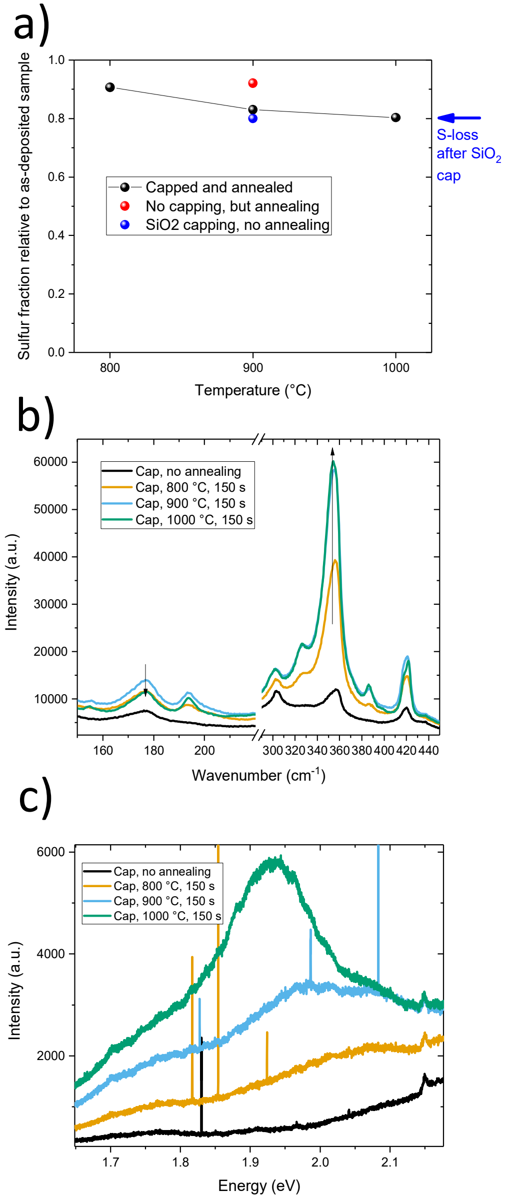

Figure 5-12: a) Sulfur loss after capping layer deposition and annealing at different temperature; b) Raman spectra after capping and annealing at different temperature; c) photoluminescence evolving after annealing at 1000 °C, which is comparable to photoluminescence spectra of an exfoliated bulk flake.

the loss of the top layer's S. Possibly, there are further ways to minimize the sulfur loss by softer techniques, such as PEALD running at even lower temperatures or by replacing the plasma-enhanced process by simple evaporation. Those techniques were not studied in this paper and were not crucial in multilayer structures in which one top layer could be sacrificed.[248,310,311]

Figure 5-12b shows the change in Raman intensity upon SiO_2 capped annealing at various temperatures. The Raman peaks increase with higher temperature and saturate above 900 °C. In addition, we observed for the first time, that the region around the LA(M) peak at 174 cm^{-1} did not scale-up with the in-plane and out-of-plane modes, but it decreased eventually at 1000 °C in comparison to the 900 °C annealing. This region around the LA(M) peak is related to the disorder in TMDs.[119,244] The decrease of the ratio LA(M) to E^1_{2g} indicates a reduction in the disorder of the

WS_2 material together with a higher crystallinity. In addition, the higher photoluminescence (PL) peak close to 1.94 eV, which is also present in high quality exfoliated WS_2 multilayer flakes, confirms the improved quality of the film despite the 20% sulfur loss by the SiO_2 plasma deposition. This PL peak corresponds to the A exciton absorption edge, which is also present in bulk material.

The preservation of 80 % sulfur in the WS_2 multilayer structure, the maximization of the Raman peak intensity, and the enhanced photoluminescence indicate that the use of a capping layer provides an effective method to avoid sulfur loss while improving the crystalline quality. The SiO_2 hinders the sublimation of sulfur from the surface. The SiO_2 cap is not a reaction partner for sulfur and prevents any permeation of sulfur. It reduces the likelihood of a precipitation formation and increase the domains that can coalesce.

5.4 Summary and conclusions

The present work describes the recrystallization of WS_2 layers with random basal plane orientation into polycrystalline films using rapid thermal annealing (RTA) in chalcogen-free atmosphere. We observed that the process window for recrystallization without considerable sulfur loss results in WS_2 grains of 10 – 20 nm size in comparison to the originally 1 – 3 nm as-deposited WS_2. Above the critical temperature of 900 °C or critical laser energy density, sulfur loss occurs and metal nanoparticles agglomerate. Excimer laser annealing was used to maximize the heat impact and simultaneously decrease the annealing period down in the ns range. Excimer laser annealing can recrystallize the film, but similarly to RTA the grains separate and tend to form 3D nanoparticles. Metallic capping was tested and Co has been identified as a good crystallization promoter for metal-induced crystallization of WS_2 in inert gas, since it is immiscible with WS_2 and therefore, decreases the recrystallization temperature from 1000 °C down to 700 °C. Highly crystalline WS_2 films are formed surrounded by Co particles. WS_2 migration is observed, which is more pronounced for thicker Co films. The use of a SiO_2 capping layer, combined with high temperature annealing, can prevent sulfur losses, since it suppresses the volatilization of S and confines the heat in the WS_2 layer.

5.5 Recent advances and vision on the field

The quality improvement of 2D materials is still an advancing field to the high number of defects and gap between the experimentally determined charge carrier mobilities and the expected, calculated values. Laser annealing for MX_2 crystallization is gaining importance on heat-sensitive substrates, especially polymers.[312] Laser annealing does not only improve the films crystallinity, but it can also remove contaminants from the growth or the storage in ambient atmosphere and improves the film's properties.[313] Laser irradiation has been also shown to be promising for the phase transformation from the 1T' to 2H phase, which could be an interesting feature for contact engineering since the properties can be changed between metallic and semiconducting.[314]

Regarding the crystallization improvement by a promoter, a similar strategy has been also used to form nanoribbons of MoS_2.[315] This is done by the formation of a crawling Na-Mo-O droplet in sulfur atmosphere at 700 °C. By this, a direct bottom up approach is found and provides ribbons without additional lithography or etch. This is quite an achievement and bridges the gap between the previous chapter on crystallization and the following section on patterned growth.

Still most of the studies focus on *ex situ* observation before and after growth. Further insight into an *in situ* observation during the crystallization will be necessary in the future in order to understand the defect formation or to suppress defect healing during the annealing.[270,316]

5.6 Appendix to the recrystallization chapter

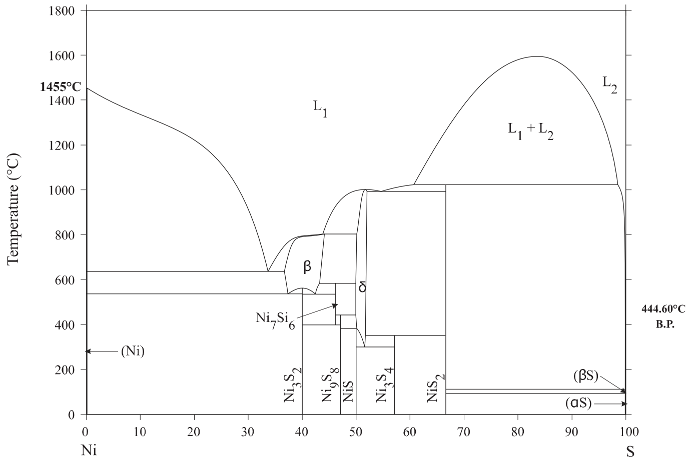

Figure 5-13: Ni-S binary phase diagram reproduced from [289]

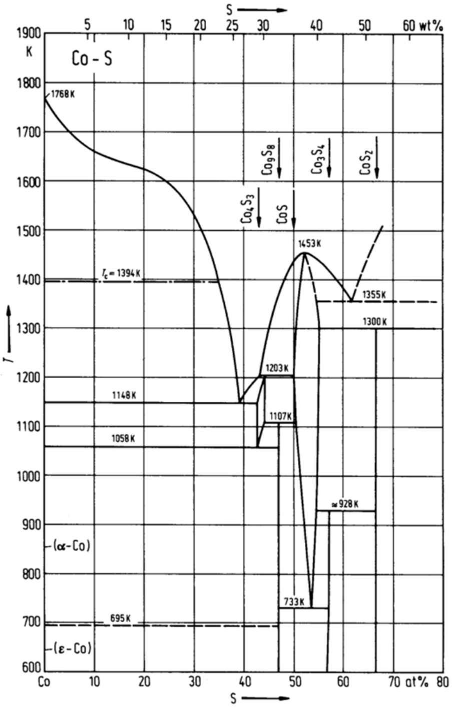

Figure 5-14: Co-S binary phase diagram reproduced from [288]

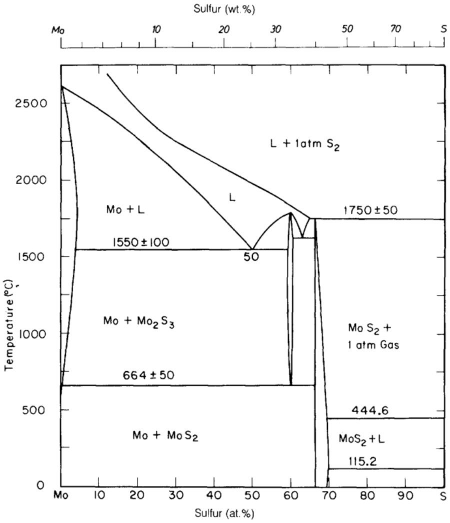

Figure 5-15: Mo-S phase diagram reproduced from [317].

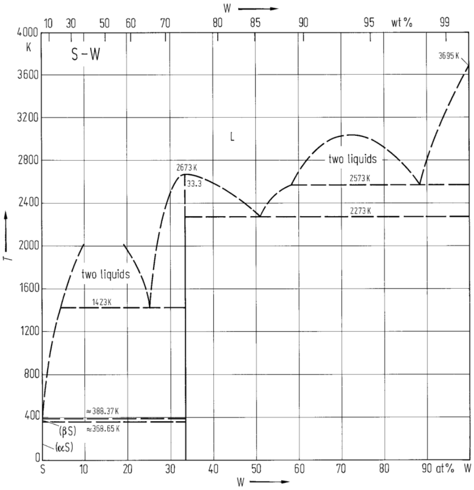

Figure 5-16: S-W phase diagram reproduced from [318].

6 Integration and selective growth

6.1 Selective conversion of Si-to-WS_2

In the previous chapter, it was described that the formation of WS_2 from WF_6 and H_2S could be achieved by means of a reducing agent Si. Since the reaction of the gas phase precursors was selective to the dielectric layer underneath, the concept of a selective conversion of patterns was investigated. A hardmask can be deposited if a thin layer of amorphous Si with defined thickness is maintained during the process. The hardmask concept allowed to pattern the Si on the dielectric substrate. After removal of the hardmask, the patterned Si could be converted into W and sulfurized to WS_2 as it was described for blanket layers in the previous chapter.

By trimming the photoresist prior to the hardmask and Si patterning, nanoribbons down to a width of 20 nm could be fabricated. Like the blanket films, the as-grown material was amorphous and needs further thermal treatment to recrystallize and align horizontally to the surface. It was found, that the template underneath had an impact on the film on 2D film on top. Nonetheless, the selectively grown ribbons are more prone to oxidation upon high-temperature annealing in sulfur-deficient environment probably due to the higher amount of edges being directly exposed to the atmosphere. By this technique, we provide for the first time a possibility to grow the TMD in any desired location or shape by utilizing the pre-patterning of the reducing agent Si for the reaction with WF_6 and H_2S.

This chapter was published as:

Heyne, M. H.; de Marneffe, J.-F.; Delabie, A.; Caymax, M.; Neyts, E. C.; Radu, I.; Huyghebaert, C.; De Gendt, S. Two-Dimensional WS_2 Nanoribbon Deposition by Conversion of Pre-Patterned Amorphous Silicon. *Nanotechnology* **2017**, *28* (4), 04LT01.

The author did the design of all experiments, sample preparation, the sulfurization experiments, analysis of the provided data, and the discussions with the co-authors.

Abstract

We present a method for area selective deposition of 2D WS_2 nanoribbons with tunable thickness on a dielectric substrate. The process is based on a WF_6-based complete conversion of a pre-patterned, H-terminated Si layer to metallic W, followed by in-situ sulfidation by H_2S. The reaction process, performed at 450 °C, yields nanoribbons with lateral dimension down to 20 nm and with random basal plane orientation. The thickness of the nanoribbons is accurately controlled by the thickness of the pre-deposited Si layer. Upon rapid thermal annealing at 900 °C under inert gas, the WS_2 basal planes align parallel to the substrate.

Due to their outstanding semiconducting properties, layered 2D transition-metal dichalcogenides (TMDC) such as WS_2 are promising candidates for transistors with ultra-short channels below 10 nm. WS_2 has a low dielectric permittivity, which is expected to reduce the parasitic short channel effects in comparison to silicon[5,126,319]. The deposition of monolayer and few-layered TMDCs are realized by thermolysis of liquid precursor or chemical vapor deposition (CVD) from the evaporation of elemental sulfur or gas phase precursors such as H_2S or organic sulfides and solid metal-oxide precursors[33,85,89,216,320]. The deposition from volatile metal-halide or metal-organic precursor with CVD or atomic layer deposition (ALD) techniques were demonstrated by other groups already[28,29,323–327,58,60,62,143,215,219,321,322]. Those techniques typically show low deposition rates, e.g. a deposition time of more than one day was reported for a monolayer film formation[46]. In addition, metalorganic precursors present the risk of carbon incorporation in the semiconducting films, degrading their properties[328]. However, conventional Si-based CMOS fabrication methods cannot be applied easily to TMDCs since several key processing steps can damage the ultra-thin, sulfur-terminated transition-metal layers. For instance, plasma-based deposition and post-etch removal of masking layers by highly reactive strip chemistries can easily damage the ultra-thin TMDC layers[103,109,110,112,118,329–331]. Strong shifts in the threshold voltage V_{th} were observed, associated with the change from depletion to enhancement mode[103,332]. Plasma-free patterning techniques can circumvent the damage and have already been demonstrated[333]. In the approach presented in this letter, we limit the patterning process to a sacrificial Si layer which is afterwards converted into WS_2 layers, so that the WS_2 is not be exposed to plasma-based patterning, thus allowing for WS_2 formation without plasma damage.

This letter describes the synthesis process for forming WS_2 nano-ribbons on full 300 mm wafer scale, through selective replacement of a pre patterned a-Si nanoribbon by W, followed by in situ sulfidation with H_2S as shown in Figure 6-1a.

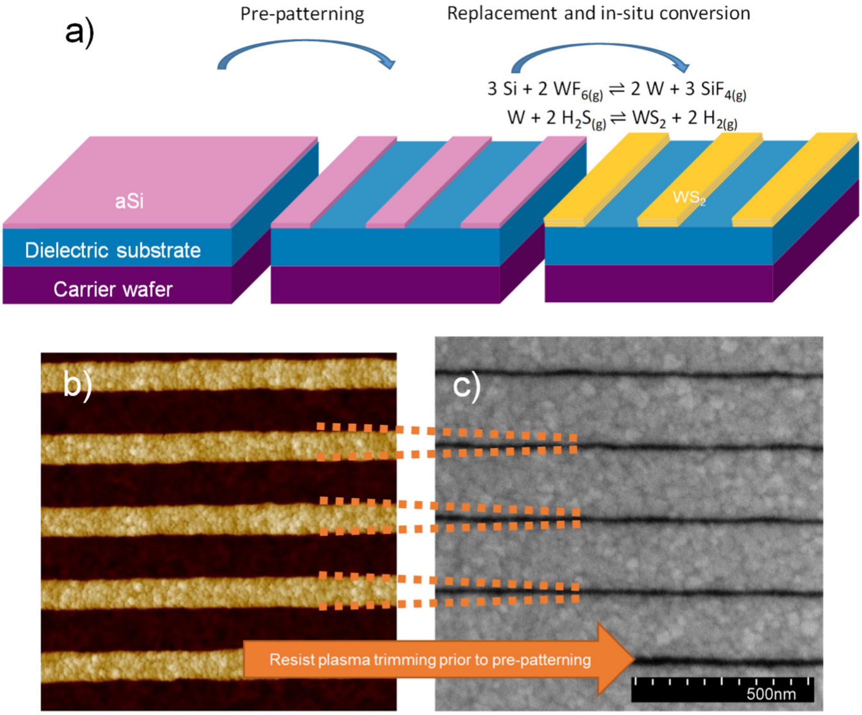

Figure 6-1: a) Schematic of the aSi replacement process; b) AFM scan on 70 nm wide WS_2 lines with 130 nm space in between. c) SEM images of 20 nm WS_2 lines with 180 nm Al_2O_3 substrate in between, fabricated by resists trimming prior to aSi patterning

The fabrication process is depicted in Figure 6-1a. A Si (100) 300 mm wafer was cleaned and coated with 10 nm Al_2O_3 deposited by ALD from trimethylaluminum (TMA) and ozone (O_3) on 20 nm dry SiO_2. This substrate was annealed at 1000 °C for 60 s in O_2-rich atmosphere to crystallize the Al_2O_3 layer and make it stable against attack of HF. Afterwards, a 3 nm amorphous Si layer (aSi) was deposited by physical vapor deposition (PVD). The aSi film was selectively patterned towards the dielectric Al_2O_3 substrate layer by means of amorphous carbon (α-C) and SiOC hard mask. Immersion lithography with a wavelength of 193 nm was used to print lines of 70 nm width separated by 130 nm, thus yielding a 200 nm pitch. The a-Si film was patterned by reactive ion etching (RIE) using a SF_6 / CH_2F_2 mixture and the α-C was removed by O_2 / Cl_2. Then the substrates were immersed in a O_3/H_2O mixture for 30 s and treated with 0.5 % HF for 200 s to remove the SiO_2 mask and to passivate the aSi with

H, in order to prevent immediate oxidation in air[241]. Finally, the wafer was exposed to 14 cycles of sequential gas exposures of WF_6, N_2, H_2S, and N_2 for 15 s each. In the first step, the WF_6 precursor reacts with the aSi layer. Depending on the process temperature either one of the following reactions occurs[231]:

$2\ WF_{6(g)} + 3\ Si \rightleftharpoons 2\ W + 3\ SiF_{4(g)}$ (6.1) mainly at 300 °C

or

$WF_{6(g)} + 3\ Si \rightleftharpoons W + 3\ SiF_{2(g)}$ (6.2) mainly at 700 °C.

The susceptor temperature was set to 450 °C. The Si-to-W conversion is very fast due to the high reactivity of WF_6 with Si. The W is replacing Si which diffuses through the W layer due to segregation. For Si segregated on W, the sticking coefficient of WF_6 is higher than on blanket Si, enabling a fast reaction[231].

The pressure in the reactor was always held at 266 Pa . The H_2S pulse caused the in-situ sulfidation of the metallic W layer. In contrast to Mo, W sulfidation from the metallic state is energetically more favorable and can be achieved at lower temperatures[218,334]. Such a sulfidation reaction occurs as follows:

$W + 2\ H_2S_{(g)} \rightleftharpoons WS_2 + 2\ H_{2(g)}$ (6.3)

The Gibbs free energy at 450 °C, calculated by HSC Chemistry®, is -140 kJ/mol for reaction 6.3, indicating that the reaction could proceed spontaneously. The activation energy for this process was determined by different groups and is around 130 to 142 kJ/mol and claim a rapid rate with a maximum at about 460-475 °C.[335] The conversion of the Si-to-W with the in situ sulfidation on blanket films was demonstrated by our group earlier[219]. We have demonstrated that an oxygen-free Si layer can be used to reduce the gaseous WF_6 precursor to metallic W, which can be easily sulfurized in situ by H_2S at 450 °C. Those as-deposited films improved in their quality upon rapid thermal annealing for 150 s in 10 sccm Ar gas flow in an AG Associates HEATPULSE 610 system.

The obtained nanostructures were inspected by scanning electron microscopy (SEM), atomic force microscope (AFM) ICON PT with a tip radius of 7 nm, Raman spectroscopy with a 633 nm laser, Rutherford backscatter spectrometry (RBS) with He^+ beam of an energy of 1.523 MeV, and X-ray photoelectron spectroscopy (XPS) with a monochromatized Al K_α source (1486.6 eV) and a spot size of 400 µm.

Figure 6-1b shows an AFM scan of the 70 nm wide WS_2 lines in the bright area and the darker 130 nm space exposing the Al_2O_3 underlying film. By applying a resist trimming process, prior to the dry etching of the hard-mask stack, it is also possible to narrow the aSi lines. As shown in Figure 6-1c, the final pattern can be trimmed down to 20 nm linewidth with reasonable linewidth roughness. The Al_2O_3 grain boundaries are visible in the bright area between the WS_2 lines and introduces also steps into the WS_2 nanostructures, indicating that a the WS_2 topography is governed to a large extend by the underlying Al_2O_3 surface topography. Those structures were also scanned by AFM and the roughness was evaluated. The roughness parameter RMS on top of the WS_2 lines was 0.6 nm and in the spaces 0.3 nm. The latter one is similar as on blanket crystallized Al_2O_3 films, indicating that the dry etching of the aSi films did not increase the substrate roughness and resulted in minimal Al_2O_3 recess. The height of the nanoribbons was around 5.5 nm according to the AFM analysis.

The chemical composition of the WS_2 was confirmed by spectroscopic analysis and the corresponding Raman and XPS spectra are shown in Figure 6-2. The measurements were performed on arrays of WS_2 lines. From the RBS measurements (not shown here), the number of atoms per area was extracted and a S/W ratio of 1.9 ± 0.2 was calculated. The XPS spectra were deconvoluted in an oxide and sulfide doublet. The as-deposited material was 31 % oxide and 69 % sulfide and upon annealing the sulfide was quantified with 63 %. This is different than in blanket films, in which the films were mainly WS_2 with residual WO_3 below 10 %. The lines have many reactive edges of the multilayer structures exposed to air, which are prone to oxidation and could explain the difference with blanket films in which only the basal planes are in direct contact with air. No traces of unreacted Si above the XPS detection limit could be found in the WS_2 lines, which

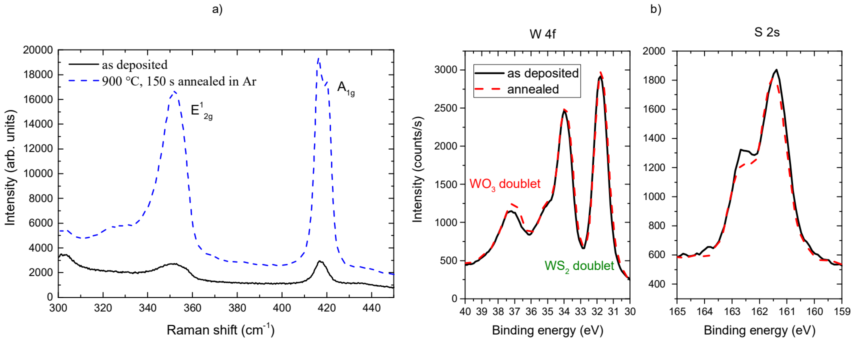

Figure 6-2: a) Raman spectra taken with a spot size of approx. 1 µm on a WS_2 array shown in Figure 1. b) W 4f and S 2s XPS spectra.

indicates that the aSi is completely consumed during the replacement reaction (XPS spectra not shown here). Also, the WS_2 Raman characteristic in-plane E^1_{2g} and out-of-plane A_{1g} vibrational modes are clearly visible on the WS_2 arrays confirming the presence of the WS_2 nanostructures. The frequency difference between the E^1_{2g} and A_{1g} peaks of more than 68 cm^{-1} evidences the multilayer structure with more than five layers[243]. In between the patterned lines, no WS_2 could be detected with Raman spectroscopy, which is in agreement with the absence of W on similar Al_2O_3 substrates exposed to WF_6 precursor[219].

Figure 6-3(a) and (b) show the cross-section TEM images taken perpendicular to the lines. The typical layered structure of TMDCs can be seen, where the dark layers represent the W atoms and the bright layers the S. These layers exhibit a low crystallinity: the basal planes in the as-deposited WS_2 areas are randomly oriented and hence, they are only nanocrystalline. To achieve the desired horizontal basal plane alignment, the structures were annealed. Since MX_2 films suffer from sulfur loss[336–341] during heat treatments in high vacuum or oxygen-containing environments, rapid thermal annealing at 900 °C for 150 s in Ar atmosphere was applied. Note that this was done without capping.

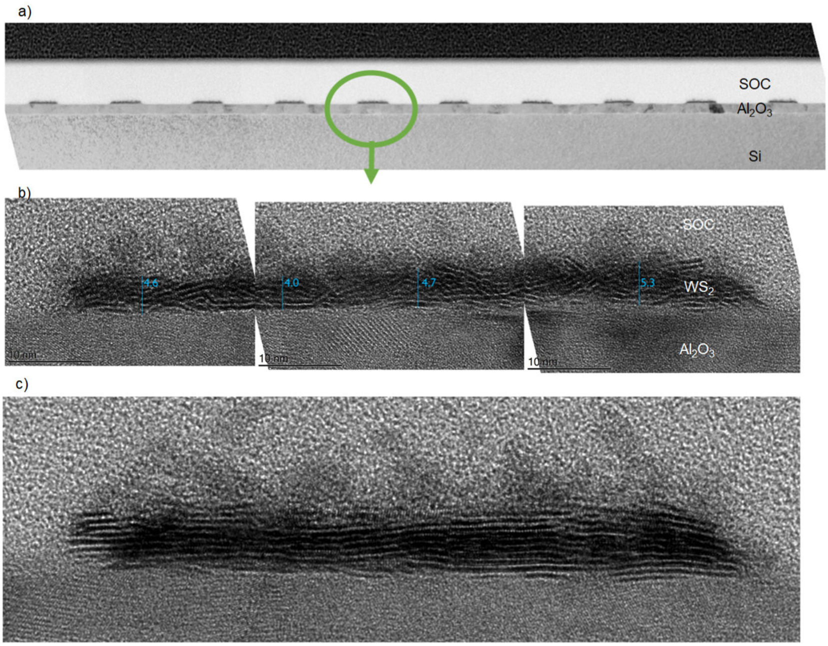

Figure 6-3: TEM cross section image with a) small and b) high magnification showing the 70 nm wide WS_2 *lines on the* Al_2O_3*; c) after RTP at 900 ℃ for 150s in Ar.*

This annealing procedure yielded horizontal basal plane alignment in the structures, as can be seen in Figure 6-3(c), indicating alignment towards the substrate occurred thanks to van der Waals forces. The WS_2 presence and its crystallinity improvement have been also confirmed by glancing incidence X-ray diffraction taken from blanket films, since the patterned samples provide only very small diffraction volume (Figure 6-4). The WS_2-characteristic peak around 14° represents the interlayer distance of the WS_2 planes. Despite the broad peak due to the limited film thickness, the peak intensity is a measure for the crystallinity of comparable diffraction volumes. The intensity increase evidences the crystallization of the weakly ordered films and is comparable to the change observed in the TEM images. The interface between the WS_2 and the Al_2O_3 underlayer is rough due to the polycrystalline character of both Al_2O_3 and WS_2.

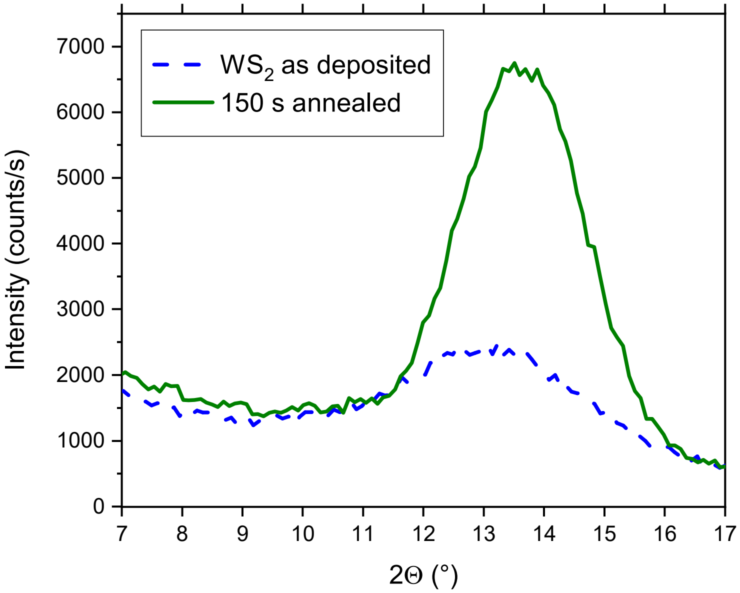

Figure 6-4: Grazing incidence X-ray diffraction peaks of the as-deposited WS₂ and the 900 °C annealed WS₂ films show the increase in crystallinity upon high-temperature treatment.

In summary, a patterning-first fabrication technique for WS_2 multilayer nanoribbons from an aSi layer and the gaseous precursors WF_6 and H_2S was developed. The aSi replacement and in situ sulfidation at 450 °C yields stoichiometric and randomly oriented WS_2, which assemble in 2D structures upon rapid thermal annealing in inert gas. By eliminating the need for WS_2 direct patterning, this process allows the creation of WS_2 nanostructures down to 20 nm of high crystalline quality. Moreover, due to its self-limiting character, this technique is applicable to large substrates. This approach has the potential to control the WS_2 layer number by adjusting the aSi thickness and the width by trimming the Si and enables the bottom-up growth of monolayer or few-layered structures with narrow width.

We believe that this deposition method by replacing pre-patterned sacrificial layers can be applied to other materials as well, and provides structures being appropriate to study size dependent electronic and morphological effects.

Recent advances and progress in the field

Up to now, this selective conversion approach is unique. To improve the quality further, we annealed also the selectively deposited samples in a sulfur-rich environment, which showed an improvement in quality as can be seen in Figure 6-5.

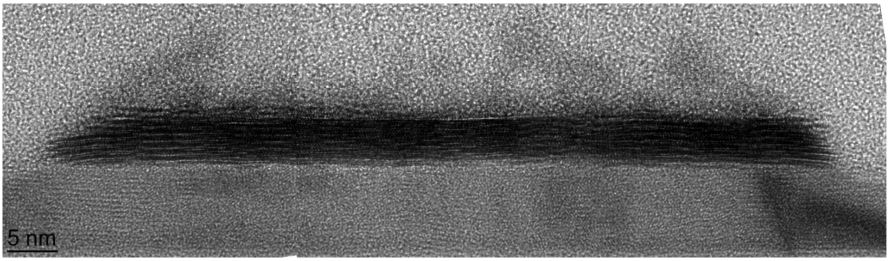

Figure 6-5: TEM image reconstructed from three cuttings shows the cross-section of an H_2S*-annealed selectively deposited* WS_2 *structure.*

The electrical characterization of such a single nanocrystal will be necessary to determine this approach's superiority to other bottom up approaches.

6.2 Heterostructure fabrication by ALEt and selective conversion

The previous chapters described the fabrication of large area MoS_2 films, the selective deposition of WS_2 structures, and the quality improvement of TMD by thermal annealing strategies. Eventually, the final goal is the combination of the investigated processes to achieve vertical heterostructures of the TMD, in which the top layer is differently patterned than the bottom TMD layer. This is necessary to form individual shapes which can be separately contacted in a device. The difficulty in this approach is the patterning of one TMD layer on top of another TMD layer. The chemical similarities between the chalcogenide complicate the patterning. To solve this dilemma, the Si layer on top of MoS_2 was patterned and subsequently converted to W and sulfurized to WS_2.

To this end, a soft-landing process had to be used. In this chapter, we investigated atomic layer etching (ALEt) to remove a thin Si layer from the MoS_2 in a layer-by-layer fashion. ALEt is based on cycles, which are separated in a Cl_2-based adsorption step, a purge step to remove remaining Cl_2, and a biased removal step, which will remove the formed $SiCl_x$ layer from the top. By means of ALEt, a defined Si thickness of 7 Å per cycle can be removed. Although, this process is not infinitely selective toward the MoS_2 underlayer, the etch rate in the MoS_2 is only half of the Si. Hence it was feasible to stop within the top surface of a few-layer MoS_2 layer. The patterned Si on top of the MoS_2 could be subsequently converted into WS_2 and a heterostructure with MoS_2 and WS_2 and areas with MoS_2-only on the same sample could be fabricated. This novel concept allows the individual patterned, seed-free growth of 2D heterostructures on wafer level with CMOS-compatible techniques.

This chapter was published as:

Heyne, M. H.; Marinov, D., Braithwaite, N.; Goodyear, A.; de Marneffe, J.F.; Cooke, M.; Radu, I.; Neyts, E.C.; De Gendt, S., A Route Towards the Fabrication of 2D Heterostructures Using Atomic Layer Etching Combined with Selective Conversion . *2D Materials*. doi:10.1088/2053-1583/ab1ba7.

The author did the design of all experiments, sample preparation, the sulfurization experiments, analysis of the provided data, and the discussions with the co-authors. The included IEDF measurements were done by Dr. Daniil Marinov.

Abstract

Heterostructures of low-dimensional semiconducting materials, such as transition metal dichalcogenides (MX_2), are promising building blocks for future electronic and optoelectronic devices. The patterning of one MX_2 material on top of another one is challenging due to their structural similarity. This prevents an intrinsic etch stop when conventional anisotropic dry etching processes are used. An alternative approach consists of a two-step process, where a sacrificial silicon layer is pre-patterned with a low damage plasma process, stopping on the underlying MoS_2 film. The pre-patterned layer is used as sacrificial template for the formation of the top WS_2 film. This study describes the optimization of a cyclic Ar/Cl_2 atomic layer etch process applied to etch silicon on top of MoS_2, with minimal damage, followed by a selective conversion of the patterned Si into WS_2. The impact of the Si atomic layer etch towards the MoS_2 is evaluated: in the ion energy range used for this study, MoS_2 removal occurs in the over-etch step over 1-2 layers, leading to the appearance of MoO_x but without significant lattice distortions to the remaining layers. The combination of Si atomic layer etch, on top of MoS_2, and subsequent Si-to-WS_2 selective conversion, allows to create a WS_2/MoS_2 heterostructure, with clear Raman

signals and horizontal lattice alignment. These results demonstrate a scalable, transfer-free method to achieve horizontally individually patterned heterostacks and open the route towards wafer-level processing of 2D materials.

6.2.1 Introduction

Two-dimensional materials are attractive due to their specific properties such as a direct bandgap in single-layer, absence of dangling bonds, smaller permittivity, and therewith related smaller short-channel effects.[342] Therefore, 2D materials are promising as channel material in 2D field effect transistors (FET), tunnel-field effect transistors (TFET), and valleytronic devices, which are based on heterostructures.[343–345] Tremendous efforts were spent in the device fabrication on films made by mechanical exfoliation or by chemical vapor deposition (CVD). Novel heterostructure device concepts were tested by stacking flakes with the pick-and-place method or by growing nanosheets on top of each other.[346] Despite those innovative device demonstrations, many of the used approaches lack manufacturability on wafer-level. The integration of a simple back-gated 2D transistor was achieved recently, but there is no vision on the wafer-level fabrication of heterostacks for new device concepts.[265,347] Water-based transfer techniques are widely used to transfer 2D films from a growth substrate to a target device wafer.[348–352] However, a mechanical transfer process remains a source of defects like cracks and wrinkles, especially for larger substrates. It leaves often organic residues behind and induces an undesired variability in the device performance. Therefore, a transfer-free, direct patterning process is highly desirable.

Heterostructures of different 2D materials were prepared by drop-casting of MoO_3 nanobelt solution, followed by sulfurization, drop-casting of WO_3 nanobelts, and final sulfurization to achieve a heterostack.[353] Also sequential chemical vapor deposition (CVD) was used to deposit one first layer and the second one on top.[354,355] These techniques lack the possibility for a controlled deposition in a desired location on the substrate. A selective deposition was achieved by pre-deposition of two different metals with shadow masks and subsequent thermal sulfurization.[175] However, a shadow mask does not fulfill the requirements for nanopatterning and alignment accuracy. Selective growth techniques are necessary to achieve regular patterns. Two-dimensional materials can be selectively grown by providing a metal seed like Pt, Ti, or Au or by providing other nucleation sites like a prepatterned SiO_2 surface.[78,356,357] Growth selectivity was also achieved by O_2 plasma pretreatment of SiO_2 surface to make areas superhydrophilic and promote preferential precursor adsorption.[79,80] Furthermore, polymer functional layers (PFL) were used to inhibit the growth of transition-metal dichalcogenide (TMD) in the areas with the PFL.[75] All those techniques enable the deposition of one 2D layer in specific locations. However, functional devices based on 2D materials consist of stacked ultrathin layers and thus, they require at least a second layer on top of the first layer to achieve a band alignment being appropriate for band-to-band tunneling (BTBT) as it is used in TFETs.[358] Stacking only two 2D layers on top of each other is not sufficient, because each needs separate contacts to the interconnect level. It is therefore necessary to create two 2D layers, with different geometries, overlapping only in the tunneling region. 2D building blocks are MX_2 materials with the metal M = Mo, W, Sn and the chalcogen X = S, Se. They consist of a metal atom which is sandwiched in between the chalcogenide layers and this structure results in a covalent in-plane bonding of a nanosheet and weak Van-der-Waals bond in between the layers. This similarity in the atomistic structure complicates selective etching processes, since each TMD materials' properties are comparable. Conventional continuous wave (CW) plasma etching processes with high bias of a few hundreds of Volts are not applicable here to stop on such sensitive few-layer materials, due to the high damage caused by ion bombardment and poor control of stopping at a defined thickness or at the interface between two nanosheets. CF_4-based CW plasmas were used to thin MoS_2 and the etching rate was minimized by grounding the sample.[109] Nevertheless, even this soft etching introduced damage requiring a restoration by annealing in sulfur-rich plasma or gas treatment afterwards.[113] Such soft etching procedure leads also to the dilemma that extreme low ion energies limit the range of other etchable materials like high-k dielectrics. Another group reported the soft plasma etching of MoS_2 or $MoSe_2$ by SF_6 / N_2 with very low input power and etch rates of 4 – 5 layers per minute.[110,111] Even pure Ar plasma thinning was reported for MX_2 thinning, though no additional information about the chemical changes in the top surface layers was provided.[112]

Ultimately, cyclic material removal using atomic layer etching concepts (ALEt) offers the possibility to better control the material removal. In ALEt, the etching process is separated into a surface reaction step and a removal step.[114] This enables the self-limited removal of material, in defined amounts, with high uniformity and is therefore often referred to as "digital etching". This layer-by-layer etch technique removes material, in principle, with atomic precision and can therefore prevent deep removal or damage of the underlying material, which is essential when patterning a film placed on top of a sensitive TMD layer.

On MX_2 materials, Cl_2-based ALEt has been used to thin down a trilayer of MoS_2 in a controlled way, by using a Cl_2 inductively-coupled plasma (ICP) for chlorination, where the plasma is separated by a metal grid to reduce ion bombardment on the sample surface. [117,118] The removal step is done separately, in a second chamber, with a dual grid and Ar plasma enabling the control of the ion energy of impinging Ar ions. Another ALEt method was demonstrated by plasma oxidation of a MX_2 nanosheet with the subsequent evaporation of the oxidized layer, which is possible due to the difference in the evaporation temperature of MoO_3 and the higher decomposition temperature of MoS_2.[359] In another approach, a top MoS_2 layer is etched by an O_2 plasma and the underlying damaged surface was recovered by sulfur-rich annealing.[113]

In this work, we explore an alternative approach and show that close-to-conventional ALEt tools can be used to pre-pattern a sacrificial Si layer on top of MoS_2 multilayers, which is afterwards converted into a stack of two transition-metal dichalcogenides (TMD), using an Si-to-WS_2 conversion process.[266,360] This process flow demonstrates a scalable, selective growth of MX_2 heterostructures in defined locations, which can be used for the fabrication of band-to-band tunneling devices based on TMDs.

6.2.2 Experimental

Si wafers were first coated with 20 nm SiO_2, then with 10 nm Al_2O_3 using atomic layer deposition (ALD) and annealed at 1000 °C for 60 s in O_2 to stabilize the substrate. MoS_2 multilayers were deposited by the sulfurization of MoO_3 prepared with physical vapor deposition (PVD) on top of the Al_2O_3 layers.[205,216] Then, 35 – 45 Å Si was deposited on top of the MoS_2 by PVD. Samples foreseen for patterning were coated with an additional 11 nm thick SiO_2 hardmask, deposited by PECVD at 150 °C. Patterns were created by optical lithography using IX845 resist and the hardmask was opened either with a CF_4/H_2 plasma or by HF wet etching, before the resist was removed in an acetone bath and eventually dipped in isopropanol.

The samples with amorphous silicon on top of MoS_2 and SiO_2 hardmask were exposed to different conditions in an Oxford Instruments PlasmaPro100 ALE system with Cobra300 ICP source.[119,120] To this end, approx. 4 cm^2 large samples were attached with Fomblin to a SiO_2-coated carrier wafer. In the preparation phase of the ALEt, either a CW Ar plasma with an equivalent of 100 V bias for 14 s or in situ ALEt cycles were applied to remove the native SiO_2 from the top Si surface. In the second phase, the actual ALEt of remaining amorphous silicon was a cyclic process consisting of 40 ms Cl_2 dosing steps, a purge step with Ar of 2 s, and an activation step of 3 s with a plasma pulse biased towards the sample substrate.[120] The ICP discharge was kept on during the entire process to dissociate the chlorine species during the dosing step and to provide Ar ions during the activation step (the substrate biasing was applied only during the pre-sputter step or the activation step of the ALEt). Bias voltages of 33 V, 45 V, and 97 V were investigated. Please note that the applied bias voltages are internally calculated values and do not present the real bias experienced by the ions. Figure 6-6 illustrates the steps of the ALEt cycle. For each condition, several samples were processed to ensure reproducibility.

To avoid inhibition of the Si etch rate or enhancement of the MoS_2 etch rate by unwanted species such as O_2, the chamber was conditioned first with 100 ALEt cycles with a SiO_2-coated wafer placed on the chuck. This ensures that the alumina chamber walls as well as the carrier wafer surface are sufficiently chlorinated and that other weakly-bound adsorbates are removed from the chamber walls.

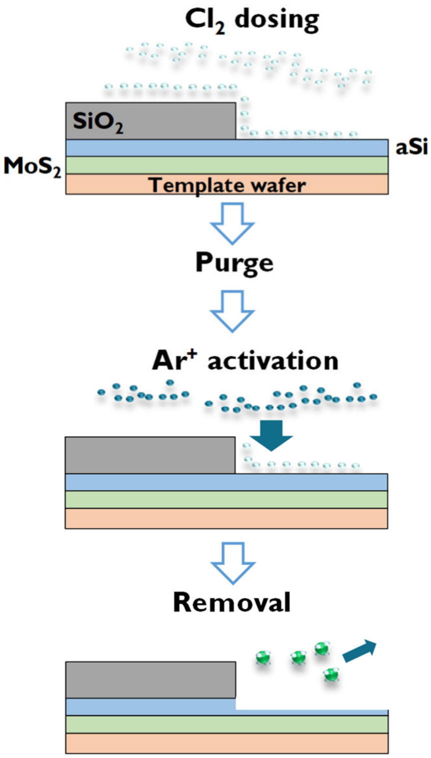

Figure 6-6: Schematic of the used ALEt process consisting of the steps of fragmentation of chlorine during the dosing, a purge with non-bias Ar plasma, and a biased Ar plasma step to remove the formed surface species and remove material in the sub-nm range.

To estimate the bias power impact in the most critical Ar plasma activation step, the ion velocity distribution functions were determined by a retarding field energy analyzer (RFEA), which was placed into the chamber. This system provided by Impedans as Semion RFEA sensor, consists of an sample orifice and an additional grid repelling the incoming electron flux. A second grid behind this orifice is used to discriminate the ion energies (retarding voltage) and eventually a collector measures the incoming ion flux (collector current). The ion velocity distribution function (IVDF) is proportional to the derivative of the collector current with respect to the retarding voltage.[361]

The remaining thickness of Si and MoS_2 was measured by spectroscopic ellipsometry. The blanket films were analyzed by a confocal microscope-based Raman spectrometer Horiba Jobin-Yvon HR800 using a laser of 532 nm (100x 0.9 NA Olympus objective, 1800 grooves/mm grating) and Rutherford backscattering spectrometry (RBS) using a 1.523

MeV He^+ beam.[125] The chemical state of the surface was determined by X-ray photoelectron spectroscopy (XPS) with a Theta300 system from ThermoInstruments (Al K_α X-ray source of 1486.6 eV). Transmission-electron microscopy (TEM) images were obtained by a FEI Titan3 G2 60-300 system and the elemental distribution was characterized by energy-dispersive X-ray analysis (EDS).

The whole fabrication flow of the heterostructure is shown in Figure 6-7. The samples with the patterned Si on top of MoS_2 were converted by a cyclic process using WF_6 and H_2S to convert Si to WS_2 .[219,360] To this end, the samples with the ALEt-patterned Si on top were dipped into 0.5 % HF solution to remove the native SiO_2 from the surface. Then this sample was placed in a CVD reactor and exposed to a pulse sequence of WF_6 at 450 °C, which is forming volatile SiF_4 and selectively converted into tungsten. This is followed by a N_2 pulse for purging and an H_2S pulse to convert the metallic W in situ to WS_2. Eventually, the samples were recrystallized using rapid thermal annealing (RTA) in H_2S-containing atmosphere above 800 °C.

6.2.3 Results and discussion

Atomic layer etching is the reverse process to atomic layer deposition (ALD). In the present study, a plasma enhanced ALEt process was applied to remove Si selectively from MoS_2. At first, the ALEt was characterized on thick amorphous silicon to determine its etch rate. Then, the impact on the interface towards the MoS_2 layer was determined and eventually the conversion of the ALEt-patterned Si into 2D heterostacks was investigated.

6.2.3.1 Amorphous silicon etching by ALEt

Silicon oxidizes quickly in air, which can hinder the ALEt process due to the strong Si-O binding energy (~ 8.27 eV). Typically, native oxide on Si grows 10 - 15 Å thick under ambient conditions. This oxide could be removed wet chemically by a HF dip. However, the used hardmask is also SiO_2 and would be quickly etched by the HF treatment as well, hence this native oxide removal method is not an option. A dry in situ removal during

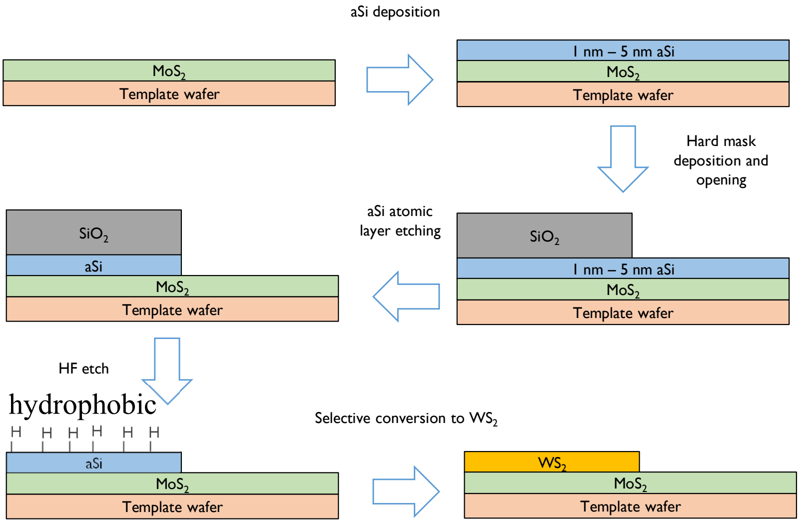

Figure 6-7: Schematic of the process flow for creating heterostack with a patterned top layer

the ALEt process was used. Two native oxide removal techniques were studied: an Ar-plasma pre-sputter clean and the *in-situ* removal by the application of the ALEt process. The pre-sputter clean consists of an Ar plasma, in which inert ions are accelerated towards the sample surface and remove the top layer by sputtering. At first, the sputtering rate for 100 V bias was determined to be 1 Å/s. To remove the native oxide layer prior to ALEt, a pre sputter clean of 14 s was applied before the Ar/Cl_2 ALEt cycles. The etch depth on a 20 nm thick Si layer is shown in Figure 6-8. The remaining Si thickness upon ALEt is a linear function with a slope of 6.6 Å/cycle. A linear fit of those points would intersect at 194 Å, whereas the pristine sample had an aSi thickness of 208 Å. The 14 Å thickness difference corresponds to the etch depth of the pre-sputter Ar plasma.

The bombardment of surfaces with high energetic noble ions is known to cause some amorphization and lattice defects of the remaining layer, over up to few nanometers. In order to determine the impact of the high voltage Ar pre-sputter step, two MoS_2 samples with 35 Å and 45 Å Si caps were exposed to 15 s Ar plasma. As can be seen in the Raman spectra in Figure 6-9, the MoS_2 related E^1_{2g} peak below a 35 Å Si layer lost already

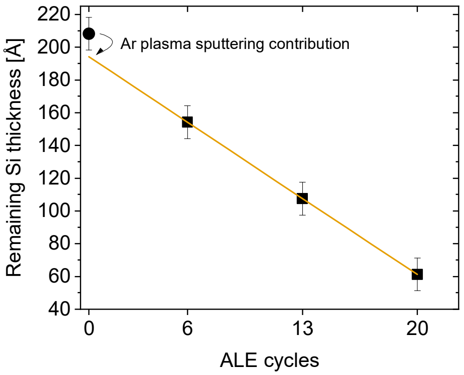

Figure 6-8: Total thickness measured by spectroscopic ellipsometry on the Si samples before 45 V biased ALEt (dot) and after pre-sputtering and different numbers of ALEt cycles (squares). The first point (pristine sample) corresponds to Si covered by native oxide (SiO_2/Si), while subsequent points, measured directly after etching, correspond to Si only. Before applying the ALEt cycles, a 14s Ar-only (97V bias) pre-sputter step is applied to remove the native oxide.

intensity, indicating damage, in contrast to the MoS_2 under the thicker 45 Å Si. Although this process is expected to only remove 14 Å of the cap layer, a degradation in the E^1_{2g} peak is seen for the thinner Si cap, whereas the observed increase in the E^1_{2g} peak for the thick cap can be related to effective thinning of the Si cap relative to MoS_2 (and thus less absorption). Although the ALEt on Si can be well controlled, the use of a pre-sputtering clean causes damage to the MoS_2 through the very thin remaining Si layers, which must be avoided.

Therefore, the *in-situ* oxide removal by the ALEt process with the chlorine pulses itself was studied. The etch depth for different bias power

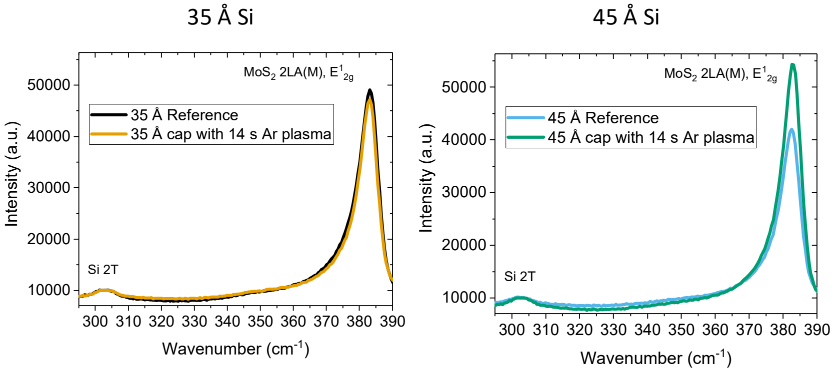

Figure 6-9: Raman spectra of the E^1_{2g} MoS_2 peak normalized to Si 2(TA). The peak intensity decreases for the thin Si cap after plasma treatment and increases for the thicker Si cap.

settings and cycles are depicted in Figure 6-10a. The Si thickness changes show a horizontal shift - we call it the ALEt delay - and a linear part with a Si removal rate of 6 - 7 Å per cycle. This shows that the native oxide can be removed by the ALEt process itself, and that the oxide removal rate varies with the applied bias power, opposite to the Si removal rate which is independent of bias in this range. It requires one extra cycle for the 97 V process, seven extra cycles for the 45 V process, and ten cycles for the 33 V process until the native SiO_2 is removed and the ALEt continues in the linear regime. These results confirm that there is a low ion energy ALEt process, which can remove native SiO_2 and Si within the ALEt window.

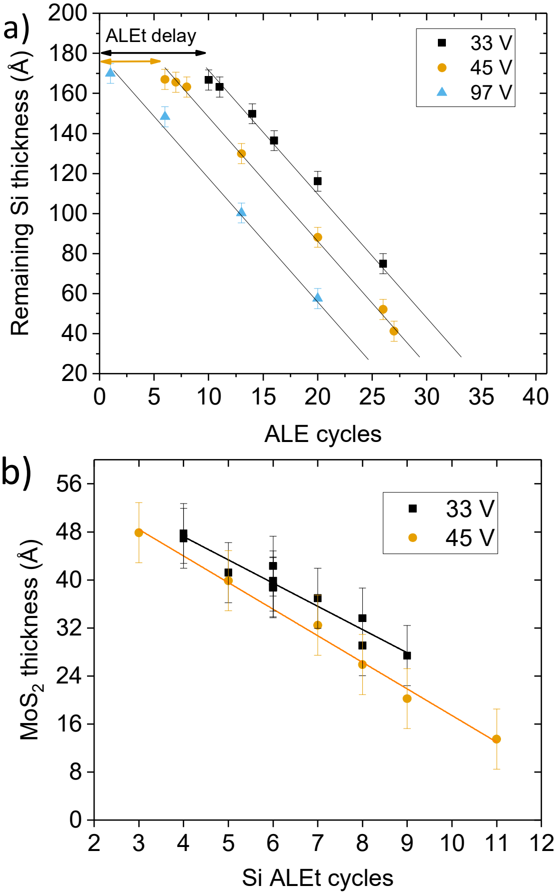

Figure 6-10: a) shows the remaining Si thickness as a function of the ALEt cycles for different bias power, measured by ellipsometry. No pre-sputtering for native oxide removal was applied. b) shows the remaining MoS_2 thickness determined by SE as a function of normalized overetch ALEt cycles; the cycles for breaking through native oxide and to remove the elemental Si are already subtracted.

The Figure 6-10a indicates that, in the investigated range of DC bias voltages applied during the ALEt cycles (33, 45, and 97V) , the Si etch rate does not vary. This is a typical fingerprint of the ALEt process, where an ion energy plateau shows a constant etch- per-cycle saturation behavior.[120] For too low bias (in our case, below 33V), the energy transfer by the inert ions to the chlorinated silicon surface is not high enough to enable the formation of volatile $SiCl_x$ species; on the contrary, for too high bias (in our case, higher than 97V), the system is above the sputtering threshold of silicon, and material removal becomes a two-component process, relying on the formation of $SiCl_x$ but also on pure sputtering.

6.2.3.2 ALEt on Si/MoS_2 heterostacks

In the next step, the chlorine based ALEt process was applied to the heterostack of Si/MoS_2 on blanket samples to remove the Si selectively from the MoS_2 and to study the impact of the etch process on the MoS_2 surface.

The ALEt process without pre-sputtering was applied to the Si/MoS_2 with different bias (33 V and 45 V) until the complete Si layer was removed (monitored by residual Si measurement by ellipsometry). The remaining MoS_2 thickness is shown in Figure 6-10b. With a 45 V bias in the removal step, MoS_2 is recessed with a rate of 4.4 Å/cycle, whereas with 33 V, only 2.9 Å/cycle were removed. This shows that the MoS_2 removal rate is more dependent on the variation in power than the Si removal rate, i.e. for the specific plasma conditions used here, when applied to MoS_2, the system is out of the ALEt energy window.

This can be explained by the mechanisms of the ALEt cycles. The ALEt is based on the removal of a chlorinated surface layer, ideally selective to the non-chlorinated ‘pristine’ atomic layer underneath.

In case of layered MX_2 materials, there are strong in-plane bonds and weak bonds in between the layers. The sulfur termination passivates the metal atoms and is expected to be stable in dry conditions at room temperature. To replace the sulfur by chlorine, the sulfur needs to be removed first. Voronina et al. calculated that chlorine adsorbs preferably on MoS_2 with defects in comparison to defect-free MoS_2.[362] The energy for the creation of one sulfur vacancy is around 2.4 eV.[363,364] This is lower than the applied bias in the range of 30 – 50 eV for the present work (see Figure 6-14). This defect formation can occur in the Si removal step, in which the biased Ar plasma can desulfurize the top layer, resulting in a deteriorated 2D film. In the next ALEt cycle, fragmented chlorine chemisorbs on the surface during the dosing step to the metal. This modified surface layer is removed during the next Ar plasma biased pulse, which simultaneously does deteriorate the adjacent layer's sulfur termination. In summary, atomic layer etching relies on the existence of self-limited adsorption and activation steps, which are existing for silicon in the ALEt parameter ranges investigated here. When applied to MoS_2, the activation step overlaps with the adsorption step by creating sulfur vacancies on the surface, which favor the chlorination. This vacancy creation process, during activation, is time- and energy-dependent, leading to variable levels of subsequent chlorine adsorption on the surface. This determines the final amount of MoS_2 removed per cycle and the absence of a constant etch- per-cycle saturation behavior.

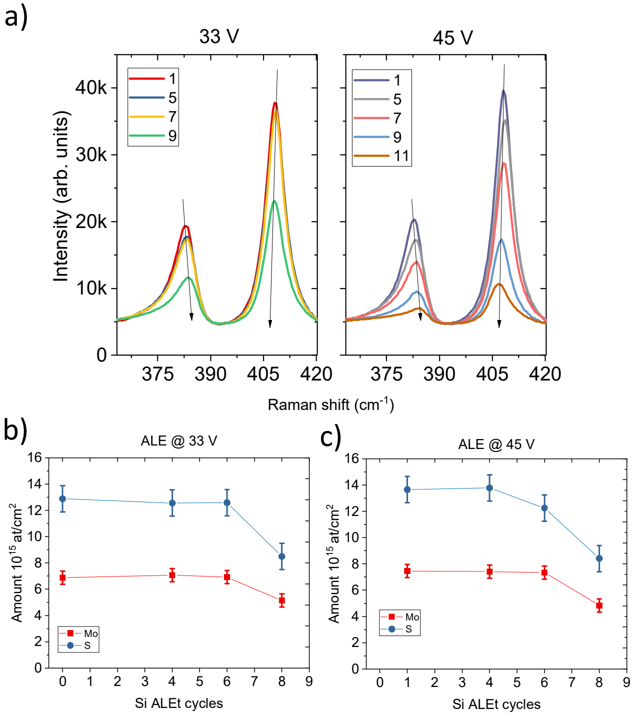

Figure 6-11: a) Raman spectra obtained after ALEt on a Si/MoS_2 heterostack for a different number of cycles and different power; b) and c) are showing the atomic area density from RBS after different number of ALEt cycles and different power; lines added for guiding the eyes.

The above assumed mechanism is supported by the observed MoS_2 etch rate, in the range of a sub-monolayer per cycle. The monolayer thickness of MoS_2 is 7 Å and hence, it takes 2 to 3 ALE cycles to etch one monolayer of MoS_2 with the 33 V bias.

To understand the impact of this ALEt etch step onto the MoS_2 surface, the Si capped MoS_2 films were etched with a different number of cycles to identify the breakthrough at the interface from Si to MoS_2. The Raman spectra after different cycle numbers (without the additional SiO_2 removal cycles) are shown in Figure 6-11a. For 33 V, the MoS_2 is stable up to a few cycles and then the intensity decreases for increasing ALEt cycles. During the first few cycles, the ALEt process etches the Si cap and MoS_2 is not in contact with the plasma yet. Once the cap is removed, the MoS_2 is recessed as well. The faster decay for the 45 V bias ALEt process in comparison to the 33 V bias confirms the higher removal rate of MoS_2, opposite to the Si etch rate which remains constant for various bias (see Figure 5a).

The region of the breakthrough from Si to MoS_2 was studied by RBS. The results in Figure 6-11b and c indicate that this breakthrough occurred after approximately 6 cycles on the 45 Å thick Si. At 45 V, the sulfur amount is reduced after the transition, but the metal remains at its initial level. For additional ALEt steps, the metal amount reduces, and the sulfur/metal ratio remains below pristine value. This confirms the proposed mechanism: the removal of MoS_2 occurs through desulfurization and depends on the bias power.

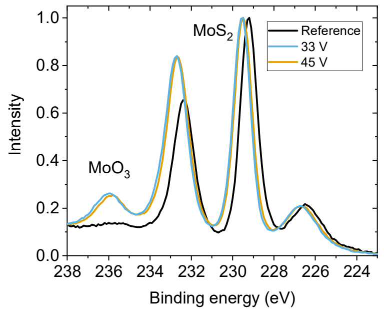

Figure 6-12: XPS spectra of reference samples and ALEt recessed samples stopping at the interface Si/MoS₂.

The surface damage was evidenced by XPS in Figure 6-12, which shows the surface chemical analysis after Si ALEt, stopping at the interface Si/MoS_2. The peak at high binding energy, characteristic for the MoO_3, increases in its relative intensity. MoO_3 forms after air exposure, once the MoS_2 surface is desulfurized (the XPS is done *ex situ*). Both the spectra, for 33 V and 45 V bias, are overlapping, indicating that the surface oxidation results in a similar damage for both bias settings.

Hence, this ALEt process can remove Si as well as MoS_2 layer-by-layer, but it leaves always a modified top surface layer behind. Since this damage is in the sub-monolayer range, it cannot be detected in the disorder-induced LA(M) mode in multilayers as this method is not sensitive enough to this top-layer damage.[119] This suggests the use of a multilayer system, in which the interface layer can be sacrificed, since it loses its function through the damage.

To determine the characteristic of the ions impinging on the surface, the collector current was measured. Its derivation is proportional to the ion velocity distribution and is shown in Figure 6-14. For zero applied bias voltage, the peak in ion distribution is at 10 eV, which represents the average ion impact energy during the dosing and in the purge step, and corresponds to the plasma self-bias for the specific geometry of this etch chamber as we have measured and can be seen in the peak for 0 V bias in Figure 6-14. This 10 eV peak shows the highest intensity in comparison to the distributions measured at higher bias, indicating that most ions hit the MoS_2 surface with the same, low kinetic energy. This energy is only one order higher than the Mo-S bond dissociation energy of 2.59 eV. With increasing bias up to 19 V, the distribution function broadens and the maximum peak intensity for the different modes reduces: less ions of a given energy are hitting the surface, but with a wider range of kinetic energy, between 20 eV and 40 eV for the 19 V bias case. At applied bias above 20 V, the IVDF splits into a bimodal distribution and shifts to higher energies. This can be explained by the sinusoidal excitation as illustrated in the schematic Figure 6-13. The peak separation is induced by the sinusoidal oscillation of the sheath electric field.[365,366] Above 40 V bias, the high energetic peak is located above 70 eV. Compared to the low molybdenum-sulfur bond energy of 2.59 eV, this explains the preferential sulfur removal during this step.[367,368] For even higher bias, this trend continues and a high energetic peak with only small intensity is present. However, these are the most damaging ions. For a bias of 82 V, the ion distribution ranges already from 60 eV to 130 eV. The high energetic ions in this distribution are already two orders of magnitude higher than the Mo-S bond energy and thus, during the activation step, sulfur vacancies are created at high rate, leaving metallic Mo behind, which is etched by Cl in the next pulse.

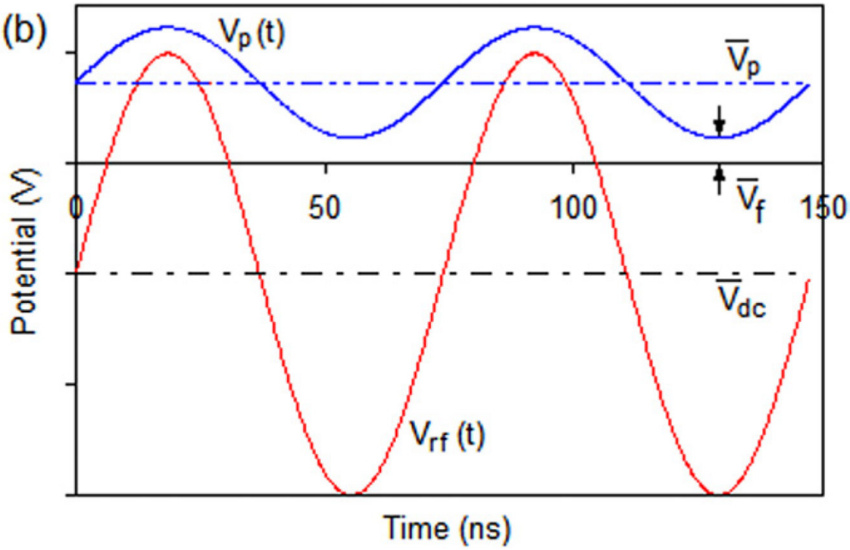

Figure 6-13: Illustration of the potential in a RF-discharged reproduced from doi: 10.1088/0963-0252/21/2/024004.

Therefore, using a plasma process within the ALE windows of Si (hence between 30 V and 80 V bias) will always lead to damage of the top TMD layer. Hence, the method described here can only be applied for multilayer MX_2 systems. In order to reduce the damage, the wafer temperature might be increased to enable the removal of surface $SiCl_x$ at lower Ar activation energy and shift the ALEt window towards lower energies. In addition, one could think of the introduction of a sulfur-containing gas in an additional step after the Ar removal step and the next chlorination step in order to replenish broken bonds immediately with sulfur. The ALEt demonstrated that Si could be etched from MoS_2 without damaging its bulk composition, which is interesting for bilayers and few-layer structures.

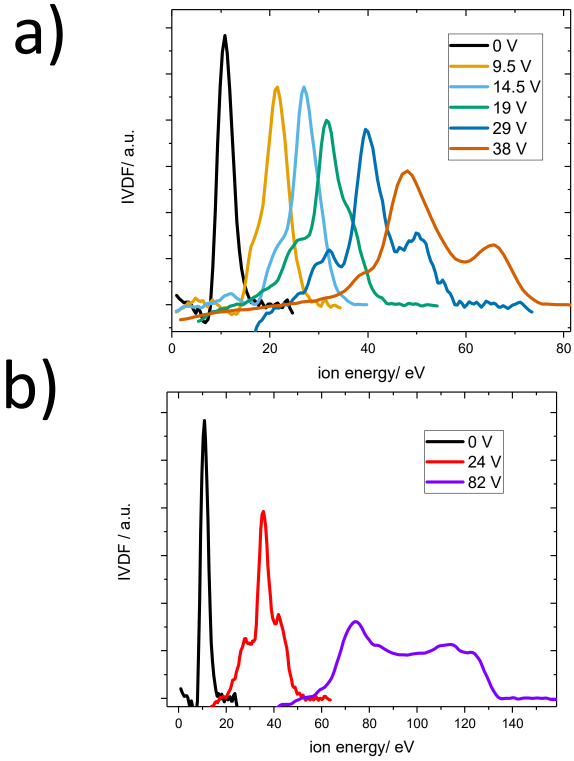

Figure 6-14: Ion velocity distribution functions for different setpoints of bias voltage for a) low bias range and b) high bias range. Above 20 V bias voltage, the ion velocity distributions becomes broad, ranging to high energies.

6.2.3.3 Conversion of the Si into W and sulfurization to WS_2 – Demonstration of selectivity

The ALEt process described above was used to remove silicon from a MoS_2 patterned sample with a small surface modification of the 2D material. Samples with ALEt-patterned Si/MoS_2 were then treated by HF to remove the SiO_2 hardmask including the native oxide from the Si and to dissolve MoO_3. The MoS_2 itself is inert against HF, since the hypothetic reaction

$$MoS_2 + 4\,HF_{(g)} \rightleftharpoons Mo + 2\,H_2S_{(g)} + F_{2(g)} \qquad (6.4)$$

is endergonic with a Gibbs free energy of 1300 kJ/mol and hence thermodynamically not favorable.[369–371] Degradation can only occur due to extensive exposure to moisture.[372]

This means that Si was removed in the regions which were not protected by the hardmask. Elemental Si was still present in the regions covered by the mask and it was converted to W by the gas phase precursor WF_6 (reaction 6.5), then sulfurized by H_2S at 450 °C (reaction 6.6):[219,266,360]

$$3\ \mathrm{Si} + 2\ \mathrm{WF}_{6(g)} \rightleftharpoons 2\ \mathrm{W} + 3\ \mathrm{SiF}_{4(g)} \qquad (6.5)$$

$$\mathrm{W} + 2\mathrm{H_2S}_{(g)} \rightleftharpoons \mathrm{WS_2} + 2\mathrm{H}_{2(g)} \qquad (6.6).$$

A linear scan with Raman spectroscopy was conducted over such a pattern and is depicted in Figure 6-15. In the ALEt patterned region, only the characteristic modes for MoS_2 are visible. Outside those regions, additional peaks indicate the presence of WS_2 resulting from the converted Si, forming a WS_2/MoS_2 heterostack. There, the signal of the MoS_2 is reduced due to the additional light absorption in the top WS_2 layer.

The selectivity of the conversion of the Si-containing region was demonstrated. MoS_2 is not reacting with WF_6, as it can be seen from the thermodynamics of reaction IV with a Gibbs free energy of 172 kJ/mol:

$$\mathrm{MoS_2} + \mathrm{WF}_{6(g)} \rightleftharpoons \mathrm{MoF}_{6(g)} + \mathrm{WS_2} \qquad (IV).$$

Figure 6-16a shows the as-deposited sample without patterning. The MoS_2 is covered by a thin elemental Si cap, which will be the reducing agent for the WS_2 deposition. The SiO_2 hardmask above covers the areas, which will not be patterned by ALEt. The TEM image in Figure 6-16b and c show the structures resulting from the combination of the ALEt and the selective conversion. In the ALEt-recessed regions the elemental Si is absent, since it was etched by the Ar/Cl_2 ALEt sequence. Consequently, there was no W-

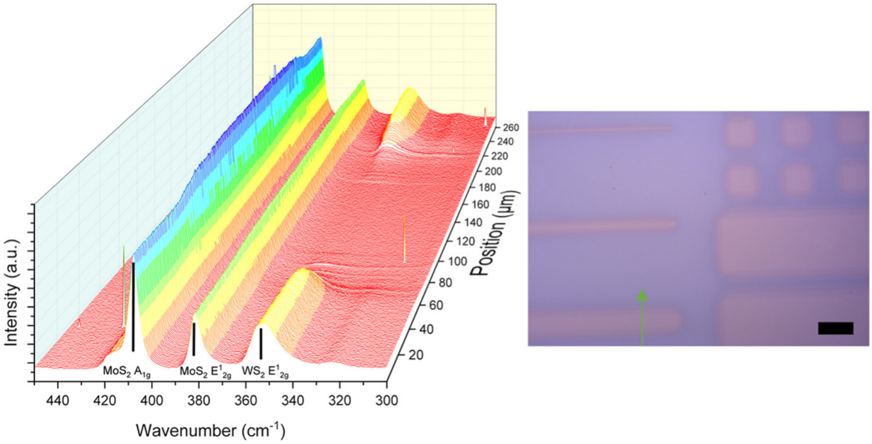

Figure 6-15: Raman linescan over the ALEt-recessed region after the conversion process. The ALEt-recessed regions show only the peaks from MoS₂. The area which was masked shows in addition the top WS₂'s characteristic peaks. The microscopy image with the arrow shows the scanning direction of the area with the heterostack and the single-material area. The scale bar is 200 µm.

related compound deposited in those regions during the WF_6/H_2S conversion.

The selective growth of WS_2 is visible on the previously masked area. The elemental EDS maps confirm the presence of the WS_2 on top of the previously masked MoS_2 and the layered structure of the MoS_2 is still visible. Nevertheless, the images and the elemental maps reveal a low interface quality. The TEM images show a thin SiO_2 interlayer between the MoS_2 and the WS_2. This oxide interfacial layer is not visible in the images taken before the conversion of the Si to WS_2. It appears only afterwards. As shown in earlier work, the conversion reaction of Si to WS_2 is non-stoichiometric in the case that the SiO_2 is not completely removed before the conversion.[266] This is the case for a too short HF-dip during the removal of the hardmask and the native oxide. Residual SiO_2 is then not reacting with the WF_6 and remains as a sediment at the interface between the MoS_2 and the WS_2 from the gas phase reaction. This could be eliminated by improving the HF wet etch step to remove the native SiO_2 fully and to passivate the Si against re-oxidation. Despite the fact that the interface it not sharp due to these SiO_2 interlayer, there are no signs of intermixing due to the clear Raman spectra and the absence of additional shifted peaks.[373,374]

In the ALEt-treated region, the number of layers decreased from nine layers (under the Si-cap) to seven layers (after Si etch), while the remaining layers retained their original crystalline quality (no amorphization). The loss of 1-2 layers confirms the surface damage induced in the top layer through the biased removal step during the cycles. This damaged layer, in the form of MoO_3, was removed during the HF-dip prior to the conversion.

These images demonstrate the proof-of-concept of a process flow allowing to create multilayer structures using a sacrificial Si patterning/conversion approach, in which one Si layer is patterned on top of a bottom MoS_2, then converted into WS_2. This is an important step towards the implementation of 2D materials with VLSI-compatible techniques, scalable to full wafer-level.

6.2.4 Conclusion

Atomic layer etching is a powerful tool to remove materials with a rate of only a few atomic layers per cycle, with the power to limit the damage towards sensitive substrate materials. In this study, the chlorine-based atomic layer etching of Si on MoS_2, using a close-to-conventional reactor was characterized. Repeatable, linear Si etch rates around 6-7 Å per cycle were achieved. It was found that the applied bias in the removal step can remove the native SiO_2 from the Si, in situ, without the need for a detrimental high bias Ar pre-sputter step. The native oxide resulted in an inhibited Si removal at start of the ALEt process, which is called the ALEt delay. After the ALEt delay, the Si etch rate was constant for different bias power, indicating that this process is within the ALEt window for Si. The developed ALEt process was applied to Si/MoS_2 heterostructures to grow a WS_2/MoS_2 stack using a subsequent WF_6/H_2S conversion. Si etching using

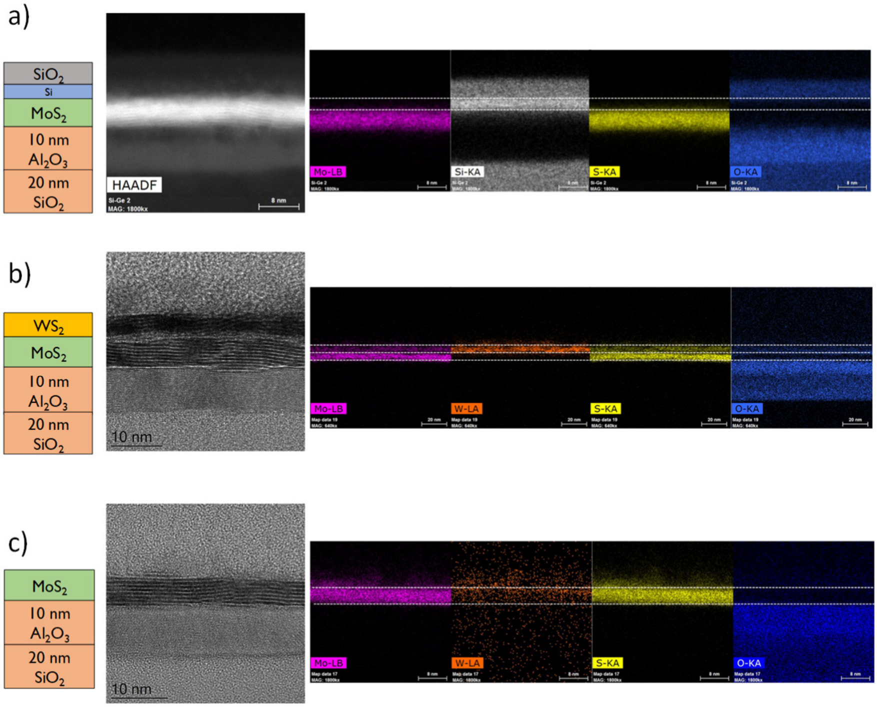

Figure 6-16: TEM cross-section images showing a) the heterostack with the elemental Si and the SiO_2 hardmask; b) the region which was covered during ALEt by the hardmask and then converted to W and sulfurized, and c) the MoS_2 from which the Si was etched by ALEt.

ALEt was studied and the selectivity and the damage towards underlying MoS_2 was characterized. Contrary to the Si removal, the ALEt impact onto the MoS_2 depends on the bias power applied during the removal step, with more MoS_2 removed at higher bias. Based on RBS observations, the layered structure of MoS_2, and the low energy required to create a sulfur vacancy, we conclude that the biased Ar plasma pulse removes previously chlorinated Mo and simultaneously desulfurizes the next layer. The plasma's ion velocity distributions indicated that the applied bias regime contains high energetic ions which cause the desulfurization of the top surface MoS_2 layer. Further research should focus on the study of bias regimes with low, sharp ion velocity distributions located around 10 eV, and their propensity to remove chlorinated layers. In the present case, despite using a low-bias process with high ALEt synergy, it is necessary to design the Si/MoS_2 stack with multilayers, considering the topmost layer as sacrificial, since it is damaged during the etch stop. Further work will focus on optimizing and widening the applicable Si ALEt window, the optimization of the residual-free hardmask removal, and the in-situ restoration of sulfur bonds to provide an optimal interface quality.

Acknowledgment

This work was supported throughout a strategic fundamental research grant for M.H. by the agency Flanders innovation & entrepreneurship (VLAIO). The authors thank T. Nuytten for the Raman characterization, H. Bender for the TEM analysis, A. Franquet for the AES measurements, and T. Conard for the XPS characterization.

The research leading to these results has received funding from the European Union's Seventh Framework Program SNM (Single Nanometer Manufacturing) project under grant agreement no. 318804.

6.3 Recent advances in the field

Regarding the WS_2 deposition from WF_6 there are no recent publications from other groups. Up to now, only imec uses recently WF_6 in combination with H_2S. In addition, routes including H_2 plasma as reducing agent to deposit in ALD fashion and self-limiting surface reactions on Al_2O_3 were explored.[70,72,375]

The field of ALEt is quickly growing and also the layer-by-layer etch of MX_2 and other materials is advancing.[111,118,119] Obviously, the Si etching shown here with an etch rate of 7 Å/cycle is larger than a Si monolayer per cycle due to the non-idealities of this ALEt process. This includes the non-ideal separation of the ALEt steps. Even though the gas supply was brought close to the chamber with fast switching valves, the conventional chamber design comprises a large volume and hence, the effects of the ALEt steps could be partially overlapping. For examples, residual Cl_2 could be still present during the removal step in which the bias is applied resulting in a contribution of reactive ion etching. To improve this, a compact chamber design with fast gas exchange would be necessary. Furthermore, during the adsorption step, the Cl_2 and Ar is ionized and could already impact the surface with the ion energy corresponding to the self-bias. Ideally, the species should be created remotely or separated by ion filters from the sample surface during the adsorption step. Possibly, the layer-by-layer removal could be also reached by decreasing the sputter yield using another inert gas, taking the sputter yield of the element to be etched into account. Another possibility for modifying the ion velocity distribution could be frequency tuning.

In addition, the ALEt of Al_2O_3 and HfO_2 are opening new possibilities for device integration with contacts on top of the MX_2 or to open area for a selective deposition of a heterostructure in a patterned high-k material layer.[376,377]

7 Conclusions

This thesis discusses the growth, patterning, and integration of 2D materials with thermal conversion processes and plasma-based atomic layer etching, which are scalable and can be done on wafer level to process many devices in parallel.

The sulfurization of a metal or metal-oxide can be used to grow TMD films of arbitrary thickness, despite single layers questionable due to limited control in the precursor deposition and concerns about layer closure. The sulfurization of a MoO_3 begins at a low temperature of 450 °C in contrast to WO_3, requiring a higher temperature to be converted. The first step in the chalcogenide formation is the oxygen-sulfur exchange, which is accompanied by volume expansion. This is followed by the second step, the recrystallization the TMD. Coherent TMD films delaminate locally during the cool-down from the high growth temperature. The sulfurization to stoichiometric TMD can proceed already at 450 °C, but the crystallization for high-quality films requires higher temperatures. The quality of the TMD films is a function of the annealing temperature and the annealing time. Large grains with an annealing time in the range of a few minutes require temperatures of 800 °C and above, hence it must have large E_A. However, such a temperature cannot be used for the co-integration with other materials, especially in conjunction with the corrosive H_2S as sulfurization gas, since it attacks substrates and hardware components. We found that the films made by this technique on an amorphous or polycrystalline substrate result only in polycrystalline grains of a few tens of nanometer length with random orientation. This relatively small grain size and their undirected orientation in comparison to large area single layer triangles will be detrimental for their electrical properties. The substrate or at least the buffer layer must be stable in the hot temperature regime around 1000 °C and in sulfur-containing atmosphere, which is needed to avoid sulfur loss in the films during the crystallization.

The grain boundaries cannot be controlled and are not avoidable over a continuous film over large areas. Therefore, the selective conversion can be attractive to control the crystals' locations. Arbitrarily shaped layered films can be fabricated by the pre-patterning of silicon and the conversion of this layer to a stoichiometric WS_2. A crystal in the defined shape can be obtained by the subsequent recrystallization. In this approach the crystal size is tailored to the device size, which can be an advantage. This deposited shape can serve also as a seed for lateral growth. The recrystallization in either sulfur-rich or sulfur-free atmosphere will start from a stoichiometric MX_2 film, which can be an advantage. Hence, there will be no volume expansion due to oxygen-sulfur exchange reaction or further sulfurization of metallic atoms. Such process starting from material containing sulfur already in combination with the nano-patterning will be less prone to strain-related delamination in contrast to its large-area continuous layer. Another important advantage is the control over the location of the film growth. Previous existing selective methods are always based either on a seed or step edge from which the crystal starts growing. Consequently, the seed as a particle remains in the center of the grain or the structure will be disturbed by substrate steps. Our approach circumvents this disadvantage by the lithographic pre-patterning of the reducing agent's film and offers high flexibility. Especially, the WS_2 investigated here is interesting, because WS_2 required the higher temperature during sulfurization. The stronger metal-oxygen bond in WO_3 causes also higher melting points in WO_3 and requires higher sulfurization temperatures than in MoO_3. Hence, the growth through the metal deposition with the in-situ sulfurization proceeding at a low temperature of 450 °C can form thin stoichiometric films up to four layers. Eventually, the advantage of the transfer-free approach should be pointed out. Even though templated-growth with subsequent transfer offers the best material for research purposes, the wrinkle-free transfer challenge being necessary for large scale integration is avoided with this direct growth approach.

The crystalline quality of the TMD devices is related to the crystallization temperature. The recrystallization of stoichiometric WS_2 in inert gas atmosphere was investigated with the result, that above 900 °C, sulfur loss occurs. These vacancies are filled with oxygen from atmosphere upon air exposure and result in sub-stoichiometric films. Long recrystallization durations and ultra-high temperature annealing are required for excellent TMD quality, but they are in contradiction with sulfur loss in sulfur-deficient atmosphere. To lower the time-impact and to maximize the energy for the recrystallization in the film, excimer laser annealing was tested with a pulse in the range of hundreds of nanoseconds. Simultaneous results to the ones after RTA were observed: with the increase in energy density of the laser pulse, the film recrystallizes, but simultaneously it is accompanied by sulfur loss. Hence, neither RTA nor ELA were appropriate to recrystallize exposed WS_2 films without degradation in inert atmosphere. Two paths were found to enable the recrystallization in inert gas atmosphere. An additional promoter lowers the recrystallization temperature. Co is appropriate to reduce the recrystallization temperature and is immiscible with WS_2. The element Co donates electrons to the metal atoms at the edges of the Van-der-Waals sheets and weakens the sulfur bonds, allowing their increased mobility. Large crystals could be already obtained at 700 °C, facilitating the co-integration with other materials. Ni as crystallization promoting metal does not work at those temperatures, since it forms already alloys at temperatures below 700 °C.

Furthermore, the sulfur-loss during the thermal treatment can be avoided by use of a dielectric capping layer. In this work, low-temperature SiO_2 from a PECVD process with low deposition rate was chosen. Despite the fact, that the PECVD process itself introduces damage of a monolayer sulfur loss, no further degradation after annealing at even 1000 °C was observed. Hence, a capping layer prevents the sulfur loss and confines the TMD volume within the substrate and the capping layer itself. Upon the high-temperature annealing, the sulfur amount was maintained, the TMD-related Raman modes intensified, and the ratio between those in-plane vibrational modes and the defect-related longitudinal acoustic LA(M) modes minimized. In addition, photoluminescence as a high-quality indicator emerged. This capped annealing can be achieved on wafer-level with currently existing CMOS-compatible techniques.

Up to now, the fabrication of patterned 2D crystals on a dielectric substrate was described. However, for the combination of two materials on top of each other, individual shaping will be required for each layer to contact them. To this end, we proposed the patterning of the Si layer acting as reducing agent for the WS_2 deposition on top of MoS_2. To achieve this goal with a plasma-based technique, a low-damaging process is necessary maintain the bottom MoS_2. In this work, atomic layer etching was evaluated for this purpose. ALEt can etch Si with a reproducible rate of 7 Å per cycle, whereas the removal rate of MoS_2 was only half this value. During ALEt, the reactant supply and the removal step are separated to minimize the synergy between the reaction with the solid and ion bombardment. The ALEt in its current configuration is not able to stop with infinite selectivity on the MoS_2 itself, but at least the removal can be repeatably controlled. In any case, the surface of the MoS_2 itself was already damaged through the ALEt removal step with its applied bias of 33 V. Eventually, the damage confined to one monolayer at the top can be acceptable when a multilayer system is used, and this one layer can be sacrificed and removed eventually in a simple cleaning step. The ion energies used here reveal already a bimodal distribution with a high and low energy peak. For lower bias energies in the ALEt's removal step, the distribution becomes unimodal and approaches the 10 eV peak being representative for the self-bias case. The damage was restricted to the topmost layer and it was possible to convert the ALEt patterned Si on MoS_2 into a 2D heterostack with patterned WS_2 on MoS_2.

We demonstrated that it is possible to integrate two TMDs on top of each other with individual shaping by large-area deposition, etching, deposition and patterning of another sacrificial material by atomic layer etching, and conversion of the same. It was also shown that the quality can be improved by annealing strategies with additional promoting layers. Several points need to receive special attention in order to improve crystal quality further: the substrate is crucial for the orientation of the crystals. For continuous films it is necessary that the grains can merge, and this requires substrates with a hexagonal lattice structure on which the films grow epitaxially. We demonstrated here that on polycrystalline substrates, only polycrystalline grains can be obtained. Furthermore, it is necessary to avoid the sulfur loss from the layers during the processing, which requires always the use of sulfur-containing environment during treatment or the encapsulation to avoid sulfur-loss during detrimental processing. Eventually, partially damaged surface layers being oxidized in air, could be also selectively removed, but for this enough dummy layers must be considered in the design. The sensitivity of the 2D layers show that the treatment with low-energetic plasmas is the only path to meet the requirements to integrate heterostacks of TMDs in nanoscale devices.

The investigated techniques can now eventually be used for a device flow. The large area sulfurization of a starting layer is promising – to maximize the quality including grain orientation towards each other, single crystalline substrates with hexagonal lattice should be used such as sapphire, BN, or SiC. This first layer should be sulfurized. Then, a sacrificial Si layer must be deposited on top should be patterned by ALEt and converted into a second TMD. The quality of the second TMD must be also improved, e.g. by another high temperature anneal in sulfur-rich atmosphere, with a capping layer preventing sulfur loss, or eventually with a crystallization promoting metal, which could be integrated directly in the contact regions. Since the second TMD is already on a first TMD with hexagonal lattice, the epitaxial recrystallization is facilitated.

8 Future research

The high-quality growth of 2D materials and its CMOS-compatible integration with plasma-based techniques was investigated in this work. However, further improvements can be made to increase the quality further and build devices with less defectivity. The grown material should be electrically characterized in a next step and the approaches for top-down growth with growth and etching should be compared to the selective growth presented here. To this end, the built structures need to be contacted with a metal and gated to determine the electrical properties and correlate them with the processing parameters.

For both presented growth approaches, more efforts will be needed in the substrate preparation to eliminate detrimental grain boundary impact. Undoubtedly, this work has shown only approaches yielding polycrystalline material with small grains and manifold crystal orientations. It has been shown that the high temperature annealing is essential, and that sulfur loss must be minimized. Nonetheless, for good conduction over several grains, they need to be aligned to each other. In order to obtain at least oriented crystals, a monocrystalline substrate would be beneficial. Grains would merge and the charge carrier transport over the grain boundaries would be better than in non-aligned grains. The charge carrier mobility would be increased, and the device performance variations would decrease. Hence, the study of the presented flow on monocrystalline substrate should be targeted. An interesting alternative approach could be the preparation of monocrystalline buffer layers, which are described in literature and demonstrated for other hexagonal materials such as ZnO, GaN, mica-like, or $SrTiO_3$.[378–380] The TMD crystal growth on such buffer layers is highly interesting and would be a strong advantage, because possibly the integration on a silicon substrate with buffer layers could be imagined. A smooth and monocrystalline substrate will be the key for high-quality 2D layers. The selective conversion concept Si-to-WS_2 can be also applied to other material systems based on volatile metal-halides and chalcogenide-precursors and would offer also a variety of other TMDs.

The base for recrystallizing MX_2 films into decent quality crystals was established with the described techniques in this thesis. Further investigation will be necessary to optimize the investigated effects for the application – for the metal induced crystallization, more controllability about the promoter-metal diffusion and the MX_2 crystal formation would be desired. The system should be designed in a way, that the separated Co will agglomerate in a region, which is outside the active area and where it could be removed e.g. by wet etching without affecting the MX_2 semiconductor.

The dielectric capped annealing is also promising. By confining the heat and the sulfur in a kind of nanoreactor under the dielectric capping layer, the detrimental sulfur vacancy creation can be suppressed to a large extent. The dielectric deposition can be tuned further towards a low damage to maintain full stoichiometry prior to annealing. Eventually, the combination with ELA for substrates with low thermal budget can be enabled with such a dielectric capping layer. The future questions to be addressed for this topic is the minimization of the damage introduced by the capping layer deposition. Low-temperature PEALD could be a viable candidate or eventually damage-less evaporation processes could minimize this damage. More characterization of the recrystallized layers is necessary besides the proven excellent quality with spectroscopic techniques: the structure of the film by means of TEM with the estimation of the grain size and eventually the electrical characterization of the films are still open items. The electrical characterization itself needs a systematic study, whether top contacts or side contacts fabricated with plasma-based techniques could be used and their impact on the device performance must be found. For benchmarking of the 2D films, a stable characterization flow is inevitable.

The investigated plasma-based techniques could provide an appropriate tool to fabricate such devices. With the atomic layer etching, the repeatable removal rate and even poor selectivity can be used. Nevertheless, within the investigated plasma bias window during the removal step, still a top surface damage of the sulfur layer was seen. Eventually, the remaining question is, whether the ion energy could be reduced further to minimize the sulfur vacancy formation and to still etch Si with a reasonable rate. So, the threshold energy for the Si removal and for the sulfur monolayer removal should be experimentally verified. Eventually, the patterning of the bottom MX_2 layer in addition to the top one with the subsequent contacting to form real artificially grown MX_2 heterostructures should be realized. Those can be used to benchmark the devices to the ones fabricated by mechanical exfoliation and stacking and could be used to optimize the integration flow to make transfer-free devices on wafer level.

We believe that we found with the investigated growth and plasma-patterning techniques important tools to bring 2D materials from the purely fundamental property investigation to an applied research level, which could be a path for future large-scale integration of 2D materials.

References

[1] G. E. Moore, *IEEE Solid-State Circuits Soc. Newsl.* **2006**, *11*, 37.

[2] R. R. Troutman, *IEEE Trans. Electron Devices* **1979**, *26*, 461.

[3] K. Roy, S. Mukhopadhyay, H. Mahmoodi-Meimand, *Proc. IEEE* **2003**, *91*, 305.

[4] M. M. Mirza, F. J. Schupp, J. A. Mol, D. A. MacLaren, G. A. D. Briggs, D. J. Paul, *Sci. Rep.* **2017**, *7*, 3004.

[5] B. Radisavljevic, A. Radenovic, J. Brivio, V. Giacometti, A. Kis, *Nat. Nanotechnol.* **2011**, *6*, 147.

[6] H. Liu, A. T. Neal, P. D. Ye, *ACS Nano* **2012**, *6*, 8563.

[7] Y. Liu, N. O. Weiss, X. Duan, H.-C. Cheng, Y. Huang, X. Duan, *Nat. Rev. Mater.* **2016**, *1*, 16042.

[8] W. Zhao, R. M. Ribeiro, M. Toh, A. Carvalho, C. Kloc, A. H. Castro Neto, G. Eda, *Nano Lett.* **2013**, *13*, 5627.

[9] R. H. Dennard, F. H. Gaensslen, Hwa-Nien Yu, V. L. Rideout, E. Bassous, A. R. Leblanc, *Proc. IEEE* **1999**, *87*, 668.

[10] S. V. Morozov, K. S. Novoselov, M. I. Katsnelson, F. Schedin, D. C. Elias, J. A. Jaszczak, A. K. Geim, *Phys. Rev. Lett.* **2008**, *100*, 016602.

[11] Y. Yamada-Takamura, R. Friedlein, *Sci. Technol. Adv. Mater.* **2014**, *15*, 64404.

[12] K. S. Novoselov, A. Mishchenko, A. Carvalho, A. H. Castro Neto, *Science* **2016**, *353*, aac9439.

[13] M. Chhowalla, H. S. Shin, G. Eda, L.-J. Li, K. P. Loh, H. Zhang, *Nat. Chem.* **2013**, *5*, 263.

[14] H. Li, Z. Yin, Q. He, H. Li, X. Huang, G. Lu, D. W. H. Fam, A. I. Y. Tok, Q. Zhang, H. Zhang, *Small* **2012**, *8*, 63.

[15] J. Brivio, D. T. L. Alexander, A. Kis, *Nano Lett.* **2011**, *11*, 5148.

[16] K. S. Novoselov, D. Jiang, F. Schedin, T. J. Booth, V. V Khotkevich, S. V Morozov, A. K. Geim, *Proc. Natl. Acad. Sci.* **2005**, *102*, 10451.

[17] K. S. Novoselov, A. K. Geim, S. V. Morozov, D. Jiang, Y. Zhang, S. V. Dubonos, I. V. Grigorieva, A. A. Firsov, *Science* **2004**, *306*, 666.

[18] A. Jain, P. Bharadwaj, S. Heeg, M. Parzefall, T. Taniguchi, K. Watanabe, L. Novotny, *Nanotechnology* **2018**, *29*, 265203.

[19] S. Tongay, W. Fan, J. Kang, J. Park, U. Koldemir, J. Suh, D. S. Narang, K. Liu, J. Ji, J. Li, R. Sinclair, J. Wu, *Nano Lett.* **2014**, *14*, 3185.

[20] J. N. Coleman, M. Lotya, A. O'Neill, S. D. Bergin, P. J. King, U. Khan, K. Young, A. Gaucher, S. De, R. J. Smith, I. V Shvets, S. K. Arora, G. Stanton, H.-Y. Kim, K. Lee, G. T. Kim, G. S. Duesberg,

T. Hallam, J. J. Boland, J. J. Wang, J. F. Donegan, J. C. Grunlan, G. Moriarty, A. Shmeliov, R. J. Nicholls, J. M. Perkins, E. M. Grieveson, K. Theuwissen, D. W. McComb, P. D. Nellist, V. Nicolosi, *Science* **2011**, *331*, 568.

[21] D. Yang, S. J. Sandoval, W. M. R. Divigalpitiya, J. C. Irwin, R. F. Frindt, *Phys. Rev. B* **1991**, *43*, 12053.

[22] D. Hu, G. Xu, L. Xing, X. Yan, J. Wang, J. Zheng, Z. Lu, P. Wang, X. Pan, L. Jiao, *Angew. Chemie* **2017**, *129*, 3665.

[23] J. B. Legma, G. Vacquier, A. Casalot, *J. Cryst. Growth* **1993**, *130*, 253.

[24] H. Schäfer, in *Festschrift Für Leo Brand. Zum 60. Geburtstag*, VS Verlag Für Sozialwissenschaften, Wiesbaden, **1968**, pp. 91–104.

[25] M. Binnewies, R. Glaum, M. Schmidt, P. Schmidt, *Zeitschrift für Anorg. und Allg. Chemie* **2013**, *639*, 219.

[26] A. Pisoni, J. Jacimovic, O. S. Barišić, A. Walter, B. Náfrádi, P. Bugnon, A. Magrez, H. Berger, Z. Revay, L. Forró, *J. Phys. Chem. C* **2015**, *119*, 3918.

[27] N. Imanishi, K. Kanamura, Z. Takehara, *J. Electrochem. Soc.* **1992**, *139*, 2082.

[28] W. Y. Lee, T. M. Besmann, M. W. Stott, *J. Mater. Res.* **1994**, *9*, 1474.

[29] I. Endler, A. Leonhardt, U. König, H. van den Berg, W. Pitschke, V. Sottke, *Surf. Coatings Technol.* **1999**, *120–121*, 482.

[30] X.-L. Li, J.-P. Ge, Y.-D. Li, *Chem. - A Eur. J.* **2004**, *10*, 6163.

[31] R. Wei, H. Yang, K. Du, W. Fu, M. Li, Q. Yu, L. Chang, Y. Zeng, Y. Sui, H. Zhu, G. Zou, *Mater. Sci. Eng. B Solid-State Mater. Adv. Technol.* **2007**, *138*, 259.

[32] I. Jahangir, G. Koley, M. V. S. Chandrashekhar, *Appl. Phys. Lett.* **2017**, *110*, 182108.

[33] W. Wu, D. De, S.-C. Chang, Y. Wang, H. Peng, J. Bao, S.-S. Pei, *Appl. Phys. Lett.* **2013**, *102*, 142106.

[34] Y. Cheng, K. Yao, Y. Yang, L. Li, Y. Yao, Q. Wang, X. Zhang, Y. Han, U. Schwingenschlögl, *RSC Adv.* **2013**, *3*, 17287.

[35] Y.-H. Lee, X.-Q. Zhang, W. Zhang, M.-T. Chang, C.-T. Lin, K.-D. Chang, Y.-C. Yu, J. T.-W. Wang, C.-S. Chang, L.-J. Li, T.-W. Lin, *Adv. Mater.* **2012**, *24*, 2320.

[36] H. Wang, L. Yu, Y.-H. Lee, W. Fang, A. Hsu, P. Herring, M. Chin, M. Dubey, L.-J. Li, J. Kong, T. Palacios, in *2012 Int. Electron Devices Meet.*, IEEE, **2012**, pp. 4.6.1-4.6.4.

[37] Y.-H. H. Lee, L. Yu, H. Wang, W. Fang, X. Ling, Y. Shi, C.-T. Te Lin, J.-K. K. Huang, M.-T. T. Chang, C.-S. S. Chang, M. Dresselhaus, T. Palacios, L.-J. J. Li, J. Kong, *Nano Lett.* **2013**, *13*, 1852.

[38] X. Ling, Y.-H. Lee, Y. Lin, W. Fang, L. Yu, M. S. Dresselhaus, J. Kong, *Nano Lett.* **2014**, *14*, 464.

[39] B. J. Modtland, E. Navarro-Moratalla, X. Ji, M. Baldo, J. Kong, *Small* **2017**, *13*, 1.

[40] J. Song, G. Hee Ryu, Y. Kim, W. Je Woo, K. Yong Ko, Y. Kim, C. Lee, I. Oh, J. Park, Z. Lee, H. Kim, *Nanotechnology* **2017**, *28*, 465103.

[41] H. Kim, D. Ovchinnikov, D. Deiana, D. Unuchek, A. Kis, *Nano Lett.* **2017**, *17*, acs. nanolett.7b02311.

[42] X. Dong, C. Yan, D. Tomer, C. H. Li, L. Li, *Appl. Phys. Lett.* **2016**, *109*, 051604.

[43] C. Ahn, J. Lee, H.-U. Kim, H. Bark, M. Jeon, G. H. Ryu, Z. Lee, G. Y. Yeom, K. Kim, J. Jung, Y. Kim, C. Lee, T. Kim, *Adv. Mater.* **2015**, *27*, 5223.

[44] S. M. Eichfeld, L. Hossain, Y.-C. Lin, A. F. Piasecki, B. Kupp, A. G. Birdwell, R. A. Burke, N. Lu, X. Peng, J. Li, A. Azcatl, S. McDonnell, R. M. Wallace, M. J. Kim, T. S. Mayer, J. M. Redwing, J. A. Robinson, *ACS Nano* **2015**, *9*, 2080.

[45] S. Cwik, D. Mitoraj, O. Mendoza Reyes, D. Rogalla, D. Peeters, J. Kim, H. M. Schütz, C. Bock, R. Beranek, A. Devi, *Adv. Mater. Interfaces* **2018**, *5*, 1800140.

[46] K. Kang, S. Xie, L. Huang, Y. Han, P. Y. Huang, K. F. Mak, C.-J. Kim, D. Muller, J. Park, *Nature* **2015**, *520*, 656.

[47] B. Kalanyan, W. A. Kimes, R. Beams, S. J. Stranick, E. Garratt, I. Kalish, A. V. Davydov, R. K. Kanjolia, J. E. Maslar, *Chem. Mater.* **2017**, *29*, 6279.

[48] F. Maury, *Le J. Phys. IV* **1995**, *05*, C5.

[49] T. Kim, J. Mun, H. Park, D. Joung, M. Diware, C. Won, J. Park, S.-H. Jeong, S.-W. Kang, *Nanotechnology* **2017**, *28*, 18LT01.

[50] Y. Zhao, J.-G. Song, G. H. Ryu, K. Y. Ko, W. J. Woo, Y. Kim, D. Kim, J. H. Lim, S. Lee, Z. Lee, J. Park, H. Kim, *Nanoscale* **2018**, *10*, 9338.

[51] Y.-C. Lin, W. Zhang, J.-K. Huang, K.-K. Liu, Y.-H. Lee, C.-T. Liang, C.-W. Chu, L.-J. Li, *Nanoscale* **2012**, *4*, 6637.

[52] X. Wang, H. Feng, Y. Wu, L. Jiao, *J. Am. Chem. Soc.* **2013**, *135*, 5304.

[53] Y. Zhan, Z. Liu, S. Najmaei, P. M. Ajayan, J. Lou, *Small* **2012**, *8*, 966.

[54] T. K. Oh, H. Ju, H. Jeon, J. K. Lee, *Appl. Phys. Lett.* **2016**, *109*, DOI 10.1063/1.4971386.

[55] T. W. Scharf, D. R. Diercks, B. P. Gorman, S. V. Prasad, M. T. Dugger, *Tribol. Trans.* **2009**, *52*, 284.

[56] J. M. Jungk, M. T. Dugger, S. M. George, S. V. Prasad, R. K. Grubbs,

N. R. Moody, T. M. Mayer, T. W. Scharf, R. S. Goeke, W. W. Gerberich, *LDRD Project 52523 Final Report :Atomic Layer Deposition of Highly Conformal Tribological Coatings*, Albuquerque, NM, and Livermore, CA (United States), **2005**.

[57] T. Scharf, S. Prasad, M. Dugger, P. Kotula, R. Goeke, R. Grubbs, *Acta Mater.* **2006**, *54*, 4731.

[58] Y. Jang, S. Yeo, H.-B.-R. Lee, H. Kim, S.-H. Kim, *Appl. Surf. Sci.* **2016**, *365*, 160.

[59] L. K. Tan, B. Liu, J. H. Teng, S. Guo, H. Y. Low, K. P. Loh, *Nanoscale* **2014**, *6*, 10584.

[60] A. Valdivia, D. J. Tweet, J. F. Conley, *J. Vac. Sci. Technol. A Vacuum, Surfaces, Film.* **2016**, *34*, 021515.

[61] L. K. Tan, B. Liu, J. H. Teng, S. Guo, H. Y. Low, K. P. Loh, *Nanoscale* **2014**, *6*, 10584.

[62] Z. Jin, S. Shin, D. H. Kwon, S.-J. Han, Y.-S. Min, *Nanoscale* **2014**, *6*, 14453.

[63] J. G. Song, J. Park, W. Lee, T. Choi, H. Jung, C. W. Lee, S. H. Hwang, J. M. Myoung, J. H. Jung, S.-H. H. Kim, C. Lansalot-Matras, H. Kim, *ACS Nano* **2013**, *7*, 11333.

[64] C. Martella, P. Melloni, E. Cinquanta, E. Cianci, M. Alia, M. Longo, A. Lamperti, S. Vangelista, M. Fanciulli, A. Molle, *Adv. Electron. Mater.* **2016**, *2*, 1600330.

[65] W. Zeng, L.-P. Feng, J. Su, H. Pan, Z.-T. Liu, *J. Alloys Compd.* **2018**, *745*, 834.

[66] J. J. Pyeon, S. K. S. H. Kim, D. S. Jeong, S.-H. Baek, C.-Y. Kang, J.-S. Kim, S. K. S. H. Kim, *Nanoscale* **2016**, *8*, 10792.

[67] Y. Kim, J. G. Song, Y. J. Park, G. H. Ryu, S. J. Lee, J. S. Kim, P. J. Jeon, C. W. Lee, W. J. Woo, T. Choi, H. Jung, H. B. R. Lee, J. M. Myoung, S. Im, Z. Lee, J. H. Ahn, J. Park, H. Kim, *Sci. Rep.* **2016**, *6*, 1.

[68] T. Jurca, M. J. Moody, A. Henning, J. D. Emery, B. Wang, J. M. Tan, T. L. Lohr, L. J. Lauhon, T. J. Marks, *Angew. Chemie Int. Ed.* **2017**, *56*, 4991.

[69] W. Jeon, Y. Cho, S. Jo, J. H. Ahn, S. J. Jeong, *Adv. Mater.* **2017**, *29*, 1.

[70] B. Groven, A. N. Mehta, H. Bender, Q. Smets, J. Meersschaut, A. Franquet, T. Conard, T. Nuytten, P. Verdonck, W. Vandervorst, M. Heyns, I. Radu, M. Caymax, A. Delabie, *J. Vac. Sci. Technol. A Vacuum, Surfaces, Film.* **2018**, *36*, 01A105.

[71] B. Groven, M. Heyne, A. Nalin Mehta, H. Bender, T. Nuytten, J. Meersschaut, T. Conard, P. Verdonck, S. Van Elshocht, W. Vandervorst, S. De Gendt, M. Heyns, I. Radu, M. Caymax, A. Delabie, *Chem. Mater.* **2017**, *29*, 2927.

[72] B. Groven, A. Nalin Mehta, H. Bender, J. Meersschaut, T. Nuytten, P. Verdonck, T. Conard, Q. Smets, T. Schram, B. Schoenaers, A. Stesmans, V. Afanas'ev, W. Vandervorst, M. Heyns, M. Caymax, I. Radu, A. Delabie, *Chem. Mater.* **2018**, *30*, 7648.

[73] A. Sharma, M. A. Verheijen, L. Wu, S. Karwal, V. Vandalon, H. C. M. Knoops, R. S. Sundaram, J. P. Hofmann, W. M. M. Kessels, A. A. Bol, *Nanoscale* **2018**, *10*, 8615.

[74] G. H. Han, N. J. Kybert, C. H. Naylor, B. S. Lee, J. Ping, J. H. Park, J. Kang, S. Y. Lee, Y. H. Lee, R. Agarwal, A. T. C. Johnson, *Nat. Commun.* **2015**, *6*, 6128.

[75] B. M. B. M. Bersch, S. M. S. M. Eichfeld, Y.-C. Lin, K. Zhang, G. R. G. R. Bhimanapati, A. F. A. F. Piasecki, M. Labella, J. A. J. A. Robinson, *2D Mater.* **2017**, *4*, 025083.

[76] H. Li, P. Li, J. K. Huang, M. Y. Li, C. W. Yang, Y. Shi, X. X. Zhang, L. J. Li, *ACS Nano* **2016**, *10*, 10516.

[77] F. Lu, A. Karmakar, S. Shahi, E. Einarsson, *RSC Adv.* **2017**, *7*, 37310.

[78] D. Sun, A. E. Nguyen, D. Barroso, X. Zhang, E. Preciado, S. Bobek, V. Klee, J. Mann, L. Bartels, *2D Mater.* **2015**, *2*, 045014.

[79] H.-J. Kim, H. Kim, S. Yang, J.-Y. Kwon, *Small* **2017**, *13*, 1702256.

[80] X. Chen, Y. J. Park, T. Das, H. Jang, J.-B. Lee, J.-H. Ahn, *Nanoscale* **2016**, *8*, 15181.

[81] T. Afaneh, P. K. Sahoo, I. A. P. Nobrega, Y. Xin, H. R. Gutiérrez, *Adv. Funct. Mater.* **2018**, *1802949*, 1.

[82] P. K. Sahoo, S. Memaran, Y. Xin, L. Balicas, H. R. Gutiérrez, *Nature* **2018**, *553*, 63.

[83] D. Dumcenco, D. Ovchinnikov, K. Marinov, A. Kis, in *2016 46th Eur. Solid-State Device Res. Conf.*, IEEE, **2016**, pp. 284–286.

[84] L. Chen, B. Liu, M. Ge, Y. Ma, A. N. Abbas, C. Zhou, *ACS Nano* **2015**, *9*, 8368.

[85] M. R. Laskar, L. Ma, S. Kannappan, P. Sung Park, S. Krishnamoorthy, D. N. Nath, W. Lu, Y. Wu, S. Rajan, *Appl. Phys. Lett.* **2013**, *102*, 252108.

[86] Q. Ji, Y. Zhang, Y. Zhang, Z. Liu, *Chem. Soc. Rev.* **2015**, *44*, 2587.

[87] Y. Zhang, Y. Zhang, Q. Ji, J. Ju, H. Yuan, J. Shi, T. Gao, D. Ma, M. Liu, Y. Chen, X. Song, H. Y. Hwang, Y. Cui, Z. Liu, *ACS Nano* **2013**, *7*, 8963.

[88] G. W. Shim, K. Yoo, S.-B. Seo, J. Shin, D. Y. Jung, I.-S. Kang, C. W. Ahn, B. J. Cho, S.-Y. Choi, *ACS Nano* **2014**, *8*, 6655.

[89] D. Dumcenco, D. Ovchinnikov, K. Marinov, P. Lazić, M. Gibertini, N. Marzari, O. L. Sanchez, Y.-C. Kung, D. Krasnozhon, M.-W. Chen, S. Bertolazzi, P. Gillet, A. Fontcuberta i Morral, A. Radenovic, A. Kis, *ACS Nano* **2015**, *9*, 4611.

[90] J. Zhu, H. Xu, G. Zou, W. Zhang, R. Chai, J. Choi, J. Wu, H. Liu, G. Shen, H. Fan, *J. Am. Chem. Soc.* **2019**, *141*, 5392.

[91] Y. Yue, J. Chen, Y. Zhang, S. Ding, F. Zhao, Y. Wang, D. Zhang, R. Li, H. Dong, W. Hu, Y. Feng, W. Feng, *ACS Appl. Mater. Interfaces* **2018**, *10*, 22435.

[92] P. Chen, W. Xu, Y. Gao, J. H. Warner, M. R. Castell, *ACS Appl. Nano Mater.* **2018**, *1*, 6976.

[93] S. M. Poh, X. Zhao, S. J. R. Tan, D. Fu, W. Fei, L. Chu, D. Jiadong, W. Zhou, S. J. Pennycook, A. H. Castro Neto, K. P. Loh, *ACS Nano* **2018**, *12*, 7562.

[94] M. Marx, A. Grundmann, Y.-R. Lin, D. Andrzejewski, T. Kümmell, G. Bacher, M. Heuken, H. Kalisch, A. Vescan, *J. Electron. Mater.* **2018**, *47*, 910.

[95] T. W. Scharf, S. V. Prasad, T. M. Mayer, R. S. Goeke, M. T. Dugger, *J. Mater. Res.* **2004**, *19*, 3443.

[96] S. Das, H.-Y. Chen, A. V. Penumatcha, J. Appenzeller, *Nano Lett.* **2012**, *13*, 100.

[97] K.-K. K. Liu, Y.-H. H. Lee, Y.-C. C. Lin, J.-K. K. Huang, X.-Q. Zhang, T.-W. Lin, L.-J. J. Li, *ECS Trans.* **2012**, *50*, 61.

[98] K. Matsuura, T. Ohashi, I. Muneta, S. Ishihara, K. Kakushima, K. Tsutsui, A. Ogura, H. Wakabayashi, *J. Electron. Mater.* **2018**, *47*, 3497.

[99] R. Ionescu, A. George, I. Ruiz, Z. Favors, Z. Mutlu, C. Liu, K. Ahmed, R. Wu, J. S. Jeong, L. Zavala, K. A. Mkhoyan, M. Ozkan, C. S. Ozkan, *Chem. Commun.* **2014**, *50*, 11226.

[100] Y. Huang, J. Wu, X. Xu, Y. Ho, G. Ni, Q. Zou, G. K. W. Koon, W. Zhao, A. H. Castro Neto, G. Eda, C. Shen, B. Özyilmaz, *Nano Res.* **2013**, *6*, 200.

[101] G. G. D. Han, K.-H. Tu, F. Niroui, W. Xu, S. Zhou, X. Wang, V. Bulović, C. A. Ross, J. H. Warner, J. C. Grossman, *Adv. Funct. Mater.* **2017**, *27*, 1703688.

[102] D. Escalera-López, R. Griffin, M. Isaacs, K. Wilson, R. E. Palmer, N. V. Rees, *Appl. Mater. Today* **2018**, *11*, 70.

[103] H. Liu, J. Gu, P. D. Ye, *IEEE Electron Device Lett.* **2012**, *33*, 1273.

[104] Z. Cheng, K. Price, A. D. Franklin, in *2017 75th Annu. Device Res. Conf.*, IEEE, **2017**, pp. 1–2.

[105] T. Völkl, T. Rockinger, M. Drienovsky, K. Watanabe, T. Taniguchi, D. Weiss, J. Eroms, *Phys. Rev. B* **2017**, *96*, 125405.

[106] Y. Chai, R. Ionescu, S. Su, R. Lake, M. Ozkan, C. S. Ozkan, *Phys. Status Solidi Appl. Mater. Sci.* **2016**, *213*, 1358.

[107] Y. Chai, S. Su, D. Yan, M. Ozkan, R. Lake, C. S. Ozkan, *Sci. Rep.* **2017**, *7*, 1.

[108] C. H. Lee, E. W. Lee, W. McCulloch, Z. Jamal-Eddine, S.

Krishnamoorthy, M. J. Newburger, R. K. Kawakami, Y. Wu, S. Rajan, *Appl. Phys. Express* **2017**, *10*, DOI 10.7567/APEX.10.035201.

[109] M. H. Jeon, C. Ahn, H. Kim, K. N. Kim, T. Z. LiN, H. Qin, Y. Kim, S. Lee, T. Kim, G. Y. Yeom, *Nanotechnology* **2015**, *26*, 355706.

[110] S. Xiao, P. Xiao, X. Zhang, D. Yan, X. Gu, F. Qin, Z. Ni, Z. J. Han, K. (Ken) Ostrikov, *Sci. Rep.* **2016**, *6*, 19945.

[111] Y. Sha, S. Xiao, X. Zhang, F. Qin, X. Gu, *Appl. Surf. Sci.* **2017**, *411*, 182.

[112] Y. Liu, H. Nan, X. Wu, W. Pan, W. Wang, J. Bai, W. Zhao, L. Sun, X. Wang, Z. Ni, *ACS Nano* **2013**, *7*, 4202.

[113] K. Chen, T. Chu, C. Wu, S. Lee, S. Lin, *2D Mater.* **2017**, *4*, 034001.

[114] K. J. Kanarik, T. Lill, E. a. Hudson, S. Sriraman, S. Tan, J. Marks, V. Vahedi, R. A. Gottscho, *J. Vac. Sci. Technol. A Vacuum, Surfaces, Film.* **2015**, *33*, 020802.

[115] K. J. Kanarik, S. Tan, W. Yang, T. Kim, T. Lill, A. Kabansky, E. A. Hudson, T. Ohba, K. Nojiri, J. Yu, R. Wise, I. L. Berry, Y. Pan, J. Marks, R. A. Gottscho, *J. Vac. Sci. Technol. A Vacuum, Surfaces, Film.* **2017**, *35*, 05C302.

[116] K. J. Kanarik, S. Tan, R. A. Gottscho, *J. Phys. Chem. Lett.* **2018**, *9*, 4814.

[117] K. S. Kim, K. H. Kim, Y. Nam, J. Jeon, S. Yim, E. Singh, J. Y. Lee, S. J. Lee, Y. S. Jung, G. Y. Yeom, D. W. Kim, *ACS Appl. Mater. Interfaces* **2017**, *9*, 11967.

[118] T. Lin, B. Kang, M. Jeon, C. Huffman, J. Jeon, S. S. Lee, W. Han, J. Lee, S. S. Lee, G. Yeom, K. Kim, *ACS Appl. Mater. Interfaces* **2015**, *7*, 15892.

[119] E. Mercado, A. Goodyear, J. Moffat, M. Cooke, R. S. Sundaram, *J. Phys. D. Appl. Phys.* **2017**, *50*, 184005.

[120] A. Goodyear, M. Cooke, *J. Vac. Sci. Technol. A Vacuum, Surfaces, Film.* **2017**, *35*, 01A105.

[121] B. S. Lee, *J. Electrochem. Soc.* **1984**, *131*, 2998.

[122] J. M. Saleh, M. W. Roberts, C. Kemball, **1963**, *199*, 189.

[123] Unknown, ‘Understanding Character Tables of Symmetry Groups’, can be found under https://chem.libretexts.org/Bookshelves/Physical_and_Theoretical_Chemistry_Textbook_Maps/Supplemental_Modules_(Physical_and_Theoretical_Chemistry)/Group_Theory/Understanding_Character_Tables_of_Symmetry_Groups, **n.d.**

[124] H. Li, Q. Zhang, C. C. R. Yap, B. K. Tay, T. H. T. Edwin, A. Olivier, D. Baillargeat, *Adv. Funct. Mater.* **2012**, *22*, 1385.

[125] J. Meersschaut, W. Vandervorst, *Nucl. Instruments Methods Phys. Res. Sect. B Beam Interact. with Mater. Atoms* **2017**, *406*, 25.

[126] K. Alam, R. K. Lake, *IEEE Trans. Electron Devices* **2012**, *59*, 3250.

[127] R. Addou, S. McDonnell, D. Barrera, Z. Guo, A. Azcatl, J. Wang, H. Zhu, C. L. Hinkle, M. Quevedo-Lopez, H. N. Alshareef, L. Colombo, J. W. P. Hsu, R. M. Wallace, *ACS Nano* **2015**, *9*, 9124.

[128] R. Addou, L. Colombo, R. M. Wallace, *ACS Appl. Mater. Interfaces* **2015**, *7*, 11921.

[129] S. McDonnell, R. Addou, C. Buie, R. M. Wallace, C. L. Hinkle, *ACS Nano* **2014**, *8*, 2880.

[130] D. Sharma, M. Amani, A. Motayed, P. B. Shah, G. Birdwell, S. Najmaei, P. M. Ajayan, J. Lou, M. Dubey, Q. Li, A. V Davydov, *Nanotechnology* **2014**, *25*, 155702.

[131] W. Zhang, J.-K. Huang, C.-H. Chen, Y.-H. Chang, Y.-J. Cheng, L.-J. Li, *Adv. Mater.* **2013**, *25*, 3456.

[132] K. K. H. Smithe, C. D. English, S. V Suryavanshi, E. Pop, in *2015 73rd Annu. Device Res. Conf.*, IEEE, **2015**, pp. 239–240.

[133] G. Plechinger, J. Mann, E. Preciado, D. Barroso, A. Nguyen, J. Eroms, C. Schüller, L. Bartels, T. Korn, *Semicond. Sci. Technol.* **2014**, *29*, 064008.

[134] D. N. Nath, L. Ma, C. H. Lee, E. Lee, A. Arehart, Y. Wu, S. Rajan, in *72nd Device Res. Conf.*, IEEE, **2014**, pp. 89–90.

[135] H. Schmidt, S. Wang, L. Chu, M. Toh, R. Kumar, W. Zhao, A. H. C. Neto, J. Martin, S. Adam, B. Oezyilmaz, G. Eda, **2014**, 5.

[136] S. Ghosh, S. Najmaei, S. Kar, R. Vajtai, J. Lou, N. R. Pradhan, L. Balicas, P. M. Ajayan, S. Talapatra, *Phys. Rev. B* **2014**, *89*, 125422.

[137] Y. Lee, J. Lee, H. Bark, I.-K. Oh, G. H. Ryu, Z. Lee, H. Kim, J. H. Cho, J.-H. Ahn, C. Lee, *Nanoscale* **2014**, *6*, 2821.

[138] J. M. Wilson, *Surf. Sci.* **1975**, *53*, 330.

[139] Y. Shi, Y. Wan, R. Liu, B. Tu, D. Zhao, *J. Am. Chem. Soc.* **2007**, *129*, 9522.

[140] L. P. Hansen, E. Johnson, M. Brorson, S. Helveg, *J. Phys. Chem. C* **2014**, *118*, 22768.

[141] J. A. Miwa, M. Dendzik, S. S. Grønborg, M. Bianchi, J. V. Lauritsen, P. Hofmann, S. Ulstrup, *ACS Nano* **2015**, *9*, 6502.

[142] D.-W. Lee, J. Lee, I. Y. Sohn, B.-Y. Kim, Y. M. Son, H. Bark, J. Jung, M. Choi, T. H. Kim, C. Lee, N.-E. Lee, *Nano Res.* **2015**, *8*, 2340.

[143] I. Song, C. Park, M. Hong, J. Baik, H.-J. Shin, H. C. Choi, *Angew. Chemie Int. Ed.* **2014**, *53*, 1266.

[144] H. G. Füchtbauer, A. K. Tuxen, Z. Li, H. Topsøe, J. V. Lauritsen, F. Besenbacher, *Top. Catal.* **2014**, *57*, 207.

[145] Y.-C. Lin, R. K. Ghosh, R. Addou, N. Lu, S. M. Eichfeld, H. Zhu, M.-Y. Li, X. Peng, M. J. Kim, L.-J. Li, R. M. Wallace, S. Datta, J. A. Robinson, *Nat. Commun.* **2015**, *6*, 7311.

[146] R. Yue, A. T. Barton, H. Zhu, A. Azcatl, L. F. Pena, J. Wang, X. Peng, N. Lu, L. Cheng, R. Addou, S. Mcdonnell, L. Colombo, J. W. P. Hsu, J. Kim, M. J. Kim, R. M. Wallace, C. L. Hinkle, *ACS Nano* **2015**, *9*, 474.

[147] B. Holländer, H. Heer, M. Wagener, H. Halling, S. Mantl, *Nucl. Instrum. Meth. B* **2000**, *161–163*, 227.

[148] N. H. Turner, A. M. Single, *Surf. Interface Anal.* **1990**, *15*, 215.

[149] J.-G. Choi, L. T. Thompson, *Appl. Surf. Sci.* **1996**, *93*, 143.

[150] M. Albiter, R. Huirache-Acuña, F. Paraguay-Delgado, J. L. Rico, G. Alonso-Nuñez, *Nanotechnology* **2006**, *17*, 3473.

[151] A. Govind Rajan, V. Sresht, A. A. H. Pádua, M. S. Strano, D. Blankschtein, *ACS Nano* **2016**, *10*, 9145.

[152] A. Kozbial, X. Gong, H. Liu, L. Li, *Langmuir* **2015**, *31*, 8429.

[153] B. Schönfeld, J. J. Huang, S. C. Moss, *Acta Crystallogr. Sect. B Struct. Sci.* **1983**, *39*, 404.

[154] A. V. Chichagov, *Kristallographiya* **1990**, *35*, 610.

[155] A. Gurarslan, Y. Yu, L. Su, Y. Yu, F. Suarez, S. Yao, Y. Zhu, M. Ozturk, Y. Zhang, L. Cao, *ACS Nano* **2014**, *8*, 11522.

[156] N. Scheuschner, O. Ochedowski, A.-M. Kaulitz, R. Gillen, M. Schleberger, J. Maultzsch, *Phys. Rev. B* **2014**, *89*, 125406.

[157] Q. Ji, Y. Y. Zhang, T. Gao, D. Ma, M. Liu, Y. Chen, X. Qiao, P.-H. Tan, M. Kan, J. Feng, Q. Sun, Z. Liu, *Nano Lett.* **2013**, *13*, 1.

[158] A. Splendiani, L. Sun, Y. Zhang, T. Li, J. Kim, C.-Y. Chim, G. Galli, F. Wang, *Nano Lett.* **2010**, *10*, 1271.

[159] K. F. Mak, K. He, C. Lee, G. H. Lee, J. Hone, T. F. Heinz, J. Shan, *Nat. Mater.* **2013**, *12*, 207.

[160] A. P. S. Gaur, S. Sahoo, M. Ahmadi, S. P. Dash, M. J. F. Guinel, R. S. Katiyar, *Nano Lett.* **2014**, *14*, 4314.

[161] T. Bakos, S. N. Rashkeev, S. T. Pantelides, *Phys. Rev. Lett.* **2002**, *88*, 055508.

[162] S. Kostinski, R. Pandey, S. Gowtham, U. Pernisz, A. Kostinski, *IEEE Electron Device Lett.* **2012**, *33*, 863.

[163] D. Kong, H. Wang, J. J. Cha, M. Pasta, K. J. Koski, J. Yao, Y. Cui, *Nano Lett.* **2013**, *13*, 1341.

[164] J. Lee, P. Dak, Y. Lee, H. Park, W. Choi, M. a. Alam, S. Kim, *Sci. Rep.* **2014**, *4*, 7352.

[165] D. Sercombe, S. Schwarz, O. Del Pozo-Zamudio, F. Liu, B. J. Robinson, E. a Chekhovich, I. I. Tartakovskii, O. Kolosov, a I. Tartakovskii, *Sci. Rep.* **2013**, *3*, 3489.

[166] N. Choudhary, J. Park, J. Y. Hwang, W. Choi, *ACS Appl. Mater. Interfaces* **2014**, *6*, 21215.

[167] M. Maeda, K. Nakamura, T. Ohkubo, *J. Mater. Sci.* **1989**, *24*, 2120.

[168] P. O. Hahn, *J. Appl. Phys.* **1981**, *52*, 4122.

[169] J. Zhang, H. Yu, W. Chen, X. Tian, D. Liu, M. Cheng, G. Xie, W. Yang, R. Yang, X. Bai, D. Shi, G. Zhang, *ACS Nano* **2014**, *8*, 6024.
[170] E. Minni, F. Werfel, *Surf. Interface Anal.* **1988**, *12*, 385.
[171] R. Kappera, D. Voiry, S. E. Yalcin, B. Branch, G. Gupta, A. D. Mohite, M. Chhowalla, *Nat. Mater.* **2014**, *13*, 1128.
[172] Y. Lu, X. Yao, J. Yin, G. Peng, P. Cui, X. Xu, *RSC Adv.* **2015**, *5*, 7938.
[173] L. Jiang, S. Zhang, S. a. Kulinich, X. Song, J. Zhu, X. Wang, H. Zeng, *Mater. Res. Lett.* **2015**, *3*, 177.
[174] K.-C. Chen, T.-W. Chu, C.-R. Wu, S.-C. Lee, S.-Y. Lin, *2D Mater.* **2017**, *4*, 034001.
[175] C.-R. Wu, X.-R. Chang, T.-W. Chu, H.-A. Chen, C.-H. Wu, S.-Y. Lin, *Nano Lett.* **2016**, *16*, 7093.
[176] Y. T. Ho, C. H. Ma, T. T. Luong, L. L. Wei, T. C. Yen, W. T. Hsu, W. H. Chang, Y. C. Chu, Y. Y. Tu, K. P. Pande, E. Y. Chang, *Phys. Status Solidi - Rapid Res. Lett.* **2015**, *9*, 187.
[177] A. J. Mughal, T. N. Walter, K. A. Cooley, A. Bertuch, S. E. Mohney, *J. Vac. Sci. Technol. A* **2019**, *37*, 010907.
[178] A. Rosová, V. Vretenár, E. Dobročka, Š. Chromik, M. Sojková, M. Hulman, *Appl. Surf. Sci.* **2016**, *395*, 232.
[179] T. G. Ivanov, R. M. Feenstra, B. Wang, J. Li, D. Ruzmetov, B. Jariwala, J. O. Lerach, R. A. Burke, N. C. Briggs, J. A. Robinson, M. Haque, K. Zhang, *Nanoscale* **2017**, *10*, 336.
[180] Z. Chen, H. Liu, X. Chen, G. Chu, S. Chu, H. Zhang, *ACS Appl. Mater. Interfaces* **2016**, *8*, 20267.
[181] Q. Ji, Y. Zhang, Z. Liu, *Chem. Soc. Rev.* **2015**, *44*, 2587.
[182] W. H. Chae, J. D. Cain, E. D. Hanson, A. A. Murthy, V. P. Dravid, *Appl. Phys. Lett.* **2017**, *111*, DOI 10.1063/1.4998284.
[183] S. Heo, R. Hayakawa, Y. Wakayama, *J. Appl. Phys.* **2017**, *121*, DOI 10.1063/1.4973491.
[184] S. Vangelista, E. Cinquanta, C. Martella, M. Alia, M. Longo, A. Lamperti, R. Mantovan, F. B. Basset, F. Pezzoli, A. Molle, *Nanotechnology* **2016**, *27*, DOI 10.1088/0957-4484/27/17/175703.
[185] J.-H. Wi, B. Shin, W. S. Han, W.-J. Lee, Y.-D. Chung, S. J. Yun, D.-H. Cho, *Phys. Chem. Chem. Phys.* **2018**, *20*, 16193.
[186] D. Pareek, M. A. Gonzalez, J. Zohrabian, M. H. Sayed, V. Steenhoff, C. Lattyak, M. Vehse, C. Agert, J. Parisi, S. Schäfer, L. Gütay, *RSC Adv.* **2019**, *9*, 107.
[187] H. Samassekou, A. Alkabsh, K. Stiwinter, A. Khatri, D. Mazumdar, *MRS Commun.* **2018**, *8*, 1328.
[188] H. Wakabayashi, K. Kakushima, K. Tsutsui, J. Shimizu, N. Ikarashi, T. Ohashi, I. Muneta, K. Matsuura, *IEEE J. Electron Devices Soc.* **2018**, *7*, 1.

[189] G. Li, K. Wang, H.-S. Kwok, W. Zhong, G. Li, R. Chen, S. Deng, *Nanomaterials* **2018**, *8*, 590.

[190] S. Ishihara, Y. Hibino, N. Sawamoto, K. Suda, T. Ohashi, K. Matsuura, H. Machida, M. Ishikawa, H. Sudoh, H. Wakabayashi, A. Ogura, **2016**, 3.

[191] S. Ishihara, Y. Hibino, N. Sawamoto, K. Suda, T. Ohashi, K. Matsuura, H. Machida, M. Ishikawa, H. Sudoh, H. Wakabayashi, A. Ogura, *Jpn. J. Appl. Phys.* **2016**, *55*, 06GF01.

[192] T. Zhang, Y. Wang, J. Xu, L. Chen, H. Zhu, Q. Sun, S. Ding, D. W. Zhang, *2D Mater.* **2017**, *5*, 015028.

[193] J. J. Pyeon, S. H. Kim, D. S. Jeong, S.-H. Baek, C.-Y. Kang, J.-S. Kim, S. K. Kim, *Nanoscale* **2016**, *8*, 10792.

[194] X. Xu, Z. Wang, S. Lopatin, M. A. Quevedo-Lopez, H. N. Alshareef, *2D Mater.* **2018**, *6*, 015030.

[195] S. Hussain, M. A. Shehzad, D. Vikraman, M. F. Khan, J. Singh, D.-C. Choi, Y. Seo, J. Eom, W.-G. Lee, J. Jung, *Nanoscale* **2016**, *8*, 4340.

[196] Y. Wang, R. He, M. Su, W. Xie, *IOP Conf. Ser. Mater. Sci. Eng.* **2017**, *167*, 012020.

[197] S.-H. Lin, J.-L. Kuo, *Phys. Chem. Chem. Phys.* **2015**, *17*, 29305.

[198] L. Liu, Y. Lu, J. Guo, *IEEE Trans. Electron Devices* **2013**, *60*, 4133.

[199] O. Lopez-Sanchez, D. Lembke, M. Kayci, A. Radenovic, A. Kis, *Nat. Nanotechnol.* **2013**, *8*, 497.

[200] Y. K. Luo, J. Xu, T. Zhu, G. Wu, E. J. McCormick, W. Zhan, M. R. Neupane, R. K. Kawakami, *Nano Lett.* **2017**, *17*, 3877.

[201] W. G. Song, H.-J. Kwon, J. Park, J. Yeo, M. Kim, S. Park, S. Yun, K.-U. Kyung, C. P. Grigoropoulos, S. Kim, Y. K. Hong, *Adv. Funct. Mater.* **2016**, *26*, 2426.

[202] K.-T. Chen, S.-T. Chang, *Vacuum* **2017**, *140*, 172.

[203] K. Chen, S. Chang, in *2016 IEEE 16th Int. Conf. Nanotechnol.*, IEEE, **2016**, pp. 139–141.

[204] Y. Yoon, K. Ganapathi, S. Salahuddin, *Nano Lett.* **2011**, *11*, 3768.

[205] D. Chiappe, I. Asselberghs, S. Sutar, S. Iacovo, V. Afanas'ev, A. Stesmans, Y. Balaji, L. Peters, M. Heyne, M. Mannarino, W. Vandervorst, S. Sayan, C. Huyghebaert, M. Caymax, M. Heyns, S. De Gendt, I. Radu, A. Thean, *Adv. Mater. Interfaces* **2016**, *3*, 1500635.

[206] A. Zafar, H. Nan, Z. Zafar, Z. Wu, J. Jiang, Y. You, Z. Ni, *Nano Res.* **2017**, *10*, 1608.

[207] S. Wang, Y. Rong, Y. Fan, M. Pacios, H. Bhaskaran, K. He, J. H. Warner, *Chem. Mater.* **2014**, *26*, 6371.

[208] Y. Kim, H. Bark, G. H. Ryu, Z. Lee, C. Lee, *J. Physics-Condensed Matter* **2016**, *28*, 6.

[209] L. Ma, D. N. Nath, E. W. Lee, C. H. Lee, M. Yu, A. Arehart, S. Rajan, Y. Wu, *Appl. Phys. Lett.* **2014**, *105*, 072105.

[210] K. Jung, C. Y. Liu, J. D. Kim, W. Choi, W. Zhou, H. C. Kuo, X. Li, *2016 IEEE Photonics Conf. IPC 2016* **2017**, 657.

[211] D. Ruzmetov, K. Zhang, G. Stan, B. Kalanyan, G. R. Bhimanapati, S. M. Eichfeld, R. A. Burke, P. B. Shah, T. P. O'Regan, F. J. Crowne, A. G. Birdwell, J. A. Robinson, A. V. Davydov, T. G. Ivanov, *ACS Nano* **2016**, *10*, 3580.

[212] N. D. Boscher, C. J. Carmalt, R. G. Palgrave, J. J. Gil-Tomas, I. P. Parkin, *Chem. Vap. Depos.* **2006**, *12*, 692.

[213] S. H. Choi, B. Stephen, J.-H. Park, J. S. Lee, S. M. Kim, W. Yang, K. K. Kim, *Sci. Rep.* **2017**, *7*, 1983.

[214] S. Dhar, V. K. Kumar, T. H. Choudhury, S. A. Shivashankar, S. Raghavan, *Phys. Chem. Chem. Phys.* **2016**, *18*, 14918.

[215] C. Gas, P. Decomposition, M. R. Close, J. L. Petersen, E. L. Kugler, *Inorg. Chem.* **1999**, *38*, 15.

[216] M. H. Heyne, D. Chiappe, J. Meersschaut, T. Nuytten, T. Conard, H. Bender, C. Huyghebaert, I. P. Radu, M. Caymax, J.-F. de Marneffe, E. C. Neyts, S. De Gendt, *J. Mater. Chem. C* **2016**, *4*, 1295.

[217] T. Weber, J. C. Muijsers, J. H. M. C. van Wolput, C. P. J. Verhagen, J. W. Niemantsverdriet, *J. Phys. Chem.* **1996**, *100*, 14144.

[218] A. Van der Vlies, A. J. van der Vlies, R. Prins, T. Weber, *J. Phys. Chem. B* **2002**, *106*, 9277.

[219] A. Delabie, M. Caymax, B. Groven, M. Heyne, K. Haesevoets, J. Meersschaut, T. Nuytten, H. Bender, T. Conard, P. Verdonck, S. Van Elshocht, S. De Gendt, M. Heyns, K. Barla, I. Radu, A. Thean, *Chem. Commun.* **2015**, *51*, 15692.

[220] M. H. Heyne, J.-F. de Marneffe, A. Delabie, M. Caymax, E. C. Neyts, I. Radu, C. Huyghebaert, S. De Gendt, *Nanotechnology* **2017**, *28*, 04LT01.

[221] E. K. Broadbent, *J. Electrochem. Soc.* **1984**, *131*, 1427.

[222] J. Carlsson, M. Boman, *J. Vac. Sci. Technol. A Vacuum, Surfaces, Film.* **1985**, *3*, 2298.

[223] Y. Pauleau, P. Lami, A. Tissier, R. Pantel, J. C. Oberlin, *Thin Solid Films* **1986**, *143*, 259.

[224] R. K. Grubbs, C. E. Nelson, N. J. Steinmetz, S. M. George, *Thin Solid Films* **2004**, *467*, 16.

[225] B. Kalanyan, P. C. Lemaire, S. E. Atanasov, M. J. Ritz, G. N. Parsons, *Chem. Mater.* **2016**, *28*, 117.

[226] G. Wang, Q. Xu, T. Yang, J. Luo, J. Xiang, J. Xu, G. Xu, C. Li, J. Li, J. Yan, C. Zhao, D. Chen, T. Ye, *ECS Trans.* **2013**, *58*, 317.

[227] G. J. Leusink, T. G. M. Oosterlaken, G. C. A. M. Janssen, S. Redelaar, *Thin Solid Films* **1993**, *228*, 125.

[228] J. C. Dupuy, A. Essaadani, A. Sibai, C. Dubois, F. C. Dassapa, Y. Pauleau, *Thin Solid Films* **1993**, *227*, 167.

[229] M. L. Green, *J. Electrochem. Soc.* **1987**, *134*, 2285.

[230] J. Yang, Z. Wang, F. Wang, R. Xu, J. Tao, S. Zhang, Q. Qin, B. Luther-Davies, C. Jagadish, Z. Yu, Y. Lu, *Light Sci. Appl.* **2016**, *5*, e16046.

[231] M. L. Yu, K. Y. Ahn, R. V. Joshi, *IBM J. Res. Dev.* **1990**, *34*, 875.

[232] O. Renner, J. Zemek, *Czechoslov. J. Phys.* **1973**, *23*, 1273.

[233] M. Morita, T. Ohmi, E. Hasegawa, M. Kawakami, M. Ohwada, *J. Appl. Phys.* **1990**, *68*, 1272.

[234] A. Kepten, *J. Electrochem. Soc.* **1992**, *139*, 2331.

[235] P. C. Yen, Y. S. Huang, K. K. Tiong, *J. Phys. Condens. Matter* **2004**, *16*, 2171.

[236] X. Mao, Y. Xu, Q. Xue, W. Wang, D. Gao, *Nanoscale Res. Lett.* **2013**, *8*, 1.

[237] J. Gao, B. Li, J. Tan, P. Chow, T. M. Lu, N. Koratkar, *ACS Nano* **2016**, *10*, 2628.

[238] F. R. McFeely, L. J. Terminello, S. P. Kowalczyk, *Appl. Phys. Lett.* **1990**, *57*, 667.

[239] M. Shinmei, T. Imai, T. Yokokawa, C. Masson, *J. Chem. Thermodyn.* **1986**, *18*, 241.

[240] F. De Smedt, C. Vinckier, I. Cornelissen, S. De Gendt, M. Heyns, *J. Electrochem. Soc.* **2000**, *147*, 1124.

[241] H. Bender, *J. Electrochem. Soc.* **1994**, *141*, 3128.

[242] A. Warren, A. Nylund, I. Olefjord, *Int. J. Refract. Met. Hard Mater.* **1996**, *14*, 345.

[243] A. Berkdemir, H. R. Gutiérrez, A. R. Botello-Méndez, N. Perea-López, A. L. Elías, C.-I. Chia, B. Wang, V. H. Crespi, F. López-Urías, J.-C. Charlier, H. Terrones, M. Terrones, *Sci. Rep.* **2013**, *3*, 1755.

[244] S. Mignuzzi, A. J. Pollard, N. Bonini, B. Brennan, I. S. Gilmore, M. A. Pimenta, D. Richards, D. Roy, *Phys. Rev. B - Condens. Matter Mater. Phys.* **2015**, *91*, 1.

[245] J. H. Kim, T. H. Kim, H. Lee, Y. R. Park, W. Choi, C. J. Lee, *AIP Adv.* **2016**, *6*, 065106.

[246] M.-W. Lin, I. I. Kravchenko, J. Fowlkes, X. Li, A. A. Puretzky, C. M. Rouleau, D. B. Geohegan, K. Xiao, *Nanotechnology* **2016**, *27*, 165203.

[247] P. Z. Si, M. Zhang, Z. D. Zhang, X. G. Zhao, X. L. Ma, D. Y. Geng, *J. Mater. Sci.* **2005**, *40*, 4287.

[248] J. H. Huang, K. Y. Deng, P. S. Liu, C. T. Wu, C. T. Chou, W. H. Chang, Y. J. Lee, T. H. Hou, *Adv. Mater. Interfaces* **2017**, *1700157*, 2.

[249] T. Irisawa, N. Okada, W. Mizubayashi, T. Mori, W.-H. Chang, K. Koga, A. Ando, K. Endo, S. Sasaki, T. Endo, Y. Miyata, *IEEE J. Electron Devices Soc.* **2018**, *6*, 1159.

[250] A. L. Elías, N. Perea-López, A. Castro-Beltrán, A. Berkdemir, R. Lv, S. Feng, A. D. Long, T. Hayashi, Y. A. Kim, M. Endo, H. R. Gutiérrez, N. R. Pradhan, L. Balicas, T. E. Mallouk, F. López-Urías, H. Terrones, M. Terrones, *ACS Nano* **2013**, *7*, 5235.

[251] X. Ma, M. Shi, *Nano-Micro Lett.* **2013**, *5*, 135.

[252] J.-W. Chung, Z. R. Dai, F. S. Ohuchi, *J. Cryst. Growth* **1998**, *186*, 137.

[253] D. K. Nandi, U. K. Sen, A. Dhara, S. Mitra, S. K. Sarkar, *RSC Adv.* **2016**, *6*, 38024.

[254] J. Yu, X. Hu, H. Li, X. Zhou, T. Zhai, *J. Mater. Chem. C* **2018**, *6*, 4627.

[255] A. A. Zaitsev, N. A. Korotkov, E. M. Lazarev, *Met. Sci. Heat Treat.* **1976**, *18*, 873.

[256] S. Ross, A. Sussman, *J. Phys. Chem.* **1955**, *59*, 889.

[257] S. X. Hou, H. Gao, X. M. Jia, *Adv. Mater. Res.* **2013**, *652–654*, 1904.

[258] S. Vangelista, E. Cinquanta, C. Martella, M. Alia, M. Longo, A. Lamperti, R. Mantovan, F. B. Basset, F. Pezzoli, A. Molle, *Nanotechnology* **2016**, *27*, 175703.

[259] P. Rai-Choudhury, A. J. Noreika, *J. Electrochem. Soc.* **1969**, *116*, 539.

[260] T. L. Chu, R. W. Keim, *J. Electrochem. Soc.* **1969**, *116*, 1261.

[261] N. P. Dasgupta, J. F. Mack, M. C. Langston, A. Bousetta, F. B. Prinz, *Rev. Sci. Instrum.* **2010**, *81*, 044102.

[262] K. Tjokro, D. J. Young, R. E. Johansson, B. G. Ivarsson, *Le J. Phys. IV* **1993**, *03*, 357.

[263] B. J. Berkowitz, F. H. Heubaum, *CORROSION* **1984**, *40*, 240.

[264] J. Cui, A. Sun, M. Reshichkov, F. Yun, A. Baski, H. Morkoç, *MRS Internet J. Nitride Semicond. Res.* **2000**, *5*, e7.

[265] T. Schram, Q. Smets, B. Groven, M. H. Heyne, E. Kunnen, A. Thiam, K. Devriendt, A. Delabie, D. Lin, M. Lux, D. Chiappe, I. Asselberghs, S. Brus, C. Huyghebaert, S. Sayan, A. Juncker, M. Caymax, I. P. Radu, in *2017 47th Eur. Solid-State Device Res. Conf.*, IEEE, **2017**, pp. 212–215.

[266] M. H. Heyne, J.-F. de Marneffe, T. Nuytten, J. Meersschaut, T. Conard, M. Caymax, I. Radu, A. Delabie, E. C. Neyts, S. De Gendt, *J. Mater. Chem. C* **2018**, *6*, 4122.

[267] M. Nakata, K. Takechi, S. Yamaguchi, E. Tokumitsu, H. Yamaguchi, S. Kaneko, *Jpn. J. Appl. Phys.* **2009**, *48*, 115505.

[268] R. Paetzel, J. Brune, F. Simon, L. Herbst, M. Machida, J. Shida, in *2010 18th Int. Conf. Adv. Therm. Process. Semicond.*, IEEE, **2010**,

pp. 98–102.

[269] F. Lan, Z. Lai, Y. Xu, H. Cheng, Z. Wang, C. Qi, J. Chen, S. Zhang, *Sci. Rep.* **2016**, *6*, 31980.

[270] L. Fei, S. Lei, W.-B. Zhang, W. Lu, Z. Lin, C. H. Lam, Y. Chai, Y. Wang, *Nat. Commun.* **2016**, *7*, 12206.

[271] I. A. Palani, *J. Laser Micro/Nanoengineering* **2010**, *5*, 150.

[272] K. Huet, C. Boniface, R. Negru, J. Venturini, *AIP Conf. Proc.* **2012**, *1496*, 135.

[273] R. Ishihara, P. C. van der Wilt, B. D. van Dijk, A. Burtsev, J. W. Metselaar, C. I. M. Beenakker, *Thin Solid Films* **2003**, *427*, 77.

[274] R. Ishihara, J. Derakhshandeh, M. R. Tajari Mofrad, T. Chen, N. Golshani, C. I. M. Beenakker, *Solid. State. Electron.* **2012**, *71*, 80.

[275] H.-J. Kwon, S. Kim, J. Jang, C. P. Grigoropoulos, *Appl. Phys. Lett.* **2015**, *106*, 113111.

[276] H. Kwon, W. Choi, D. Lee, Y. Lee, J. Kwon, B. Yoo, C. P. Grigoropoulos, S. Kim, *Nano Res.* **2014**, *7*, 1137.

[277] J. Kwon, Y. Ki Hong, H.-J. Kwon, Y. Jin Park, B. Yoo, J. Kim, C. P. Grigoropoulos, M. Suk Oh, S. Kim, *Nanotechnology* **2015**, *26*, 035202.

[278] S. Brunken, R. Mientus, K. Ellmer, *Thin Solid Films* **2009**, *517*, 3148.

[279] S. Brunken, M. Wollgarten, K. Ellmer, *J. Appl. Phys.* **2016**, *120*, 165307.

[280] S. Brunken, R. Mientus, K. Ellmer, *Phys. Status Solidi* **2012**, *209*, 317.

[281] S. Y. Yoon, S. J. Park, K. H. Kim, J. Jang, *Thin Solid Films* **2001**, *383*, 34.

[282] P. Wang, H. Liu, D. Qi, Q. Sun, S. Chen, C. Li, W. Huang, H. Lai, *J. Cryst. Growth* **2015**, *416*, 106.

[283] S. Brunken, R. Mientus, S. Seeger, K. Ellmer, *J. Appl. Phys.* **2008**, *103*, DOI 10.1063/1.2875679.

[284] M. Regula, C. Ballif, J. H. Moser, F. Lévy, *Thin Solid Films* **1996**, *280*, 67.

[285] M. Regula, C. Ballif, M. Remškar, *J. Vac. Sci. Technol. A Vacuum, Surfaces, Film.* **1997**, *15*, 2323.

[286] M. Regula, C. Ballif, F. Levy, *J. Cryst. Growth* **1998**, *193*, 109.

[287] C. Ballif, M. Regula, F. Lévy, *Sol. Energy Mater. Sol. Cells* **1999**, *57*, 189.

[288] B. Predel, *Ca-Cd – Co-Zr*, Springer-Verlag, Berlin/Heidelberg, **1993**.

[289] H. Okamoto, *J. Phase Equilibria Diffus.* **2009**, *30*, 123.

[290] W. Zhao, Z. Ghorannevis, L. Chu, M. Toh, C. Kloc, P.-H. Tan, G. Eda, *ACS Nano* **2013**, *7*, 791.

[291] F. Bozheyev, D. Friedrich, M. Nie, M. Rengachari, K. Ellmer, *Phys. Status Solidi Appl. Mater. Sci.* **2014**, *211*, 2013.

[292] K. Ellmer, S. Seeger, R. Mientus, *Phys. Status Solidi Appl. Mater. Sci.* **2006**, *203*, 2457.

[293] K. Ellmer, *Phys. Status Solidi Basic Res.* **2008**, *245*, 1745.

[294] E. Galun, H. Cohen, L. Margulis, A. Vilan, T. Tsirlina, G. Hodes, R. Tenne, M. Hershfinkel, W. Jaegermann, K. Ellmer, *Appl. Phys. Lett.* **1995**, *67*, 3474.

[295] C. R. M. Wronski, *Br. J. Appl. Phys.* **1967**, *18*, 1731.

[296] L. Harbury, *J. Phys. Chem.* **1946**, *50*, 190.

[297] G. Berhault, L. Cota Araiza, A. Duarte Moller, A. Mehta, R. R. Chianelli, *Catal. Letters* **2002**, *78*, 81.

[298] S. Harris, R. R. Chianelli, *J. Catal.* **1986**, *98*, 17.

[299] X. Zhao, *J. Catal.* **1994**, *147*, 429.

[300] Y.-J. Oh, J.-H. Kim, C. V. Thompson, C. A. Ross, *Nanoscale* **2013**, *5*, 401.

[301] Y. J. Oh, C. A. Ross, Y. S. Jung, Y. Wang, C. V. Thompson, *Small* **2009**, *5*, 860.

[302] K.-K. Liu, W. Zhang, Y. Lee, Y.-C. Lin, M.-T. Chang, C.-Y. Su, C.-S. Chang, H. Li, Y. Shi, H. Zhang, C.-S. Lai, L.-J. Li, *Nano Lett.* **2012**, *12*, 1538.

[303] M. Kuzuhara, T. Nozaki, T. Kamejima, *J. Appl. Phys.* **1989**, *66*, 5833.

[304] S. S. Gill, B. J. Sealy, P. J. Topham, N. J. Barrett, K. G. Stephens, *Electron. Lett.* **1981**, *17*, 623.

[305] S. H. Xin, W. J. Schaff, C. E. C. Wood, L. F. Eastman, *Appl. Phys. Lett.* **1982**, *41*, 742.

[306] M. Bettini, K. J. Bachmann, E. Buehler, J. L. Shay, S. Wagner, *J. Appl. Phys.* **1977**, *48*, 1603.

[307] P. Rai-Choudhury, *J. Electrochem. Soc.* **1971**, *118*, 266.

[308] F. Ran, Z. Xiao, H. Hiramatsu, H. Hosono, T. Kamiya, *Appl. Phys. Lett.* **2014**, *104*, 072106.

[309] K. J. Bachmann, M. H. Bettini, E. Buehler, J. L. Shay, S. Wagner, *Etching of III-V Semiconductor Materials with H_2S in the Preparation of Heterodiodes to Facilitate the Deposition of Cadmium Sulfide*, **1978**, US4039357 A.

[310] G. Dingemans, C. van Helvoirt, M. C. M. van de Sanden, W. M. Kessels, in *ECS Trans.*, **2011**, pp. 191–204.

[311] H. Zhang, G. Arutchelvan, J. Meersschaut, A. Gaur, T. Conard, H. Bender, D. Lin, I. Asselberghs, M. Heyns, I. Radu, W. Vandervorst, A. Delabie, *Chem. Mater.* **2017**, *29*, 6772.

[312] B. Sirota, N. Glavin, A. A. Voevodin, *Vacuum* **2019**, *160*, 133.

[313] C. Rogers, D. Gray, N. Bogdanowicz, H. Mabuchi, *Phys. Rev. Mater.*

2018, *2*, 094003.

[314] Y. Yu, G.-H. Nam, Q. He, X.-J. Wu, K. Zhang, Z. Yang, J. Chen, Q. Ma, M. Zhao, Z. Liu, F.-R. Ran, X. Wang, H. Li, X. Huang, B. Li, Q. Xiong, Q. Zhang, Z. Liu, L. Gu, Y. Du, W. Huang, H. Zhang, *Nat. Chem.* **2018**, *10*, 638.

[315] S. Li, Y.-C. Lin, W. Zhao, J. Wu, Z. Wang, Z. Hu, Y. Shen, D.-M. Tang, J. Wang, Q. Zhang, H. Zhu, L. Chu, W. Zhao, C. Liu, Z. Sun, T. Taniguchi, M. Osada, W. Chen, Q.-H. Xu, A. T. S. Wee, K. Suenaga, F. Ding, G. Eda, *Nat. Mater.* **2018**, *17*, 535.

[316] N. Zink, H. A. Therese, J. Pansiot, A. Yella, F. Banhart, W. Tremel, *Chem. Mater.* **2008**, *20*, 65.

[317] L. Brewer, R. H. Lamoreaux, *Bull. Alloy Phase Diagrams* **1980**, *1*, 93.

[318] B. Predel, in *Pu-Re – Zn-Zr*, Springer-Verlag, Berlin/Heidelberg, **n.d.**, pp. 1–3.

[319] T. Agarwal, D. Yakimets, P. Raghavan, I. Radu, A. Thean, M. Heyns, W. Dehaene, *IEEE Trans. Electron Devices* **2015**, *62*, 4051.

[320] H. Liu, M. Si, S. Najmaei, A. T. Neal, Y. Du, P. M. Ajayan, J. Lou, P. D. Ye, *Nano Lett.* **2013**, *13*, 2640.

[321] L. K. Tan, B. Liu, J. H. Teng, S. Guo, H. Y. Low, K. P. Loh, *Nanoscale* **2014**, *6*, 10584.

[322] J. A. Rodriguez, J. Dvorak, T. Jirsak, J. Hrbek, *Surf. Sci.* **2001**, *490*, 315.

[323] J. Etzkorn, H. A. Therese, F. Rocker, N. Zink, U. Kolb, W. Tremel, *Adv. Mater.* **2005**, *17*, 2372.

[324] J. P. Shupp, A. S. Kinne, H. D. Arman, Z. J. Tonzetich, *Organometallics* **2014**, *33*, 5238.

[325] S. Shin, Z. Jin, D. H. Kwon, R. Bose, Y.-S. Min, *Langmuir* **2015**, *31*, 1196.

[326] S. J. Yeo, H. Oh, T.-S. You, D. J. Jeon, T.-M. Chung, B. K. Park, C. G. Kim, *Polyhedron* **2015**, *100*, 199.

[327] S. Ganorkar, J. Kim, Y.-H. Kim, S.-I. Kim, *J. Phys. Chem. Solids* **2015**, *87*, 32.

[328] K.-S. Kim, J.-Y. Kim, H.-B. Kang, B.-Y. Lee, S.-M. Park, *J. Electrochem. Soc.* **2008**, *155*, H426.

[329] N. Ninomiya, T. Mori, N. Uchida, E. Watanabe, D. Tsuya, S. Moriyama, M. Tanaka, A. Ando, *Jpn. J. Appl. Phys.* **2015**, *54*, 046502.

[330] A. Nipane, D. Karmakar, N. Kaushik, S. Karande, S. Lodha, *ACS Nano* **2016**, *10*, 2128.

[331] Q. Ma, P. M. Odenthal, J. Mann, D. Le, C. S. Wang, Y. Zhu, T. Chen, D. Sun, K. Yamaguchi, T. Tran, M. Wurch, J. L. McKinley, J. Wyrick, K. Magnone, T. F. Heinz, T. S. Rahman, R. Kawakami, L.

Bartels, *J. Phys. Condens. Matter* **2013**, *25*, 252201.
[332] Y. Cai, G. Zhang, Y.-W. Zhang, *J. Am. Chem. Soc.* **2014**, *136*, 6269.
[333] M. I. B. Utama, X. Lu, D. Zhan, S. T. Ha, Y. Yuan, Z. Shen, Q. Xiong, *Nanoscale* **2014**, *6*, 12376.
[334] J. Li, L. Zhou, Q. Zhu, H. Li, *Chem. Eng. J.* **2014**, *249*, 54.
[335] J. E. Dutrizac, *J. Less Common Met.* **1973**, *31*, 281.
[336] X. Lee, X. X. Li, X. Zang, M. Zhu, Y. He, K. Wang, D. Xie, H. Zhu, X. X. Li, X. Zang, M. Zhu, Y. He, K. Wang, D. Xie, H. Zhu, *Nanoscale* **2015**, *7*, 8398.
[337] M. Donarelli, F. Bisti, F. Perrozzi, L. Ottaviano, *Chem. Phys. Lett.* **2013**, *588*, 198.
[338] A. S. Berdinsky, L. T. Chadderton, J. B. Yoo, A. K. Gutakovsky, V. E. Fedorov, L. N. Mazalov, D. Fink, *Appl. Phys. A* **2005**, *80*, 61.
[339] H. Nan, Z. Wang, W. Wang, Z. Liang, Y. Lu, Q. Chen, D. He, P. Tan, F. Miao, X. Wang, J. Wang, Z. Ni, *ACS Nano* **2014**, *8*, 5738.
[340] R. Ionescu, A. George, I. Ruiz, Z. Favors, Z. Mutlu, C. Liu, K. Ahmed, R. Wu, J. S. Jeong, L. Zavala, K. A. Mkhoyan, M. Ozkan, C. S. Ozkan, *Chem. Commun.* **2014**, *50*, 11226.
[341] X. Wei, Z. Yu, F. Hu, Y. Cheng, L. Yu, X. Wang, M. Xiao, J. Wang, X. Wang, Y. Shi, *AIP Adv.* **2014**, *4*, 123004.
[342] M. Chhowalla, D. Jena, H. Zhang, *Nat. Rev. Mater.* **2016**, *1*, 16052.
[343] T. Roy, M. Tosun, X. Cao, H. Fang, D. H. Lien, P. Zhao, Y. Z. Chen, Y. L. Chueh, J. Guo, A. Javey, *ACS Nano* **2015**, *9*, 2071.
[344] W. Cao, J. Kang, D. Sarkar, W. Liu, K. Banerjee, *IEEE Trans. Electron Devices* **2015**, *62*, 3459.
[345] J. R. Schaibley, H. Yu, G. Clark, P. Rivera, J. S. Ross, K. L. Seyler, W. Yao, X. Xu, *Nat. Rev. Mater.* **2016**, *1*, DOI 10.1038/natrevmats.2016.55.
[346] H. Lim, S. I. Yoon, G. Kim, A. R. Jang, H. S. Shin, *Chem. Mater.* **2014**, *26*, 4891.
[347] T. Schram, Q. Smets, M. H. Heyne, B. Graven, E. Kunnen, A. Thiam, K. Devriendt, A. Delabie, D. Lin, D. Chiappe, I. Asselberghs, M. Lux, S. Brus, C. Huyghebaert, S. Sayan, A. Juncker, M. Caymax, I. P. Radu, in *2017 Silicon Nanoelectron. Work.*, IEEE, **2017**, pp. 139–140.
[348] Y. Yu, P. W. K. Fong, S. Wang, C. Surya, *Sci. Rep.* **2016**, *6*, 1.
[349] H. Yu, M. Liao, W. Zhao, G. Liu, X. J. Zhou, Z. Wei, X. Xu, K. Liu, Z. Hu, K. Deng, S. Zhou, J. A. Shi, L. Gu, C. Shen, T. Zhang, L. Du, L. Xie, J. Zhu, W. Chen, R. Yang, D. Shi, G. Zhang, *ACS Nano* **2017**, *11*, 12001.
[350] H. Van Ngoc, Y. Qian, S. K. Han, D. J. Kang, *Sci. Rep.* **2016**, *6*, 1.
[351] H. D. Phan, Y. Kim, J. Lee, R. Liu, Y. Choi, J. H. Cho, C. Lee, *Adv. Mater.* **2017**, *29*, 1603928.

[352] N. Huo, J. Kang, Z. Wei, S.-S. Li, J. Li, S.-H. Wei, *Adv. Funct. Mater.* **2014**, *24*, 7025.
[353] R. Ionescu, I. Ruiz, Z. Favors, B. Campbell, M. R. Neupane, D. Wickramaratne, K. Ahmed, C. Liu, N. Abrahamian, R. K. Lake, M. Ozkan, C. S. Ozkan, *Chem. Commun.* **2015**, *51*, 11213.
[354] K. Chen, X. Wan, W. Xie, J. Wen, Z. Kang, X. Zeng, H. Chen, J. Xu, *Adv. Mater.* **2015**, *27*, 6431.
[355] K. Chen, X. Wan, J. Wen, W. Xie, Z. Kang, X. Zeng, H. Chen, J.-B. Xu, *ACS Nano* **2015**, *9*, 9868.
[356] Z. Wang, Q. Huang, P. Chen, S. Guo, X. Liu, X. Liang, L. Wang, *Sci. Rep.* **2016**, *6*, 38394.
[357] Y. Xi, M. I. Serna, L. Cheng, Y. Gao, M. Baniasadi, R. Rodriguez-Davila, J. Kim, M. A. Quevedo-Lopez, M. Minary-Jolandan, *J. Mater. Chem. C* **2015**, *3*, 3842.
[358] Y. Balaji, Q. Smets, C. J. L. de la Rosa, A. K. A. Lu, D. Chiappe, T. Agarwal, D. Lin, C. Huyghebaert, I. Radu, D. Mocuta, G. Groeseneken, *IEEE J. Electron Devices Soc.* **2018**, *6734*, 1.
[359] H. Zhu, X. Qin, L. Cheng, A. Azcatl, J. Kim, R. M. Wallace, *ACS Appl. Mater. Interfaces* **2016**, *8*, 19119.
[360] M. H. Heyne, J.-F. de Marneffe, A. Delabie, M. Caymax, E. C. Neyts, I. Radu, C. Huyghebaert, S. De Gendt, *Nanotechnology* **2017**, *28*, 04LT01.
[361] N. Gulbrandsen, Fredriksen, J. Carr, E. Scime, *Phys. Plasmas* **2015**, *22*, DOI 10.1063/1.4913990.
[362] E. N. Voronina, L. S. Novikov, T. V Rakhimova, *Inorg. Mater. Appl. Res.* **2018**, *9*, 175.
[363] D. Liu, Y. Guo, L. Fang, J. Robertson, *Appl. Phys. Lett.* **2013**, *103*, 183113.
[364] K. Santosh, R. C. Longo, R. Addou, R. M. Wallace, K. Cho, *Nanotechnology* **2014**, *25*, 375703.
[365] D. Gahan, S. Daniels, C. Hayden, D. O. Sullivan, M. B. Hopkins, *Plasma Sources Sci. Technol.* **2012**, *21*, 015002.
[366] D. Gahan, S. Daniels, C. Hayden, P. Scullin, D. O'Sullivan, Y. T. Pei, M. B. Hopkins, *Plasma Sources Sci. Technol.* **2012**, *21*, 024004.
[367] P. Hess, *RSC Adv.* **2017**, *7*, 29786.
[368] H. Toulhoat, P. Raybaud, S. Kasztelan, G. Kresse, J. Hafner, *Catal. Today* **1999**, *50*, 629.
[369] F. Yu, Q. Liu, X. Gan, M. Hu, T. Zhang, C. Li, F. Kang, M. Terrones, R. Lv, *Adv. Mater.* **2017**, *29*, 1603266.
[370] W. M. R. Divigalpitiya, S. R. Morrison, R. F. Frindt, *Thin Solid Films* **1990**, *186*, 177.
[371] J. W. Christopher, M. Vutukuru, D. Lloyd, J. S. Bunch, B. B. Goldberg, D. J. Bishop, A. K. Swan, *J. Microelectromechanical Syst.*

2019, *VV*, 1.

[372] A. Leonhardt, D. Chiappe, I. Asselberghs, C. Huyghebaert, I. Radu, S. De Gendt, *IEEE Electron Device Lett.* **2017**, *38*, 1606.

[373] X.-F. Qiao, X.-L. Li, X. Zhang, W. Shi, J.-B. Wu, T. Chen, P.-H. Tan, *Appl. Phys. Lett.* **2015**, *106*, 223102.

[374] Z. Wang, P. Liu, Y. Ito, S. Ning, Y. Tan, T. Fujita, A. Hirata, M. Chen, *Sci. Rep.* **2016**, *6*, 21536.

[375] B. Groven, D. Claes, A. Nalin Mehta, H. Bender, W. Vandervorst, M. Heyns, M. Caymax, I. Radu, A. Delabie, *J. Chem. Phys.* **2019**, *150*, 104703.

[376] Y. Lee, J. W. Dumont, S. M. George, *J. Phys. Chem. C* **2015**, *119*, 25385.

[377] Y. Lee, J. W. DuMont, S. M. George, *ECS J. Solid State Sci. Technol.* **2015**, *4*, N5013.

[378] S. W. Whangbo, Y. K. Choi, K. B. Chung, Y. D. Chung, W. S. Koh, H. K. Jang, H. W. Yeom, K. Jeoung, S. K. Kang, D.-H. Ko, C. N. Whang, *J. Mater. Chem.* **2002**, *12*, 2559.

[379] M. Kumar, R. M. Mehra, A. Wakahara, M. Ishida, A. Yoshida, *J. Appl. Phys.* **2003**, *93*, 3837.

[380] Y. Liao, D. Zhou, S. Shrestha, S. Huang, S. Bremner, G. Conibeer, *Adv. Mater. Interfaces* **2017**, *4*, 2.

List of awards

1. Four-year IWT scholarship for strategic basic research awarded in Dec 2013
2. 2nd place for the oral presentation given in the panel for Inorganic Chemistry at ChemCYS 2016, Blankenberge, Belgium
3. Best student award for oral presentation at Plasma Etch & Strip Conference (PESM) 2017, Leuven, Belgium
4. Best ALE 2017 Student Poster Award at AVS Atomic layer etching workshop, Denver, Colorado

List of patents

1. WO2015091781A3; Method of producing transition metal dichalcogenide layer; Matty Caymax, Markus Heyne, 27.05.2015: Method of producing one or more transition metal dichalcogenide (MX_2) layers on a substrate, comprising the steps of: obtaining a substrate having a surface and depositing MX_2 on the surface using ALD deposition, starting from a metal halide precursor and a chalcogen source (H_2X), at a deposition temperature of about 300°C. Suitable metals are Mo and W, suitable chalcogenides are S, Se and Te. The substrate may be (111) oriented. Also, mixtures of two or more MX_2 layers of different compositions can be deposited on the substrate, by repeating at least some of the steps of the method.
2. US9842734B2; Method of forming a feature of a target material on a substrate; Annelies Delabie, Markus Heyne, 12.12.2017: A method is provided for forming a feature of a target material on a substrate. The method including: forming a feature of a sacrificial material on the substrate; and forming the feature of the target material by a deposition process during which the feature of the sacrificial material is removed from the substrate by forming a volatile reaction product with a precursor of the deposition process, wherein the sacrificial material is replaced by the target material and

the target material is selectively deposited on surface portions of the substrate, which portions were covered by the feature of the sacrificial material, to form the feature of the target material.

List of publications

1. M. H. Heyne; D. Marinov; N. Braithwaite; A. Goodyear; J.-F. de Marneffe; M. Cooke; I. Radu; E.C. Neyts; S. De Gendt, A Route Towards the Fabrication of 2D Heterostructures Using Atomic Layer Etching Combined with Selective Conversion . *2D Materials* **2019**.
2. M. H. Heyne, J.-F. de Marneffe, I. Radu, E. C. Neyts, S. De Gendt, S. Thermal Recrystallization of Short-Range Ordered WS$_2$ Films. *J. Vac. Sci. Technol. A* **2018**, *36*, 05G501.
3. M. H. Heyne, J.-F. de Marneffe, T. Nuytten, J. Meersschaut, T. Conard, M. Caymax, I. Radu, A. Delabie, E. C. Neyts, S. De Gendt, The Conversion Mechanism of Amorphous Silicon to Stoichiometric WS$_2$. *J. Mater. Chem. C* **2018**, *6*, 4122.
4. M. H. Heyne, J.-F. de Marneffe, A. Delabie, M. Caymax, E. C. Neyts, I. Radu, C. Huyghebaert, S. De Gendt, Two-Dimensional WS$_2$ Nanoribbon Deposition by Conversion of Pre-Patterned Amorphous Silicon. *Nanotechnology* **2017**, *28*, 04LT01.
5. M. H. Heyne, D. Chiappe, J. Meersschaut, T. Nuytten, T. Conard, H. Bender, C. Huyghebaert, I. P. Radu, M. Caymax, J.-F. de Marneffe, E. C. Neyts, S. De Gendt, Multilayer MoS$_2$ Growth by Metal and Metal Oxide Sulfurization. *J. Mater. Chem. C* **2016**, *4*, 1295.
6. T. Schram, Q. Smets, B. Groven, M. H. Heyne, E. Kunnen, A. Thiam, K. Devriendt, A. Delabie, D. Lin, M. Lux, D. Chiappe, I. Asselberghs, S. Brus, C. Huyghebaert, S. Sayan, A. Juncker, M. Caymax, I. P. Radu, WS$_2$ Transistors on 300 mm Wafers with BEOL Compatibility, in *2017 47th Eur. Solid-State Device Res. Conf.*, IEEE, **2017**, pp. 212–215.
7. T. Schram, Q. Smets, M. H. Heyne, B. Groven, E. Kunnen, A. Thiam, K. Devriendt, A. Delabie, D. Lin, D. Chiappe, I.

Asselberghs, M. Lux, S. Brus, C. Huyghebaert, S. Sayan, A. Juncker, M. Caymax, I. P. Radu, BEOL Compatible WS_2 Transistors Fully Fabricated in a 300 mm Pilot Line, in *2017 Silicon Nanoelectron. Work.*, IEEE, **2017**, pp. 139–140.

8. B. Groven, M. Heyne, A. Nalin Mehta, H. Bender, T. Nuytten, J. Meersschaut, T. Conard, P. Verdonck, S. Van Elshocht, W. Vandervorst, S. De Gendt, M. Heyns, I. Radu, M. Caymax, A. Delabie, Plasma-Enhanced Atomic Layer Deposition of Two-Dimensional WS_2 from WF_6, H_2 Plasma, and H_2S. *Chem. Mater.* **2017**, *29*, 2927.
9. C. J. Lockhart de la Rosa, A. Nourbakhsh, M. Heyne, I. Asselberghs, C. Huyghebaert, I. Radu, M. Heyns, S. De Gendt, Highly efficient and stable MoS_2 FETs with reversible n-doping using a dehydrated poly(vinyl-alcohol) coating. *Nanoscale* **2017**, *9*, 258.
10. D. Chiappe, I. Asselberghs, S. Sutar, S. Iacovo, V. Afanas'ev, A. Stesmans, Y. Balaji, L. Peters, M. Heyne, M. Mannarino, W. Vandervorst, S. Sayan, C. Huyghebaert, M. Caymax, M. Heyns, S. De Gendt, I. Radu, A. Thean, Controlled Sulfurization Process for the Synthesis of Large Area MoS_2 Films and MoS_2 /WS_2 Heterostructures. *Adv. Mater. Interfaces* **2016**, *3*, 1500635.
11. A. Delabie, M. Caymax, B. Groven, M. Heyne, K. Haesevoets, J. Meersschaut, T. Nuytten, H. Bender, T. Conard, P. Verdonck, S. Van Elshocht, S. De Gendt, M. Heyns, K. Barla, I. Radu, A. Thean, Low Temperature Deposition of 2D WS_2 Layers from WF_6 and H_2S Precursors: Impact of Reducing Agents. *Chem. Commun.* **2015**, *51*, 15692.

Poster and Conference Contributions

1. Plasma Etch and Strip in Microfabrication, October 19-20, 2017, Presentation "Atomic layer etching of amorphous silicon with selectivity towards MoS_2 for novel MX_2 heterostructure device concepts"

2. ALE Workshop, July 15 – 18, 2017, Denver; Poster "Atomic layer etching of amorphous silicon with selectivity towards MoS_2"
3. iPlasmaNano-VIII, July 2-6, 2017, Antwerp; Poster "Atomic layer etching of amorphous Si on MoS_2 for selectively patterned MX_2 heterostructures"
4. Graphene, March 28-31, 2017, Barcelona; Poster "Selective patterning of amorphous silicon on MoS_2 to fabricate transition-metal dichalcogenide heterostructures"
5. ChemCYS, March 16-18, 2016, Blankenberge; Presentation "Sulfurization of Metallic and Oxidized Molybdenum Thin Films"
6. ISPC, July 5-10, 2015, Antwerp; Poster "Investigations on the Plasma-Surface Interaction during Atomic Layer Etching of Thin Transition-Metal Dichalcogenide Films"
7. 1st Conference on Nanospectroscopy for 2D Materials, September 8-10, 2015, Chemnitz; Presentation "Growth of Multilayer Transition-Metal Dichalcogenide Layers by High Temperature Sulfurization in H_2S"

Environment, Safety, Health

This work was conducted in the facilities of imec in Heverlee. The safety standards within the organization are very high. The performed works were conducted always with the necessary personal protective equipment (PPE). Since all tasks were done in a cleanroom, it is obligatory to wear always Nitrile gloves, safety glasses, and a cleanroom suit. For the wet treatments, the protective equipment was complemented by acid-resistant gloves, face shield, and apron where necessary. These works were done in perforated wet benches or fume hoods ensuring the gas transport away from the operator. Adjacent to the wet treatment areas, emergency eye wash and safety showers are installed. The use of latter ones calls automatically further help from a 24h operating control room with first aid trained staff.

The gas phase conversions and annealings were done in respective closed tools, which were either completely sealed and only accessible through a loadlock or which could be opened only at room temperature to load the samples. All the processing chambers were equipped with pressure, temperature, or flow sensors and interlocks preventing chamber opening under dangerous conditions, e.g. high temperature or flowing gas while operating in or at the chamber manually. In addition to the internal safety interlocks, the chambers' casings are connected to an exhaust system ensuring the outgoing airflow, which is also monitored by gas sensors of the used gases and connected to an automatic control system. In case of exceeding alarm limits, an automatic alarm with visual and acoustic signal is triggered and all people in the adjacent lab areas must leave the working place until an all-clear signal is given. The work in areas without frequent occupation requires the use of a deadman sensor, which is connected to a control room.

The disposal of waste was done carefully to avoid safety risks and protect the environment. Wet waste was separated in acid waste, contaminated (metal-containing) acid waste, and solvent waste which related to appropriate tubing to avoid corrosion or explosion risks. Gaseous waste was cleaned in scrubbers.

Several chemicals were used within this project. The solids used here were the precursor metals Mo and W in their oxidized or sulfurize form, Si and SiO_2, Al_2O_3, Co, Ni, and Au. When cleaving sample containing those materials or handling in their particle form, FFP3 face masks were used as protection.

Different liquids were used for resist-coating, development, sample cleaning, and etching including C_3H_6O, C_3H_8O, tetramethylammonium hydroxide (TMAH), H_2SO_4, HNO_3, H_2O_2, and HF. Acids, bases, and solvents were used in separated wet benches or fume hoods and were also disposed accordingly.

A variety of gases were used for dry etching including Ar, Cl_2, BCl_3, CF_4, CH_2F_2, and H_2. All gases were used within sealed reactors and were sufficiently long pumped from the samples before exposing them to air again. Moreover, gases were used for the conversion of solids into metal and the metal conversion into sulphides. WF_6 and H_2S were used for this purpose. Due to the high sticking coefficients of H_2S, samples had be stored in vacuum until their cool-down to room temperature at which they were stable.